

**Modelling Damage in Turbine Blades
and Their Coatings**

By

Farnaz Ostovari

A thesis submitted to Imperial College London
for the degree of Doctor of Philosophy

Mechanical Engineering Department as part of the
CDT in Theory and Simulation of Materials

November 24, 2018

Declarations

Copyright Declaration

The copyright of this thesis rests with the author. Unless otherwise indicated, its contents are licensed under a Creative Commons Attribution-Non Commercial 4.0 International Licence (CC BY-NC). Under this licence, you may copy and redistribute the material in any medium or format. You may also create and distribute modified versions of the work. This is on the condition that: you credit the author and do not use it, or any derivative works, for a commercial purpose.

When reusing or sharing this work, ensure you make the licence terms clear to others by naming the licence and linking to the licence text. Where a work has been adapted, you should indicate that the work has been changed and describe those changes. Please seek permission from the copyright holder for uses of this work that are not included in this licence or permitted under UK Copyright Law.

Declaration of Originality

I, Farnaz Ostovari, confirm that the work presented in this thesis is my own. Wherever the information is taken from other sources, careful consideration has gone into referencing and acknowledging their work.



Acknowledgments

The time has finally come! As I am writing this acknowledgement I am thinking back to four years ago when I started my PhD at Imperial College London, which was right after my MSc in TSM-CDT at Imperial. I thought it was as hard as it gets, but then the PhD started. These four years have been a real roller coaster ride with countless ups and downs, and slow and fast paces; the only thing that got me through all of this was the support and motivation I got from my amazing family, friends and colleagues.

This journey would have not been possible without the support and loving care of my wonderful parents, Farah and Sohrab, who patiently supported me; or the wise and supporting words that my lovely husband, Soroush, told me at my lowest hours; or the wonderful gifts that my cousins, Vista and Nikta, and my aunt, Mojdeh, gave me every time I achieved something; or the wonderful wishes and positive support that my kind parents-in-law, Kati and Rostam, my aunt, Marya, cousin Ariyana, and the rest of my family send through to me.

When it comes to emotional support and motivation, in addition to my family I had the biggest support from my wonderful friends and colleagues Dr Elnaz Salehzadeh Nobari, Shirin Amani, Miranda Smith, Veena Dhulipala, Val Crawford, Drew Pearce, Dr Nichola Molinari, Mitesh Patel, Dr Tasnuva Khaleque, Yizhou Li (Sherry), Dr Eduard Minoux, Dr Jisoo Ahn, Dr Teddy Szemberg O'Connor, Dr James Tebutt, Alex Sanches, Joel Henry, Dr Michele Pettina, Dr Morad Karimpour, Dr Yong Li, Dr Kang Ji, Dr Bruce Chen, Dr Soraia Pimenta, Prof. Kamran Nikbin, Dr Frank Abdi, Prof. Peter Haynes, Prof. Adrain Sutton, Prof. Craig Carter, and many more wonderful people who supported

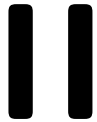
me through this challenging yet rewarding journey.

On the technical side, firstly, I would like to thank my supervisors for their support and guidance. My first supervisor, Dr D. Balint supported me throughout this PhD, particularly, for the development of the analytical models, studying the relationship between swelling and rumpling in thermal barrier coatings; and my second supervisor, Prof. M.H. (Ferri) Aliabadi, who provided the relevant support and resources for understanding meshfree methods and their application.

I would also like to thank Prof. Daniele Dini who provided a very helpful guidance on the structure of this PhD, particularly, in the contact modelling part of this work; Dr Catrin Davies who supported me on writing subroutines for Abaqus, Prof. Arash Mostofi for supporting me emotionally through the tough times in my PhD, and all of my wonderful colleagues from MOM and TSM-CDT at Imperial College for their help and support.

My biggest gratitude is to Prof. Ali Salehzadeh Nobari who not only supported me emotionally throughout my work but also had a significant influence on my progress in the meshfree part of this work. As a part of the contact development in the RPIM method, Prof. Nobari arranged for me to go to Amir Kabir University of Tehran to work along side him on the development of my meshfree contact model. Without his wise guidance and helpful ideas this would not have been possible, so thank you. Additionally, I met my husband, Soroush, because of my PhD times at Amir Kabir and I truly can say it was one of the most important gifts of life that I came across in this journey.

At the end, I would like to dedicate this thesis to all the wonderful people in my life, especially my grandparents, all of whom I have lost; particularly, my mum's mother, mamani, who died this year and made the end of this journey really difficult for me. But her wonderful memories and amazing life lessons will always stay with me.



Abstract

In the process of modelling damage in turbine blades and their coatings, four studies were carried out in this thesis. The first two chapters focus on modelling the damage in thermal barrier coatings or TBCs which are commonly used for Ni-based turbine blades. The second two chapters focus on development of meshfree methods for modelling micro-cracks in woven $\text{SiC}_f/\text{SiC}_m$ composites which are a potential future material to be used for turbine blades. A brief summary of the main achievements from each chapter is given here as an insight into what is expected from each work.

- **Swelling as the Main Source of Rumpling in TBC, chapter 2:** Previously it was believed that the main source of rumpling growth in TBC systems is from phenomenon such as phase transformation and thermal mismatch that occur during the heating and cooling processes of a thermal cycle. However, the findings from an experimental work by Tolpygo & Clarke could not be explained with the previously suggested theories, where no difference in the rumpling amplitude was observed as the lower temperature of the thermal cycles was changed, except for the isothermal case. This behaviour was puzzling because it mitigated the effects of phase transformation and thermal mismatch. In this work, the existing analytical model of rumpling by Balint *et al.* was modified to include a relatively new phenomenon known as swelling, and used to reproduce and explain the experimental results. The analysis of the data from the developed model revealed that most of rumpling occurs during the dwell which is caused by swelling; its effects are also apparent during heating and cooling processes. Therefore, swelling proves to be the main source of rumpling growth.
- **Lateral Growth in the Bond Coat and Inter-diffusion Layers, chapter 3:** In the process of understanding the puzzling outcome from the experimental work of Chen *et al.* on measuring

the lateral growth of the bond coat/inter-diffusion layers of TBC system after 50 hours of isothermal heat treatment at 1150°C, two finite element models of the system were produced; one with the coating modelled as two layers and another with the coating modelled as four layers. Chen *et al.* experimental results showed a large lateral deformation for the bond coat and almost none for the inter-diffusion layer, which was surprising because swelling effect which is a volumetric phenomenon, was observed in both layers, hence, it should have led to lateral swelling for the inter-diffusion layer as well. In this work, it was shown that because of the non-uniform nature of the Ni/Al inter-diffusion the two-layered model is not detailed enough to capture the real behaviour of the system, hence, the four-layered model is introduced which more closely matches the experimental results. This outcome indicated that modelling this system with two layers can create implications when modelling rumpling, therefore, a multi-layered coating system, such as the four-layered model shown in this work, is needed for modelling rumpling more accurately.

- **MQ-RPIM Optimisation for Engineering Single Body Problems, chapter 4:** Multi-quadrics radial point interpolation meshfree (MQ-RPIM) method is one of the common meshfree methods currently used. However, the shape parameters involved in the generalised multi-quadric method have a strong influence on the accuracy of the solutions. In addition to the shape parameters, there are variables related to the integrations involved in the MQ-RPIM method that affect its accuracy. In this work a novel systematic algorithm was introduced which produces the best values for the variables involved in the MQ-RPIM method, including the integration and MQ shape parameters, for any engineering problem. For demonstration, this method is applied to three solid mechanic problems in both two- and three-dimensional forms.
- **MQ-RPIM Model of Plain Woven Composite with Frictionless Contact, chapter 5:** In the process of developing an explicit model for the micro-cracks at the yarn-matrix interface of a woven SiC_f/SiC_m composite using meshfree methods, the first three-dimensional MQ-RPIM frictionless contact code is developed from scratch and successfully applied to the preliminary model of a plain woven composite unit cell for two limiting conditions; i) full-stick (0% delamination) and ii) full-slip (100% delamination). As part of the development for this contact model, a two-dimensional frictionless contact model is also produced, where both two- and three-dimensional forms of the contact code are verified against analytical and finite element results for two Hertzian contact problems. The MQ-RPIM results for the Hertzian examples made a use of optimisation algorithm introduced in chapter 4, confirming the use of this algorithm and flexibility of the MQ-RPIM method compared to the FEM for models with non-uniform distribution of nodes, particularly at contact regions.

Contents

I Acknowledgments	i
II Abstract	iii
Contents	v
List of Figures	x
List of Tables	xix
1 Introduction	1
1.1 TBC Coated Ni Superalloy	2
1.2 EBC Coated SiC/SiC Woven Composite	4
1.3 Thesis Structure	6
1.4 Bibliography	6
2 Swelling as the Main Source of Rumpling in TBC	8
2.1 Introduction	8
2.1.1 Literature Review	10
2.1.2 Objective	16
2.2 Mathematical Model and Implementation	16

2.2.1	Mathematical Model	16
2.2.2	Rumpling Equation	18
2.2.2.1	TGO	20
2.2.2.2	Bond Coat	21
2.2.3	Model Set Up	25
2.3	Results & Discussion	26
2.3.1	Swelling	30
2.3.2	Initial Conditions	33
2.3.3	Rumpling During Heating and Cooling	35
2.4	Conclusion	37
2.5	Table of variables	39
2.6	Bibliography	40
3	Lateral Growth in the Bond Coat and Inter-diffusion Layers	43
3.1	Introduction	43
3.1.1	Literature Review	44
3.1.2	Objective	46
3.2	Materials and Methods	47
3.2.1	Experimental Procedure	47
3.2.1.1	Results of the Experiment	48
3.2.2	Modelling	50
3.2.2.1	Fitting the experimental Data	51
3.2.2.2	Analytical Models	52
3.2.2.3	Creep Property Sensitivity Study	55
3.2.2.4	Verification of Finite Element Model	57
3.2.2.5	Two-Layered Coating Model	66
3.2.2.6	Four-Layered Coating Model	72
3.3	Results & Discussion	77
3.4	Conclusion	78
3.5	Table of variables	80
3.6	Bibliography	81
3.A	Appendix	83
4	MQ-RPIM Optimisation for Engineering Single Body Problems	88
4.1	Introduction	88
4.1.1	Literature Review	89
4.1.2	Objective	94

4.2	Materials and Method	94
4.2.1	Radial Point Interpolation Method	94
4.2.1.1	Gaussian Approximation	96
4.2.1.2	Radial Basis Function	97
4.2.1.3	System of Linear Equations	100
4.2.2	Step-by-Step Optimisation Method	102
4.2.2.1	Error Indicators	103
4.2.2.2	Convergence	104
4.2.2.3	Optimisation	106
4.2.3	Single Body Examples	106
4.2.3.1	Cantilever Beam Bending	107
4.2.3.2	Uniform Compression on a Cube	108
4.2.3.3	Line Compression on a Cylinder	109
4.3	Results & Discussion	110
4.3.1	Verification - Cantilever Beam	110
4.3.1.1	Convergence	110
4.3.1.2	Optimisation	120
4.3.2	Square/Cube	124
4.3.2.1	Convergence	124
4.3.2.2	Optimisation	130
4.3.3	Circle/Cylinder	134
4.3.3.1	Convergence	134
4.3.3.2	Optimisation	141
4.4	Conclusion	144
4.5	Table of variables	146
4.6	Bibliography	147
5	MQ-RPIM Model of Plain Woven Composite with Frictionless Contact	152
5.1	Introduction	152
5.1.1	Literature Review	153
5.1.1.1	Woven Composites	153
5.1.1.2	Meshfree Contact Modelling	158
5.1.2	Objective	161
5.2	Materials & Methods	163
5.2.1	Contact Theory	164
5.2.2	Contact Algorithm	167

5.2.2.1	Pre-contact Search	169
5.2.2.2	Contact Detection	170
5.2.2.3	Post-Contact Detection	171
5.2.3	Contact Incrementation	172
5.2.4	Contact Verification	172
5.2.4.1	Hertzian Contact Model	173
5.2.4.2	RPIM Contact Verification	174
5.2.5	Preliminary model of the plain woven composite unit cell	176
5.3	Results & Discussion	178
5.3.1	Hertzian Contact - Deformable Cylinder/Rigid Plane	178
5.3.1.1	Convergence	178
5.3.1.2	Size of the Support Domain	181
5.3.1.3	Optimisation	183
5.3.2	Hertzian Contact - Deformable Cylinder/Deformable Plane	186
5.3.2.1	Convergence	186
5.3.2.2	Size of the Support Domain	189
5.3.2.3	Optimisation	191
5.3.3	Preliminary Model of the Woven Unit Cell	193
5.3.3.1	Full Stick	193
5.3.3.2	Full Slip	194
5.4	Conclusion	195
5.5	Table of variables	197
5.6	Bibliography	198
6	Conclusion	206
7	Future Work	209
7.1	Outputs	211
AppendixA	MQ-RPIM Code Structure	212
A.1	Introduction	212
A.2	RPIM Single Body Code Structure	213
A.2.1	Input	214
A.2.2	Define Geometry and Background Cells	214
A.2.2.1	Geometry	214
A.2.2.2	Background Cells	214
A.2.3	Define Material Property Matrix	215

A.2.4	Define Gauss Point Coefficients	215
A.2.5	Mapping to the Parent Domain	215
A.2.6	Compute Jacobian	215
A.2.7	Compute and Assemble \mathbf{K}	215
A.2.8	Apply Boundary Conditions	216
A.2.9	Solve $\mathbf{KU} = \mathbf{F}$	216
A.2.10	Compute Stress and Strain	217
A.3	RPIM Frictionless Contact Code Structure	217
A.3.1	Pre-Contact Search	218
A.3.2	Contact Detection	218
A.3.3	Checking the Normal Contact Forces	218

List of Figures

1.1	An annotated image of a jet engine with an outline of a turbine blade. The image of the jet engine was taken from Bennett on Flickr.com	2
1.2	A schematic of materials used in the two types of turbine blades studied here. Left: TBC coated Ni superalloy and right: EBC coated woven $\text{SiC}_f/\text{SiC}_m$ composite.	3
2.1	An outline of the thermal barrier coating system on the substrate.	9
2.2	A schematic of the Ni-Al inter-diffusion between the substrate and the bond coat leading to swelling.	13
2.3	Temperature change for thermal cycling and isothermal experiments carried out by Tolpygo & Clarke [1].	14
2.4	The experimental results from [1] for the root-mean-square (RMS) of roughness amplitude, δ_{RMS} , on the bond coat's surface after $100 \times 1\text{h}$ thermal cycles, versus T_2	15
2.5	Schematic of the TBC system that is modelled here, (The image is drawn based on the infographic taken from [15].)	17
2.6	Change of $E^{(2)}$ and $\alpha^{(1)} - \alpha^{(2)}$ with temperature; $\alpha^{(1)}$ and $\alpha^{(2)}$ were taken from [25]. In this image, positive value of $\alpha^{(1)} - \alpha^{(2)}$ means the bond coat is under tensile stress during heating and compressive stress during cooling and vice versa.	18
2.7	Swelling related stress, as it changes with temperature and number of cycles for both thermal cycle and isothermal case. Here the creep and thermal mismatch effects are not included.	25
2.8	The root-mean-square (RMS) amplitude of roughness on the bond coat's surface, δ_{RMS} , after $100 \times 1\text{h}$ thermal cycles versus T_2 for both experimental [1] and analytical model.	27
2.9	Left: Rumpling amplitude, δ_{RMS} , at the end of each cycle. Right: Rumpling amplitude, δ_{RMS} for the first three cycles/hours.	28
2.10	Change in the rumpling amplitude at every step of every thermal cycle and every isothermal hour for the three cases under study.	29
2.11	Change in bond coat stress during dwell, i.e. $ \sigma_{11_{\text{end dwell}}} - \sigma_{11_{\text{start dwell}}} $	29
2.12	Change of bond coat stress for the dwell duration in the 1 st , 2 nd , 5 th , 10 th , 50 th and 100 th cycles for $T_2 = 25, 1050$ and 1150°C . Please note that the x-axis is the normalised time where t_{cycle} is 3600s for isothermal case and 4680s for thermal cycling case.	32
2.13	$\sigma_{11}^{(2)}$, and temperature change of the pre-steps for $T_2 = 25, 1050$ and 1150°C vs time. Negative time here means before the start of the actual experiment.	33

2.14	Stress changes from creep, swelling and thermal mismatch separately for the heating pre-step of $T_2 = 1050^\circ\text{C}$ and 1150°C	34
2.15	Stress changes of the heating and cooling processes in the cycles 1,2,5,10,50 and 100 for $T_2 = 25$ and 1050°C vs time.	36
3.1	A summary of the two- and three-layered bond coat and IDZ, and their phases as a result of the manufacturing process, (This infographic has been adapted for this thesis from [15].)	45
3.2	The experimental lateral swelling of the bond coat and inter-diffusion layer after 50 hours annealing at $T = 1150^\circ\text{C}$ obtained by Chen <i>et al.</i> a) The image of the system's edge, b) the dimensions of the edge profile and c) the composition of the layers from the surface of the sample. (Images are taken from personal communication with Chen <i>et al.</i>)	48
3.3	The experimental data for thickening of the bond coat (left plot) and the inter-diffusion layer (right plot) in comparison their corresponding power law fit. (The experimental data are taken from personal communication with Chen <i>et al.</i> , i.e. Table 3.1)	51
3.4	In-plane stress (on the left) and swelling strain (on the right) of the bond coat layer computed analytically for 200 hrs at 1150°C , in addition to the comparison between the use of engineering and true strains for the calculations.	55
3.5	Left: the effect of creep reference strain rate, $\dot{\epsilon}_0$, on the in-plane stress, σ_{11} . Right: the effect of the creep exponent, n , on σ_{11} . In each plot the black line represents the stress behaviour of the bond coat material.	56
3.6	The stress relaxation plot of the bond coat with creep properties of $n = 4$ and $\dot{\epsilon}_0 = 0.2$, compared to stress relaxation of the inter-diffusion layer with the chosen creep properties of $n = 3$ and $\dot{\epsilon}_0 = 2.2$	57
3.7	The boundary conditions of the finite element model used for the creep verification . . .	58
3.8	Left: comparison of σ_{11} results and right: comparison of $\bar{\epsilon}_{11}^{cr}$ results. The “Analytic-Complete” in the legend refers to the analytical model based on the multi-axial principal equation and the “Analytic-Equivalent” refers to the model using the equivalent creep strain.	59
3.9	Comparison between the Abaqus results and the experimental results for thickening caused by swelling. The analytical results of the displacement are also shown.	61
3.10	The dimensions and boundary conditions of the inter-diffusion and substrate system used for the verification of the Abaqus model.	63

3.11	The top left plot shows the experimental thickening data for the inter-diffusion layer during 200hrs annealing, in comparison to the thickening results computed by the analytical and Abaqus models of the swelling in this layer. The top right and bottom plots show the swelling strain rate and in-plane stress of the inter-diffusion layer computed by the analytical and Abaqus models of the swelling in this layer. Please note, the legend in the bottom plot is applicable to the other two plots as well.	66
3.12	The dimensions and boundary conditions of the “Two-Layered Coating Model” in Abaqus (Not to scale).	67
3.13	The lateral deformation of the right edge of the coating system (inter-diffusion + bond coat) computed by my Abaqus model for the first step of the sensitivity study compared to the experimental results.	68
3.14	Lateral growth results of the sensitivity study on the elastic property of the inter-diffusion layer, i.e. Top plot - $E^{(2)}$, middle plot - $\nu^{(2)}$ and bottom plot - $\alpha^{(2)}$	70
3.15	Lateral growth results of the sensitivity study on the creep property of the inter-diffusion layer, i.e. Top plot - $\dot{\varepsilon}_0^{(2)}$, and bottom plot - $n^{(2)}$	71
3.16	Top: The image of the system under study before and after the experiment. Bottom: The composition of the layers in the system before and after the experiment. These images are taken from personal contact with Chen <i>et al.</i> Please note the A to F labels here are added manually based on the middle plot in Figure 3.2.	73
3.17	The dimensions and boundary conditions of the two-layered and four-layered models of the coating system. (Not to scale)	74
3.18	Comparison of the right edge profile of the inter-diffusion and bond coat layers when the two-layered and four-layered coating models are used.	77
3.19	The Abaqus UEXPAN subroutine written for the simplified swelling strain rate of the freely expanding cube.	84
3.20	The Abaqus USDFLD and UEXPAN subroutines written for the complete swelling strain rate model of the freely expanding cube.	87
4.1	Demonstration of the support domain around the point of interest in the problem domain, Ω , bounded by Γ	94
4.2	Mapping between the real (left figure) and parent (right figure) space for the Gauss points and the background cell in two-dimensions.	97
4.3	An overview of the convergence and optimisation method introduced here.	102
4.4	The three-dimensional cantilever beam used for verifications.	107
4.5	The boundary conditions for the two- and three-dimensional examples of the cube.	108
4.6	The boundary conditions for the two- and three-dimensional examples of the cylinder.	109

4.7	In each plot the computed energy error from the results of the RPIM code for the two-dimensional version of the beam is shown versus the α_{gp} factor from Equation 4.41. These plots show how increasing N_{FN} and changing the distribution of integration points per background cell, i.e. n_{gp} , affect the energy error. For these calculations $\alpha_s = 3.0$, $\alpha_c = 0.71$ and $q = 1.03$	111
4.8	In each plot the computed energy error from the results of the RPIM code for the three-dimensional version of the beam is shown versus the α_{gp} factor from Equation 4.41. These plots show how increasing N_{FN} and changing the distribution of integration points per background cell, i.e. n_{gp} , affect the energy error. For these calculations $\alpha_s = 3.0$, $\alpha_c = 0.71$ and $q = 1.03$	112
4.9	The plot on the left shows the change of energy error with α_{gp} when the linear polynomial term is not included in the RPIM shape function calculations, for two cases of N_{FN} . The right plot shows the same data as the left plot except that now for the calculations linear polynomial terms are included in the RPIM shape function calculations.	114
4.10	The convergence plots of the two-dimensional RPIM model of the beam using the energy error, maximum percentage error in deflection and maximum percentage error in the shear stress, τ_{zx} , at the mid-length of the beam. The bottom right plot shows the corresponding cpu times.	114
4.11	The deflection and the shear stress profiles of the two-dimensional beam for the converged case in the RPIM code.	115
4.12	The convergence plots of the three-dimensional RPIM model of the beam using the energy error, maximum percentage error in deflection and maximum percentage error in the shear stress, τ_{zx} , at the mid-length of the beam. The bottom right plot shows the corresponding cpu times.	116
4.13	The deflection and the shear stress profiles of the three-dimensional beam for the converged case in my RPIM code.	117
4.14	The deflection of the beam at the neutral axis and the shear stress at the mid-length of the beam computed by two-dimensional RPIM, three-dimensional RPIM, three-dimensional FE and analytical models.	117
4.15	The plots here show the effect of total number of nodes on maximum percentage error in beam deflection, shear stress at the mid-length of the beam, and computational time for the 3D-FE and 3D-RPIM models.	118

4.16	These plots show effect of α_s on energy error, maximum percentage error in deflection, maximum percentage error in shear stress at the mid-length of the beam, and the computational time for two- and three-dimensional RPIM models. The parameters other than α_s for the 2D model are $N_{\text{FN}} = 1235$, $n_{\text{gp}} = 4$, $\alpha_c = 0.71$, $q = 1.03$, $d_c = 2.0$ and $\alpha_{\text{gp}} = 13$, and for the 3D model are $N_{\text{FN}} = 2385$, $n_{\text{gp}} = 4$, $\alpha_c = 0.71$, $q = 1.03$, $d_c = 2.0$ and $\alpha_{\text{gp}} = 4$.	120
4.17	The plots here show the effect of α_c and q on the energy error, maximum percentage error in deflection, and maximum percentage error in τ_{zx} of the two-dimensional beam. The left plots are for the case with linear polynomial included and the right plots are for when no polynomial is included. Here, $N_{\text{FN}} = 1235$, $n_{\text{gp}} = 4$, $\alpha_s = 3.0$, $d_c = 2.0$, and $\alpha_{\text{gp}} = 13$.	122
4.18	The plots here show the effect of α_c and q on the energy error, maximum percentage error in deflection, and maximum percentage error in τ_{zx} of the three-dimensional beam. The left plots are for the case with linear polynomial included and the right plots are for when no polynomial is included. Here, $N_{\text{FN}} = 2385$, $n_{\text{gp}} = 4$, $\alpha_s = 1.5$, $d_c = 2.0$, and $\alpha_{\text{gp}} = 4$.	123
4.19	Computed energy error, e_E , from my 2D RPIM code for the square example versus the α_{gp} factor from Equation 4.41. The plots in this figure also show the effect of N_{FN} and n_{gp} on e_E .	125
4.20	Computed energy error, e_E , from my 2D RPIM code for the cube example versus the α_{gp} factor from Equation 4.41. The plots in this figure also show the effect of N_{FN} and n_{gp} on e_E .	126
4.21	The plots here show convergence of the RPIM model of the square using e_E , maximum percentage error in u_z , and maximum percentage error in σ_{zz} for every n_{gp} . The bottom right plot shows their corresponding cpu time.	127
4.22	The vertical displacement and stress profiles of the two-dimensional cube for the converged case in the RPIM code.	128
4.23	The plots here show convergence of my RPIM model of the cube using e_E , maximum percentage error in u_z , and maximum percentage error in σ_{zz} for every n_{gp} . The bottom right plot shows their corresponding cpu time.	128
4.24	The vertical displacement and stress profiles of the three-dimensional cube for the converged case in the RPIM code.	129
4.25	These plots show effect of α_s on energy error, maximum percentage error in u_z , maximum percentage error in σ_{zz} , and the computational time for two- and three-dimensional RPIM models of the cube. The parameters other than α_s for the square are $N_{\text{FN}} = 289$, $n_{\text{gp}} = 4$, $\alpha_c = 0.71$, $q = 1.03$, $d_c = 2.0$ and $\alpha_{\text{gp}} = 13$, and for the cube are $N_{\text{FN}} = 729$, $n_{\text{gp}} = 4$, $\alpha_c = 0.71$, $q = 1.03$, $d_c = 2.0$ and $\alpha_{\text{gp}} = 2$.	130

4.26	The effect of α_c and q on the energy error, maximum percentage error in u_z , and maximum percentage error in σ_{zz} of the two-dimensional version of the cube. The left plots are for the case with linear polynomial included and the right plots are for when no polynomial is included in the RPIM shape function calculations. Here, $N_{\text{FN}} = 289$, $n_{\text{gp}} = 4$, $\alpha_s = 1.2$, $d_c = 2.0$, and $\alpha_{\text{gp}} = 13$	131
4.27	The effect of α_c and q on the energy error, maximum percentage error in u_z , and maximum percentage error in σ_{zz} of the three-dimensional version of the cube. The left plots are for the case with linear polynomial included and the right plots are for when no polynomial is included in the RPIM shape function calculations. Here, $N_{\text{FN}} = 729$, $n_{\text{gp}} = 4$, $\alpha_s = 2.0$, $d_c = 2.0$, and $\alpha_{\text{gp}} = 2$	133
4.28	Percentage error of the computed reaction force from the 2D RPIM code for the circle example versus the α_{gp} factor from Equation 4.41. The plots in this figure also show the effect of N_{FN} and n_{gp} on the percentage error.	135
4.29	Percentage error of the computed reaction force from the 3D RPIM code for the cylinder example versus the α_{gp} factor from Equation 4.41. The plots in this figure also show the effect of N_{FN} and n_{gp} on the percentage error.	136
4.30	The plots show convergence of the RPIM model of the circle using the percentage error in the reaction force, percentage difference between the top and bottom forces and the percentage error in σ_{yy} at the centre of the circle for every n_{gp} . The bottom right plot shows the corresponding cpu time.	137
4.31	The vertical displacement and stress profiles of the two-dimensional circle for the converged case in the RPIM code.	138
4.32	The plots show convergence of the RPIM model of the cylinder using the percentage error in the reaction force, percentage difference between the top and bottom forces and the percentage error in σ_{yy} at the centre of the circle for every n_{gp} . The bottom right plot shows the corresponding cpu time.	138
4.33	The vertical displacement and stress profiles of the three-dimensional cylinder for the converged case in the RPIM code.	139
4.34	These plots show effect of α_s on the percentage error in the reaction force, percentage difference between the top and bottom forces, percentage error in σ_{yy} at the centre of the cylinder, and the computational time for two- and three-dimensional RPIM models of the cylinder. The parameters other than α_s for the circle are $N_{\text{FN}} = 1261$, $n_{\text{gp}} = 4$, $\alpha_c = 0.71$, $q = 1.03$, $d_c = 2.0$ and $\alpha_{\text{gp}} = 3$, and for the cylinder are $N_{\text{FN}} = 3641$, $n_{\text{gp}} = 4$, $\alpha_c = 0.71$, $q = 1.03$, $d_c = 2.0$ and $\alpha_{\text{gp}} = 4$	140

4.35	The plots here show the effect of α_c and q on the percentage error in the reaction force, percentage difference between the top and bottom forces, and the percentage error in σ_{yy} at the centre of the two-dimensional model of the cylinder. The left plots are for the case with linear polynomial included and the right plots are for when no polynomial is included in the RPIM shape function calculations. Here, $N_{FN} = 1261$, $n_{gp} = 4$, $\alpha_s = 2.0$, $d_c = 2.0$, and $\alpha_{gp} = 3$	142
4.36	The plots here show the effect of α_c and q on the percentage error in the reaction force, percentage difference between the top and bottom forces, and the percentage error in σ_{yy} at the centre of the three-dimensional model of the cylinder. The left plots are for the case with linear polynomial included and the right plots are for when no polynomial is included in the RPIM shape function calculations. Here, $N_{FN} = 3641$, $n_{gp} = 4$, $\alpha_s = 1.5$, $d_c = 2.0$, and $\alpha_{gp} = 4$	144
5.1	Different types of composite, showing various combinations of fibres and matrix, (Images are drawn based on the infographic taken from [8]).	154
5.2	A few different architectures of 2D woven composites and their properties, (the images are drawn based on the infographic taken from [15]).	155
5.3	Demonstration of the proposed idea for modelling the micro-crack at the yarn-matrix interface when each part is considered as an individual body.	162
5.4	Required simplified steps for obtaining the final model of the woven unit cell with delaminations at the yarn-matrix interface.	163
5.5	Frictionless contact algorithm flow chart used in the RPIM codes.	168
5.6	Left diagram: Red and green lines show the contact territories of the disc and square. The highlighted region shows the common contact territory between these two bodies while the thick black lines show the field nodes regions that fall in the common contact territory. Right diagram: Segment contact territory for a two-dimensional target segment. The green contactor node is within the segment contact territory and forms a test-pair with the segment, whereas the red node does not.	169
5.7	Point of intersection (red point) between the contactor, C., and the target segment, T.S., as the contactor node crosses the target segment for both two- and three-dimensional cases. The intersection point must be within the path of the contactor and the limits of the target segment.	170
5.8	The boundary conditions and geometry of the contact models used in this verification for both two- and three-dimensional cases.	175
5.9	Steps taken from the full woven composite material to the smallest cell that can be used to model the property of the whole composite without addition of unnecessary information.	176

-
- 5.10 **Left:**The smooth definition of the yarn cross section introduced by [39]. (The image is drawn based on the infographic from [39].) **Right:** The dimensions of the plain woven composite sub-cell modelled here. 177
- 5.11 The applied strain boundary condition to the preliminary model of the plain woven composite. 178
- 5.12 The plots here show the convergence results for error indicators of the two- and three-dimensional frictionless Hertzian contact between a deformable cylinder and a rigid plane modelled with the developed RPIM code, and their corresponding simulation times. The first row of plots show the maximum percentage error in the contact stresses, i.e. $p(x)$; the second row of plots show the percentage error in the central contact stress, i.e. p_0 ; the third row of plots show the percentage error in the contact area, i.e. a ; and finally the fourth row of plots show their corresponding computational time. 180
- 5.13 The plots here show the converged RPIM stress profile of the contact region against the analytical solution for **left:** two-dimensional, and **right:** three-dimensional contact examples between a deformable cylinder and a rigid plane. 181
- 5.14 The plots here show change of the three error indicators and their corresponding computational time for the two- and three-dimensional versions of the contact between a deformable cylinder and a rigid plane as size of the support domain or α_s changes. The right axis of the plots and the blue line correspond to the three-dimensional case, and the left axis of the plots with all the other coloured lines corresponds to the two-dimensional case. 182
- 5.15 The left plots show change of the three error indicators with α_c and q , for the two-dimensional contact between a deformable cylinder and a rigid plane modelled by the developed RPIM code. The right plots show the same information but for the three-dimensional version of this contact example. 184
- 5.16 The figures here show the comparison between the two-dimensional RPIM contact code and FE (Abaqus/CAE 6.14-4) for the computed vertical stress and displacement profile of the deformable cylinder and the rigid plane. **Left two figures:** the vertical stress (σ_{yy}) profile, and **Right two figures:** the vertical displacement (u_y) profile. 185
- 5.17 The figures here show the comparison between the three-dimensional RPIM contact code and FE (Abaqus/CAE 6.14-4) for the computed vertical stress and displacement profile of the deformable cylinder and the rigid plane. **Left two figures:** the vertical stress (σ_{zz}) profile, and **Right two figures:** the vertical displacement (u_z) profile. 186
-

5.18 The plots here show the convergence results for error indicators of the two- and three-dimensional frictionless Hertzian contact between a cylinder and a plane of the same material modelled with the developed RPIM code, and their corresponding simulation times. The first row of plots show the maximum percentage error in the contact stresses, i.e. $p(x)$; the second row of plots show the percentage error in the central contact stress, i.e. p_0 ; the third row of plots show the percentage error in the contact area, i.e. a ; and finally the fourth row of plots show their corresponding computational time. 188

5.19 The plots here show the converged RPIM stress profile of the contact region against the analytical solution for **left**: two-dimensional, and **right**: three-dimensional contact examples between a deformable cylinder and a deformable plane. 189

5.20 The plots here show change of the three error indicators and their corresponding computational time for the two- and three-dimensional versions of the contact between a deformable cylinder and a deformable plane as size of the support domain or α_s changes. The right axis of the plots and the blue line correspond to the three-dimensional case, and the left axis of the plots with all the other coloured lines corresponds to the two-dimensional case. 190

5.21 The left plots show change of the three error indicators with α_c and q , for the two-dimensional contact between a deformable cylinder and a deformable plane modelled by the RPIM code. The right plots show the same information but for the three-dimensional version of this contact example. 191

5.22 The figures here show the comparison between the two-dimensional RPIM contact code and FE (Abaqus/CAE 6.14-4) for the computed vertical stress and displacement profile of the deformable cylinder and the deformable plane. **Left two figures**: the vertical stress (σ_{yy}) profile, and **Right two figures**: the vertical displacement (u_y) profile. 192

5.23 The figures here show the comparison between the three-dimensional RPIM contact code and FE (Abaqus/CAE 6.14-4) for the computed vertical stress and displacement profile of the deformable cylinder and the deformable plane. **Left two figures**: the vertical stress (σ_{zz}) profile, and **Right two figures**: the vertical displacement (u_z) profile. 193

5.24 Comparison between FEM and the developed RPIM code in computing the displacement profile of the yarns and unit cell for the full-stick condition when a strain is applied in the xx direction. 194

5.25 The displacement profile of the yarns for the full-slip case when a strain is applied in the xx direction, comparing the RPIM code results with FEM. 195

A.1 The code structure used for the RPIM single body and frictionless contact problems. 213

List of Tables

2.1	Swelling parameters for thermal cycling and isothermal cases based on the data taken from [13].	22
2.2	A summary of the material properties and data used in the analytical model of rumpling.	26
2.3	Variables and terms used in this chapter and their definitions.	39
3.1	The experimental data and their relative errors for the thickness of bond coat and inter-diffusion layers, and the lateral growth of the bond coat layer. (Data taken from personal communication by Chen <i>et al.</i>)	49
3.2	Power-law fit parameters for the experimental results of the thickening in the bond coat and inter-diffusion layers.	52
3.3	Material properties of Ni-based single-crystal CMSX-4 taken from [18], used for the finite element model.	63
3.4	Material properties of the bond coat used for the finite element model.	64
3.5	The elastic, creep and swelling properties of each layer used in my two Abaqus models. The column “Swell” gives the material from which the swelling data was used. This table needs to be read together with Figure 3.17.	77
3.6	Variables and terms used in this chapter and their definitions.	80
4.1	The best choice of α_{gp} for a given N_{FN} and n_{gp} in the two- and three- dimensional beam.	113
4.2	The best choice of α_{gp} for a given N_{FN} and n_{gp} in the square and cube examples.	127
4.3	The best choice of α_{gp} for a given N_{FN} and n_{gp} for the circle and cylinder example.	136
4.4	The summary of optimum RPIM shape parameters for the examples in this chapter.	145
4.5	Variables and terms used in this chapter and their definitions.	146
5.1	The best choice of α_{gp} for a given N_{FN} and n_{gp} in the two- and three-dimensional versions of the frictionless contact between a deformable cylinder and a rigid plane.	179
5.2	The best choice of α_{gp} for a given N_{FN} and n_{gp} in the two- and three-dimensional versions of the frictionless contact between a cylinder and a plane of the same material.	186
5.3	Variables and terms used in this chapter and their definitions.	197

1

Introduction

As the need for faster, cheaper and more environmentally friendly aeroplanes is increasing, the need for more efficient and cleaner jet engines is becoming very important as well; as a result, design of both current and future jet engine technologies needs to be adjusted accordingly. Jet engines are multi-functional and complex systems with a need for various materials; Figure 1.1 shows an image of a jet engine with its main sections annotated. One of the most important parts of a jet engine is its turbine which is placed right after the combustion chamber, as shown in Figure 1.1; this section of the jet engine has a very high temperature and humid environment. In the modern engines the typical working temperature of a turbine could reach up to about $1150^{\circ}C$ [1]. Under certain circumstances, such as one engine failure, this temperature may elevate to about $1700^{\circ}C$, [1], leading to large thermal stresses on the blades. The role of turbine system in a jet engine is to expand the hot air while providing the power to rotate the compressors, therefore, its functionality is essential to the efficiency and life of a jet engine. Turbine system is a series of consecutive discs which have a large number of blades around their circumference. As the hot air comes out of the combustor, it speeds up by passing through these blades leading to rotation of the discs and the shaft that connects them to the compressors.

One of the most important factors in defining the efficiency and life of a turbine is the damage that forms and grows in its blades; this is why understanding the mechanisms that can lead to failure of a turbine blade is of importance. Using simulation and modelling techniques is an efficient and effective way of studying damage, which is why it has formed the main topic of this thesis.

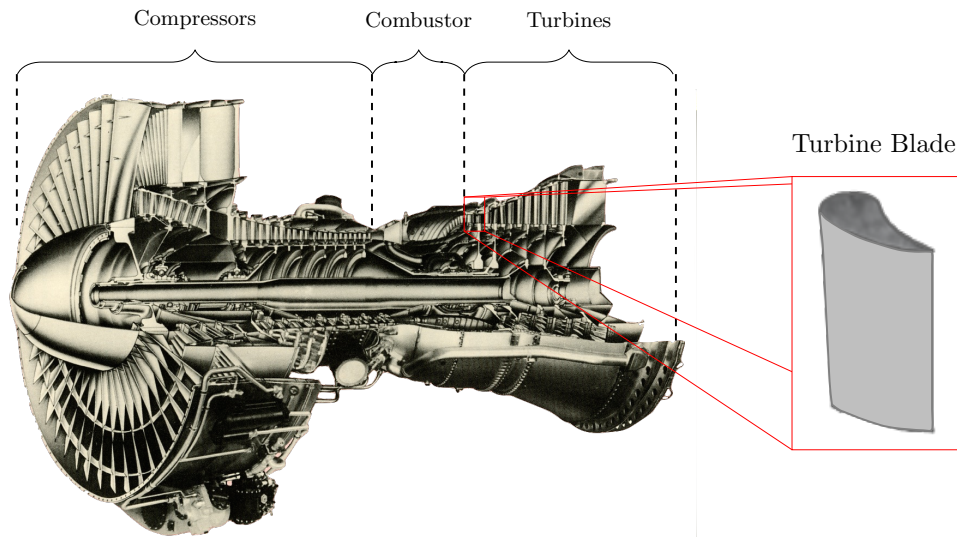


Figure 1.1: An annotated image of a jet engine with an outline of a turbine blade. The image of the jet engine was taken from Bennett on Flickr.com ¹

Most of the damage formed in a turbine blade depends on the behaviour of the material used for building it under the harsh environment of a jet engine; this is why understanding the material properties, and the way that damages form and grow in a turbine blade are important design factors. Because of the limitations in the existing turbine materials and the harsh environment of a turbine, turbine blades require protective coatings. This system of protective coatings is formed of thin layers manufactured over the main turbine material, protecting it against the hot and corrosive environment of a jet engine.

The main objective of this thesis is development of modelling tools for the damage in current and future turbine blades, and their coatings. In this context, current turbine blades refer to the ones with Ni superalloy as their main material which are covered by thermal barrier coatings or TBCs; and future turbine blades refer to the ones using woven $\text{SiC}_f/\text{SiC}_m$ composite as the base material covered by environmental barrier coatings or EBCs; Figure 1.2 shows the material structure of each of these turbines.

1.1 TBC Coated Ni Superalloy

The first turbine blade system to consider is the one with Ni superalloy as the main material or substrate of the blade; this type of turbine blades are currently used in the jet engines. Ni superalloys are attractive because not only they have excellent high temperature properties but also they are very strong at elevated temperatures. As strong as a Ni superalloy is at elevated temperatures, if used on its own it can shorten the life of turbine blade, because in a jet engine environment temperatures can

¹<https://www.flickr.com/photos/bennett4senate/178464723/>

exceed Ni's melting temperature. Therefore, to protect the turbine blades against the high temperature and corrosive environment of a jet engine, thermal barrier coatings (TBCs) have been introduced which are applied on the surface of the superalloy. These coatings consist of three layers; i) bond coat which sticks the rest of the TBC to the substrate, ii) thermally grown oxide (TGO) which forms as oxygen reacts with the Al from the bond coat, and iii) top coat which has columnar structure and protects the lower layers against the high temperature, as shown in Figure 1.2.

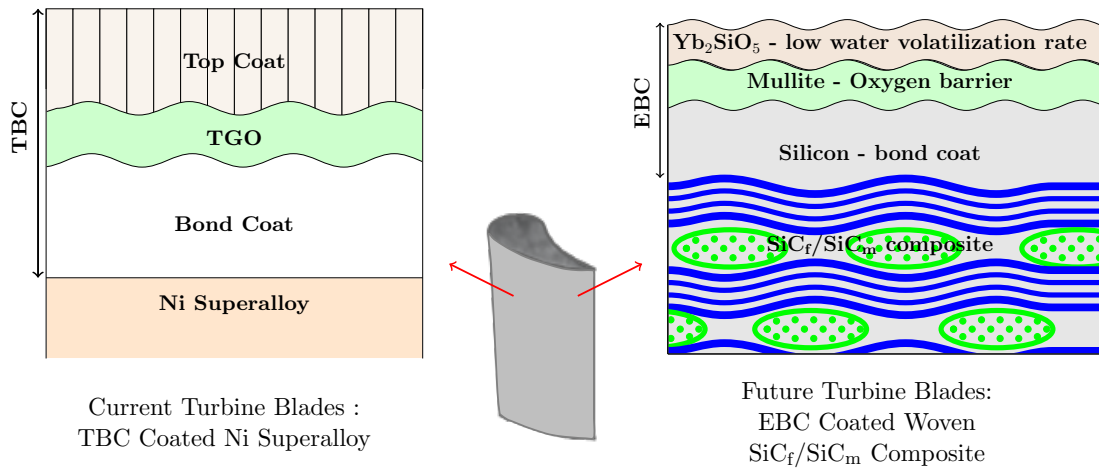


Figure 1.2: A schematic of materials used in the two types of turbine blades studied here. **Left:** TBC coated Ni superalloy and **right:** EBC coated woven SiC_f/SiC_m composite.

Even though the TBC system is designed to protect the substrate against heat and corrosion, over time the compressed TGO starts to buckle, leading to the formation of undulations which after a certain time leads to failure of the TBC system and consequently the turbine blade. This undulation growth is known as rumpling which is a common failure mode for turbine blades, particularly the ones which use (Ni,Pt)Al as the bond coat. This is why understanding rumpling and the main mechanism behind its formation is of great importance.

As a result, chapter 2 of this thesis is dedicated to revealing the underlying source of rumpling growth. In this process a relatively new phenomenon, known as swelling, is incorporated into formulation of an existing analytical model of rumpling by Balint et al., [2], and used together with the experimental results from Tolpygo & Clarke's work, [3], to reveal the underlying source of rumpling. The novelty of this chapter lies in both modification of the analytical model of rumpling and the analysis done to reveal the underlying source of it. The outcome from this chapter can be used to design better and longer lasting turbine blades or for better maintenance of the existing ones.

The next chapter on the current turbine blade technology is chapter 3, which is a continuation to the swelling study from chapter 2. The work presented in this chapter is in collaboration with

Chen *et al.* from Manchester, who provided a set of experimental results on the lateral swelling of the bond coat and inter-diffusion layers after 50 hours isothermal annealing at 1150°C. Inter-diffusion layer is an intermediate layer formed between the bond coat and the substrate as the Ni diffuses from the substrate into the bond coat and Al from the bond coat into the substrate at high temperatures. The objectives for this chapter are understanding the swelling behaviour of the bond coat and inter-diffusion layer in the TBC system from their characteristic lateral swelling, and getting an insight into the material properties of the inter-diffusion layer. In this chapter an analytical model of the stress in the coating layers and a finite element model of the lateral swelling in the coating system under study are developed. The results from this work can then be used to understand the role of inter-diffusion layer, and near-TGO bond coat layer, on rumpling growth and other behaviours in turbine blades.

1.2 EBC Coated SiC/SiC Woven Composite

The second part of this thesis is on the future turbine blades where “future” refers to a new generation of turbine blades with different materials than the ones currently in use. While Ni based turbine blades are excellent and have been in use for years, their melting temperature puts a limitation on the highest temperature and therefore, the efficiency that a jet engine can reach. Given the limitations that Ni-based turbine blades have, new form of materials are required that not only have a very good high temperature and stress properties but also are light enough to be used in an aeroplane. One of the possible solutions to this problem is the use of SiC as the main material for turbine blades; because SiC has covalent bonding, its melting temperature is about 2650°C [4]. In addition to high melting temperature, SiC has high creep resistance and excellent mechanical properties at high temperatures, [5, 6]; it also reduces the CO/NO_x emissions [6, 7], complexity in component design [6] and weight of the components [5, 6].

In spite of all the excellent properties that SiC has, it is a very brittle material and using it in its natural form is not suitable for high stress and impact applications of a jet engine. One solution to this problem is to manufacture it in the form of a woven composite. In this type of composites SiC fibres bundle to form yarns, which are then used to create weave patterns in the x , y and z directions, and finally are bonded together through a matrix of SiC. The resultant composite is called Silicon Carbide fibre reinforced Silicon Carbide matrix (SiC_f/SiC_m) woven composite which has a high specific strength (strength/density) and specific modulus (modulus/density) in addition to its high fatigue life and corrosion resistance [8, 9]. Manufacturing SiC in the form of woven composite reduces the brittleness of this material because at a high enough stresses or during manufacturing, micro-cracks form at the interface of the fibres and the matrix, which allow for yielding and more strain energy absorption in the system, i.e. higher toughness. In spite of their superior properties, woven SiC_f/SiC_m

composites are susceptible to moisture at a high temperature and moist environment, such as a jet engine, therefore, environmental barrier coatings (EBC) are introduced as a protective layer for these composites, as shown in Figure 1.2. EBC is a complex system which is dependent on many parameters across different scales, one of which is the effective property of the composite substrate.

Developing a model to compute the effective properties of woven $\text{SiC}_f/\text{SiC}_m$ composite, given the desired micro-cracks or delaminations at the yarn-matrix interface, formed the main motivation for chapter 4 and chapter 5; here the aim is modelling the yarn-matrix micro-cracks explicitly and computing the effective property of woven $\text{SiC}_f/\text{SiC}_m$ composite given these micro-cracks. One of the most common modelling methods is finite elements, however, for complex geometries such as woven composite, finite elements has mesh distortions issues. Therefore, in order to meet the objectives of these two chapters, multi-quadric radial point interpolation method or MQ-RPIM is used, where RPIM is a branch of meshfree methods. The MQ-RPIM method is easy to implement and has more flexibility for modelling complex geometries than FE, because there is no need for elements; additionally, convergence can be reached with less nodes than FE while allowing for non uniform node distribution.

In spite of the advantages that MQ-RPIM method has its accuracy is dependent on a number of parameters; this is why in chapter 4 an algorithm, which does not exist in the literature, is introduced to give a systematic approach in choosing these parameters for any given problem. This algorithm is then tested on and verified by three single body examples in both two- and three-dimensions where the MQ-RPIM codes used for the calculations are developed from scratch. The outcome from this chapter gives guidance on how to best choose the MQ-RPIM parameters for any given problem.

In the second chapter on this topic, i.e. chapter 5, a frictionless contact code using MQ-RPIM method is developed from scratch in two- and three-dimensions; this is the first three-dimensional contact code using MQ-RPIM method. This contact model is then verified using two Hertzian contact examples in both two- and three-dimensions. The second novelty of this chapter is applying the developed three-dimensional MQ-RPIM frictionless contact code for modelling the yarn-matrix delamination of a plain woven composite under uniform displacement. Given that developing a fully frictional RPIM contact model in three-dimensions is out of the scope of this PhD, only a frictionless contact model is developed and applied to a woven composite unit cell. However, this frictionless contact model forms the building block towards a complete and more realistic model of the micro-cracks at the yarn-matrix interface of woven $\text{SiC}_f/\text{SiC}_m$ composite with frictional contact at the yarn-matrix interface.

1.3 Thesis Structure

Given the difference in the material system of each turbine blade technology, this thesis is formed of two distinct parts; in the first part which includes chapter 2 and chapter 3, the damage mechanism in Ni based turbine blades is modelled, and in the second part which includes chapter 4 and chapter 5, a meshfree code for modelling damage in woven composite based turbine blade is developed. The structure of the RPIM codes developed in this work are summarised in appendix A. The first part of this thesis focuses on modelling rumpling in the coating of Ni superalloy based turbine blades, i.e. TBC, using analytical and finite element modelling; and the second part of this thesis focuses on development of meshfree methods for modelling yarn-matrix delamination in the woven $\text{SiC}_f/\text{SiC}_m$ composites.

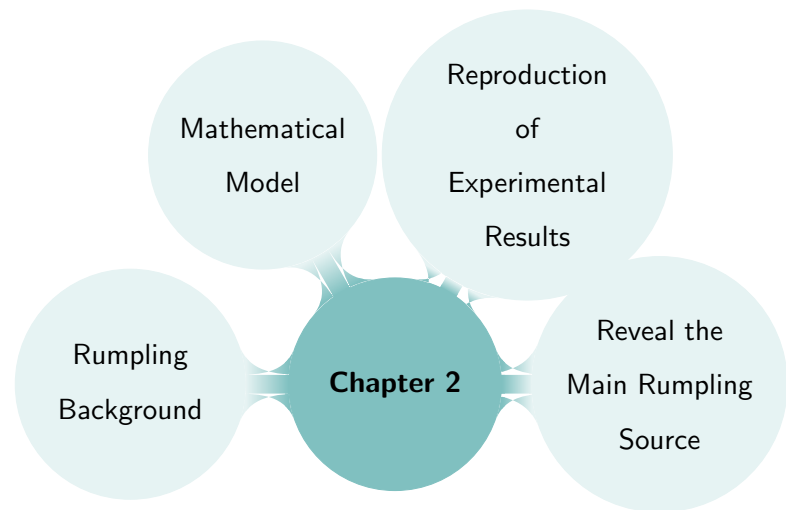
Given the nature of the research in this thesis, each chapter is treated as a separate study having its own introduction, materials and methods, and results and discussion. The abstract of all chapters is collectively presented in the Abstract chapter; similarly for the future work, where a summary of the future possibilities from each chapter is given in Future Work chapter. Additionally, the ways by which the methods developed in this work can be interchanged, are also discussed. For the conclusion, on the other hand, while the outcome from each chapter is summarised in the Conclusion chapter, for convenience of the reader a more detailed conclusion is also given at the end of each chapter.

1.4 Bibliography

- [1] Rolls-Royce. *The jet engine*. Rolls-Royce plc, 1996.
- [2] D S Balint and J W Hutchinson. Undulation instability of a compressed elastic film on a nonlinear creeping substrate. *Acta Materialia*, 51:3965–3983, 2003.
- [3] V K Tolpygo and D R Clarke. Rumpling of CVD (Ni , Pt) Al diffusion coatings under intermediate temperature cycling. *Surface & Coatings Technology*, 203:3278–3285, 2009.
- [4] GoodFellow. Silicon Carbide (SiC), Material Information.
- [5] J.J Brennan. Interfacial Characterization of a Slurry-Cast Melt-Infiltrated SiC/SiC Ceramic-Matrix Composite. *Acta Materialia*, 48(18-19):4619–4628, dec 2000.
- [6] R. Naslain. Design, Preparation and Properties of Non-Oxide CMCs for Application in Engines and Nuclear Reactors: An Overview. *Composites Science and Technology*, 64(2):155–170, feb 2004.
- [7] A.M. Calomino and M.J. Verrilli. SiC Composite Turbine Vanes, 2006.
- [8] David Roylance. Introduction to composite materials. pages 1–7, 2000.

- [9] F. C. Campbell. Introduction to Composite Materials. In *Structural Composite Materials*, chapter One. ASM International, 2010.

2



Swelling as the Main Source of Rumpling in TBC

2.1 Introduction

Turbines are one of the key components in the jet engine and power generation design which perform under high temperature and stress; the typical working temperature for some of the modern turbines is about 1150°C [3]. Under certain circumstances, such as one engine failure, this temperature may elevate to about 1700°C , [3], leading to large thermal stresses on the turbine blades. In these harsh environments, different mechanisms damage the blades and reduce their working life; examples of these mechanisms are creep, thermo-mechanical fatigue and vibration.

To reduce the effect of these damaging mechanisms, while improving the engine's efficiency (i.e. higher burner exit temperature), ceramic coatings have been introduced. Using ceramic coatings as thermal protection has been around since 1942 when NASA's earliest turbine blade oriented ceramic coating was being studied, [4], with a paper published about it in 1947 [5]. Since then, many research works have gone into development and application of ceramic coatings on turbine blades, e.g. [6–11]. These ceramic coatings are generally known as thermal barrier coatings (TBC), whose main functionality is protection of turbine blade's base material, known as substrate, from the high temperature environment and oxidation.

TBCs typically consist of three layers; bond coat, thermally grown oxide (TGO) and top coat, Figure 2.1, where the bond coat is the layer adjacent to the substrate. This layer acts as an adhesive between the substrate and the upper layers of TBC, which is a very important durability factor. There are two common types of material used for the bond coat; i) NiCoCrAlY and ii) Platinum-modified

diffusion nickel aluminide (Ni,Pt)Al; these materials produce Al_2O_3 when undergoing oxidation at high temperature, which is a deliberate part of the TBC design. This Al_2O_3 layer is known as thermally grown oxide (TGO) which grows as the coating spends time at oxidation temperature; very good adherence and low oxygen diffusivity are the important properties of TGO because they protect the lower layers from corrosion and oxidation [8].

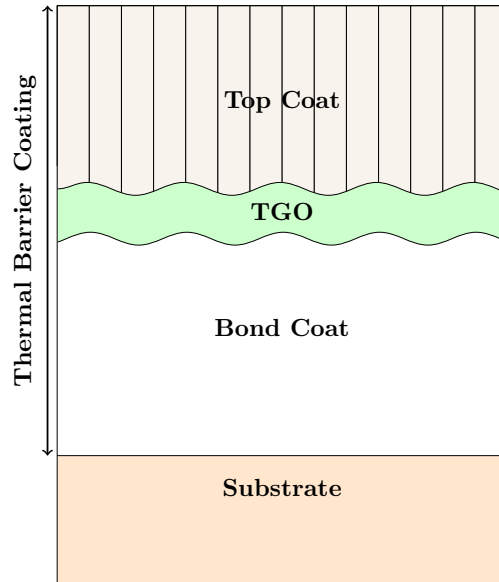


Figure 2.1: An outline of the thermal barrier coating system on the substrate.

The layer above the TGO, which is the highest layer, is known as top coat; in some texts in the literature, top coat is also referred to as the TBC, however in this work, TBC only describes the whole system including the bond coat, TGO and the top coat. Top coat has a columnar structure to allow for oxygen penetration and formation of TGO, nevertheless, its main functionality is thermal protection with the help of internal cooling, which is why materials used for its design have very low thermal conduction. A very common top coat material is yttria-stabilised zirconia (YSZ) [12].

In spite of their exceptional properties, TBCs fail because of a number of chemical and thermochemical factors such as Al depletion, Ni diffusion through TGO, presence of imperfections on the surface, undulation growth or wrinkling at the interface of the layers, and finally, foreign object impact [8]. Undulation growth, known as rumpling, is a very common failure mode for some TBCs such as the ones that use platinum-modified nickel aluminide, (Ni,Pt)Al, which is the focus of this chapter. Rumpling is a surface roughening effect which grows in the bond coat and TGO over the life of TBC. At some point of the rumpling growth process, cracks due to a normal tensile stress at the TGO-bond coat interface, nucleate, grow and coalesce leading to spallation of the top coat and failure of the TBC.

There have been many works in the literature, which will be discussed below, trying to explain the underlying mechanism for rumpling; in most of them, factors such as thermal mismatch, yield in the bond coat and TGO, TGO growth, phase transformation, and the local volume changes were identified as main sources for rumpling growth. However, a relatively recent experimental finding by Tolpygo & Clarke [1], questioned all the previous recommendations as the underlying mechanism of rumpling. This outcome led to formation of my objective, which is to develop an analytical model for analysing these new findings, and identifying the actual underlying mechanism for rumpling growth.

The rest of this chapter shows the theory behind the analytical model of rumpling and how it is used with the new experimental findings to show that swelling is the underlying source for rumpling growth; swelling is a relatively new phenomenon discovered in 2004 [13]. In the next subsection a review on the literature about rumpling is given, at the end of which my objectives are clearly identified. Following that, a detailed explanation of the analytical model developed here is given, which is a modified version of the rumpling model, first introduced by Balint *et al.* [2]; this version of the model includes swelling. As will be clear in the later sections, the results obtained from this model show the same qualitative behaviour as the experimental results which is used to show and explain why swelling is the underlying source for rumpling growth.

2.1.1 Literature Review

In order to understand rumpling, parameters involved in its formation are explored, which are divided into two groups; i) material dependent and ii) the external or environmental. Material dependent includes parameters such as molecular structure or mechanical and thermal properties. In one of the early works on rumpling, the effect of chemical bonding, crystal structure and surface orientation on rumpling was demonstrated [14]. Effect of bond coat material properties, especially creep, is known to be a key factor in rumpling growth [15–17]. For example, it was reported that a reduction in rumpling is observed with an increase in the creep strength of the bond coat [2, 17].

One of the popular experimental works on measuring the mechanical properties of (Ni,Pt)Al was carried out by Pan *et al.* in 2003 [18]. They employed a new tensile test method to measure the mechanical behaviour of (Ni,Pt)Al at 0% and 28% of its cyclic life for a temperature range of 25°C to 1150°C. The result of these measurements showed a ductile to brittle transition in the bond coat at temperature of approximately 600°C, above which the creep and yield strengths of the bond coat decreased rapidly. While within one cycle the creep and yield strengths decreased at temperatures above 600°C, over many cycles they increased with increase in number of cycles. At the peak temperature, however, these properties stayed the same with increase in number of cycles; martensitic transformations are suggested to be the cause of this behaviour.

The second group of parameters for rumpling, i.e. external parameters, includes thermal cycling or isothermal working condition, thermal mismatch between the layers, operating temperature, centrifugal stresses, incremental growth of the oxide layer, and the surface finish of the coatings. There are two main working conditions for TBC; i) isothermal and ii) thermal cycling. Isothermal is the case where the system undergoes constant high temperatures for long periods of time; this condition is typically seen for power generation applications. Thermal cycling, on the other hand, is typically used for propulsion applications such as jet engines, during which temperature of the coating system cycles between a lower temperature (typically the room temperature) and a peak temperature (typically the operating temperature).

Depending on the application and operating conditions, different failure mechanisms become dominant. For example, in an isothermal application, stresses due to the TGO growth and thermal mismatch are found to be responsible for the TBC failure. Whereas, in a thermal cycling application, ratcheting of the TGO into the bond coat is the dominant failure mechanism, [8,9]. There are many differences between the isothermal and thermal cycling effects on rumpling. Here some of the main differences and possible reasons for them are discussed.

In year 2000 Tolpygo and Clarke, [7], showed that more rumpling growth forms on an initially flat (Ni,Pt)Al under a thermal cycling condition compared to an isothermal one for the same amount of time at the high temperature. This observation was later supported by the analytical model developed by Balint *et al.* [2]. In their work, Balint *et al.* showed a strong non-linear interaction between the bond coat in-plane stress and the normal traction at the layer interface, which was suggested to be the reason for this difference in rumpling growth because the in-plane stress in the bond coat regenerates in every thermal cycle. This analytical model of rumpling will be explained in more detail in the later sections.

In another work, Karlsson *et al.* suggested that the reason for the observed difference between the thermal cycling and isothermal condition is the in-plane strain growth of the TGO and its yield behaviour. Up to when TGO is elastic, isothermal and cyclic cases behave the same, however, when TGO yields at the peak temperature more rumpling growth is observed in the thermal cycling case [10]. As the TBC undergoes thermal cycling, the TGO experiences a large compressive stress because of the thermal mismatch and incremental growth [11,19]. In order to reduce that stress, TGO elongates itself through out-of-plane displacement and buckling. The stress is then redistributed by creep and yielding of the bond coat, [19], the rate of which is related to the life of TBC [20]. The time scale for this stress decay is suggested to be central to undulation growth, which occurs at the beginning of each

cycle. This time scale is dependent on the material property and the initial stress in the bond coat [2]. For the softer bond coats most of the displacement occurs during the oxide growth because the growth can be accommodated without TGO yielding. However, for the stronger bond coats TGO reaches its yielding point and stress changes become zero, which leads to a smaller rumpling growth [19]; this result suggests that reduction in the yield strength of the TGO would result in less rumpling growth [15].

In addition to the yielding properties of the TGO and the bond coat, some geometrical parameters were also believed to affect the rumpling growth process; two of these parameters have been addressed by [2, 8, 10, 15, 19, 21]; i) the initial roughness of the bond coat and ii) thickness of the TGO. Initial roughness of the bond coat is typically characterised by its average amplitude and wavelength. According to [21], rumpling amplitude of systems with wavelength greater than a threshold value grows monotonically with increase in the number of cycles. It is believed that more rumpling occurs in thick TGOs compared to the thin ones for the same initial undulation. This is because of the compressive stress in the TGO overcoming its bending stiffness and promoting undulation growth [15]. Therefore, the most effective way of reducing the rumpling growth is the reduction of the TGO stress for a given bond coat material and initial wavelength [2, 19].

Most of rumpling occurs at the peak temperature where three main diffusions happen; i) outward flux of Al towards the bond coat surface to form the TGO, ii) inward flux of Ni from the substrate into the bond coat and iii) the outward flux of Al into the substrate. Some of the major changes in the bond coat are because of oxidation and inward Ni diffusion [7]. The outward flux of Al is believed to create localised volume reduction, which is suggested to be an important source for rumpling initiation. These localised volume changes form by decomposition of the β -(Ni,Pt)Al phase and precipitation of γ -Ni₃Al phase [7,9]. The localised imperfections are then amplified as the thermal mismatch between the bond coat and the substrate occurs during thermal cycling [8,9,22]. Therefore, bond coats with β -phase such as (Ni,Pt)Al, which also have lower high temperature strength, are most susceptible to rumpling [19].

As seen so far, there were different theories and suggestions about the source of rumpling such as thermal mismatch, yield in the bond coat and TGO, TGO growth, and the local volume changes. In 2004 Tolpygo & Clarke published two papers on their experimental work on test and analysis of a large number of parameters affecting rumpling [13,23]. In their first paper the effect of oxidation condition, cycle length, surface roughness and martensitic phase transformation in the bond coat were discussed. To test the effect of oxidation and TGO on rumpling growth, Tolpygo & Clarke put the samples through thermal cycling but in a vacuum environment with virtually no oxidation. The findings of this experiment showed no major difference in rumpling growth between a vacuum or no

vacuum environment, which led to the conclusion that growth of TGO does not play a major role in rumpling growth [23]. In another part of this experiment it was found that while initial undulation may help rumpling, it is not required for its formation.

To address the effect of martensitic transformation on rumpling growth, Tolpygo & Clarke measured the rumpling growth for thermal cycling with an intermediate temperature as the lowest temperature of the cycle; this intermediate temperature was chosen to be above the martensite transformation temperature. The rumpling result from this experiment was then compared to an equivalent experiment with the room temperature as the lowest temperature of the cycle. This comparison revealed no major differences between the two cases leading to the conclusion that martensitic transformation does not have a significant effect on rumpling [23]. The outcome of this work showed while oxidation condition, surface roughness and phase transformation did not show any significant effect on rumpling growth, rumpling grew strongly with higher cycle duration and number.

The second part of Tolpygo & Clarke's work on rumpling in 2004, [13], shed light on a new parameter that has not been investigated previously; this parameter is called swelling. Swelling in the bond coat is a volumetric expansion effect observed in the form of thickening which happens as a result of inter-diffusion between the bond coat and the substrate, Figure 2.2.

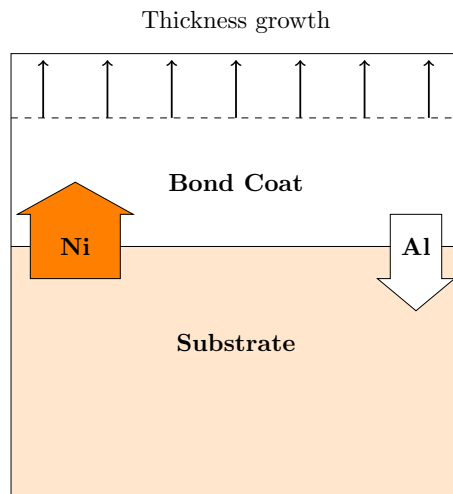


Figure 2.2: A schematic of the Ni-Al inter-diffusion between the substrate and the bond coat leading to swelling.

As mentioned previously, there are Ni and Al diffusions taking place between the bond coat and the substrate at the peak temperature; in a binary Ni-Al system, Ni diffuses three times faster into the bond coat than Al out of it and into the substrate. This action leads to thickening of the bond coat which in turn induces stress in the bond coat and accommodates rumpling growth [13]. Results of this experiment showed that the bond coat became 10% thicker in the first hours of oxidation for both thermal cycling and isothermal conditions. After the first few hours into the experiment and the

initial 10% thickening, thermal cycling results showed a continuous thickening with a smaller rate for the rest of the experiment. For the isothermal case, on the other hand, after the first few hours, rate of bond coat thickening reduced rapidly and towards the end of the experiment it became negative [13].

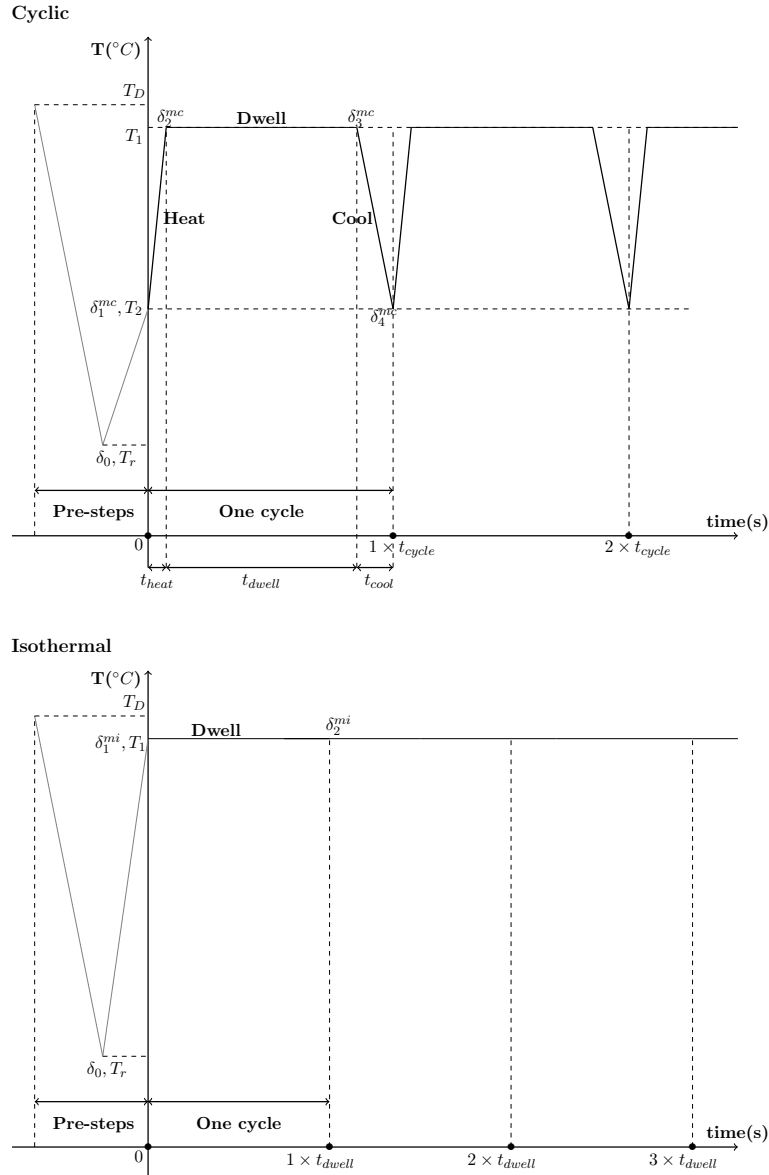


Figure 2.3: Temperature change for thermal cycling and isothermal experiments carried out by Tolpygo & Clarke [1].

In most of the rumpling studies carried out on thermal cycling condition, the temperature was varied between the room temperature and the peak temperature of $1150^{\circ}C$. According to these studies local phase transformations such as martensitic transformations, were believed to be one of the key factors in rumpling initiation and growth. In 2009 Tolpygo & Clarke, [1], carried out a series of experiments to investigate the effect of lower temperature of the thermal cycling, i.e. T_2 , on rumpling growth. In these experiments, the martensitic transformation temperature for the (Ni,Pt)Al samples was well below the room temperature, therefore, no phase transformation was present. Additionally,

the top coat was omitted from these test because the underlying rumpling mechanism is the same with or without the top coat.

There were ten experiments carried out to measure the rumpling amplitude of the bond coat after 100×1 hr cycles for ten different T_2 temperatures. Each experiment corresponds to one T_2 value from the range $T_2 = [25, 150, 275, 400, 525, 650, 775, 900, 1050, 1150]$; please note, here $T_2 = 1150^\circ\text{C}$ corresponds to the isothermal case. Figure 2.3 demonstrates a schematics of the isothermal and thermal cycle condition used by Tolpygo & Clarke [1]. Each thermal cycle consisted of 6min heating, 60min dwell and 12min cooling as shown in Figure 2.3; dwell in this context refers to the time for which the samples were held at the peak temperature. Because the isothermal case or $T_2 = 1150^\circ\text{C}$ does not have heating and cooling steps, the experimental procedure for it was 100 hours annealing at 1150°C . Please note for a direct comparison with thermal cycling cases in the later analysis, every hour at the peak temperature of the isothermal case is also referred to as a “dwell” step.

The results of these experiments, which are shown in Figure 2.4, were unexpected; because using what were believed to be the underlying sources of rumpling, such as phase transformation and thermal mismatch effects, the results of this experiment must have shown a noticeable difference in the final rumpling amplitude for each T_2 . However, as can be seen in Figure 2.4, rumpling amplitude did not vary significantly by changing T_2 , except for the isothermal case. This outcome raised the question for what actually the underlying source for rumpling is; and that question formed the objective for this project.

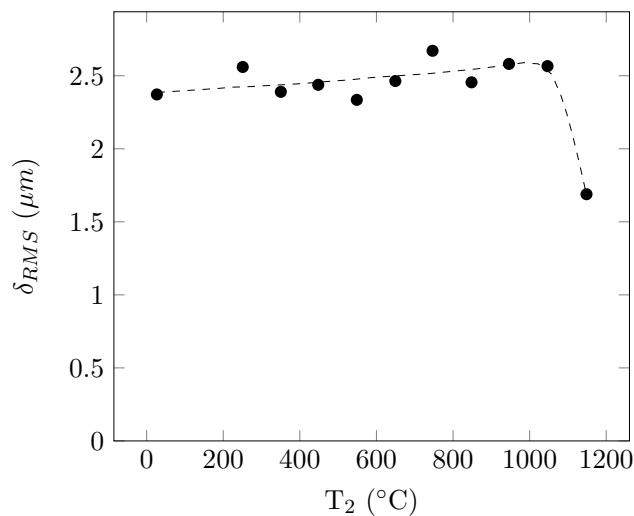


Figure 2.4: The experimental results from [1] for the root-mean-square (RMS) of roughness amplitude, δ_{RMS} , on the bond coat’s surface after 100×1 h thermal cycles, versus T_2 .

2.1.2 Objective

The objective of this study is to find the reason for the unexpected outcome of Tolpygo & Clarke's work, [1], and identify the underlying source of rumpling growth. The approach taken here is to incorporate the swelling phenomenon into the existing analytical model of rumpling by Balint *et al.*, [2], and use that to answer the research question here. As will become clear in the later sections, the results obtained from this modified model of rumpling shows the same qualitative behaviour as the experimental results which confirms that the model developed in this work has captured the underlying source for rumpling. Therefore, by analysing the results from this model, the rest of this chapter will show and explain why swelling is the underlying source for rumpling growth.

2.2 Mathematical Model and Implementation

2.2.1 Mathematical Model

The mathematical model used here is a modified version of the first analytical model of rumpling introduced by Balint *et al.* in 2003 [2]. Over the years, this model has been modified and improved for various other applications, [15, 24], however, these past versions did not include swelling which is essential for this study. Therefore, in this work, this analytical model is modified to include the effects of swelling on rumpling growth, and is used to find the underlying source for rumpling. In this section, a detailed description of this model, including swelling is given.

Thermal barrier coatings can be modelled as a system of layers, such as the one shown in Figure 2.5, where superscripts (1), (2), (3) and (4) represent the substrate, bond coat, TGO, and the top coat, respectively. In this system, rumpling is modelled with the assumption that the undulation takes a sinusoidal form with a wavelength of $2L$ and an initial amplitude of δ_0 . The undulation wavelength is taken to be fixed because according to the experimental findings, [1, 13], wavelength of the undulations has a negligible change as rumpling grows. Additionally, for all the layers a uniform temperature across the thickness and width is assumed.

The lowest layer in this system is the substrate, and is assumed to be infinitely thick and elastically isotropic; infinitely thick here means that substrate constrains the upper layers in the x_1 and x_3 directions. The elastic properties of the substrate do not affect rumpling and are not shown in Figure 2.5; because if thickness of the bond coat is much larger than the undulation half-wavelength (i.e. $h^{(2)} \gg L$) then no sinusoidal stresses reach the bond coat-substrate interface. Therefore, the only influence of the substrate on the coating layers becomes through the difference in the coefficient of thermal expansions (CTE), i.e. α , between the substrate and other layers. This thermal mismatch is a source of stress generation in the layers, and it changes with temperature.

Figure 2.6 shows an example of the difference in the CTEs, which is between (Ni,Pt)Al as the bond coat, and the René N5 as the substrate; the temperature dependent data for $\alpha^{(1)}$ and $\alpha^{(2)}$ is taken from [25]. For $\alpha^{(3)}$, however, temperature dependent data is not available, hence the constant value of $8.5 \times 10^{-6}/^\circ\text{C}$ is used [24].

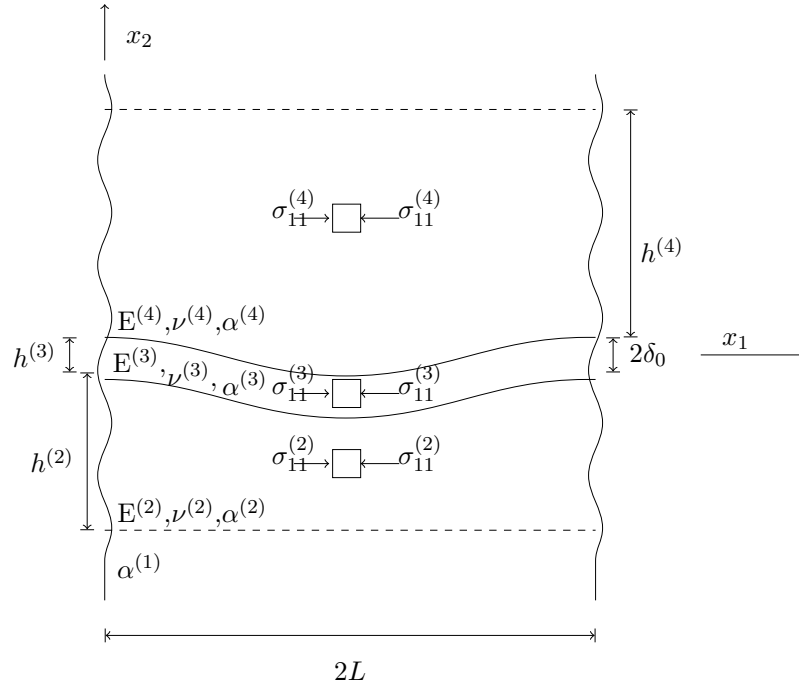


Figure 2.5: Schematic of the TBC system that is modelled here, (The image is drawn based on the infographic taken from [15].)

The second layer with the superscript (2) is the bond coat and main material of this study which is assumed to be isotropic and initially stress-free. In the case that thickness of the bond coat layer is much larger than the half-wavelength of its undulation, i.e. $h^{(2)} \gg L$, it can be assumed that the bond coat is infinite, because extension of the sinusoidal stresses from the top surface of the bond coat to the bond coat-substrate interface become negligible. Bond coat has a Poisson ratio of $\nu^{(2)}$, and a Young's modulus of $E^{(2)}(T)$ which, according the work of Pan *et al.*, [18], depends on temperature in the form of $E^{(2)}[GPa] = 118 - 0.024T[^\circ\text{C}]$, Figure 2.6. Inelastic properties of the bond coat are characterised by the power-law creep with a creep reference strain rate, stress and temperature of $\dot{\epsilon}_0^{(2)}$, $\sigma_R^{(2)}$ and $T_R^{(2)}$, respectively, and creep exponent of $n^{(2)}$.

The third layer in the system is the thermally grown oxide (TGO) which is assumed to be isotropic with a Young's modulus of $E^{(3)}$, a Poisson ratio of $\nu^{(3)}$ and a CTE of $\alpha^{(3)}$, (given that the information on creep and constitutive laws for the TGO were not available at the development time of this model, they are not included). The yield strength of TGO is important because once the stress in the TGO reaches the yielding point, its bending stiffness becomes zero, therefore, the stress for the duration of plastic deformation stays constant which prevents further rumpling growth [15]. As the temperature

changes the yield strength of the TGO also changes, e.g. low yield for high temperatures [26].

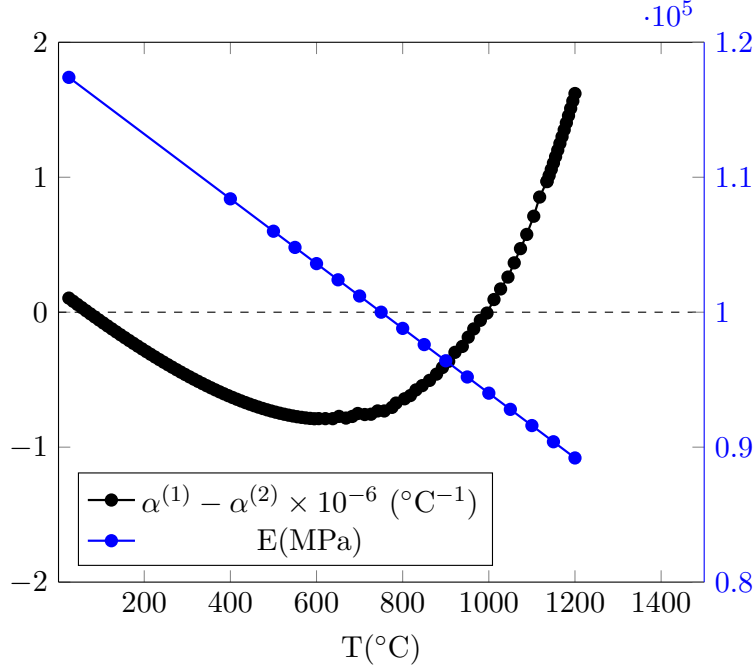


Figure 2.6: Change of $E^{(2)}$ and $\alpha^{(1)} - \alpha^{(2)}$ with temperature; $\alpha^{(1)}$ and $\alpha^{(2)}$ were taken from [25]. In this image, positive value of $\alpha^{(1)} - \alpha^{(2)}$ means the bond coat is under tensile stress during heating and compressive stress during cooling and vice versa.

The final layer of this system is the top coat with superscript (4), which is a highly non-linear material in both elastic and inelastic aspects. While this mathematical model is capable of simulating the effect of top coat, it is not explained and included in the calculations here. This is because top coat is not included in the experimental work of Tolpygo & Clarke, [1].

2.2.2 Rumpling Equation

The equation for growth rate of rumpling amplitude, i.e. Equation 2.9, is the heart of this model. This equation is taken from [2], where an analytical model was developed to clarify the link between rumpling and non-linear creep behaviour of the bond coat. Here a brief explanation about this equation and its development is given, for more detail on this equation please refer to [2, 15, 24].

Considering a bond coat layer under equi-biaxial compressive stress where a normal stress, resulting from the normal traction of p , is superimposed on its top surface; the power-law creep behaviour of the bond coat accommodating the rumpling growth; and a dimensional analysis of the system, the rate of change of undulation amplitude, i.e. $\dot{\delta}^{(2)}$, is taken to have the form of

$$\dot{\delta}^{(2)} = L \dot{\epsilon}_0^{(2)} \left(\frac{p}{\sigma_R^{(2)}} \right) \left| \frac{p}{\sigma_R^{(2)}} \right|^{n^{(2)}-1} f \left(\left| \frac{p}{\sigma_R^{(2)}} \right|, n^{(2)} \right), \quad (2.1)$$

if $h^{(2)} \gg L$, so the bond coat can be approximated as an infinite layer without the effect of p reaching the substrate. There are two well-defined limiting cases associated with Equation 2.1; i)

when $\left| \frac{p}{\sigma_R^{(2)}} \right| \ll 1$ such that Equation 2.1 becomes

$$\dot{\delta}^{(2)} = a(n^{(2)}, \sigma_s^{(2)}) L \dot{\varepsilon}_0^{(2)} \left(\frac{p}{\sigma_R^{(2)}} \right) \left(\frac{\sigma^{(2)}}{\sigma_R^{(2)}} \right)^{n^{(2)}-1}, \quad (2.2)$$

where based on perturbation analysis $a(n^{(2)}, \sigma_s^{(2)})$ is computed to be

$$a(n^{(2)}, \sigma_s^{(2)}) = \frac{6n^{(2)} [1 - \sigma_s^{(2)}(1 - \sigma_s^{(2)})] \cos(\theta(n^{(2)}, \sigma_s^{(2)})/2)}{\pi [3 + n^{(2)} - 4n^{(2)}\sigma_s^{(2)}(1 - \sigma_s^{(2)})]} \quad (2.3)$$

where

$$\theta(n^{(2)}, \sigma_s^{(2)}) = \tan^{-1} \left(\frac{\sqrt{4 - g^2(n^{(2)}, \sigma_s^{(2)})}}{g(n^{(2)}, \sigma_s^{(2)})} \right) + m\pi, \quad (2.4)$$

and

$$g(n^{(2)}, \sigma_s^{(2)}) = \frac{3 - n^{(2)} - 2n^{(2)}\sigma_s^{(2)}(1 - \sigma_s^{(2)})}{n^{(2)}(1 - \sigma_s^{(2)}(1 - \sigma_s^{(2)}))}, \quad (2.5)$$

and

$$m = \begin{cases} 1 & \text{if } n^{(2)} > 2 \text{ and } \frac{-\sqrt{3}\sqrt{n^{(2)}-2} + \sqrt{n^{(2)}}}{2\sqrt{n^{(2)}}} < \sigma_s^{(2)} \\ & < \frac{\sqrt{3}\sqrt{n^{(2)}-2} + \sqrt{n^{(2)}}}{2\sqrt{n^{(2)}}} \\ 0 & \text{Otherwise,} \end{cases} \quad (2.6)$$

In the above equations $\sigma_s^{(2)}$ is $\frac{\sigma_{33}^{(2)}}{\sigma_{11}^{(2)}}$. ii) when $\left| \frac{p}{\sigma_R^{(2)}} \right| \gg 1$ such that Equation 2.1 becomes

$$\dot{\delta}^{(2)} = b(n^{(2)}) L \dot{\varepsilon}_0^{(2)} \left(\frac{p}{\sigma_R^{(2)}} \right) \left| \frac{p}{\sigma_R^{(2)}} \right|^{n^{(2)}-1}, \quad (2.7)$$

where using finite element program $b(n^{(2)})$ is computed to be

$$b(n^{(2)}) = 1.152 - 0.6117n^{(2)} + 0.1551n^{(2)2} - 0.02081n^{(2)3} + 0.001170n^{(2)4} \quad (2.8)$$

Using a finite element model, [2] has shown that Equation 2.9 provides a very good approximation of $\dot{\delta}$ for the whole range of $\frac{p}{\sigma^{(2)}}$.

$$\dot{\delta}^{(2)} = L \dot{\varepsilon}_0^{(2)} \exp\left(\frac{-T_R^{(2)}}{T}\right) \left(\frac{p}{\sigma_R^{(2)}} \right) \left[a(n^{(2)}) \left(\frac{\sigma^{(2)}}{\sigma_R^{(2)}} \right)^{n^{(2)}-1} + b(n^{(2)}) \left| \frac{p}{\sigma_R^{(2)}} \right|^{n^{(2)}-1} \right] \quad (2.9)$$

p , which is the normal traction, is the only traction accounted for at the interface because the tangential tractions are relaxed due to the creep relaxation in the layers; one key source for these interface tractions is the growth of the thermally grown oxide or TGO; therefore, the effect of the TGO layer enters the rumpling growth equation through p . Having explained the main equation for rumpling growth here, in the next two parts an expression for p and one for $\sigma^{(2)}$ are obtained.

2.2.2.1 TGO

Ideally, in an as-manufactured state, the thickness of the TGO should be zero but in reality as the coating is deposited at a high temperature, a thin layer of TGO will form; this thin layer of TGO is included in the analytical model of rumpling through an initial thickness of $h_0^{(3)}$. While temperature approaches the peak temperature, the oxide layer grows both normal and lateral to the layer's interface, however, in this model it is assumed that growth only occurs at the peak temperature. This assumption is valid while the TGO thickness is much less than the undulation wavelength, i.e. $h^{(3)} \ll L$ and $\left(\frac{\partial w_0}{\partial x_1}\right)^2 \ll 1$ and $\left(\frac{\partial w}{\partial x_1}\right)^2 \ll 1$, where $w_0(x_1)$ and $w(x_1)$ are the initial and current normal displacements of the sinusoidal profile of rumpling, respectively; these displacements are defined as $w_0(x_1) = \delta_0^{(3)} \cos(\pi x_1/L)$ and $w(x_1) = \delta^{(3)} \cos(\pi x_1/L)$ where $\delta^{(3)}$ is the current amplitude of rumpling in the TGO.

Due to the unavailability of the information on the creep properties of TGO, the stress calculations for TGO only comes from the thermal mismatch with the substrate, and the normal and lateral growth of the layer, i.e. Equation 2.10 and Equation 2.11, taken from [24], assuming that TGO is elastic-perfectly plastic.

$$\dot{\sigma}_{11}^{(3)} = \bar{E}^{(3)} \left[\left(1 - \nu^{(1)}\nu^{(3)}\right) \dot{\varepsilon}_{11}^{(1)} + \left((1 + \nu^{(1)})\nu^{(3)}\alpha^{(1)} - (1 + \nu^{(3)})\alpha^{(3)}\right) \dot{T} - (1 + \nu^{(3)})\dot{\varepsilon}_G^{(3)} + \frac{\pi^2(\delta_0^{(3)} + \delta^{(3)})\dot{\delta}^{(3)}}{L^2} \right] \quad (2.10)$$

$$\dot{\sigma}_{33}^{(3)} = \bar{E}^{(3)} \left[\left(\nu^{(3)} - \nu^{(1)}\right) \dot{\varepsilon}_{11}^{(1)} + \left((1 + \nu^{(1)})\alpha^{(1)} - (1 + \nu^{(3)})\alpha^{(3)}\right) \dot{T} - (1 + \nu^{(3)})\dot{\varepsilon}_G^{(3)} + \frac{\pi^2(\delta_0^{(3)} + \delta^{(3)})\dot{\delta}^{(3)}}{L^2} \right] \quad (2.11)$$

Here $\bar{E}^{(3)} = E^{(3)}/(1 - \nu^{(3)2})$, $\dot{\varepsilon}_G^{(3)}$ is the lateral growth strain rate given by Equation 2.12, and $\dot{\delta}^{(3)}$ is the rate of growth of rumpling amplitude given by Equation 2.9 which is assumed to be small compared to the total undulation amplitude, i.e. $\frac{\Delta\delta^{(3)}}{\delta_0^{(3)} + \delta^{(3)}} \ll 1$.

$$\dot{\varepsilon}_G^{(3)} = \frac{\dot{h}^{(3)}}{d} \quad (2.12)$$

Equation 2.12 shows the relationship between lateral growth strain rate, $\dot{\varepsilon}_G^{(3)}$, and the rate of TGO thickening, $\dot{h}^{(3)}$, where d is a constant chosen in such a way that 5% of lateral growth occurs in 100h at 1150°C [24]. The rate of growth of TGO thickness is given as,

$$\dot{h}^{(3)} = At^{-0.6} \exp\left(\frac{-Q}{kT}\right), \quad [24] \quad (2.13)$$

where Q is the activation energy, k is the Boltzmann constant in eV/K, and A is a constant taken from the data of [13]. The current amplitude of rumpling in the TGO, i.e. $\delta^{(3)}$, is given by Equation 2.14, where p is the normal traction at the interface between the bond coat and the TGO.

$$\delta^{(3)} = \frac{p - P\delta_0^{(3)}}{V} \quad (2.14)$$

where

$$P = -\text{sgn}(\sigma_{11}^{(3)}) \frac{\sigma^{(3)} h^{(3)} \pi^2}{L^2}, \quad (2.15)$$

$$V = -\frac{\sigma^{(3)} h^{(3)} \pi^2}{L^2} \left[\text{sgn}(\sigma_{11}^{(3)}) + \frac{L^{*2}}{L} \right], \quad (2.16)$$

and

$$L^* = h^{(3)} \sqrt{\frac{\pi^2 \bar{E}^{(3)}}{12\sigma^{(3)}}} \quad (2.17)$$

Rearranging the above equations, an expression for computing p can be obtained, which is then used in Equation 2.9. Please note, the explanation in ‘‘TGO’’ subsection is based on [2] which is given here only for completeness of the work, therefore, for more detail about how these terms are obtained please refer to [2]. The novelty introduced into the analytical model of rumpling in this work will be discussed in the next subsection, i.e. 2.2.2.2.

Having defined an expression for the normal traction at the interface of the TGO and the bond coat, i.e. p , looking at Equation 2.9, it is clear that there is a strong relationship between rumpling growth and creep in the bond coat. This dependency is shown through two stress terms of $\left(\frac{\sigma^{(2)}}{\sigma_R^{(2)}}\right)$ and $\left|\frac{p}{\sigma_R^{(2)}}\right|$ with their corresponding coefficients $a(n^{(2)})$ and $b(n^{(2)})$ which are defined by Equation 2.3 and Equation 2.8 respectively. When $|p/\sigma^{(2)}| \ll 1$, which is the case here, there is a strong relationship between rumpling growth and the stress in the bond coat, $\delta^{(2)} \propto \sigma^{(2)n^{(2)}-1}$, therefore, in order to understand rumpling growth, the equation defining the stress in the bond coat is defined; this part of the model is where a modification is made to the existing analytical model of rumpling.

2.2.2.2 Bond Coat

The most complete version of the constitutive law for the total strain rate, $\dot{\varepsilon}_{ij}^{(2)}$ in the bond coat is given as

$$\dot{\varepsilon}_{ij}^{(2)} = \frac{1+\nu^{(2)}}{E^{(2)}} \dot{\sigma}_{ij}^{(2)} - \frac{\nu^{(2)}}{E^{(2)}} \dot{\sigma}_{kk}^{(2)} \delta_{ij} + \left(\alpha^{(2)} \dot{T} + \dot{\varepsilon}_P^{(2)} + \dot{\varepsilon}_S^{(2)} \right) \delta_{ij} + \frac{3}{2} \dot{\varepsilon}_0^{(2)} \left(\frac{\sigma_e^{(2)}}{\sigma_R^{(2)}} \right)^{n^{(2)}-1} \left(\frac{s_{ij}^{(2)}}{\sigma_R^{(2)}} \right) e^{-T_R^{(2)}/T} \quad (2.18)$$

where $\dot{\varepsilon}_P^{(2)}$ is the strain rate due to martensite phase transformation, $\sigma_e^{(2)}$ is the effective stress given by $\sqrt{3/2 s_{kl}^{(2)} s_{kl}^{(2)}}$, s_{ij} is the deviatoric stress given by $\sigma_{ij}^{(2)} - \frac{1}{3} \sigma_{kk}^{(2)}$, and finally, $\dot{\varepsilon}_S^{(2)}$ is the strain rate due to swelling. Swelling is a volumetric expansion of the bond coat layer because of Ni and Al inter-diffusion between the bond coat and the substrate, however, given that the thickness of the bond coat compared to the substrate is very small, the bond coat is taken to be constrained in the lateral direction by the

substrate. As a result of that, it is assumed that the bond coat cannot expand laterally, hence swelling is measured experimentally as the increase in thickness of the bond coat, i.e. $\dot{\varepsilon}_{22}^{(2)}$, data for which is taken from [13].

Given that diffusion rate of Ni into the bond coat is three times faster than the diffusion rate of Al out of the bond coat, there is a net increase in the thickness of the bond coat; this percentage increase in the bond coat thickness, $\dot{\varepsilon}_{22}^{(2)}$, affects its stress condition and so the rumpling growth in the bond coat. Value of $\dot{\varepsilon}_{22}^{(2)}$ as measured from experiment, has a time dependent exponential form, as shown in Equation 2.19 where the best mathematical fit for the experimental data is found.

$$\dot{\varepsilon}_{22}^{(2)} = MBt^{M-1} \exp\left(\frac{-Q}{kT}\right), \quad (2.19)$$

Here M is the time exponent, B is a constant in h^{-M} , and t is time in hours. Values of M and B which are found from the experiment, differ between thermal cycling and isothermal cases, Table 2.1.

Table 2.1: Swelling parameters for thermal cycling and isothermal cases based on the data taken from [13].

	B (h^{-M})	M
Isothermal	0.0402×10^7	-0.52
Thermal Cycling	78.056×10^7	0.0036

Substituting Equation 2.19 into the constitutive law, i.e. Equation 2.18, gives

$$\begin{aligned} \dot{\varepsilon}_{22}^{(2)} &= MBt^{M-1} \exp\left(\frac{-Q}{kT}\right) \\ &= \frac{1 + \nu^{(2)}}{E^{(2)}} \dot{\sigma}_{22}^{(2)} - \frac{\nu^{(2)}}{E^{(2)}} \dot{\sigma}_{kk}^{(2)} + \left(\alpha^{(2)} \dot{T} + \dot{\varepsilon}_P^{(2)} + \dot{\varepsilon}_S^{(2)}\right) + \frac{3}{2} \dot{\varepsilon}_0^{(2)} \left(\frac{\sigma_e^{(2)}}{\sigma_R^{(2)}}\right)^{n^{(2)}-1} \left(\frac{s_{22}^{(2)}}{\sigma_R^{(2)}}\right) e^{-T_R^{(2)}/T}, \end{aligned} \quad (2.20)$$

which when rearranged, gives the swelling strain rate in terms of $\dot{\varepsilon}_{22}^{(2)}$, i.e.

$$\dot{\varepsilon}_S^{(2)} = \dot{\varepsilon}_{22}^{(2)} - \frac{1 + \nu^{(2)}}{E^{(2)}} \dot{\sigma}_{22}^{(2)} + \frac{\nu^{(2)}}{E^{(2)}} \dot{\sigma}_{kk}^{(2)} - \left(\alpha^{(2)} \dot{T} + \dot{\varepsilon}_P^{(2)}\right) - \frac{3}{2} \dot{\varepsilon}_0^{(2)} \left(\frac{\sigma_e^{(2)}}{\sigma_R^{(2)}}\right)^{n^{(2)}-1} \left(\frac{s_{22}^{(2)}}{\sigma_R^{(2)}}\right) e^{-T_R^{(2)}/T} \quad (2.21)$$

Given that the experimental condition from [13] was such that no martensitic phase transformation was present during the experiment, therefore, the strain due to martensitic phase transformation is set to zero, i.e. $\dot{\varepsilon}_P^{(2)} = 0$. Additionally, one of the other important assumptions here is that the normal stresses in the bond coat, i.e. $\dot{\sigma}_{22}^{(2)}$, are negligible compared to the in-plane stresses, i.e. $\dot{\sigma}_{11}^{(2)}$ and $\dot{\sigma}_{33}^{(2)}$ which is true because the coating is unconstrained in that direction. This is why Equation 2.21 reduces to

$$\dot{\varepsilon}_S^{(2)} = \dot{\varepsilon}_{22}^{(2)} + \frac{\nu^{(2)}}{E^{(2)}}(\dot{\sigma}_{11}^{(2)} + \dot{\sigma}_{33}^{(2)}) - \alpha^{(2)}\dot{T} - \frac{3}{2}\dot{\varepsilon}_0^{(2)} \left(\frac{\sigma_e^{(2)}}{\sigma_R^{(2)}} \right)^{n^{(2)}-1} \left(\frac{s_{22}^{(2)}}{\sigma_R^{(2)}} \right) e^{-T_R^{(2)}/T} \quad (2.22)$$

Having defined an expression for the swelling strain which depends on the in-plane stress rates of the bond coat, it is time to find the expression for $\dot{\sigma}_{11}^{(2)}$ and $\dot{\sigma}_{33}^{(2)}$. Once a mechanical uni-axial strain together with temperature change is applied to the substrate in the x_1 direction, i.e. $\dot{\varepsilon}_{11}^{(1)}$, the corresponding strain in the x_3 direction, i.e. $\dot{\varepsilon}_{33}^{(1)}$, due to the Poisson effect becomes

$$\dot{\varepsilon}_{33}^{(1)} = -\nu^{(1)} \left(\dot{\varepsilon}_{11}^{(1)} - \alpha^{(1)}\dot{T} \right) + \alpha^{(1)}\dot{T} = (1 + \nu^{(1)}) \alpha^{(1)}\dot{T} - \nu^{(1)}\dot{\varepsilon}_{11}^{(1)} \quad (2.23)$$

Given that assumption for the substrate is to be infinitely thick, it constrains the bond coat in the x_1 and x_3 directions; as a result, the in-plane strain is the same for both the substrate and the bond coat, i.e. $\dot{\varepsilon}_{11}^{(2)} = \dot{\varepsilon}_{11}^{(1)}$ and $\dot{\varepsilon}_{33}^{(2)} = \dot{\varepsilon}_{33}^{(1)}$.

Using this result together with Equation 2.18 used for x_1 and x_3 directions, and the fact that $\dot{\sigma}_{22}^{(2)} = 0$, leads to an expression for $\dot{\varepsilon}_{11}^{(1)}$ and $\dot{\varepsilon}_{33}^{(1)}$ in terms of the stress and strains in the bond coat; rearranging the resultant equations to solve for $\dot{\sigma}_{11}^{(2)}$ and $\dot{\sigma}_{33}^{(2)}$ gives

$$\dot{\sigma}_{11}^{(2)} = \overline{E}^{(2)} \left[\dot{\varepsilon}_{11}^{(1)} + \nu^{(2)}\dot{\varepsilon}_{33}^{(1)} - (1 + \nu^{(2)}) \left(\alpha^{(2)}\dot{T} + \dot{\varepsilon}_S^{(2)} \right) - \frac{3}{2}\dot{\varepsilon}_0^{(2)} \left(\frac{\sigma_e^{(2)}}{\sigma_R^{(2)}} \right)^{n^{(2)}-1} \left(\frac{s_{11}^{(2)} + \nu^{(2)}s_{33}^{(2)}}{\sigma_R^{(2)}} \right) e^{-T_R^{(2)}/T} \right] \quad (2.24)$$

$$\dot{\sigma}_{33}^{(2)} = \overline{E}^{(2)} \left[\dot{\varepsilon}_{33}^{(1)} + \nu^{(2)}\dot{\varepsilon}_{11}^{(1)} - (1 + \nu^{(2)}) \left(\alpha^{(2)}\dot{T} + \dot{\varepsilon}_S^{(2)} \right) - \frac{3}{2}\dot{\varepsilon}_0^{(2)} \left(\frac{\sigma_e^{(2)}}{\sigma_R^{(2)}} \right)^{n^{(2)}-1} \left(\frac{s_{33}^{(2)} + \nu^{(2)}s_{11}^{(2)}}{\sigma_R^{(2)}} \right) e^{-T_R^{(2)}/T} \right] \quad (2.25)$$

where $\overline{E}^{(2)} = E^{(2)}/(1 - \nu^{(2)^2})$. When there is no external stress applied to the substrate, which is the case in this study, the only substrate strain is due to thermal expansion, i.e. $\dot{\varepsilon}_{11}^{(1)} = \alpha^{(1)}\dot{T}$ and it is the same in both x_1 and x_3 directions; thus substituting $\dot{\varepsilon}_{11}^{(1)}$ and $\dot{\varepsilon}_{33}^{(1)}$ into Equation 2.24 and Equation 2.25 will result in Equation 2.26, which is an equi-biaxial case, where $s_{33}^{(2)} = s_{11}^{(2)}$ and

$$\dot{\sigma}_{33}^{(2)} = \dot{\sigma}_{11}^{(2)} = \frac{E^{(2)}}{1 - \nu^{(2)}} \left[\underbrace{\left(\alpha^{(1)} - \alpha^{(2)} \right) \dot{T}}_{\text{Thermal mismatch}} - \underbrace{\dot{\varepsilon}_S^{(2)}}_{\text{Swelling}} - \underbrace{\frac{3}{2}\dot{\varepsilon}_0^{(2)} \left(\frac{\sigma_e^{(2)}}{\sigma_R^{(2)}} \right)^{n^{(2)}-1} \left(\frac{s_{11}^{(2)}}{\sigma_R^{(2)}} \right) e^{-T_R^{(2)}/T}}_{\text{Creep}} \right] \quad (2.26)$$

According to Equation 2.26, there are three main factors contributing to the stresses in the bond coat; i) thermal mismatch between the bond coat and the substrate, ii) swelling of the bond coat due to inter-diffusion of Ni and Al between the bond coat and the substrate, and finally iii) creep. During any process that includes temperature change, such as the initial cooling/heating of isothermal cases or all the heating and cooling processes of thermal cycling, the thermal mismatch term of Equation 2.26

becomes activated and affects the bond coat stress.

The swelling term in Equation 2.26, is defined by Equation 2.22 where both thermal mismatch and creep effects are present. However, in order to obtain an understanding of swelling behaviour as an independent phenomenon, the creep, phase transformation and thermal strain rates are removed from Equation 2.18; and the resultant constitutive equation is solved for a system of bond coat layer with the same conditions as the case under study here, i.e. equi-biaxial condition with no stress in the 22 direction and zero strain in the 11 and 33 directions. In other words, the simplified version of Equation 2.18 is solved for both $\dot{\epsilon}_{11}^{(2)} = \dot{\epsilon}_{33}^{(2)} = 0$ and $\dot{\sigma}_{22}^{(2)} = 0$.

$$\begin{aligned} \dot{\epsilon}_{11}^{(2)} = 0 &= \frac{1 + \nu^{(2)}}{E^{(2)}} \dot{\sigma}_{11}^{(2)} - \frac{\nu^{(2)}}{E^{(2)}} (\dot{\sigma}_{11}^{(2)} + \dot{\sigma}_{33}^{(2)}) \delta_{ij} + \dot{\epsilon}_S^{(2)} \\ &\frac{1 + \nu^{(2)}}{E^{(2)}} \dot{\sigma}_{11}^{(2)} - \frac{2\nu^{(2)}}{E^{(2)}} \dot{\sigma}_{11}^{(2)} \delta_{ij} + \dot{\epsilon}_S^{(2)} \end{aligned} \quad (2.27)$$

Rearranging Equation 2.27 to find an expression for $\dot{\sigma}_{11}^{(2)}$, substituting it into

$$\dot{\epsilon}_{22}^{(2)} = -\frac{2\nu^{(2)}}{E^{(2)}} \dot{\sigma}_{11}^{(2)} \delta_{ij} + \dot{\epsilon}_S^{(2)}, \quad (2.28)$$

and rearranging to find an expression for $\dot{\epsilon}_S^{(2)}$ leads to

$$\dot{\epsilon}_S^{(2)} = \frac{1 - \nu^{(2)}}{1 + \nu^{(2)}} \dot{\epsilon}_{22}^{(2)} \quad (2.29)$$

Using the assumption of swelling without creep and thermal mismatch in Equation 2.26, with the data from Table 2.1, Figure 2.7 is produced which shows that swelling is a temperature activated phenomenon; for example, in the thermal cycling case swelling is activated at temperatures above 1000°C and for isothermal case above 900°C. In reality, both creep and thermal mismatch will be available and will affect the stress in the bond coat but Figure 2.7 is produced to give an overview of the swelling effect on stress in the bond coat.

As can be seen here, for both cases of thermal cycling and isothermal, the swelling related stress is only activated between 900 – 1000°C and increases in magnitude as the temperature increases. For isothermal case, the overall stress magnitude decreases as the number of hours increases; however, for thermal cycling not only the overall magnitude of the stress is much higher than isothermal case but also it is increasing with the number of cycles.

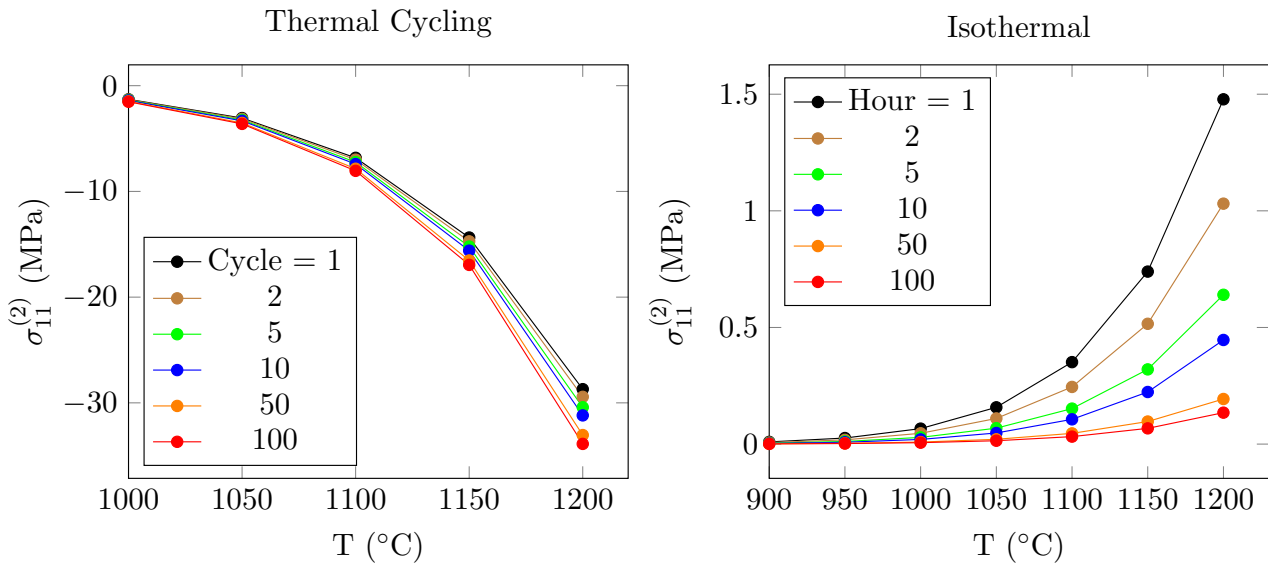


Figure 2.7: Swelling related stress, as it changes with temperature and number of cycles for both thermal cycle and isothermal case. Here the creep and thermal mismatch effects are not included.

The last term in Equation 2.26 is the creep term which follows a power-law creep; this term is a stress relaxation factor; if for any reasons, such as swelling, the stresses in the bond coat elevate in magnitude, the creep deformation of the bond coat acts against the increase in stress. As can be deduced from the creep term in Equation 2.26, the higher the magnitude of stress, the higher the amount of stress relaxation due to creep.

2.2.3 Model Set Up

Having modified the analytical model of rumpling by adding the swelling phenomenon into it, it is used to study the outcome of experimental work from Tolpygo & Clarke, [1], i.e. Figure 2.4. In this process, the modified analytical model is used to compute the final rumpling amplitude of the TBC system under the same conditions as the experiment. In order to study this experimental result further, the model is used to look at system's behaviour for three important T_2 temperatures which are $T_2 = 25, 1050$ and 1150°C ; because the first one includes “other” sources of strain mismatch upon thermal cycling, the second one mostly excludes them, and the third one it the isothermal case. The comparison between these three cases reveals the answer to the question “What is the underlying source for rumpling growth?”.

Table 2.2: A summary of the material properties and data used in the analytical model of rumpling.

Property/Variable (Unit)	Value	Reference	Property/Variable (Unit)	Value	Reference
L (μm)	43.948076087	[1]	$\nu^{(3)}$	0.2	[24]
$h_0^{(3)}$ (μm)	10^{-20}		$\nu^{(1)}$	0.3	[24]
A ($\mu\text{m h}^{-0.4}$)	1.12×10^{13}	[24]	$h^{(2)}$ (μm)	40	[1]
Q (eV)	3.96	[27]	$\alpha^{(1)}$ ($^{\circ}\text{C}$)	Figure 2.6	[25]
d (m)	33.25	[24]	$\alpha^{(2)}$ ($^{\circ}\text{C}$)	Figure 2.6	[25]
$n^{(2)}$	4	[28]	$\alpha^{(3)}$ ($^{\circ}\text{C}$)	8.5×10^{-6}	[24]
$\sigma_R^{(2)}$ (MPa)	25	[28]	$E^{(2)}$	$118 - 0.024T$ [$^{\circ}\text{C}$]	[18]
$\dot{\epsilon}_0^{(2)}$ s^{-1}	0.2	[28]	$E^{(3)}$ (MPa)	375000	[24]
T_R (K)	15000	[28]	$\sigma_y^{(3)}$ (MPa)	Figure 1 in [26]	[26]
$\nu^{(2)}$	0.27	[24]	δ_0 (μm)	1.1	[1]

The experimental set up for this study consists of $100 \times 1\text{h}$ thermal cycles with addition of 6min heating and 12min cooling for every cycle; and $100 \times 1\text{h}$ for the isothermal case which in this work may also be referred to as $T_2 = 1150^{\circ}\text{C}$. Figure 2.3 shows an outline of the temperature change during each thermal cycle and every hour of isothermal conditions; it also defines some of the variables used in the results section. During this experimental work no external strain is applied to the substrate, therefore, $\dot{\epsilon}^{(1)} = \alpha^{(1)}\dot{T}$ which is in accordance with the derivations in the previous subsection. The bond coat material used for the samples here is (Ni,Pt)Al, and for substrate the material is René N5.

Using the required information for the simulation, as shown in Table 2.2, the rumpling and stress behaviour of the TBC during this experiment is computed. The result from this simulation for the final rumpling amplitude, which is given in the form of Root-Mean-Square (RMS), is compared to the experimental result; here δ_{RMS} is $\delta^{(2)}/\sqrt{2}$ [13]. Once the result of the code for final rumpling amplitude is shown to agree with the experiment, it is used to compute the stress and rumpling behaviour of the bond coat; using which the underlying source of rumpling is identified, as will be shown in the next subsection.

2.3 Results & Discussion

The final rumpling amplitude results from the model, for the same experimental procedure as Tolpygo and Clarke [1], are shown in Figure 2.8 where they are compared to the experimental results for the same parameter. This comparison shows a very good qualitative but not quantitative match between the model developed here and the experimental findings. The quantitative difference is expected because the model is a simplified version of the reality with the important features included, where factors such as initial amplitude of the undulations, presence of localised volume expansions and many more similar factors are not included. The important outcome from this figure is the qualitative agreement between the experiment and the model in the trend of the plot, which proves that this model has captured the main source for rumpling growth.

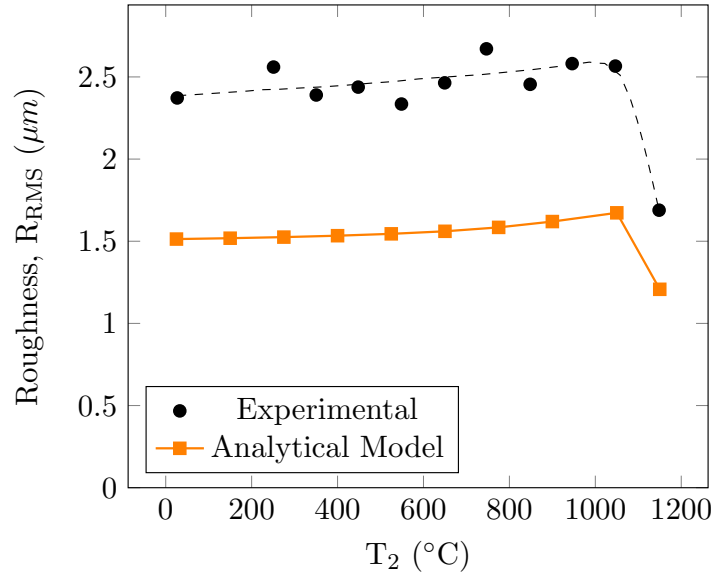


Figure 2.8: The root-mean-square (RMS) amplitude of roughness on the bond coat’s surface, δ_{RMS} , after $100 \times 1h$ thermal cycles versus T_2 for both experimental ^[1] and analytical model.

Having verified that our model has captured the main rumpling source, the next step is to show what this source is. Using the model with the computed stress and rumpling magnitude for the three cases of $T_2 = 25, 1050$ and $1150^\circ C$, it will be revealed that swelling is the underlying force behind rumpling growth. In the process of showing how this conclusion is obtained, there are other factors that come out to be effective in rumpling growth, two of which are discussed in more detail here.

In the first step of this procedure, the change of δ_{RMS} with increasing number of cycles is plotted for the three chosen cases, as shown Figure 2.9; this plot shows how the amplitude of rumpling is changing during the whole experimental procedure, as computed by the model. For all the cases shown in Figure 2.9, initially there is a sharp rate in the rumpling growth which then settles in a lower and constant rate. In the overall picture, i.e. left image in Figure 2.9, the total rumpling growth for the isothermal or $T_2 = 1150^\circ C$ is much less than the thermal cycling cases except in the first three hours. During these three hours the rumpling growth rate of the isothermal case is higher and equal to the thermal cycling cases (right image in Figure 2.9), where this initially sharp growth rate is responsible for about 18% of isothermal’s total rumpling amplitude. This figure not only shows a general comparison between the three cases but also shows the importance of initial conditions on the final rumpling amplitude. The difference in the initial conditions also initiates the difference between the final rumpling amplitude of $T_2 = 25^\circ$ and $1050^\circ C$; as a result, initial condition and its effect on rumpling are considered as a category to be discussed in more detail later in this section. Please note for convenience from here on δ refers to the RMS value, unless specified otherwise.

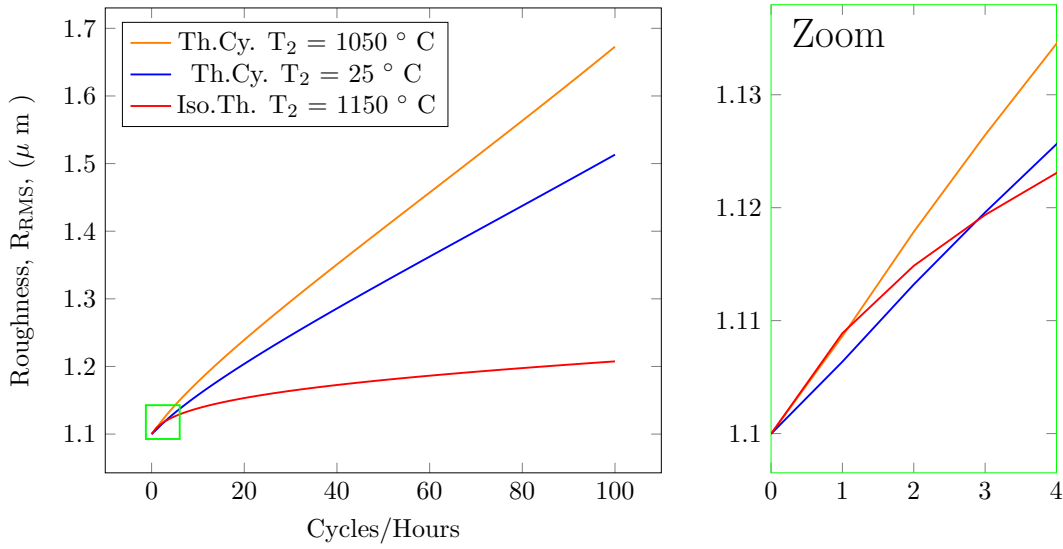


Figure 2.9: **Left:** Rumpling amplitude, δ_{RMS} , at the end of each cycle. **Right:** Rumpling amplitude, δ_{RMS} for the first three cycles/hours.

Having looked at the overall change in the rumpling amplitude i.e. Figure 2.9, in order to understand when the most growth happens, change in the rumpling amplitude at every step of every thermal cycle and every isothermal hour is plotted in Figure 2.10. For the two thermal cycling cases, this change in amplitude is defined as $\Delta\delta^{mc} = \delta_{i+1}^{mc} - \delta_i^{mc}$, where mc is the cycle number, and i is the current step in the cycle, taking only values of 1-4; for example $\delta_{\frac{1}{2}}$ means the rumpling amplitude at the end of heating process of the first cycle. Similarly, for the isothermal case, $\Delta\delta^{mi} = \delta_{i+1}^{mi} - \delta_i^{mi}$ represents the change in rumpling amplitude after every isothermal hour, i.e. mi , and i is the current step in the hour, taking only values of 1-2; Figure 2.3 demonstrates the definition of these variables.

The green line here shows the total change of rumpling amplitude in the cycle where the accumulative summation of it, i.e. the area under the green line in Figure 2.10, is consistent with the rumpling amplitude in Figure 2.9. All the cases in Figure 2.10 show an initially large growth rate in rumpling amplitude followed by a converges; in the later parts of this section it will be shown why this is the case. The difference between the rumpling growth in the two thermal cycling cases with the isothermal case is also captured here in Figure 2.10.

It is clear from the results in Figure 2.10 that for the two thermal cycling cases, the main contributor to rumpling growth is the black line, i.e. the dwell duration. This outcome is a new finding that is not emphasised on in the previous works of the literature, where presence of swelling as a source for rumpling was not known; because without swelling the main rumpling effect came from parameters such as phase changes and thermal mismatch that mainly occur during heating and cooling processes. While the effect of thermal mismatch and phase transformation are important and cannot be ignored, it is clear that the rumpling growth during the dwell is the main contributor to the final rumpling

amplitude, when swelling is present.

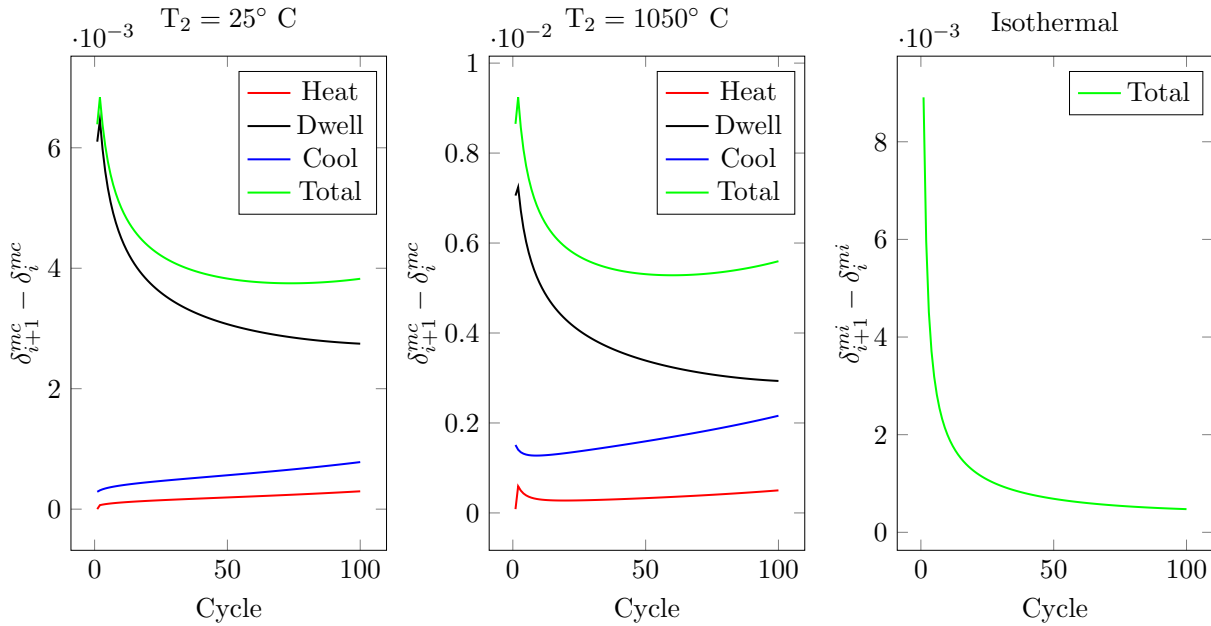


Figure 2.10: Change in the rumpling amplitude at every step of every thermal cycle and every isothermal hour for the three cases under study.

To investigate this further, the stress change during the dwell step of every cycle is plotted in Figure 2.11; this plot shows that the rumpling growth during dwell is accompanied by an increase in the stress magnitude of the bond coat, i.e the black and blue lines in Figure 2.11. In Figure 2.11 a positive value means an increase in the magnitude of the stress and a negative one means reduction in stress level.

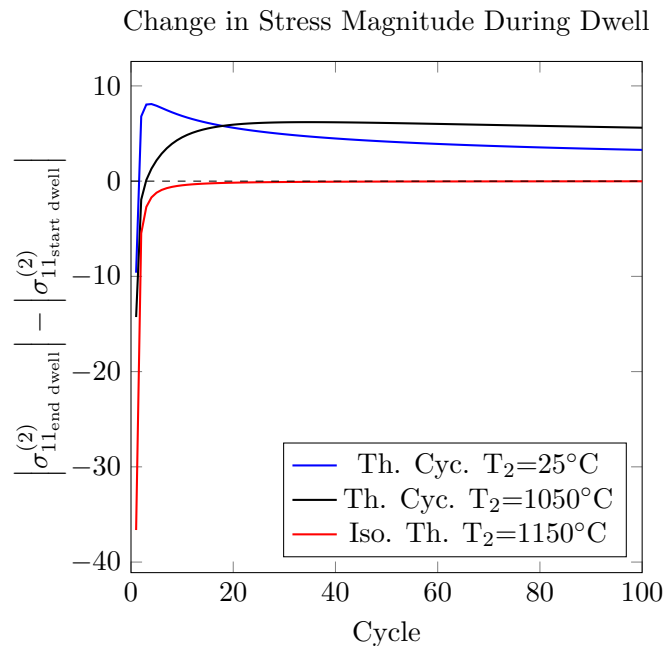


Figure 2.11: Change in bond coat stress during dwell, i.e. $|\sigma_{11_{\text{end dwell}}^{(2)}}| - |\sigma_{11_{\text{start dwell}}^{(2)}}|$

It is clear from Figure 2.11 that there is an initial sharp stress relaxation for all the three cases

under study, which for the isothermal case ends at a zero stress change; for the thermal cycling cases, on the other hand, after the initial stress relaxation there is a continuous raise in the stress magnitude after every dwell duration, i.e the positive value for the blue and black lines in Figure 2.11.

During the dwell period, thermal mismatch is not present which means that the only two active factors from Equation 2.26 are creep and swelling. Given that creep leads to stress relaxation in a system, it can be argued that the initial large rumpling growth rate shown in Figure 2.9 corresponds to the initial sharp decrease in the stress magnitude of the bond coat as shown in Figure 2.11; because this large stress relaxation is a result of large creep deformation at high temperature, following from Equation 2.26. Additionally, in the absence of thermal mismatch, the only term in Equation 2.26 that has the possibility of increasing the stress is swelling which is in accordance with the previously shown Figure 2.7; therefore, it can be argued that swelling is responsible for the changes in the stress level of the bond coat during the dwell period as shown in Figure 2.11. In the later subsections, a more in depth discussion is made about the change in bond coat stress during the dwell period and its relation with rumpling growth.

In addition to the rumpling growth during the dwell period, Figure 2.10 shows that rumpling also grows during heating and cooling processes which is one source of difference between the isothermal and thermal cyclic cases. The rumpling growth during cooling is almost double the growth during heating; this is because the cooling duration is twice that of the heating duration, hence, more time for growth. In addition to the difference between the thermal cycling cases and the isothermal case, there is a difference between the two thermal cyclic cases, i.e. rumpling growth for $T_2 = 1050^\circ$ is greater than $T_2 = 25^\circ\text{C}$. This difference is because for the fixed duration of heating and cooling processes swelling and creep in the $T_2 = 1050^\circ\text{C}$ case are active for longer, given that creep and swelling are activated above 900°C .

Having looked at the overall picture, three factors were identified that affect rumpling growth; i) swelling induced stresses, ii) the initial conditions, and iii) rumpling growth during heating and cooling processes. As I have touched upon in the above discussion, stresses induced from swelling lead to the largest part of rumpling growth, therefore, it is the main factor to be discussed in more detail. Nevertheless, the other two factors also affect rumpling, hence for completeness, deserve further discussion.

2.3.1 Swelling

As the discussion of Figure 2.10 went, the maximum rumpling growth occurs at the dwell duration of all the cases. The terminology “dwell” is used for both thermal cycling and isothermal conditions; in

both cases it refers to the one hour period during which the system is working at the peak temperature. During dwell there is no temperature change, therefore, no thermal expansion or contraction effects are present. Considering this condition and Equation 2.26, it is clear that the two main active roles at the peak temperature are stress terms from swelling and creep. Stress term due to creep is a relaxing term which means that it acts to reduce the magnitude of the stress in the system through creep deformation; the creep effect is a temperature and stress dependent term, i.e. at high temperatures and under high stresses the stress relaxation term becomes very large.

Looking at the second active term in Equation 2.26 during dwell, which is swelling, it can be seen from Figure 2.7, Equation 2.19 and Equation 2.22 that it is a stress, temperature and time dependent phenomenon. Effect of creep in the bond coat's behaviour has been a known fact since the early works on the TBC system, however, effects of swelling is considerably new and its relations to the rumpling was not known, therefore, finding this relationship between swelling and rumpling is a novel and important finding.

Given the experimental data on swelling [13], it is known that the bond coat's thickness increases sharply in the first few hours of the experiment for both thermal cycling and isothermal cases but in the following hours the trend changes; for the isothermal case the increase in the thickness slows down and after a certain time starts to decline, whereas, for the thermal cycling case it continues to increase at a much slower but constant rate. This difference in the swelling behaviour of the bond coat under these two conditions is a key factor for the difference in the rumpling growth of these two cases.

The sharp initial thickness growth due to swelling leads to a sharp increase in the stress level of the system, which is followed by a large creep deformation and stress relaxation, hence the large initial increase in the rumpling growth as shown in Figure 2.9 and Figure 2.10. This trade-off between creep and swelling continues throughout the experiment; taking the thermal cycling case, for instance, the swelling stress as shown in Figure 2.7 continues to grow with time. Looking at Figure 2.10 it is clear that after the large initial rumpling growth, there is a lower but continuous rumpling growth during dwell. This rumpling growth is a result of creep deformation that takes place in order to reduce the stresses raised from swelling. In other words, the increase in the bond coat stress level at the peak temperature due to swelling, keeps the creep deformation and rumpling growth highly active; this is true for both thermal cycling and isothermal cases.

Figure 2.12 shows the bond coat stress profile in time during the dwell process, and how this profile changes with cycles; this figure is to give a clearer evidence of the point made above. As is evident from Figure 2.12, the difference between the 1st and 2nd cycles for the stress in the bond coat is much

larger than the difference between the 50th and 100th cycles. This significant difference between the first few cycles and the final cycles is also stemmed from the nature of swelling which has a large initial rate followed by a shallower and constant rate.

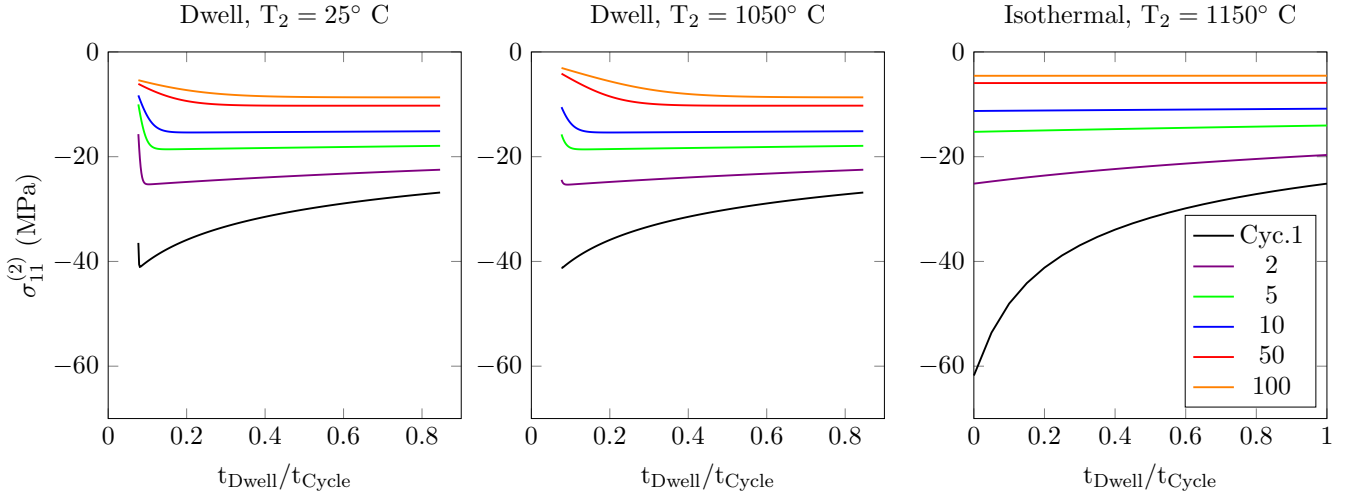


Figure 2.12: Change of bond coat stress for the dwell duration in the 1st, 2nd, 5th, 10th, 50th and 100th cycles for $T_2 = 25, 1050$ and 1150°C . Please note that the x-axis is the normalised time where t_{cycle} is 3600s for isothermal case and 4680s for thermal cycling case.

In addition to the trend of stress with number of cycles, there is a characteristic shape for the stress profiles in the dwell duration of each thermal cycle; there is an initial increase in the stress magnitude for all the cycles followed by a stress relaxation for the first cycle and convergence of stress for the rest of the cycles. This initial rise in stress is because of swelling which at this temperature activates creep, leading to stress relaxation for the rest of the dwell duration. The reason for the difference between the first cycle and the rest of them is that in the first cycle the overall magnitude of stress is much higher than the rest of the cycles, as a result of which the activated creep is stronger. For the isothermal case, on the other hand, the trend is different; in this case there is a continuous stress relaxation from the first cycle to the last where the initial high stress is caused by a combination of swelling and thermal mismatch.

Apart from the general comments made about the dwell process in all the cases, there is a specific comparison that can be made between the plots for $T_2 = 25^\circ\text{C}$ and 1050°C ; this comparison is the difference in their starting stresses. Given that the swelling data used for all the thermal cycling cases is taken to be the same, this initial difference comes from the difference in the heating rates before the start of dwell. This assumption of same swelling behaviour for all the thermal cycles, is due to the limited availability of experimental data on swelling; the current swelling data used for this study are for thermal cycles between the room and peak temperatures, as a result of which, the effect of swelling on the system is computed to be the same, only for the thermal cycling cases. As a future experimental work, it is worth measuring the swelling effect for thermal cycles with different lower

cycle temperatures. In conclusion to this subsection, it is clear that swelling provides the main stress source for rumpling growth.

2.3.2 Initial Conditions

As identified at the beginning of this section, initial conditions of the thermal cycling and isothermal cases also have an effect on the final rumpling amplitude. In this study, the initial conditions are set through the “Pre-steps” of the simulation, as defined in Figure 2.3. “Pre-steps” consist of a cooling step from the deposition temperature of the coating to the room temperature, and a heating step from the room temperature to the desired T_2 temperature.

The cooling in the “Pre-steps” of all the cases is the same, with a fixed temperature change over the time of 360s as shown in Figure 2.13. However, for the pre-step heating, while the duration is fixed at 360s for all cases, the rate of temperature change is different; this means for different T_2 values the temperature rate becomes different which leads to different stress and rumpling amplitudes at the end of pre-step heating, Figure 2.13. This difference in the heating rate gives one of the reasons for the initial rumpling amplitude of isothermal case in Figure 2.9 to be as high as others; because higher temperature rate means larger thermal mismatch effect. For isothermal case this is the only time during the analysis where the bond coat stress is affected by thermal mismatch. For $T_2 = 25^\circ\text{C}$ case there is no temperature change during the heating pre-step, leading to no stress change or rumpling growth which explains the initial difference between $T_2 = 25^\circ\text{C}$ and 1050°C cases in Figure 2.9. In addition to these findings, its clear from the plot in Figure 2.13 that for both cases, $T_2 = 1050^\circ\text{C}$ and 1150°C their stress behaviour changes when they reach the time of about -75s (corresponding to 900°C); clearly marking the presence of swelling and creep.

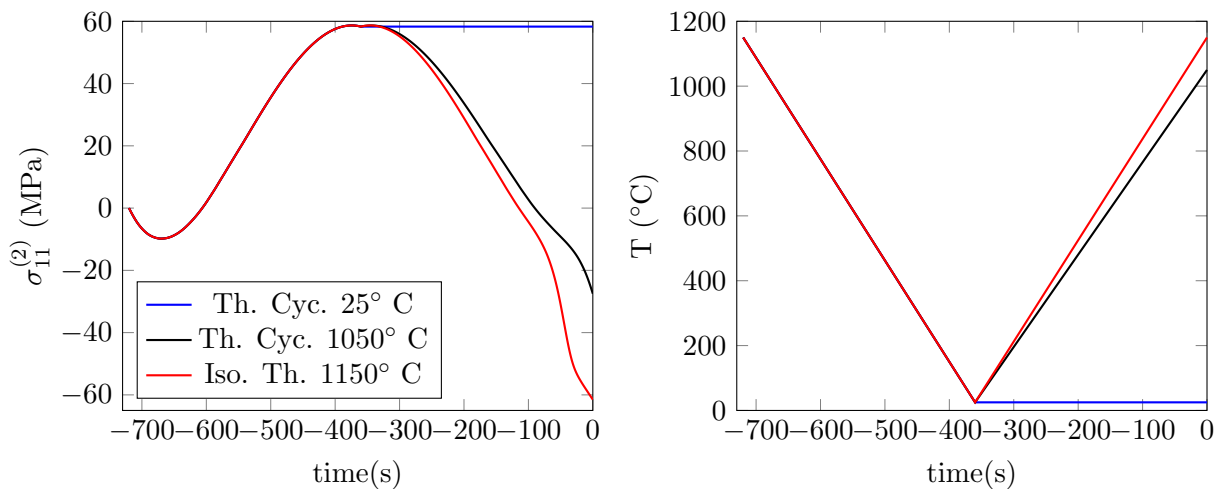


Figure 2.13: $\sigma_{11}^{(2)}$, and temperature change of the pre-steps for $T_2 = 25, 1050$ and 1150°C vs time. Negative time here means before the start of the actual experiment.

In order to explain the form that the bond coat stress has taken in the pre-step heating of Figure 2.13, effect of each term in Equation 2.26 is plotted separately. To do this, the stress in the bond coat is computed with Equation 2.26 using one term at a time; for example, for the “Creep Only” case, the thermal mismatch and swelling terms are removed from the equation and stress in the bond coat is computed. The results of this study are shown in Figure 2.14; please note, since there is no temperature change in the heating pre-step of $T_2 = 25^\circ\text{C}$ and none of the factors are activated at this temperature, there is no pre-step stress change for it, therefore it is not shown in this figure.

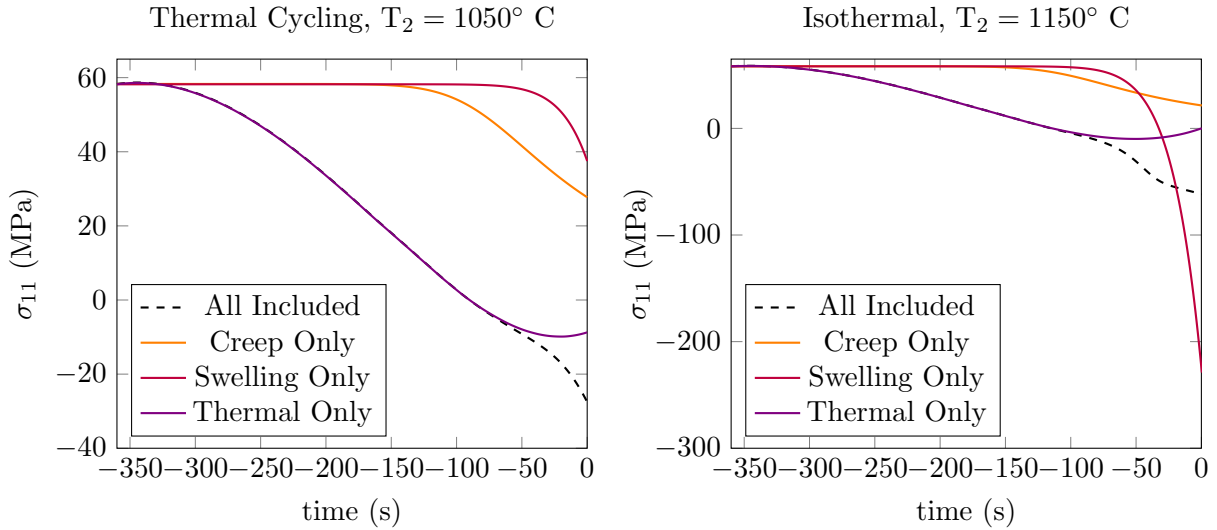


Figure 2.14: Stress changes from creep, swelling and thermal mismatch separately for the heating pre-step of $T_2 = 1050^\circ\text{C}$ and 1150°C .

Considering the effect of thermal expansion term only, i.e. “Thermal only”, it is clear from the experimental data that the CTE of the bond coat and substrate change with temperature, as shown in Figure 2.6. In this figure the positive difference between the CTEs refers to higher expansion of the substrate compared to the bond coat during heating and higher contraction upon cooling, with the negative difference having the opposite effect. As can be seen in Figure 2.14 the stress change for “Thermal only” case, i.e. the purple line, is consistent with the difference in the CTEs from Figure 2.6.

“Creep only” is the second term in this sensitivity study; as is clear from Figure 2.14, the orange line which represents the “Creep Only” case, shows a stress change only more than half way through the pre-step heating. This behaviour means that creep effects only become active at around this temperature if initial stress is about 60MPa and other factors are not present, which is about $700 - 800^\circ\text{C}$; once activated, creep clearly leads to stress relaxation in the system.

The final factor to consider is the swelling term, i.e. the red line in Figure 2.14; it is clear that the stress effect from swelling activates at around time of -75s, meaning 75s left to the start of the whole experiment, which corresponds to 900°C ; this is true for both thermal cycling and isothermal cases. Once activated, swelling increases the stress level in the compressive direction. As the comparison between the thermal cycling and isothermal cases show, the stress magnitude from swelling in the

isothermal case is much higher than the thermal cycling case. This difference is because of the final temperature at the end of the pre-step heating; the higher the temperature the more pronounced the swelling effect, as shown in Figure 2.7. Therefore, for the isothermal case where the end temperature at the pre-step heating is 1150°C compared to 1050°C , the stress from swelling is higher. This finding suggests that for the $T_2 = 1050^{\circ}\text{C}$ case a stress spike must be observed in the first thermal cycle of the experiment when the peak temperature is reached; as will be seen in Figure 2.15, this is the case.

The black dashed line in Figure 2.14 shows the case where the effect of thermal mismatch, creep and swelling are all included. As is clear from this figure, up to about -75s (i.e. 900°C) there is only thermal mismatch affecting the stress, however, after this temperature both swelling and creep are activated leading the shape change that the black dashed line has compared to the purple one. Please note that when all the effects are combined, creep activation occurs at a later time than the “Creep only” case; this is because in the combined case the stress magnitude at an earlier time is very weak to activate creep, whereas, at -75s stress from swelling appears and activates creep at the same time. In addition to creep stress relaxation, after -75s there is a tensile stress from thermal mismatch opposing the compressive stress from swelling. This mechanism and interaction between the terms of Equation 2.26 is the same for the pre-step heating of both $T_2 = 1050$ and 1150°C cases; the difference between them stems from the difference in their swelling behaviour and rate of increase in temperature. It is concluded from this analysis that rumpling growth starts as soon as swelling effect appears.

2.3.3 Rumpling During Heating and Cooling

The final identified parameter that has a contribution to rumpling growth, is the heating and cooling steps of thermal cycling condition only, therefore, this last parameter does not effect the isothermal case. As a result, in addition to the difference in the swelling behaviour, the rumpling growth from the heating and cooling steps is another source of difference between these two working conditions. As the results in Figure 2.10 showed, noticeable rumpling growth occurs during heating and cooling steps which continuously raise with number of cycles. In order to investigate this further, the bond coat stress profile for heating and cooling steps are shown for a number of cycles, i.e. Figure 2.15.

For the $T_2 = 25^{\circ}\text{C}$ case, the stress profile of the bond coat in the first heating step is similar to the pre-step heating of the isothermal case, i.e. Figure 2.13; this is because in both cases the system is heated from the room temperature to the peak temperature within the same time period; the slight difference between them comes from the difference in their swelling behaviour.

For $T_2 = 1050^{\circ}\text{C}$, however, there is an initial increase in the magnitude of stress followed by

convergence to a constant value. The sudden change in the stress at the beginning of the first cycle is due to the reduction in heating rate from the heating pre-step which was also mentioned in the previous subsection. This sudden change of stress in the first cycle reduces the thermal mismatch effect, allowing for swelling to make the stress more compressive while creep becomes activated and relaxes the stress. The interaction between swelling, thermal mismatch and creep is similar to the one explained in the previous subsection.

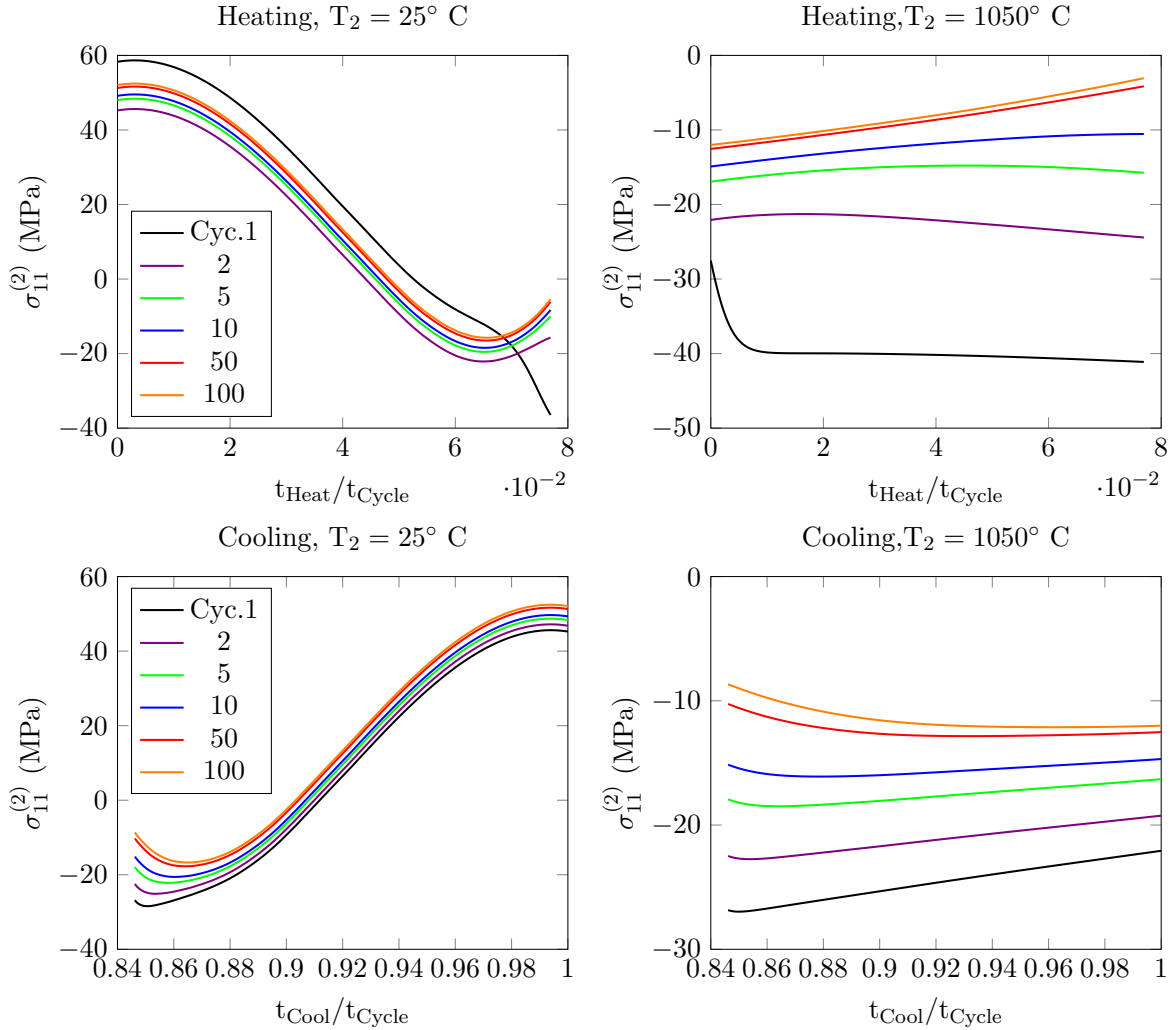


Figure 2.15: Stress changes of the heating and cooling processes in the cycles 1,2,5,10,50 and 100 for $T_2 = 25$ and 1050°C vs time.

Similarly, during the cooling step as shown in Figure 2.15, high stresses induced by swelling at the high temperature region is dominant, however, these high stresses are relaxed via creep deformation and the initial compressive stresses from thermal mismatch. As temperature drops, the effect of swelling and creep diminishes for the $T_2 = 25^\circ\text{C}$ case, but only reduces for $T_2 = 1050^\circ\text{C}$. It is important to note that the cooling duration is twice that of heating; for that reason, the time for which creep and swelling are activated is longer, leading to more rumpling growth in the cooling step, as is apparent from Figure 2.10. For $T_2 = 1050^\circ\text{C}$ case, all three factors are active throughout the heating and cooling steps; this is why for this case there is more rumpling growth than $T_2 = 25^\circ\text{C}$,

however, because the heating and cooling durations are much smaller than the dwell duration, where most of rumpling growth occurs, the difference in rumpling amplitude of the two thermal cycling case is not as significant as the difference with the isothermal case.

The change in the stress profiles as the number of cycles increase, is not uniform; the difference between the first 10 cycles is much more than the difference between the final 50 cycles. This behaviour was also observed when looking at the stress profile of the dwell duration in the subsection 2.3.1. Given that stress from thermal mismatch alone does not change with the number of cycles, therefore, it is not responsible for the difference in the stress profile of the cycles. Creep effect is a temperature and stress activated phenomenon which on its own does not change between cycles, therefore, the only factor remaining is swelling which not only changes with temperature but also changes with time. Hence this difference between the stress behaviour of cycles, as they increase, comes from the swelling behaviour of the bond coat under thermal cycling condition.

2.4 Conclusion

Over the course of this work, it was shown that swelling is the underlying source of rumpling growth in the TBC systems. Previously it was believed that source of rumpling growth in TBC systems is from phenomenon such as phase transformation and thermal mismatch that occur during the heating and cooling processes of a thermal cycle. However, the findings from an experimental work by Tolpygo & Clarke, [1], could not be explained using those theories; in this experiment they measured the rumpling amplitude of the TBC system after $100 \times 1\text{hr}$ cycles between a range of lower temperatures, T_2 , and a peak temperature of 1150°C . They found that changing the lower temperature of the thermal cycle has negligible effect on the final rumpling amplitude of the system, except for when the lower temperature is the same as the peak temperature which is equivalent to an isothermal case. This behaviour was puzzling and could not be explained with the previously suggested theories for rumpling.

In this work the existing analytical model of rumpling by Balint *et al.* [2] was modified to include the swelling effect which is relatively new, and was used to reproduce the experimental results. At first, the model was verified by qualitatively reproducing the experimental results, and then was used to find the source of rumpling. As shown in the model, there is a strong relationship between the rumpling growth and the in-plane stresses in the bond coat. Using the results from the model, it was shown that swelling is activated at high temperatures and increases the stress level of the system which in turn activates creep, leading to rumpling growth.

During the analysis of the data from the model, it was found that most of the rumpling growth

occurs in the dwell duration where only creep and swelling effects are present. Rumpling growth is a result of trade-off between the stress rise from swelling and stress relaxation from creep. Not only swelling is the driving force for the rumpling growth during the dwell but also it shows its effects in the heating and cooling processes. While other parameters such as phase transformation and thermal mismatch affect rumpling growth, it was shown that swelling is the main source for it.

The swelling data used in the developed model is based on one set of experimental data by [13], which is measured for thermal cycles between the room and peak temperature, therefore, in order to use this model in a more accurate manner it would be useful to have experimental data on the swelling of the bond coat for thermal cycles with different lower temperatures.

2.5 Table of variables

Table 2.3: Variables and terms used in this chapter and their definitions.

T_D	Deposition temperature
T_1	Peak or oxidation temperature
T_2	Lowest temperature of a thermal cycle
T_r	Room temperature
$T_R^{(2)}$	The creep reference temperature of the bond coat layer
T	Temperature of the system
\dot{T}	Temperature rate of the system
Dwell	The longest time that the system is at its operation (oxidation) temperature
δ_0	Initial rumpling amplitude
$\delta^{(k)}$	Current rumpling amplitude of the k^{th} layer
δ_{ij}	Kronecker delta
δ_{RMS}	Root mean square amplitude of the rumpling, i.e. $= \delta/\sqrt{2}$
L	Half wavelength of the undulation in the model of rumpling
mc	Thermal cycle number
mi	The hour of isothermal case
δ_1^{mc}	RMS Rumpling amplitude at the start of heating process of the mc^{th} cycle
δ_2^{mc}	RMS Rumpling amplitude at the start of dwell process of the mc^{th} cycle
δ_3^{mc}	RMS Rumpling amplitude at the start of cooling process of the mc^{th} cycle
δ_4^{mc}	RMS Rumpling amplitude at the end of the mc^{th} cycle
δ_1^{mi}	RMS Rumpling amplitude at the start of the mi^{th} isothermal hour
δ_2^{mi}	RMS Rumpling amplitude at the end of the mi^{th} isothermal hour
$\dot{\delta}^{(2)}$	Rate of growth of the rumpling amplitude in the bond coat layer
t_{heat}	Duration of heating
t_{dwell}	Duration of dwell
t_{cool}	Duration of cooling
t_{cycle}	Duration of a cycle
t	Time
TGO	Thermally grown oxide
TBC	Thermal barrier coating
$\square^{(1)}$	Properties and variables related to the substrate
$\square^{(2)}$	Properties and variables related to the bond coat
$\square^{(3)}$	Properties and variables related to the TGO
$\square^{(4)}$	Properties and variables related to the top coat
$h^{(k)}$	Current height of the k^{th} layer
$h_0^{(k)}$	Initial height of the k^{th} layer
\dot{h}	Rate of thickening of the TGO
$\nu^{(k)}$	Poisson ratio of the k^{th} layer

$E^{(k)}$	Young's modulus of the k^{th} layer
$\bar{E}^{(k)}$	$E^{(k)} / (1 - \nu^{(i)})^2$
$\alpha^{(k)}$	Coefficient of thermal expansion of the k^{th} layer
$\sigma_{ij}^{(k)}$	Stress term of the k^{th} layer in the ij direction, where i & j change between 1, 2 and 3
$\dot{\sigma}_{ij}^{(k)}$	Stress rate of the k^{th} layer in the ij direction, where i & j change between 1, 2 and 3
$s_{ij}^{(k)}$	k^{th} layer deviatoric stress in the ij direction, where i & j change between 1, 2 and 3
$\sigma_R^{(2)}$	The creep reference stress of the bond coat layer
$\sigma_s^{(2)}$	$\sigma_{33}^{(2)} / \sigma_{11}^{(2)}$
$\sigma_e^{(2)}$	Effective stress in the bond coat
$\sigma_y^{(3)}$	Yield strength of the TGO
$n^{(2)}$	The creep exponent of the bond coat layer
$\dot{\epsilon}_0^{(2)}$	The creep reference strain rate of the bond coat layer
$\dot{\epsilon}_{ij}^{(k)}$	Strain rate of the k^{th} layer in the ij direction, where i & j change between 1, 2 and 3
$\dot{\epsilon}_G^{(3)}$	Lateral growth strain rate of the TGO
$\dot{\epsilon}_P^{(2)}$	Strain rate of the bond coat due to phase transformation
$\dot{\epsilon}_S^{(2)}$	Strain rate of the bond coat due to swelling
d	A constant chosen as such that 5% of the lateral growth occurs in 100h at 1150°C
Q	Activation energy
A	A constant to be found from the experimental data
k	Boltzmann's constant
p	The normal traction between the layers of the system
$\theta(n^{(2)}, \sigma_s^{(2)})$	Refer to equation Equation 2.4
$g(n^{(2)}, \sigma_s^{(2)})$	Refer to equation Equation 2.5
m	Refer to equation Equation 2.6
M	time exponent for Equation 2.19
$a(n^{(2)}, \sigma_s^{(2)})$	Refer to equation Equation 2.3
$b(n^{(2)})$	Refer to equation Equation 2.8
P	Refer to equation Equation 4.21
V	Refer to equation Equation 2.16
L^*	Refer to equation Equation 2.17
$w_0(x_1)$	Initial normal displacement of the sinusoidal profile of rumpling
$w(x_1)$	Current normal displacement of the sinusoidal profile of rumpling

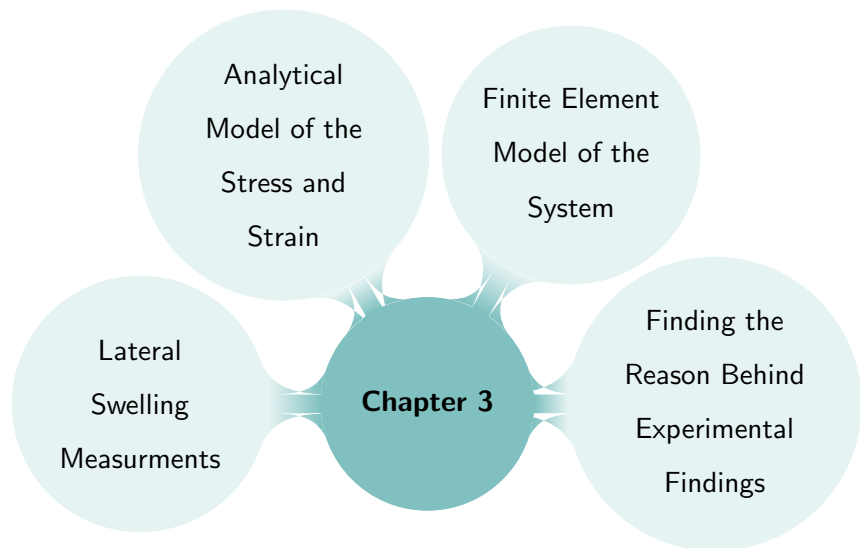
2.6 Bibliography

- [1] V K Tolpygo and D R Clarke. Rumpling of CVD (Ni , Pt) Al diffusion coatings under intermediate temperature cycling. *Surface & Coatings Technology*, 203:3278–3285, 2009.
- [2] D S Balint and J W Hutchinson. Undulation instability of a compressed elastic film on a nonlinear creeping substrate. *Acta Materialia*, 51:3965–3983, 2003.
- [3] Rolls-Royce. *The jet engine*. Rolls-Royce plc, 1996.

-
- [4] Robert A Miller (Glenn Research Center, Cleveland, Ohio). History of Thermal Barrier Coatings for Gas Turbine Engines Emphasizing NASA ' s Role From 1942 to 1990. *Nasa/Tm*, 215459(March), 2009.
- [5] W.N. Harrison, D.G. Moore, and J.C. Richmond. Ceramic coatings for high-temperature protection of steel. *Journal of Research of the National Bureau of Standards*, 38:293–307, 1947.
- [6] Warnes et al. Platinum Modified Aluminide Diffusion Coating and Method, 1998.
- [7] V K Tolpygo. SURFACE RUMPLING OF A (Ni , Pt) Al BOND COAT INDUCED BY CYCLIC OXIDATION. *Acta Materialia*, 48:3283–3293, 2000.
- [8] A G Evans, D R Mumm, J W Hutchinson, G H Meier, and F S Pettit. Mechanisms controlling the durability of thermal barrier coatings. *Progress in Materials Science*, 46:505–553, 2001.
- [9] Anette M Karlsson and A G Evans. A Numerical Model for the Cyclic Instability of Thermally Grown Oxides in Thermal Barrier Systems. *Acta*, 49(10):1793–1804, 2001.
- [10] A M Karlsson, J W Hutchinson, and A G Evans. A fundamental model of cyclic instabilities in thermal barrier systems. *Journal of Mechanics and Physics of Solids*, 50:1565–1589, 2002.
- [11] V Tolpygo and D R Clarke. Morphological evolution of thermal barrier coatings induced by cyclic oxidation. *Surface & Coatings Technology*, 163:81–86, 2003.
- [12] D.R. Clarke and C.G. Levi. Materials Design for the Next Generation Thermal Barrier Coatings. *Annual Review of Materials Research*, 33(1):383–417, 2003.
- [13] V K Tolpygo and D R Clarke. On the rumpling mechanism in nickel-aluminide coatings Part II : characterization of surface undulations and bond coat swelling. *Acta Materialia*, 52:5129–5141, 2004.
- [14] J. GRONIAKOWSKI and C. NOGUERA. Relaxation and rumpling mechanisms on oxide surfaces. *Surface science*, 323(1-2):129–141, 1995.
- [15] D S ˜A Balint and J W Hutchinson. An analytical model of rumpling in thermal barrier coatings. *Journal of Mechanics and Physics of Solids*, 53:949–973, 2005.
- [16] V. K. Tolpygo and D. R. Clarke. Temperature and cycle-time dependence of rumpling in platinum-modified diffusion aluminide coatings. *Scripta Materialia*, 57(7):563–566, 2007.
- [17] Vladimir Tolpygo, K S Murphy, and David R Clarke. Effect of Hf , Y and C in the underlying superalloy on the rumpling of diffusion aluminide coatings. *Acta Materialia*, 56(February 2015):489–499, 2008.
-

- [18] D. Pan, M. W. Chen, P. K. Wright, and K. J. Hemker. Evolution of a diffusion aluminide bond coat for thermal barrier coatings during thermal cycling. *Acta Materialia*, 51(8):2205–2217, may 2003.
- [19] A M Karlsson, J W Hutchinson, and A G Evans. The displacement of the thermally grown oxide in thermal barrier systems upon temperature cycling. *Materials Science and Engineering: A*, 351:244–257, 2003.
- [20] X. Wang, G. Lee, and A. Atkinson. Investigation of TBCs on turbine blades by photoluminescence piezospectroscopy. *Acta Materialia*, 57(1):182–195, 2009.
- [21] Rahul Panat, Sulin Zhang, and K Jimmy Hsia. Bond coat surface rumpling in thermal barrier coatings. *Acta Materialia*, 51:239–249, 2003.
- [22] Y Chen, X Zhao, M Bai, L Yang, C Li, L Wang, J A Carr, and P Xiao. A mechanistic understanding on rumpling of a NiCoCrAlY bond coat for thermal barrier coating applications. *Acta Materialia*, 128:31–42, 2017.
- [23] V K Tolpygo and D R Clarke. On the rumpling mechanism in nickel-aluminide coatings Part I : an experimental assessment. *Acta Materialia*, 52:5115–5127, 2004.
- [24] D S Balint, S Kim, Yu-fu Liu, R Kitazawa, Y Kagawa, and A G Evans. Anisotropic TGO rumpling in EB-PVD thermal barrier coatings under in-phase thermomechanical loading. *Acta Materialia*, 59(6):2544–2555, 2011.
- [25] J. A. Haynes, B. A. Pint, W. D. Porter, and I. G. Wright. Comparison of thermal expansion and oxidation behavior of various high-temperature coating materials and superalloys. *Materials at High Temperatures*, 21(2):87–94, 2004.
- [26] A H Heuer, N J Tighe, and R M Cannon. Plastic Deformation of Fine-Grained Alumina (Al_2O_3): II, Basal Slip and Nonaccommodated Grain-Boundary Sliding. *Journal of the American Ceramic Society*, 83(1-2):53–58, 1980.
- [27] H J Grabke, M Steinhorst, M Brumm, and D Wiemer. Oxidation and Intergranular Disintegration of the Aluminides NiAl and NbAl₃ and Phases in the System Nb-Ni-Al. *Oxidation of Metals*, 35(3):199–222, 1991.
- [28] D S Balint, T. Xu, J.W. Hutchinson, and A.G. Evans. Influence of bond coat thickness on the cyclic rumpling of thermally grown oxides. *Acta Materialia*, 54:1815–1820, 2006.

3



Lateral Growth in the Bond Coat and Inter-diffusion Layers

3.1 Introduction

As discussed in the previous chapter, turbines and their blades are essential parts of a jet engine which operate in a high temperature environment, therefore, thermal barrier coatings (TBC) are applied to them. In addition to the three main layers of the TBC, i.e. the top coat, TGO and bond coat, there is a fourth layer, called inter-diffusion, which is a mixed layer between the bond coat and the substrate forming as a result of Ni diffusing from the substrate into the bond coat and Al diffusing out of the bond coat and into the substrate. This layer is not counted as part of the TBC design because as most of the work on that layer have suggested, it is an undesirable layer [1–5]; the reason for that will be discussed more later in this section.

As turbine blades function, TBCs undergo rumpling, which is a roughening effect that can lead to spallation of the top coat and failure of the turbine blade. As discussed in chapter 2, the main source of rumpling is swelling, in both thermal cycling and isothermal conditions. Swelling in the bond coat material is a relatively new topic which was first introduced by Tolpygo and Clarke [6] in 2004. In their study, Tolpygo and Clarke showed that there is volumetric expansion in the bond coat layer as a result of Ni diffusion from the substrate into the bond coat, which diffuses at least three times faster than Al out of the bond coat and into the substrate; this volumetric expansion was named “swelling”. Given that the swelling phenomenon is relatively new and its relationship with rumpling was not known until the work in chapter 2, as far as the author of this thesis is aware, there are not many relevant literature

work carried out on this topic, (The reader is referred to the literature review section of chapter 2 for information about the literature on rumpling). While there are not many literature available on the topic of swelling in the bond coat and its relation to rumpling, it has got the attention of a few current research works, one of which is Chen *et al.* group in Manchester, with whom a collaboration was formed for this chapter. In this collaboration the focus is on understanding the relationship between swelling, lateral growth of the bond coat and inter-diffusion layer, and rumpling.

In their experimental work on measuring the lateral growth of the bond coat / inter-diffusion layers, Chen *et al.* came across a surprising result which formed the basis of this collaboration. Their experimental work consists of CMSX-4 substrate samples covered by (Pt,Ni)Al coating placed under an isothermal condition at 1150°C for 50hrs, where the lateral growth of the bond coat and the inter-diffusion layer on the edge of the system were monitored. The result from this experiment showed a significant lateral growth for the bond coat and almost none for the inter-diffusion layer, which was puzzling because one would expect for two adjacent layers to have similar expansions at their common interface. In other words, as the bond coat expands laterally, one would expect the inter-diffusion layer to also expand laterally at the interface between these layers, which was not the case here. Additionally, because swelling was observed in both layers, one would expect for inter-diffusion layer to laterally expand as well.

Understanding the reason behind this experimental results is important because it indicates some unknown facts about the inter-diffusion layer; either in terms of its material property or its swelling behaviour. Given that swelling is identified as the main source of rumpling, finding the cause for this puzzling behaviour can be a key to making more accurate predictions about the rumpling behaviour of the system. As a start to this understanding process, a brief literature review is given next.

3.1.1 Literature Review

There are two bond coat types that are used in the turbine blade design; i) overlays (MCrAlY) and ii) diffusion aluminides (Pt- β NiAl); the latter type bond coats are commonly used because of their ability to form slow growing TGOs at high temperatures [4]. As this type of bond coat work under high temperatures, an inter-diffusion layer forms between them and the substrate as a result of Al and Ni diffusion, effect of which has been studied by many researchers [2–5, 7–13, 13–15]. In most of these research works, this layer is called inter-diffusion zone or IDZ. During the heat exposure process, the Ni from the substrate diffuses into the bond coat and the Al and Pt from the bond coat diffuse into the substrate; the Ni increase and Al decrease in the bond coat result in a phase transformation from β (Pt,Ni)Al to γ' (Ni₃Al) and γ (Ni,Pt), [4,5,9,13], which are accompanied by topologically closed packed (TCP) phases in the γ' matrix at the inter-diffusion zone [4, 5, 9, 13].

TCPs are crystal structures that consist of closed packed layers of smaller atoms such as nickel, with the larger atoms such as rhenium, placed at specific location between these layers; depending on the location of the larger atom, a wide range of TCP phases can form [16]. In most cases the TCP phases have a plate like morphology parallel to the $\{111\}$ planes which leads to a needle-like appearance when viewed from the $\{100\}$ plane. TCPs are brittle in nature and are known to have disadvantageous effect on the mechanical behaviour of the superalloy [1–3].

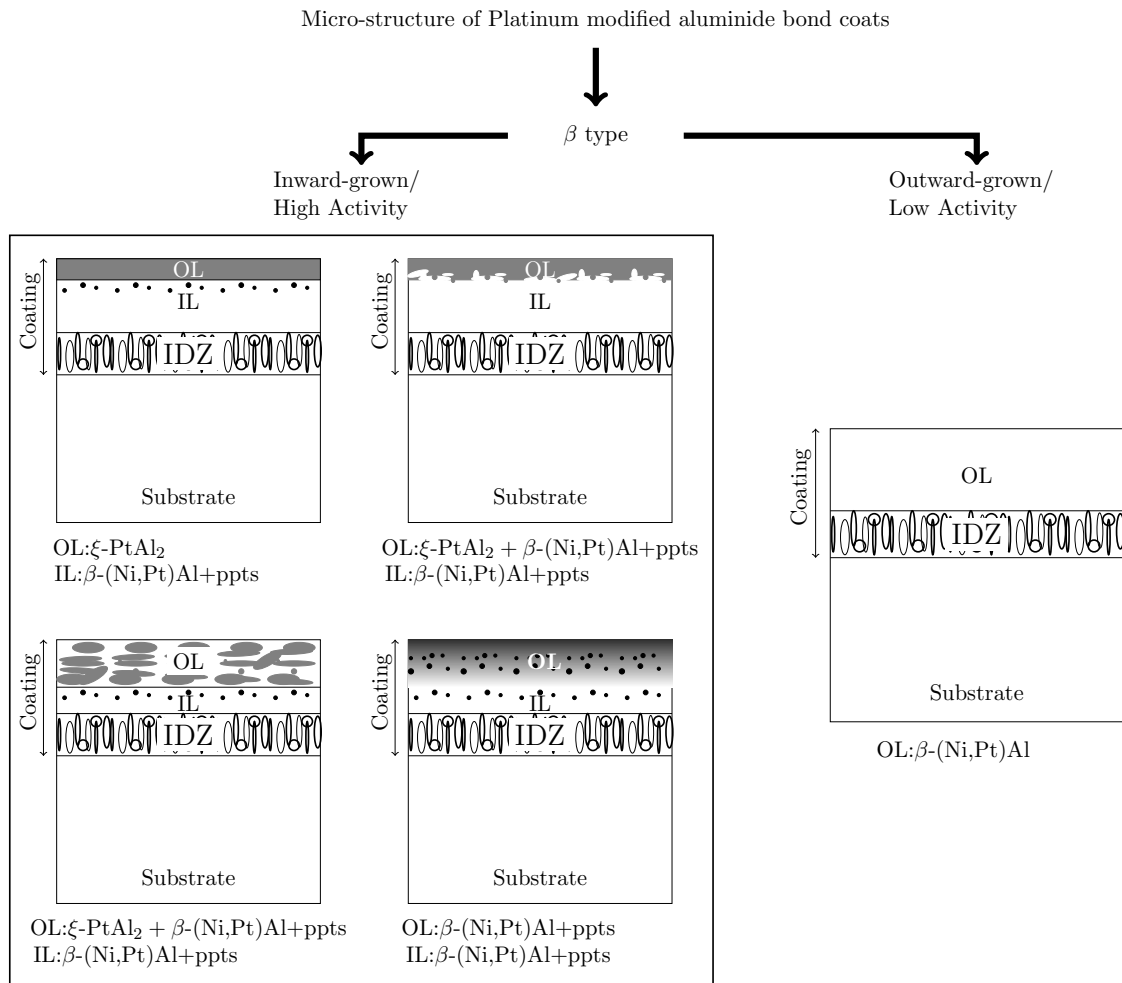


Figure 3.1: A summary of the two- and three-layered bond coat and IDZ, and their phases as a result of the manufacturing process, (This infographic has been adapted for this thesis from [15].)

It has been shown that the characteristics of the bond coat and IDZ depend on the activity of the Al applied to the surface of the substrate during the manufacturing process [4, 7, 10, 15]. Based on the growth mechanism used in formation of the bond coat during their aluminisation process, the type of the inter-diffusion layer that forms differ; it can either be two-layered (β -NiAl with no precipitates+IDZ) or three-layered (β -NiAl with fine precipitates + β -NiAl with strip precipitates + IDZ) where in both cases the IDZ has complex precipitates distributed in an matrix of phase β . The

two or three layered format is decided by the aluminisation of the manufacturing process of the bond coat; either “inward” or “outward”, a summary of which is shown in Figure 3.1. Here inward means that during the aluminisation process the coating grows inwards into the substrate starting from its initial surface which is done through low temperature high activity aluminisation process, whereas, for the outward the coating grows outwards from the surface of the substrate which is done through high temperature low activity aluminisation process [2, 4, 15, 17].

During aluminisation process or TBC deposition or oxidation, formation of a secondary reaction zone (SRZ) beneath the IDZ is a very common problem [3, 8]; SRZ is also called cellular transformation of the substrate which consists of typical alloy phases such as γ -Ni and γ' -Ni₃Al in CMSX-4, and TCPs. SRZs continuously consume the useful elements such as Re, W and Mo, from the superalloy making it susceptible to cellular precipitation which can reduce the creep rupture properties of the superalloy significantly at high temperatures [4, 5]. It has been shown that presence of elements such as Re, W, and Ru in the substrate can lead to formation of SRZ at the dendritic core regions of the coating, and exposure to high temperature can lead to significant SRZ growth [11].

Presence of Al in the bond coat is of importance because it is the main ingredient for formation of the protective TGO layer, however, at a high temperature environment there are three ways of reducing Al content in the β NiAl phase of the bond coat; i) TGO formation, ii) inward diffusion of Al into the substrate and iii) an outward Ni-dilution effect from the substrate. These factors lead to effects such as accelerated phase transformation in the bond coat from β to γ' phase, [4], or the swelling of the bond coat from the Ni diffusion from the substrate [4, 6].

Given the adverse effect that inter-diffusion between the bond coat and the substrate has on the mechanical properties of the substrate and oxidation behaviour of the bond coat, there have been some works on finding ways of reducing the IDZ effect [3, 4, 12, 14]. The inter-diffusion between the bond coat and the substrate is controllable by both exposure time and temperature, [4, 14], but also it has been shown that by adding elements such as Re and Ru a diffusion barrier overlay can be formed that reduces the inter-diffusion between the substrate and the bond coat [12, 14].

3.1.2 Objective

The objective of the work in this chapter is to understand and explain the surprising lateral growth behaviour of the bond coat and inter-diffusion layer after 50hrs of isothermal heat treatment, as provide by Chen *et al.*. In the process of answering this question, a postulation is put forward which suggests that inter-diffusion layer has lower creep resistance than the bond coat leading to rapid reduction in the in-plane stress. It is possible that this rapid reduction in the in-plane stress is responsible for no

lateral swelling of the inter-diffusion layer. In order to check the plausibility of this postulation, an analytical model of the stress and strain in the bond coat and inter-diffusion layers is developed. Once the plausibility of the postulation is verified, a finite element model is developed to model the lateral swelling of the edge of the system; the definition of swelling strain rate used in this FE model is taken from the analytical model. First, a two-layered coating model is introduced in finite element but for the reasons that will become apparent in this chapter, a final four-layered coating model is produced. This model is used to give an insight into the material property of the inter-diffusion layer which is not very well known, and how the characteristic lateral swelling forms on the edge of this system.

In the rest of this chapter first an explanation of the experimental procedure and its findings will be given, followed by the development and verification of the mathematical model for the stress and strain in the bond coat and inter-diffusion layers. Once developed, the analytical model is used to check the plausibility of the suggested postulation. Following that, the process for development of the finite element models and their corresponding outcomes are outlined. At the end the chapter is ended with results and conclusions drawn from the models.

3.2 Materials and Methods

Given that this work is a collaboration with the experimental group in Manchester, i.e. Chen *et al.*, this section is described in two main subsections; i) experimental procedure, and ii) modelling. In the first subsection, the experimental procedure and its findings are demonstrated, clearly showing the question raised from the outcome; and in the modelling subsection, the development and verification of the analytical model for the stress and strain in the layers, and the development of the two- and four-layered finite element models are shown.

3.2.1 Experimental Procedure

The bond coat material used in this experimental work is platinum modified aluminide or (Pt,Ni)Al which is deposited on to the Ni-based single-crystal CMSX-4. The samples used for the experimental work are cuboids with $10 \times 10 \times 1.5 \text{ mm}^3$ dimensions where the smallest dimension is the thickness with the top coat omitted from the system. In order to monitor the lateral growth of the bond coat, a clean initial profile of the sample edge is prepared and recorded as a reference. After polishing and cleaning the samples, they are annealed at 1150°C for 50 hours inside a vacuum furnace under a partial pressure of ($\sim 1 \times 10^{-3} \text{ Pa}$); after which the samples are cooled down to the room temperature when the microstructure of the samples is measured using SEM machine equipped with X-ray spectroscopy and electron backscatter diffraction.

3.2.1.1 Results of the Experiment

The geometry profile of the sample edge after the heat treatment is extracted using Image J software and compared to the initially flat edge which is aligned with the edge of the substrate. Figure 3.2 shows the obtained experimental image of the sample after 50 hours of annealing at 1150°C; according to the definitions obtained from Chen *et al.*, the layers A to C as labeled in Figure 3.2, are part of the bond coat, and the C to F layers are part of the inter-diffusion layer. This micrograph from the edge of the sample shows a major lateral swelling for the bond coat which gradually decreases in magnitude as the normal distance from the surface of the sample increases; i.e the A-B-C layers in the left image of Figure 3.2. The second observation from this micrograph is the sudden drop in the lateral growth of the system as the inter-diffusion layer is reached. This outcome is surprising because the analysis of the images taken from the sample before and after the heat treatment indicates thickening and swelling of the inter-diffusion layer after 50 hours annealing. In other words, how can there be a swelling effect in the inter-diffusion layer without it affecting its lateral displacement, given that swelling is a volumetric phenomenon? Answering this question formed the main objective of this work.

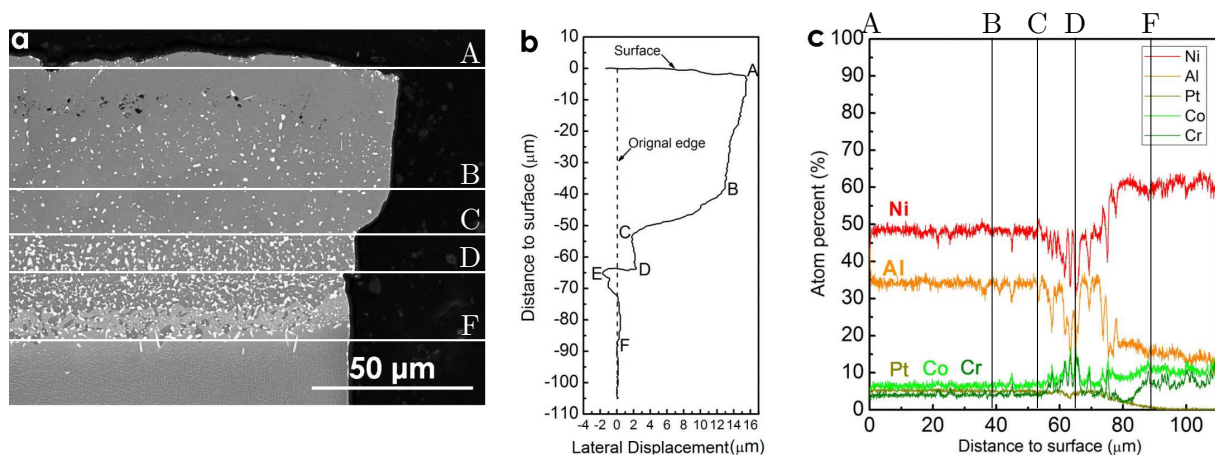


Figure 3.2: The experimental lateral swelling of the bond coat and inter-diffusion layer after 50 hours annealing at $T= 1150^{\circ}\text{C}$ obtained by Chen *et al.* **a)** The image of the system's edge, **b)** the dimensions of the edge profile and **c)** the composition of the layers from the surface of the sample. (Images are taken from personal communication with Chen *et al.*)

In addition to the micrographic results of the sample's edge after 50 hours of annealing, there is a set of data for thickening of the bond coat and inter-diffusion layer, and the lateral growth of the bond coat after 200 hours at 1150°C which are shown in Table 3.1.

Table 3.1: The experimental data and their relative errors for the thickness of bond coat and inter-diffusion layers, and the lateral growth of the bond coat layer. (Data taken from personal communication by Chen *et al.*)

Heat Treatment Time (Hours) at 1150°C	Bond Coat Thickness (μm)	Error Bar
0	46.57	0.6
10	49.21	0.76
50	53.06	1.155
100	55.23	1.05
200	56.89	1.375

Heat Treatment Time (Hours) at 1150°C	Interdiffusion Zone Thickness (μm)	Error Bar
0	23.43	0.74
10	34.79	1.065
50	41.94	1.62
100	49.77	2.29
200	59.71	2.545

Heat Treatment Time (Hours) at 1150°C	Bond Coat Lateral Expansion (μm)	Error Bar
0	0	0
10	4.59	0.1
50	12.59	0.37
100	13.56	0.14
200	16.62	0.31

One might suggest that lateral growth of the bond coat layer is a result of TGO's lateral growth, however, given that the thickness of the TGO is very small compared to the bond coat, the stored strain energy, i.e. W , in the TGO is not enough to deform the bond coat significantly; an indicative mathematical calculation is shown here to confirm this. Assuming that as the TGO grows laterally, the bond coat grows with the same amount, i.e. $\varepsilon_{\text{TGO}} = \varepsilon_{\text{BC}} = \varepsilon_{11}$, and the TGO grows uniformly in both 11 and 33 directions, i.e. equi-biaxial, the energy required to deform the bond coat becomes

$$W_{\text{BC}} = \frac{1}{2} V_{\text{BC}} \cdot E_{\text{BC}} \cdot (\varepsilon_{11}^2 + \varepsilon_{33}^2) = V_{\text{BC}} \cdot E_{\text{BC}} \cdot \varepsilon_{11}^2, \quad (3.1)$$

where the V_{BC} is the volume of the bond coat layer, and the strain term can be written in terms of the strain energy in the TGO, i.e.

$$W_{\text{BC}} = V_{\text{BC}} \cdot E_{\text{BC}} \cdot \frac{W_{\text{TGO}}}{V_{\text{TGO}} \cdot E_{\text{TGO}}}, \quad (3.2)$$

leading to

$$W_{\text{BC}} = \frac{V_{\text{BC}}}{V_{\text{TGO}}} \cdot \frac{E_{\text{BC}}}{E_{\text{TGO}}} \cdot W_{\text{TGO}} \quad (3.3)$$

Taking the Young's modulus of the bond coat and TGO at 1150°C to be 90.4 and 375GPa, respectively, the Young's modulus ratio in the above equation becomes 0.2411; and taking into account that the volume ratio is the same as the height ratio, Equation 3.3 simplifies to

$$W_{\text{BC}} = 0.2411 \cdot \frac{h_{\text{BC}}}{h_{\text{TGO}}} \cdot W_{\text{TGO}} \quad (3.4)$$

Therefore, if $h_{BC} \gg h_{TGO}$ then the energy required to deform the bond coat with the same amount as the TGO, becomes unrealistically large. As a result, it is shown mathematically that as long as the thickness of the TGO is very small compared to the bond coat, it cannot affect its lateral deformation. Additionally, this theory was tested experimentally by Chen *et al.*, where they observed no lateral deformation of bulk NiAl while lateral growth of TGO was observed, therefore, the results obtained in Figure 3.2 is not a result of TGO growing.

3.2.2 Modelling

As observed in the experiment, there is a significant lateral growth in the bond coat which suddenly drops to almost zero at the inter-diffusion layer. Given that experimentally there is no information available regarding the properties of the inter-diffusion layer, it is postulated that the creep properties could be higher in the inter-diffusion layer compared to that of the bond coat, which leads to faster stress relaxation in the in-plane directions. This faster stress reduction can reduce the stored energy in the inter-diffusion layer and mitigate the propensity for the lateral expansion compared to the bond coat, leading to much less lateral growth for the inter-diffusion layer. In order to test this postulation and model the lateral deformation of the system's edge, the following steps are taken:

1. Find a mathematical fit for the relevant experimental data from Table 3.1.
2. Derive an analytical model of swelling strain rate and in-plane stress rate, starting from the constitutive equation and using the mathematical fit from the previous step.
3. Once developed, use the analytical model to manipulate the creep properties of the inter-diffusion layer to extreme cases, in order to test the proposed postulation. Once the plausibility of the postulation is verified with a combination of creep properties, use that combination in the following steps to model the lateral swelling of edge profile of the system with FE. (Please note this combination of creep properties will not be unique but it will give a good indication for verification of the postulation.)
4. Use the mathematical fit from the experimental data together with the chosen creep properties for the inter-diffusion layer, verify the developed swelling strain rate, and compute the in-plane stress of the inter-diffusion layer.
5. Input the verified analytical model of swelling strain rate and creep for the inter-diffusion layer into Abaqus, and verify their implementation.
6. Develop an Abaqus model of the system with three layers; bond coat, inter-diffusion and substrate system, and measure the lateral growth of each layer under the same conditions as the experiment.

- If the lateral growth that results from the three-layered system agrees with the experimental findings, then the postulation is validated and a conclusion is reached.
- If the results from the model do not match the experiment, carry out a sensitivity study on the creep and elastic properties of the inter-diffusion layer to find out more.
- If the findings from the sensitivity study matches the experimental results, then a combination of the material properties that produces the experimental outcome is found which provides an insight into the properties of the inter-diffusion layer.
- If the results from the sensitivity study do not produce the solution, then it suggests a complexity in the swelling, creep and elastic properties of the inter-diffusion layer or maybe both layers. Therefore, a five-layered model of the system is proposed; two-layers of bond coat, two-layers of inter-diffusion and one layer of substrate.

3.2.2.1 Fitting the experimental Data

Given that swelling of a layer is directly related to its thickening, the mathematical fit is found for the thickening data of the bond coat and inter-diffusion layers from Table 3.1. Figure 3.3 shows the experimental measures of thickening for the bond coat and inter-diffusion layers with their corresponding error bars, in comparison with their mathematical fit.

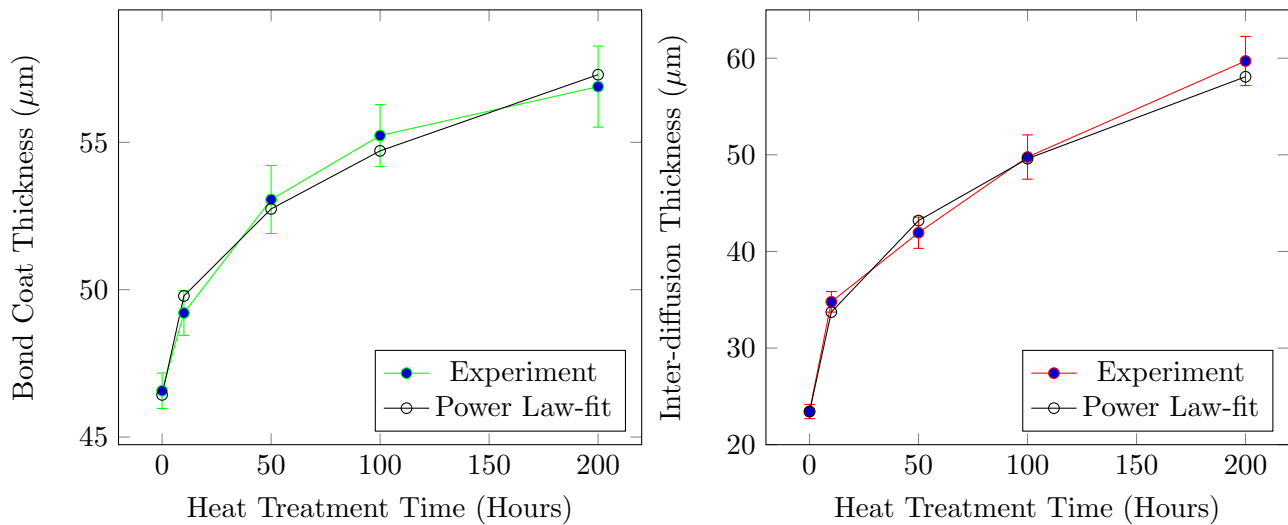


Figure 3.3: The experimental data for thickening of the bond coat (left plot) and the inter-diffusion layer (right plot) in comparison their corresponding power law fit. (The experimental data are taken from personal communication with Chen *et al.*, i.e. Table 3.1)

The mathematical fit for both of these layers is a power-law fit which has the form of

$$h = at^b + c, \quad (3.5)$$

where h is the thickness of the layer, t is the heat treatment time in hours, and a , b and c are the fitting parameters for the power-law fit. Values of a , b and c for the bond coat and inter-diffusion layers are given in Table 3.2

Table 3.2: Power-law fit parameters for the experimental results of the thickening in the bond coat and inter-diffusion layers.

	a	b	c
Bond Coat	1.365	0.3917	46.43
Inter-diffusion	4.053	0.405	23.43

Having obtained the mathematical fit for the thickness, computing both the engineering and true strain rates is straight forward; firstly, the thickness growth rate is computed by differentiating Equation 3.5 with respect to time, leading to

$$\dot{h} = abt^{b-1} \quad (3.6)$$

Then, the engineering and true strains in the direction normal to plane are computed by

$$\dot{\epsilon}_{22}^{\text{eng}} = \frac{\dot{h}}{h_0} = \frac{abt^{b-1}}{c}, \quad (3.7)$$

and

$$\dot{\epsilon}_{22}^{\text{true}} = \frac{\dot{h}}{h} = \frac{abt^{b-1}}{at^b + c}, \quad (3.8)$$

respectively, where h_0 is the initial thickness of the layer. Please note that the experimental result of thickness growth are given in micrometers, therefore, the order of magnitude of the resultant strain rate becomes micron as well, hence for simplicity in computations, unit of stress is taken to be MPa.

3.2.2.2 Analytical Models

Swelling Strain Rate

Starting from the constitutive law for strain rate, i.e. $\dot{\epsilon}_{ij}^{(l)}$, the analytical definition of swelling strain rate is derived.

$$\dot{\epsilon}_{ij}^{(l)} = \frac{1+\nu^{(l)}}{E^{(l)}} \dot{\sigma}_{ij}^{(l)} - \frac{\nu^{(l)}}{E^{(l)}} \dot{\sigma}_{kk}^{(l)} \delta_{ij} + \dot{\epsilon}_S^{(l)} \delta_{ij} + \dot{\epsilon}_P^{(l)} \delta_{ij} + \alpha^{(l)} \dot{T} \delta_{ij} + \frac{3}{2} \dot{\epsilon}_0^{(l)} \left(\frac{\sigma_e^{(l)}}{\sigma_R^{(l)}} \right)^{n^{(l)}-1} \left(\frac{s_{ij}^{(l)}}{\sigma_R^{(l)}} \right) e^{-T_R^{(l)}/T}, \quad (3.9)$$

where superscript l defines the layer for which the strain is being computed; in this work $l = 1$ corresponds to the substrate, $l = 2$ to inter-diffusion layer and $l = 3$ to the bond coat. In Equation 3.9, E and ν are the Young's modulus and Poisson ratio, respectively; $\dot{\epsilon}_P$ and $\dot{\epsilon}_S$ are the strain rates due to phase transformation and swelling of the layers, respectively; $\dot{\epsilon}_0$ is the creep reference strain rate in per second; n is the creep exponent; σ_R is the creep reference stress in MPa; T_R is the creep reference

temperature in Kelvin; α is the coefficient of thermal expansion; and σ_e is the equivalent stress which is equal to $\sqrt{\frac{3}{2}s_{ij}s_{ij}}$ where s_{ij} is the deviatoric stress computed as

$$s_{ij} = \sigma_{ij} - \frac{1}{3}(\sigma_{11} + \sigma_{22} + \sigma_{33}) \quad (3.10)$$

Given that the experimental condition is isothermal, there is no temperature change, except for the initial cooling from the deposition temperature and heating to the peak temperature. As a result, in the main part of the calculations there is no thermal strain, i.e. $\alpha\dot{T} = 0$, and phase transformation strain i.e. $\dot{\epsilon}_P = 0$; because phase transformation also mainly occurs in the heating and cooling processes. Implementing these two information into Equation 3.9, leads to

$$\dot{\epsilon}_{ij}^{(l)} = \frac{1 + \nu^{(l)}}{E^{(l)}}\dot{\sigma}_{ij}^{(l)} - \frac{\nu^{(l)}}{E^{(l)}}\dot{\sigma}_{kk}^{(l)}\delta_{ij} + \dot{\epsilon}_S^{(l)}\delta_{ij} + \frac{3}{2}\dot{\epsilon}_0^{(l)}\left(\frac{\sigma_e^{(l)}}{\sigma_R^{(l)}}\right)^{n^{(l)}-1}\left(\frac{s_{ij}^{(l)}}{\sigma_R^{(l)}}\right)e^{-T_R^{(l)}/T} \quad (3.11)$$

Under the conditions studied here, which imposes no constraint in the 22 direction, the stress in the normal direction to the surface of the layers, i.e. $\dot{\sigma}_{22}^{(l)}$, becomes zero. Implementing this information into Equation 3.11, an expression for the strain rate in the normal direction is obtained,

$$\dot{\epsilon}_{22}^{(l)} = -\frac{\nu^{(l)}}{E^{(l)}}(\dot{\sigma}_{11}^{(l)} + \dot{\sigma}_{33}^{(l)}) + \dot{\epsilon}_S^{(l)} + \frac{3}{2}\dot{\epsilon}_0^{(l)}\left(\frac{\sigma_e^{(l)}}{\sigma_R^{(l)}}\right)^{n^{(l)}-1}\left(\frac{s_{22}^{(l)}}{\sigma_R^{(l)}}\right)e^{-T_R^{(l)}/T} \quad (3.12)$$

Then, rearranging Equation 3.12 for the swelling strain rate gives

$$\dot{\epsilon}_S^{(l)} = \frac{\nu^{(l)}}{E^{(l)}}(\dot{\sigma}_{11}^{(l)} + \dot{\sigma}_{33}^{(l)}) + \dot{\epsilon}_{22}^{(l)} - \frac{3}{2}\dot{\epsilon}_0^{(l)}\left(\frac{\sigma_e^{(l)}}{\sigma_R^{(l)}}\right)^{n^{(l)}-1}\left(\frac{s_{22}^{(l)}}{\sigma_R^{(l)}}\right)e^{-T_R^{(l)}/T}, \quad (3.13)$$

where Equation 3.13 shows the general expression for the swelling strain rate of any given coating layer in this system, i.e. $l = 2$ and 3 , provided that the experimental data are available for it. The $\dot{\epsilon}_{22}$ in Equation 3.13 is the experimental strain rate of the coating layer in the normal direction, computed by Equation 3.8 using the relevant constants from Table 3.2.

The expression here for the swelling strain rate is the same as the one from chapter 2; the only difference is that here no thermal strain rate is present because of the isothermal nature of the experiment. Having developed an expression for the swelling strain rate, the swelling strain can be computed with the Euler method as $\epsilon_S^{m+1} = \epsilon_S^m + \dot{\epsilon}_S^m \Delta t$, where Δt is fixed, and m represents the current time increment.

In-Plane Stress Rates

As is clear from Equation 3.13, the swelling strain rate depends on the in-plane stresses and stress rates in the layer, therefore, an expression for these stress rates is required. Given that Equation 3.9 is spatially independent, it is not possible to model the lateral strain of the TBC system on the edge,

using this equation; in other words, the strain rates computed in each direction with Equation 3.9 are the same along the thickness and through the width of each layer. Therefore, the bond coat and the inter-diffusion layers are assumed to be constrained by the substrate; because their thickness is much less than that of the substrate. The expressions obtained from this derivation is used for defining swelling strain rate in the Abaqus model where the lateral growth of the system on the edge can be computed.

In the absence of external load the only source of strain for the substrate is from thermal expansion, however, given that the system is under isothermal condition, then $\dot{\varepsilon}_{11}^{(1)} = \dot{\varepsilon}_{33}^{(1)} = 0$. Additionally, because the bond coat and inter-diffusion layers are taken to be constrained laterally by the substrate, then $\dot{\varepsilon}_{11}^{(2)} = \dot{\varepsilon}_{11}^{(3)} = \dot{\varepsilon}_{11}^{(1)} = \dot{\varepsilon}_{33}^{(2)} = \dot{\varepsilon}_{33}^{(3)} = \dot{\varepsilon}_{33}^{(1)} = 0$; incorporating these conditions into Equation 3.11 for the 11 direction leads to

$$\dot{\varepsilon}_{11}^{(l)} = 0 = \frac{1 + \nu^{(l)}}{E^{(l)}} \dot{\sigma}_{11}^{(l)} - \frac{\nu^{(l)}}{E^{(l)}} (\dot{\sigma}_{11}^{(l)} + \dot{\sigma}_{33}^{(l)}) + \dot{\varepsilon}_S^{(l)} + \frac{3}{2} \dot{\varepsilon}_0^{(l)} \left(\frac{\sigma_e^{(l)}}{\sigma_R^{(l)}} \right)^{n^{(l)}-1} \left(\frac{s_{11}^{(l)}}{\sigma_R^{(l)}} \right) e^{-T_R^{(l)}/T} \quad (3.14)$$

Rearranging for $\dot{\sigma}_{11}^{(l)}$ and $\dot{\sigma}_{33}^{(l)}$ gives

$$\dot{\sigma}_{11}^{(l)} = \nu^{(l)} \dot{\sigma}_{33}^{(l)} - E^{(l)} \left[\dot{\varepsilon}_S^{(l)} + \frac{3}{2} \dot{\varepsilon}_0^{(l)} \left(\frac{\sigma_e^{(l)}}{\sigma_R^{(l)}} \right)^{n^{(l)}-1} \left(\frac{s_{11}^{(l)}}{\sigma_R^{(l)}} \right) e^{-T_R^{(l)}/T} \right], \quad (3.15)$$

and

$$\dot{\sigma}_{33}^{(l)} = \nu^{(l)} \dot{\sigma}_{11}^{(l)} - E^{(l)} \left[\dot{\varepsilon}_S^{(l)} + \frac{3}{2} \dot{\varepsilon}_0^{(l)} \left(\frac{\sigma_e^{(l)}}{\sigma_R^{(l)}} \right)^{n^{(l)}-1} \left(\frac{s_{33}^{(l)}}{\sigma_R^{(l)}} \right) e^{-T_R^{(l)}/T} \right] \quad (3.16)$$

Given that in the analytical model the layers are assumed to be constrained by the substrate in the in-plane directions, the strain rates in these two directions become the same, i.e. $\dot{\varepsilon}_{11}^{(l)} = \dot{\varepsilon}_{33}^{(l)} = 0$ which forms an an equi-biaxial case; as a result, $s_{11} = s_{33}$ and $\dot{\sigma}_{11}^{(l)} = \dot{\sigma}_{33}^{(l)}$, and the equation defining the stress rate in the layers simplifies to

$$\dot{\sigma}_{11}^{(l)} = -\frac{E^{(l)}}{1 - \nu^{(l)}} \left[\dot{\varepsilon}_S^{(l)} + \frac{3}{2} \dot{\varepsilon}_0^{(l)} \left(\frac{\sigma_e^{(l)}}{\sigma_R^{(l)}} \right)^{n^{(l)}-1} \left(\frac{s_{11}^{(l)}}{\sigma_R^{(l)}} \right) e^{-T_R^{(l)}/T} \right], \quad (3.17)$$

Because of the creep term in Equation 3.17, the stress rate becomes non-linear and dependent on the stress values. Therefore, to compute the stress values, the Euler method is used, i.e. $\sigma_{11}^{i+1} = \sigma_{11}^i + \dot{\sigma}_{11}^i \Delta t$, where Δt is the fixed time step and i represents the current time increment. The accuracy and convergence of the Euler method depends on the choice of initial stress and value of time increment. The time increment is chosen as the largest Δt that gives a converged solution; and for a good initial stress, the stress equation is solved for an initial cooling and heating pre-step where the thermal expansion term is also included in Equation 3.17. The pre-step represents the cooling

down process from the deposition temperature, and the heating up process to the isothermal temperature where the total time taken for these processes is chosen to be 720s, similar to the case in chapter 2.

Using the end results of the pre-step processes as initial conditions for the main computation, i.e. Equation 3.13 and Equation 3.17, the stress and swelling strain profiles of either coating layers under study can be plotted after 200 hrs annealing at 1150°C. Figure 3.4 shows the stress and swelling strain of the bond coat as an example, where the creep properties are $n^{(3)} = 4$, $\sigma_R^{(3)} = 25\text{MP}$, $T_R^{(3)} = 15000\text{K}$, and $\dot{\epsilon}_0^{(3)} = 0.2$, carried forward from the previous chapter.

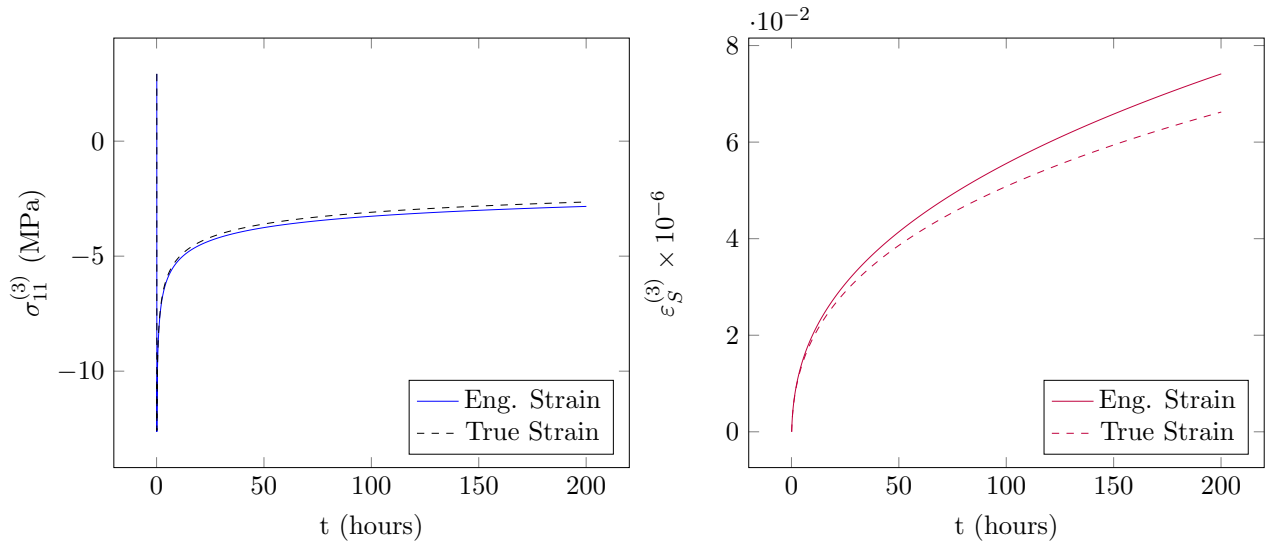


Figure 3.4: In-plane stress (on the left) and swelling strain (on the right) of the bond coat layer computed analytically for 200 hrs at 1150°C, in addition to the comparison between the use of engineering and true strains for the calculations.

Figure 3.4 also represents the difference between using true and engineering strains when computing the swelling strain rate, i.e. Equation 3.8 and Equation 3.7; which shows a negligible effect on the in-plane stress, therefore, when looking at the in-plane stresses, either the engineering or true strains can be used. However, the effect of true or engineering strain is more apparent on the swelling strain. Given that both the in-plane stress and swelling strain outcomes are important for the computations, it is better to use the true thickening strain for the rest of the calculations.

3.2.2.3 Creep Property Sensitivity Study

The creep property of inter-diffusion layer is the basis of our postulation which states faster stress relaxation in the inter-diffusion layer can reduce the stored energy in the layer and prevent lateral expansion compared to that of the bond coat. In order to test this postulation, first an educated guess is made for the creep properties of the inter-diffusion layer; this educated guess is done based on a sensitivity study on the two main creep properties, i.e. n and $\dot{\epsilon}_0$. Given that material properties of the inter-diffusion layer are not known, in this creep sensitivity study all the other material properties

of the inter-diffusion layer are taken to be the same as bond coat. Figure 3.5 shows the effect of this sensitivity study on the in-plane stress profile as computed by Equation 3.17, where in the left plot creep exponent is fixed as the creep reference strain rate is changed, and in the right plot the reference strain rate is fixed while the exponent is changed.

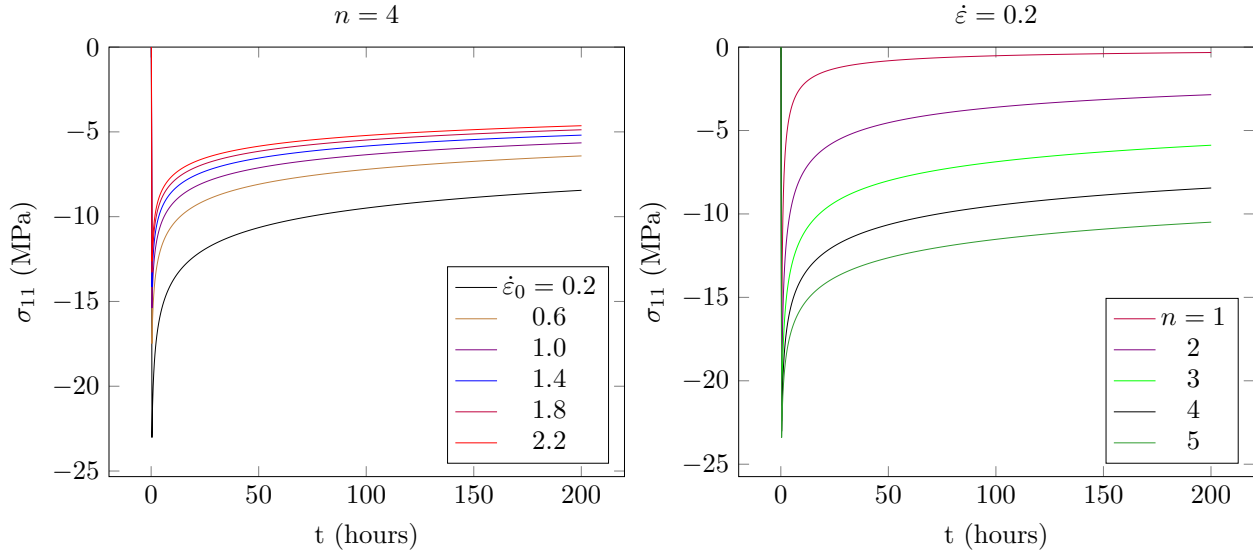


Figure 3.5: **Left:** the effect of creep reference strain rate, $\dot{\epsilon}_0$, on the in-plane stress, σ_{11} . **Right:** the effect of the creep exponent, n , on σ_{11} . In each plot the black line represents the stress behaviour of the bond coat material.

Results of the sensitivity study show an increase in the stress relaxation by increase in the strain rate and decrease in creep exponent, where the effect of $\dot{\epsilon}_0$ and n on the stress relaxation is not linear; for example, while $\dot{\epsilon}_0$ is increased from 0.2 to 2.2 with a fixed interval, the increase in the stress relaxation is much higher for the first few cases than the last ones, as is apparent from the left plot in Figure 3.5. This outcome suggests that it is plausible to get higher stress relaxation and lower stored energy in the in-plane direction of the layers with material properties that have higher creep deformation. Next step would be to test this postulation in a finite element model where it is possible to visualise the resultant lateral growth of the system edge.

Considering the effect that $\dot{\epsilon}_0$ and n have on the stress relaxation, an example combination of $\dot{\epsilon}_0 = 2.2$ and $n = 3$, which produces an extreme stress relaxation case, is chosen to be used for the finite element model of the inter-diffusion layer, so the proposed postulation can be tested. Figure 3.6 shows the comparison in the computed stress relaxation of the case with $\dot{\epsilon}_0 = 0.2$ and $n = 4$ for the bond coat, and $\dot{\epsilon}_0 = 2.2$ and $n = 3$ for the inter-diffusion layer.

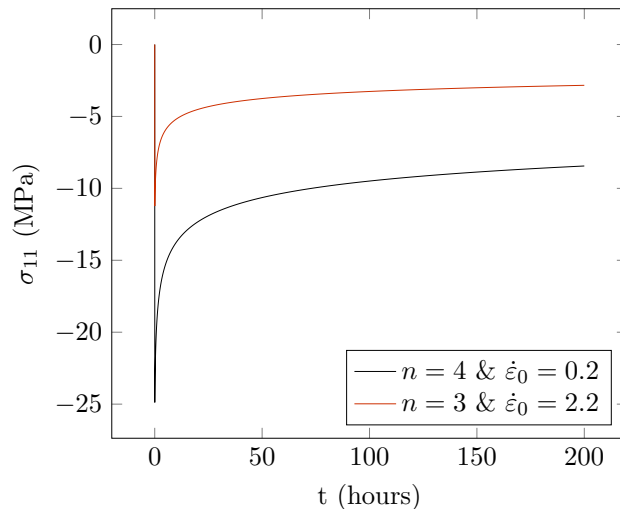


Figure 3.6: The stress relaxation plot of the bond coat with creep properties of $n = 4$ and $\dot{\epsilon}_0 = 0.2$, compared to stress relaxation of the inter-diffusion layer with the chosen creep properties of $n = 3$ and $\dot{\epsilon}_0 = 2.2$.

3.2.2.4 Verification of Finite Element Model

Given the limitations that the analytical model has in capturing the lateral expansion of the layers, it is important to use a finite element model of the system for testing the proposed postulation. The finite element models in this study are created with Abaqus/CAE 6.14. In order to create an accurate model in Abaqus, it is important to ensure that the material properties of each layer, particularly creep and swelling are implemented correctly. Therefore, before creating the final model of the TBC system, the implementation of creep and swelling properties in Abaqus are tested separately and together through simple examples; this verification process is shown in three parts; Abaqus creep verification, Abaqus swelling verification, and Abaqus inter-diffusion layer verification.

In the first two parts, implementation of creep and swelling in Abaqus are verified separately, and in the final part a combination of swelling and creep properties is defined for a system of inter-diffusion and substrate layers. For each of these cases, solution from the Abaqus model is compared to the analytical solution. For the last case with the inter-diffusion and substrate, the sides of the model in Abaqus are fixed in order to have the same condition as the analytical model with no lateral expansion. The numerical values used for comparison between the finite element model of the inter-diffusion and substrate system, and the analytical one, are the thickening and in-plane stress of the inter-diffusion layer.

Abaqus Creep Verification

To verify the implementation of creep properties into Abaqus/CAE 6.14, the stress relaxation behaviour of a cube of length $1\mu\text{m}$ under a uniform initial stress is considered. The yz face of the cube at $x=0$ is fixed in the x direction, while the yz face at $x=1\mu\text{m}$ is strained by 0.001 in the x direction

to reach an initial stress of 90.4MPa, and all the other faces are free to deform. Given the symmetry of the problem in the y and z directions, the cube is reduced to a smaller cuboid with symmetry boundary conditions, as shown in Figure 3.7. The simulation for this study was of implicit type with the use of coupled temperature-displacement approach and elements of type C3D8T.

Once the required initial stress is reached, the yz face at $x=1\mu\text{m}$ is fixed in the x -direction to allow stress relaxation in the x -direction at $T = 1150^\circ\text{C}$ to occur. The creep properties of the cube are defined as $\sigma_R = 25\text{MP}$, $T_R = 15000\text{K}$, $n = 3$, and $\dot{\epsilon}_0 = 2.2$. Given that the cube is free in the y and z

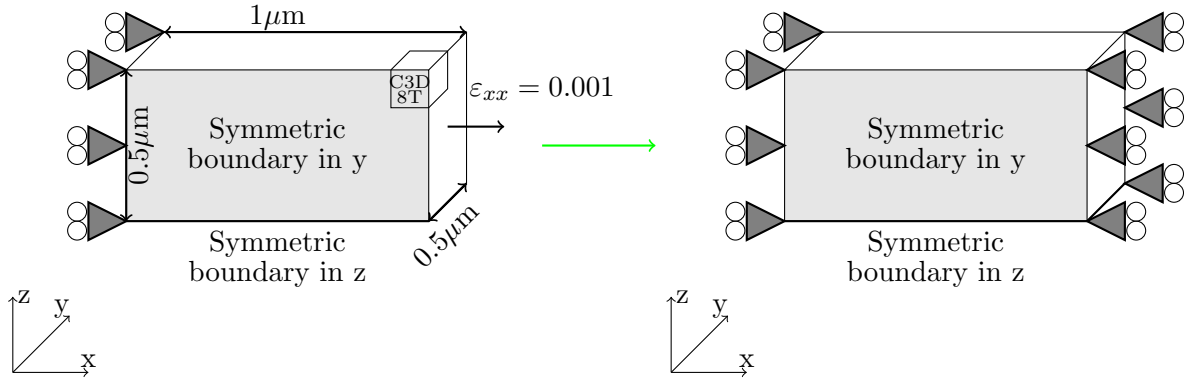


Figure 3.7: The boundary conditions of the finite element model used for the creep verification

directions, the stresses in these directions are zero. Strain rate in the x directions is also zero because both yz faces at $y=0$ and $y=1\mu\text{m}$ are fixed after the initial elastic strain. Using these conditions in the constitutive equation, i.e. Equation 3.9, the analytical definition of the stress relaxation for this cube becomes

$$\dot{\sigma}_{11} = E \left[-\frac{3}{2} \dot{\epsilon}_0 \left(\frac{\sigma_e}{\sigma_R} \right)^{n-1} \frac{s_{11}}{\sigma_R} e^{-T_R/T} \right] \quad (3.18)$$

Abaqus has four options when defining the creep properties of a material; I) power-law Time Hardening, II) power-law Strain Hardening, III) Hyperbolic-sine law and IV) user defined subroutine. The material of the bond coat and inter-diffusion layers follow power-law creep, therefore, the first two options can be used to model them correctly. In power-law creep options, Abaqus computes the uniaxial equivalent creep strain rate, $\dot{\tilde{\epsilon}}^{cr}$, which is defined as $\sqrt{\frac{2}{3} \dot{\epsilon}^{cr} : \dot{\epsilon}^{cr}}$. For the ‘‘Time-Hardening’’ option, $\dot{\tilde{\epsilon}}^{cr}$ is computed as

$$\dot{\tilde{\epsilon}}^{cr} = A \tilde{q}^n t^m, \quad (3.19)$$

where \tilde{q} is the uniaxial equivalent deviatoric stress, t is the total time, n is the creep exponent, A is the constant defined by the user, and m is the time exponent. For the ‘‘Strain-Hardening’’ option, while the variables maintain their meaning, the equivalent creep strain rate is computed as

$$\dot{\varepsilon}^{cr} = (A\tilde{q}^n [(m+1)\bar{\varepsilon}^{cr}]^m)^{\frac{1}{m+1}}, \quad (3.20)$$

where $\bar{\varepsilon}^{cr}$ is the equivalent creep strain. In the examples considered here, creep property of the materials does not have a direct time dependency, therefore, $m = 0$. This means the “Time Hardening” and the “Strain-Hardening” options of Abaqus give exactly the same results, therefore, for the verifications, the “Strain-Hardening” approach is used which is the default option. In addition to m , “Strain-Hardening” asks the user for the values of A and n . Value of A here is the same as $\frac{3}{2}\dot{\varepsilon}_0 \left(\frac{\sigma_e}{\sigma_R}\right)^n e^{-T_R/T}$.

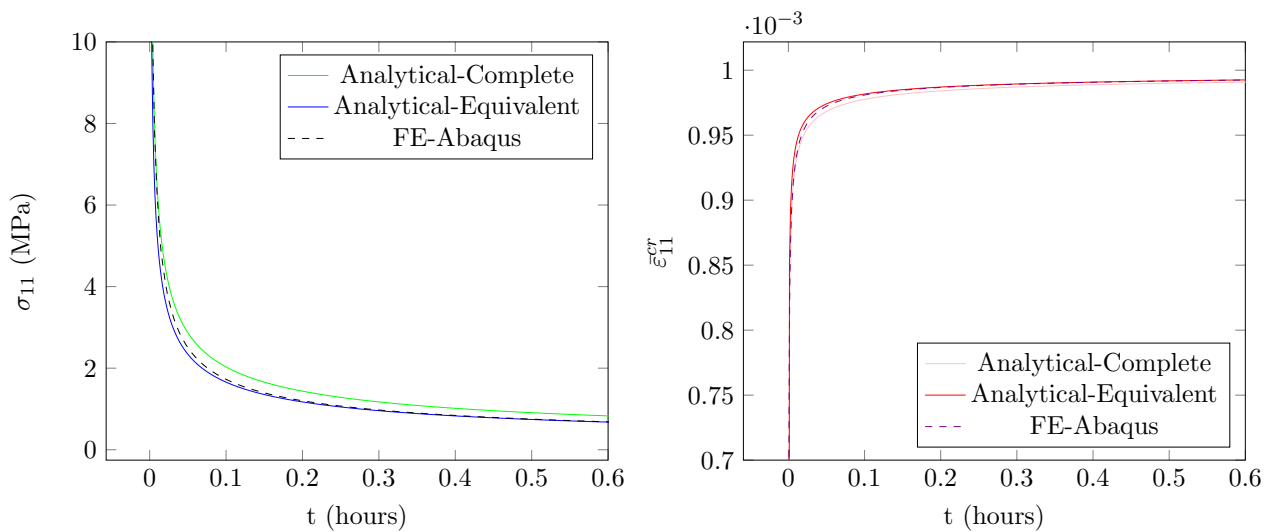


Figure 3.8: **Left:** comparison of σ_{11} results and **right:** comparison of $\bar{\varepsilon}_{11}^{cr}$ results. The “Analytic-Complete” in the legend refers to the analytical model based on the multi-axial principal equation and the “Analytic-Equivalent” refers to the model using the equivalent creep strain.

To verify the implementation of creep into Abaqus the stress relaxation and creep strain results of the cube in the x-direction are compared to the results from the analytical model, as shown in Figure 3.8. The analytical model uses an exact value of the creep strain in stress calculations whereas Abaqus uses an equivalent creep strain, therefore, in addition to using the exact creep strain, an analytical solution is produced where the stress relaxation and creep strain are based on equivalent creep strain. In other words, instead of using $\left(\frac{\sigma_e}{\sigma_R}\right)^{n-1} \frac{s_{11}}{\sigma_R}$, $\left(\frac{\sigma_e}{\sigma_R}\right)^n$ is used in Equation 3.18. The results from this additional case is labeled as “Analytical-Equivalent” in Figure 3.8.

Looking at the results in Figure 3.8 it is clear that all the cases are in very close agreement, however, the “Analytical-Equivalent” plot shows a much better agreement with the results from Abaqus in both stress and creep strain results which was expected. Regardless of the small difference between the exact analytical results, i.e. “Analytic-Complete”, and Abaqus results, it can be accepted that the implementation of creep properties into Abaqus is verified and can be used in this format for the final model; because this Abaqus model is going to be used for a conceptual and qualitative study of the inter-diffusion layer so a small difference with the exact solution, such as the one obtained here,

does not affect the final outcome.

Abaqus Swelling Verification

Given that swelling in the context of this study is a relatively new phenomenon, Abaqus does not have that option in its material definition, however, since swelling is a uniform and isotropic volume expansion, it can be modelled using the thermal expansion option in Abaqus. Keeping in mind that the condition for the TBC system in this study is isothermal, the default definition of thermal expansion cannot be used. As a result, a customised definition of thermal expansion strain is required which is achieved through the use of Abaqus UEXPAN subroutine.

In order to verify the use of UEXPAN for implementation of swelling into Abaqus, example of a freely expanding cube with a single element of type C3D20RT is used in a coupled temperature-displacement process. Three faces of the cube which are along the x,y and z axes, are placed on the roller while the other three faces are free to expand under the thermal expansion property defined by the UEXPAN subroutine. The main output variable from UEXPAN is EXPAN(1) which is the increment of thermal expansion strain inside the subroutine. For this study EXPAN(1) represents the swelling strain increment or $\dot{\epsilon}_S \Delta t$, where the definition of $\dot{\epsilon}_S$ is derived from Equation 3.9, given the boundary conditions for a freely expanding cube. Please note, the definition of $\dot{\epsilon}_S$ for problems with different boundary conditions will be different; for example when modelling the full TBC system $\dot{\epsilon}_S$ is defined by Equation 3.13, whereas for the freely expanding cube, it has to be derived from Equation 3.9 implementing the new boundary conditions.

In a freely expanding cube stresses are zero in all the directions while at the same time the strains are equal. Incorporating these conditions into Equation 3.11, leads to an expression for the swelling strain rate of the freely expanding cube. There are two versions of the swelling strain rate that can be obtained; i) a simplified model based on the assumption that creep does not significantly influence the swelling strain rate, and ii) a complete model including the effects of creep on swelling strain rate. Because the stresses are zero in the freely expanding cube, the outcome for the complete swelling model is the same as the simplified one, however, for the example of the TBC system, the swelling strain rate will not be the same between the simplified and the complete models. This is why it is important to verify the implementation of both models of swelling in Abaqus.

Simplified Model of Swelling

In the simplified model of swelling, the creep term is only dropped from the strain rate equation

that is used to derive the swelling strain rate. This means that Equation 3.11 simplifies to

$$\dot{\epsilon}_{ij} = \frac{1 + \nu}{E} \dot{\sigma}_{ij} - \frac{\nu}{E} \dot{\sigma}_{kk} \delta_{ij} + \dot{\epsilon}_S \quad (3.21)$$

In the swelling verification, the computed displacement of the cube in each direction as a result of swelling is compared to the experimental data on thickening of the inter-diffusion. In order to achieve the correct displacement for each direction of the expanding cube, the strain rate in one direction of the cube, e.g. 22, is equated to the experimental strain rate, i.e. Equation 3.8. Please note, because of the symmetry in the cube the choice of direction for the strain rate is not important, whereas, in cases such as the TBC system it is important to use the correct direction.

$$\dot{\epsilon}_{22} = \frac{abt^{b-1}}{at^b + c} = \frac{1 + \nu}{E} \dot{\sigma}_{22} - \frac{\nu}{E} \dot{\sigma}_{kk} + \dot{\epsilon}_S \quad (3.22)$$

Taking into account that stresses are zero for a freely expanding cube, this simplifies Equation 3.22 to $\dot{\epsilon}_S = \dot{\epsilon}_{22}$ which is the analytical equation for the simplified swelling strain rate of this example. This definition of swelling is implemented in the UEXPAN subroutine of Abaqus and used to compute the thickening of the cube as a result of swelling, result of which is shown in Figure 3.9. The UEXPAN subroutine used for the case of simplified swelling strain is shown in [Appendix 3.A](#).

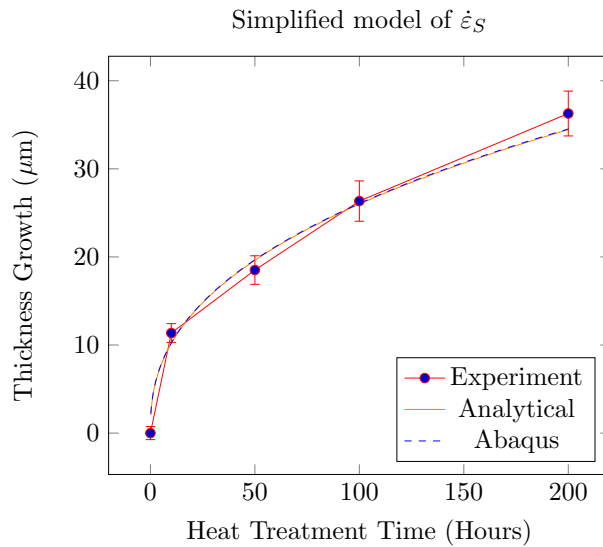


Figure 3.9: Comparison between the Abaqus results and the experimental results for thickening caused by swelling. The analytical results of the displacement are also shown.

Figure 3.9 shows the results of the simplified model of swelling from Abaqus and analytical model in comparison to the experimental thickening data. As is clear from this figure, the displacement computed by the analytical model and the Abaqus model match perfectly, and both have a very good agreement with the experimental data. This outcome verifies the implementation of simplified swelling strain rate into the Abaqus model.

Complete Model of Swelling

Verifying the implementation of the simplified model of the swelling strain rate in Abaqus was the first step towards understanding the use of UEXPAN. The difference between the “Complete Model of Swelling” and the “Simplified Model of Swelling” is the presence of creep term in computing the swelling strain rate. For the simplified model of swelling, Equation 3.21 was used, whereas, for the complete model of swelling Equation 3.11 is used. Using the same boundary conditions as before, i.e. for the freely expanding cube, Equation 3.11 for the 22 direction simplifies to $\dot{\epsilon}_{22} = \dot{\epsilon}_S$ which is the same as the simplified swelling model for this example, as expected.

Implementation of the complete swelling strain rate requires the use of an additional subroutine to UEXPAN. This additional subroutine is the user-defined field and is called USDFLD. Purpose of this subroutine is to allow the UEXPAN subroutine access the stress values from within the simulation and use them for calculations. An example of the subroutines used for the complete model of swelling is shown in [Appendix 3.A](#). The displacement results obtained for the complete model of swelling from Abaqus and analytical model are the same as the ones shown in Figure 3.9 which verifies the implementation of complete model of swelling in Abaqus through the use of UEXPAN and USDFLD subroutines.

Abaqus Inter-diffusion Layer Verification

Having verified the implementation of swelling and creep separately into Abaqus, it is time for verifying them when they are both implemented in the Abaqus model of inter-diffusion layer and substrate. In this verification, the computed stress and thickening terms from the Abaqus model are compared to the analytical ones, so in order for the outcome from the Abaqus model to be directly comparable to the analytical one, the lateral expansion of the inter-diffusion layer is constrained. Once this model of inter-diffusion layer in Abaqus is verified, the lateral constraint will be removed and the bond coat will be added so the proposed postulation can be tested with the complete system.

The dimensions and boundary conditions of the Abaqus model for the laterally constrained inter-diffusion layer on substrate are given in Figure 3.10 where the initial thickness of the inter-diffusion layer is taken from Table 3.1 which is $23.43\mu\text{m}$, thickness of the substrate is given to be 1.5mm , and the width of the system is chosen to be $300\mu\text{m}$. Width is chosen to be wide enough so the stress and strains at the central section of the system become uniform and directly comparable to the results from the analytical model. As is shown in the figure, the right edge of the inter-diffusion layer is tied to the right edge of the substrate (i.e. constrained), so the finite element model is consistent with the analytical model; and the left side has the symmetry boundary condition in x. The element type used

for this model in Abaqus was CPE4T with a coupled temperature-displacement step.

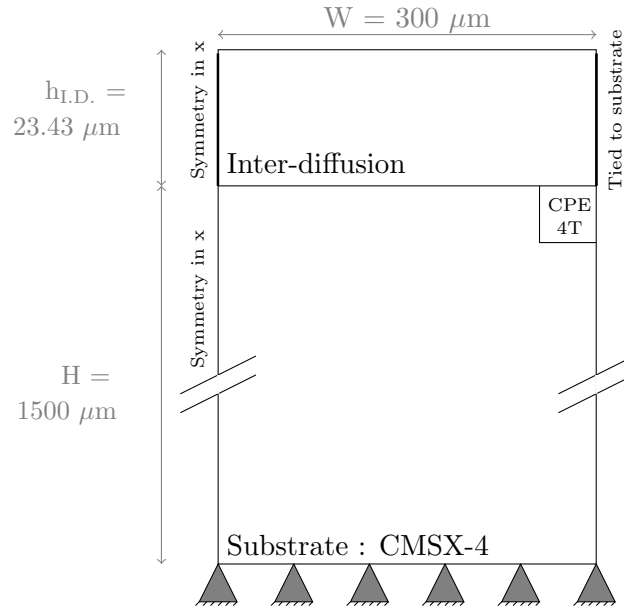


Figure 3.10: The dimensions and boundary conditions of the inter-diffusion and substrate system used for the verification of the Abaqus model.

The substrate material used in this study is the Ni-based single-crystal CMSX-4 for which the properties are shown in Table 3.3. For the inter-diffusion layer, on the other hand, there are no material properties available in the literature, therefore, in the Abaqus model, except for creep and swelling properties, the same material properties as the bond coat material are used, i.e. Table 3.4. The creep properties of the inter-diffusion layer are taken to be $\dot{\epsilon}_0^{(2)} = 2.2$, $\sigma_R^{(2)} = 25\text{MPa}$, $n^{(2)} = 3$, and $T_R^{(2)} = 15000\text{K}$.

Table 3.3: Material properties of Ni-based single-crystal CMSX-4 taken from [18], used for the finite element model.

Temperature (°C)	Thermal Conductivity ($\text{Wm}^{-1}\text{K}^{-1}$)	Density (kgm^{-3})	Specific Heat Capacity ($\text{J kg}^{-1}\text{K}^{-1}$)	Young's Modulus ($\times 10^3 \text{MPa}$)	Poisson's ratio (-)	Mean Coeff. of Thermal Expansion ($\times 10^{-6}$)
20	8.65	8700	397	127.3	0.389	11.1
100	8.65	8665	415	125.0	0.391	11.8
200	10.1	8618	431	122.0	0.394	12.8
300	11.6	8572	445	118.0	0.395	13.7
400	13.4	8525	456	115.0	0.395	14.7
500	14.9	8479	466	111.0	0.395	15.6
600	16.8	8433	488	106.0	0.396	16.5
700	19.4	8387	532	101.0	0.398	17.4
800	20.6	8342	530	96.0	0.403	18.3
900	21.8	8296	540	90.2	0.41	19.2
1000	22.3	8251	550	82.7	0.42	20.1
1100	23.9	8206	560	75.1	0.43	21.0
1200	25.8	8161	570	67.6	0.44	21.8

Table 3.4: Material properties of the bond coat used for the finite element model.

Temperature (°C)	Thermal Conductivity ^[4] (Wm ⁻¹ K ⁻¹)	Density ^[19] (kgm ⁻³)	Specific Heat Capacity ^[19] (J kg ⁻¹ K ⁻¹)	Young's Modulus ^[20] (×10 ³ MPa)	Poisson's ratio ^[21] (-)	Mean Coeff. of Thermal Expansion ^[22] (×10 ⁻⁶)
25	28.85	7950	668	117.4	0.27	12.80
400				108.4		13.89
500				106		14.18
550				104.8		14.32
600				103.6		14.46
650				102.4		14.61
700				101.2		14.75
750				100		14.90
800				98.8		15.04
850				97.6		15.19
900				96.4		15.33
950				95.2		15.48
1000				94		15.62
1050				92.8		15.76
1100				91.6		15.91
1150				90.4		16.06

The elastic and thermal expansion properties of the layers are defined based on the two tables above; for the swelling property, on the other hand, the two versions of swelling model which were introduced in the “Abaqus Swelling Verification” subsection are used, i.e. simplified and complete swelling models. As explained previously, change of boundary conditions changes the definition of the swelling strain rate for both simplified and complete models. For the inter-diffusion and substrate system the swelling strain rate has already been derived in subsection 3.2.2.2, i.e. Equation 3.13. Therefore, using the simple and complete versions of Equation 3.13, the in-plane stress and thickening of the inter-diffusion layer are computed in the Abaqus model and compared to the analytical solution. The first step of simulation process consists of a cooling process from the deposition temperature of the coating to the room temperature and a heating process to the peak temperature, i.e. 1150°C over 720s. The second step of the simulation is the isothermal heat treatment when the whole system is kept at 1150°C for 200 hours.

Simplified Model of Swelling

Starting from Equation 3.13, for the simplified model of the swelling strain rate, the creep term of the equation is removed, which leads to

$$\dot{\epsilon}_S = \frac{\nu}{E} \dot{\sigma}_{kk} + \dot{\epsilon}_{22}, \quad (3.23)$$

where $\dot{\sigma}_{kk} = \dot{\sigma}_{11} + \dot{\sigma}_{33}$; $\dot{\sigma}_{11}$ and $\dot{\sigma}_{33}$ are found from simplified version of Equation 3.17, leading to the simplified model of the swelling strain rate,

$$\dot{\epsilon}_S = \left(\frac{1 - \nu}{1 + \nu} \right) \dot{\epsilon}_{22} = \left(\frac{1 - \nu}{1 + \nu} \right) \frac{abt^{b-1}}{at^b + c}, \quad (3.24)$$

where $\dot{\epsilon}_{22}$ is taken from Equation 3.8. Then Equation 3.24 is used together with complete version of Equation 3.17 to compute the simplified analytical model of thickening and in-plane stress of the layer. Equation 3.24 is then implemented into the Abaqus model through an UEXPAN subroutine, and its results are compared against the analytical solutions, as shown in Figure 3.11. Additionally, the thickening results from both the analytical and Abaqus models are compared to the experimental data for thickening of the inter-diffusion layer, i.e. Figure 3.11.

Complete Model of Swelling

The equation defining the complete swelling strain rate model of the layers is the same as Equation 3.13, where the creep term brings a stress dependency into the calculations. The analytical process for obtaining the swelling strain rate for a given system is explained in more detail in subsection 3.2.2.2 where the Euler method is used to compute the swelling strain and in-plane stress.

Given the stress dependency of the swelling strain rate, in order to implement it into the Abaqus model, the use of USDFLD and UEXPAN subroutines is required. The procedure by which Abaqus uses these subroutines is as follows: stress terms are called into the USDFLD subroutine where they are stored in state variables, then these state variables are used in the UEXPAN subroutine for computing the swelling strain increment. For a given integration and material point, the coupled temperature-displacement step, which is the one used for these Abaqus simulations, calls the UEXPAN subroutine twice per time increment. During the first call, values of the variables in the subroutine get updated in the subroutine, starting from the values at the start of the time increment. During the second call of the subroutine, however, while the time increment is still the same, the variables get updated again but this time starting from the values at the end of the first call; in other words the variables get updated twice per time increment. Therefore, in order to avoid double update of the swelling strain increment, a factor of 0.5 is multiplied by the strain rate.

Results of the complete model of swelling from both the analytical and Abaqus models are plotted in Figure 3.11 where also for complete comparison, the results for the simplified model of swelling and the experimental data are plotted. There are three main conclusions that can be drawn from Figure 3.11; i) the thickening results from the analytical and Abaqus models of the inter-diffusion layer, using the complete model of swelling, match the experimental results for thickening of this layer (can be seen in the top left plot of Figure 3.11); ii) using the simplified model of swelling is not a valid assumption, given that the thickening obtained by this model is much higher than that of the experimental one; and iii) while the computed swelling strain and thickening show a much better match between the analytical and Abaqus models than that of the stress, it can be considered an acceptable match

between the two models because this difference in the stresses can be from the numerical errors in the Abaqus model and the fact that Abaqus uses the equivalent creep strain rate for creep calculations.

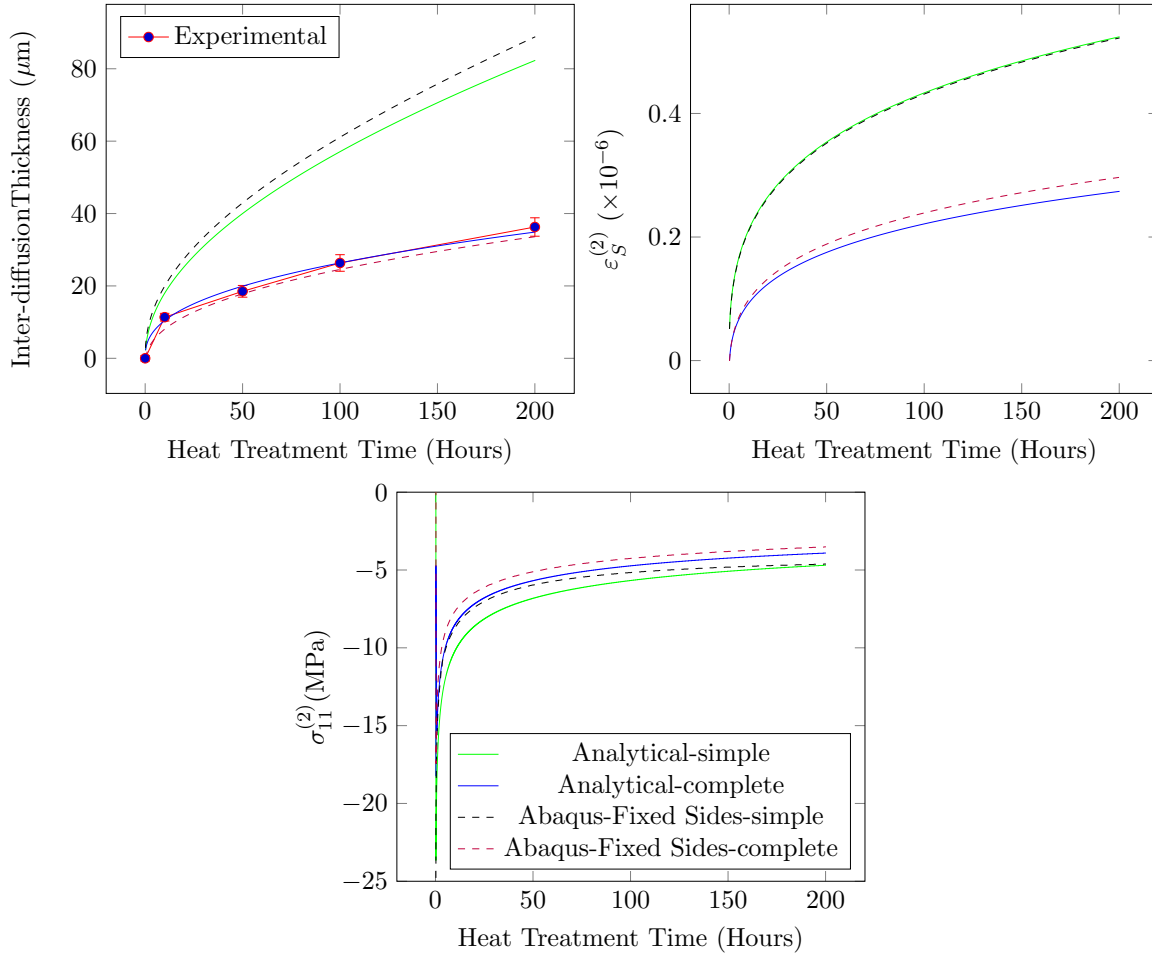


Figure 3.11: The top left plot shows the experimental thickening data for the inter-diffusion layer during 200hrs annealing, in comparison to the thickening results computed by the analytical and Abaqus models of the swelling in this layer. The top right and bottom plots show the swelling strain rate and in-plane stress of the inter-diffusion layer computed by the analytical and Abaqus models of the swelling in this layer. Please note, the legend in the bottom plot is applicable to the other two plots as well.

Despite the small difference between the analytical and Abaqus models in computing the stresses, swelling strain and thickening match quite well, therefore, the implementation of swelling and creep into the Abaqus model of the inter-diffusion layer is considered as verified. This verification shows that for the rest of the Abaqus models used in this work the complete model of swelling, i.e. Equation 3.13 must be used.

3.2.2.5 Two-Layered Coating Model

Having verified the Abaqus model of inter-diffusion layer with its lateral growth prevented, the next step is removing the lateral constraint of the inter-diffusion layer and adding the bond coat layer to the system. This model is called “Two-Layered Coating Model” because it consists of the bond coat

and the inter-diffusion layer as the two layers of coating on the substrate. In this model the material property of the bond coat and the substrate are kept fixed as the ones given in Table 3.4 and Table 3.3. For simplicity it is assumed that the substrate does not creep, whereas, the bond coat does, and its creep properties are taken to be $n^{(3)} = 4$, $\dot{\epsilon}_0^{(3)} = 0.2$, $T_R^{(3)} = 15000\text{K}$ and $\sigma_R^{(3)} = 25\text{MPa}$.

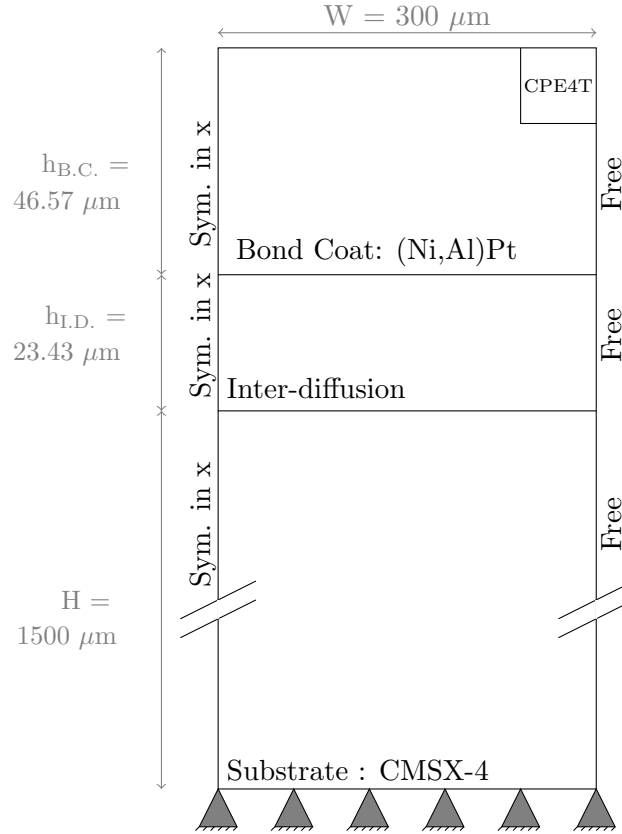


Figure 3.12: The dimensions and boundary conditions of the “Two-Layered Coating Model” in Abaqus (Not to scale).

To start with, for the inter-diffusion layer, the material properties including creep, elasticity and thermal expansion, are taken to be the same as the ones used for the Abaqus model verification. However, given that the material properties of the inter-diffusion layer are not known, during the course of this work, the relevant material properties of this layer are changed in a logical and systematic fashion until a combination that gives the closest outcome to the experimental results is found giving a better understanding of the inter-diffusion layer. The material properties that are changed during this sensitivity study are Young’s modulus (E), Poisson ratio (ν), coefficient of thermal expansion (α), and the creep properties. The creep properties of the inter-diffusion layer are represented by $n^{(2)}$, the creep stress exponent, and $\dot{\epsilon}_0^{(2)}$, the creep reference rate of the material.

Using the information regarding the initial thickness of the inter-diffusion and bond coat layers from Table 3.1, the dimensions and boundary conditions of the Abaqus model from Figure 3.10 are updated to Figure 3.12. Here while the substrate has a built-in condition on the bottom face, all the layers, including the substrate are free to expand laterally, i.e. no lateral constraints are applied

on the right edge; the left edge has symmetric boundary condition in x . In this model the coupled temperature-displacement step is used together with elements of type CPE4T. The same element type was used for all of the layers.

Effect of E , ν , and α

The first material property to consider in this sensitivity study is the elastic properties of the inter-diffusion layer, i.e. $E^{(2)}$, $\nu^{(2)}$ and $\alpha^{(2)}$, while its creep properties are taken to be $n^{(2)} = 3$, $\dot{\epsilon}_0^{(2)} = 2.2$, $T_R^{(2)} = 15000\text{K}$ and $\sigma_R^{(2)} = 25\text{MPa}$. Two steps are taken in studying the effect of elastic properties on lateral growth; i) given that inter-diffusion is a mixture of the bond coat and the substrate, it is not clear whether its elastic properties are closer to the bond coat or the substrate or in between, therefore, in the sensitivity study on the elastic properties, once properties of the bond coat and once properties of the substrate are used to see which one gives a closer lateral deformation to the experimental data. ii) in the second step of the sensitivity study on the elastic properties, once the reference elastic properties is chosen, the individual elastic properties are changed one by one to find out their effect on the lateral growth of the inter-diffusion layer. The swelling property of the inter-diffusion layer in this sensitivity study is based on Equation 3.5 with use of the relevant data from Table 3.2.

In order to assess the outcome of this sensitivity study, the lateral deformation of the right edge of the coating system computed by the Abaqus model, is plotted against the experimental one after 50 hours annealing at $T = 1150^\circ\text{C}$, as shown in Figure 3.13. The experimental lateral deformation of the coating's edge is labelled by a number of capital letters; A, B, and C letters mark the bond coat and C, D,E, and F mark the inter-diffusion layers.

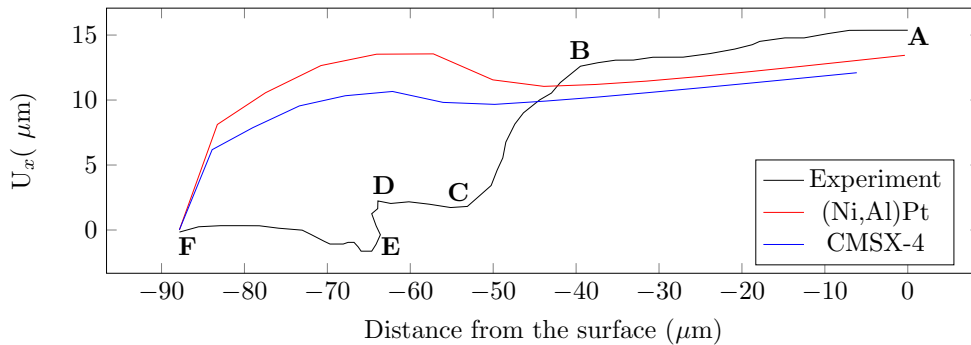


Figure 3.13: The lateral deformation of the right edge of the coating system (inter-diffusion + bond coat) computed by my Abaqus model for the first step of the sensitivity study compared to the experimental results.

Figure 3.13 shows the comparison between experimental results for lateral deformation of right edge of the system and the computed results from the Abaqus model for the first step of the sensitivity study on the elastic properties. The red line in Figure 3.13 shows the edge profile of the coating system

when the elastic properties of the inter-diffusion layer are taken to be the same as the bond coat, i.e. (Ni,Al)Pt, and the blue line is when they are taken to be the same as the substrate, i.e. CMSX-4.

As is clear from Figure 3.13, when the elastic properties of the inter-diffusion layer are taken to be the same as the substrate, i.e. the blue line, the inter-diffusion layer swells less compared to when the elastic properties of the inter-diffusion layer are taken to be the same as the bond coat. Additionally, not only the red line shows a greater swelling compared to the blue line, but also the lateral swelling of the inter-diffusion layer is as high as or higher than that of the bond coat; this outcome is not in accordance with the experimental observations for the inter-diffusion layer where the lateral swelling is almost negligible for the inter-diffusion layer compared to that of the bond coat. Therefore, based on these results, the elastic properties of the inter-diffusion layer are chosen to be closer to the substrate than the bond coat.

In the second step of sensitivity study on the elastic properties of the inter-diffusion layer, each of the elastic properties are changed individually, starting from the properties of CMSX-4, to see how much they separately affect the lateral swelling of the inter-diffusion layer. There are three elastic properties involved in this study; E , ν , and α . For E three cases of $E \in [E_{\text{CMSX-4}}/10, E_{\text{CMSX-4}}, E_{\text{CMSX-4}} \times 10]$ MPa; for ν the five cases of $\nu \in [\nu_{\text{CMSX-4}} - 0.05, \nu_{\text{CMSX-4}}, \nu_{\text{CMSX-4}} + 0.03, \nu_{\text{CMSX-4}} + 0.04, \nu_{\text{CMSX-4}} + 0.05]$; and for α the three cases of $\alpha \in [\alpha_{\text{CMSX-4}} - 10^{-6}, \alpha_{\text{CMSX-4}}, \alpha_{\text{CMSX-4}} + 10^{-6}]$ are considered; the results from all of these cases are shown in Figure 3.14.

The top plot in Figure 3.14 shows the effect of Young's modulus on the lateral growth; in this case it is clear that decreasing E by a factor of 10 leads to more lateral deformation than the original case, whereas, increasing it by a factor of 10 does not show any changes. While the lateral growth of the bond coat is getting closer to the experimental result with decreasing E , but the characteristic lateral growth of the inter-diffusion layer is not captured, therefore, changing E is not enough on its own to shed light on the reason behind this characteristic lateral growth. It is clear from this plot that the higher the stiffness of inter-diffusion layer the lower the amount of its lateral growth.

The second parameter in this part of sensitivity study is the Poisson ratio or $\nu^{(2)}$, results of which are shown in the middle plot of Figure 3.14. It is clear from this plot that increasing the Poisson ratio leads to a smaller swelling effect, both lateral and normal, however, this effect is not linear because decreasing the Poisson ratio by 0.05 does not have the same amount of effect as increasing it by the same amount. Looking at the results for this elastic property, it is clear that as the Poisson ratio increases, the solution gets closer to the characteristic behaviour of the inter-diffusion layer obtained from the experiments, however, while the lateral swelling gets closer to the experimental results in

shape but the actual value of the swelling in both normal and lateral direction does not. The conclusion here is that it is possible for the Poisson ratio of the inter-diffusion layer to be higher than that of CMSX-4, i.e. $\nu^{(2)} > \nu^{(1)}$ but it is not a stand alone effect.

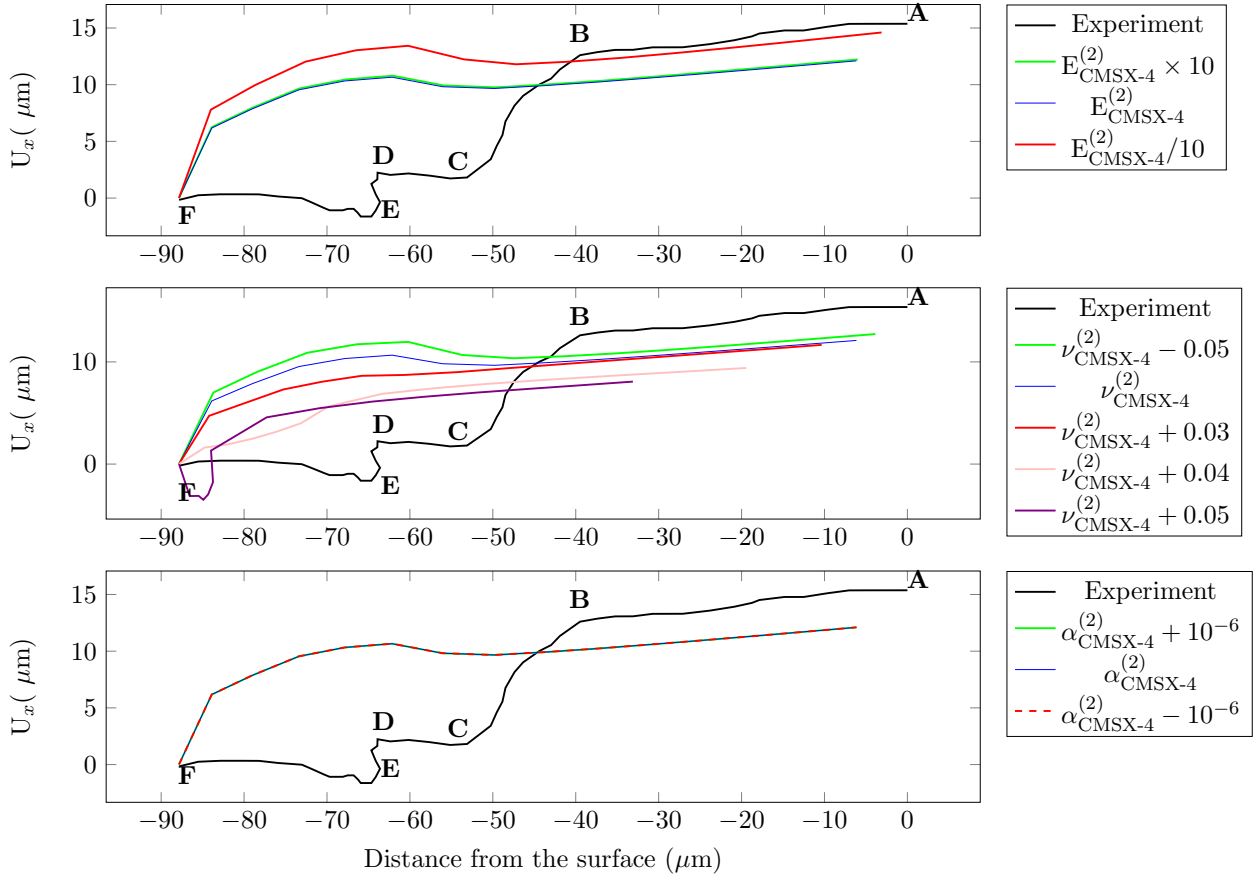


Figure 3.14: Lateral growth results of the sensitivity study on the elastic property of the inter-diffusion layer, i.e. Top plot - $E^{(2)}$, middle plot - $\nu^{(2)}$ and bottom plot - $\alpha^{(2)}$.

The last elastic property in this part of the sensitivity study is the coefficient of thermal expansion or $\alpha^{(2)}$ of the inter-diffusion layer during the initial cooling and heating steps of the isothermal experiment. The results for this elastic property are demonstrated in the bottom plot of Figure 3.14 which shows no change in the lateral growth of the coatings as the coefficient of thermal expansion changes. As a result, it is a good approximation to use the thermal expansion property of the substrate for the inter-diffusion layer.

Effect of Creep Properties

Having looked at the effect of elastic properties of inter-diffusion layer on lateral deformation of the layers, the next most important property is creep. Creep property of the inter-diffusion layer is taken to follow the power-law creep with its definition shown as

$$\dot{\varepsilon}_{\text{creep}_{ij}}^{(2)} = \frac{3}{2} \dot{\varepsilon}_0^{(2)} \left(\frac{\sigma_e^{(2)}}{\sigma_R^{(2)}} \right)^{n^{(2)}-1} \left(\frac{s_{ij}^{(2)}}{\sigma_R^{(2)}} \right) e^{-T_R^{(2)}/T}, \quad (3.25)$$

As can be seen in Equation 3.25, there are a number of parameters that can affect the creep behaviour of the inter-diffusion layer, such as $n^{(2)}$, $\dot{\varepsilon}_0^{(2)}$, $T_R^{(2)}$ and $\sigma_R^{(2)}$. Therefore, to simplify the sensitivity study, only $n^{(2)}$ and $\dot{\varepsilon}_0^{(2)}$ are considered while all the parameters are fixed. The effect of these parameters on the edge profile of the coating system is studied one at the time, as shown in Figure 3.15.

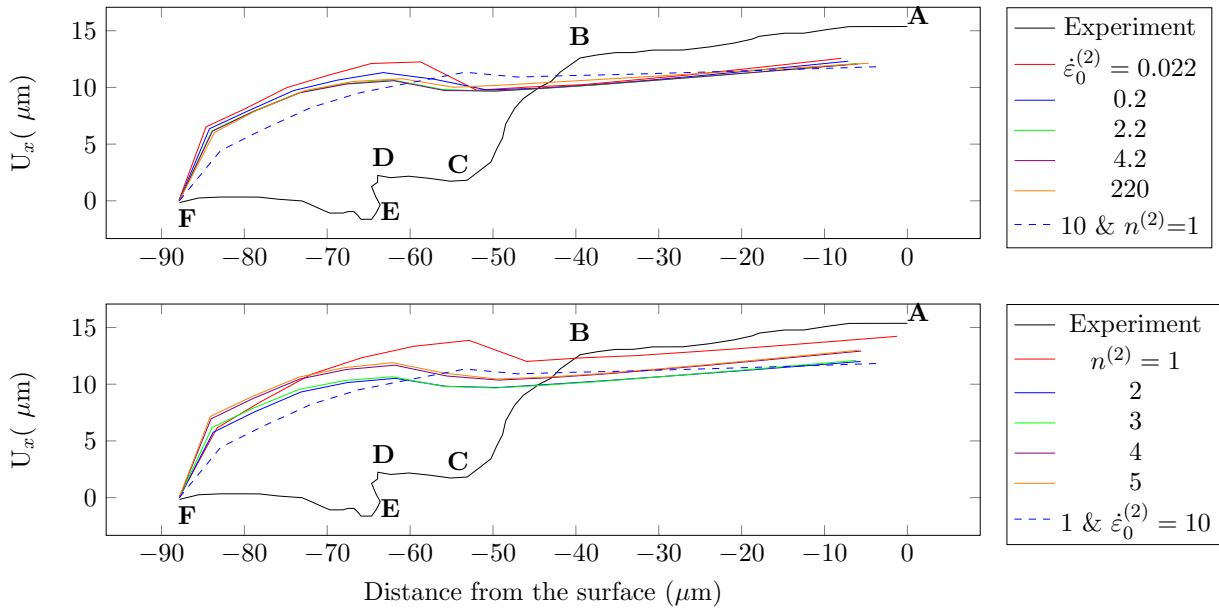


Figure 3.15: Lateral growth results of the sensitivity study on the creep property of the inter-diffusion layer, i.e. Top plot - $\dot{\varepsilon}_0^{(2)}$, and bottom plot - $n^{(2)}$.

The top plot in Figure 3.15 shows the effect of creep reference strain rate or $\dot{\varepsilon}_0^{(2)}$ on the edge profile while the creep exponent or $n^{(2)}$ is kept equal to 3. The bottom plot in Figure 3.15 shows the effect of $n^{(2)}$ on the edge profile of the system while $\dot{\varepsilon}_0^{(2)}$ is kept at 2.2.

Looking at the top plot in Figure 3.15, it is clear increasing the creep reference strain rate decreases the lateral swelling, however, as is clear from the figure, for $n^{(2)} = 3$, effect of $\dot{\varepsilon}_0^{(2)}$ on the lateral growth is very small. The higher the creep reference strain rate the higher the creep deformation and stress relaxation, which explains the reduction in lateral growth, however, this reduction in lateral swelling is not enough to produce the experimental results. Nevertheless this result is in favour of validating the proposed postulation.

The next creep parameter to consider is the creep exponent which has a very strong effect on the creep behaviour of a material, as can be seen from Equation 3.25; the bottom plot in Figure 3.15 shows the effect of this property on the lateral deformation of the system's right edge. As is clear from the figure, there is a decrease in the lateral swelling as $n^{(2)}$ decreases from 5 to 2, but not for $n^{(2)} = 1$ which has the highest lateral growth. Looking back at Figure 3.5 for how the stress relaxation of the bond coat material changes with the creep exponent, it is clear that the higher the creep exponent the

less the stress relaxation, as a results, there is less creep deformation. Applying this argument to the situation here, explains that with higher $n^{(2)}$ there is less creep deformation from the stress relaxation opposing the lateral growth of the inter-diffusion layer; which is why there is more lateral growth for higher values of $n^{(2)}$.

When $n^{(2)} = 1$, is an exceptional case because not only the effect of the equivalent stress in the creep strain rate equation, i.e. Equation 3.25, is removed but also as Figure 3.5 shows, the in-plane stress drops to zero which means that the swelling strain rate in Equation 3.11 takes over the lateral deformation of the inter-diffusion layer, hence, the larger lateral growth. The interesting fact about the $n^{(2)} = 1$ case is that because its creep behaviour becomes independent of the equivalent stress, based on Equation 3.25, its creep behaviour can now be controlled by $\dot{\epsilon}_0^{(2)}$. Therefore, the higher the creep reference strain rate, it is expected to have more creep deformation opposing the lateral swelling and vice versa; because of this, an additional case of $n^{(2)} = 1$ and $\dot{\epsilon}_0^{(2)} = 10$ is also shown in both of the plots in Figure 3.15 for comparison and demonstration.

As is clear from the dashed blue line in Figure 3.15, for this additional case a lower lateral growth is obtained for the inter-diffusion layer compared to all the other ones. This sensitivity result confirms that higher creep deformation leads to lower lateral swelling which was the basis of the postulation in this work. However, as is clear from Figure 3.15, the characteristic lateral growth of the layers, which was obtained from the experiment, is not captured by the two-layered coating model, as suggested by [4]. As one would expect, two adjacent layers would have the same lateral deformation at their common interface, which is the results captured by the two-layered model. However, the experimental results does not follow this trend which suggested that this model has not captured the main source of this behaviour. As will become more apparent in the next subsection, because of the complexity in the inter-diffusion of Ni and Al between the bond coat and the substrate, the swelling across the thickness of the bond coat and inter-diffusion is not uniform. Therefore, a more detailed model such as a four-layered coating model is required which divides the system into layers based on their compositional gradient .

3.2.2.6 *Four-Layered Coating Model*

It is clear from the sensitivity study in the previous subsection that even with the manipulation of the elastic and creep properties, the characteristic lateral behaviour of the inter-diffusion layer is not obtained using the two-layered coating. The closest edge profile to the experimental result was obtained for $\nu^{(2)} \geq \nu_{\text{CMSX-4}}^{(2)} + 0.03$, which not only reduced the lateral deformation of the inter-diffusion layer but also its normal one. This is not acceptable on its own because it is important to reach the experimentally measured thickness while obtaining the characteristic lateral deformation profile

for the inter-diffusion layer. Therefore, while the two-layered coating model gave a good insight into the sensitivity of the inter-diffusion layer to the creep and elastic properties, it did not capture the characteristic behaviour that was required i.e. the lateral growth shown in Figure 3.2.

As a result, a new approach to modelling this coating system is suggested; instead of two-layered coating, a four-layered coating system is used which will be described here. There are two reasons for suggesting this model; first, the experimental results as described by the Chen *et al.*, consist of five sections; A-B, B-C, C-D, D-E, and E-F as shown in Figure 3.2 where each section can be considered a separate layer except for D-E which is ignored in this model. The sections A-B and B-C are considered to be parts of the bond coat layer, and the C-D and D-F sections are considered to be parts of the inter-diffusion layer, as described by Chen *et al.*

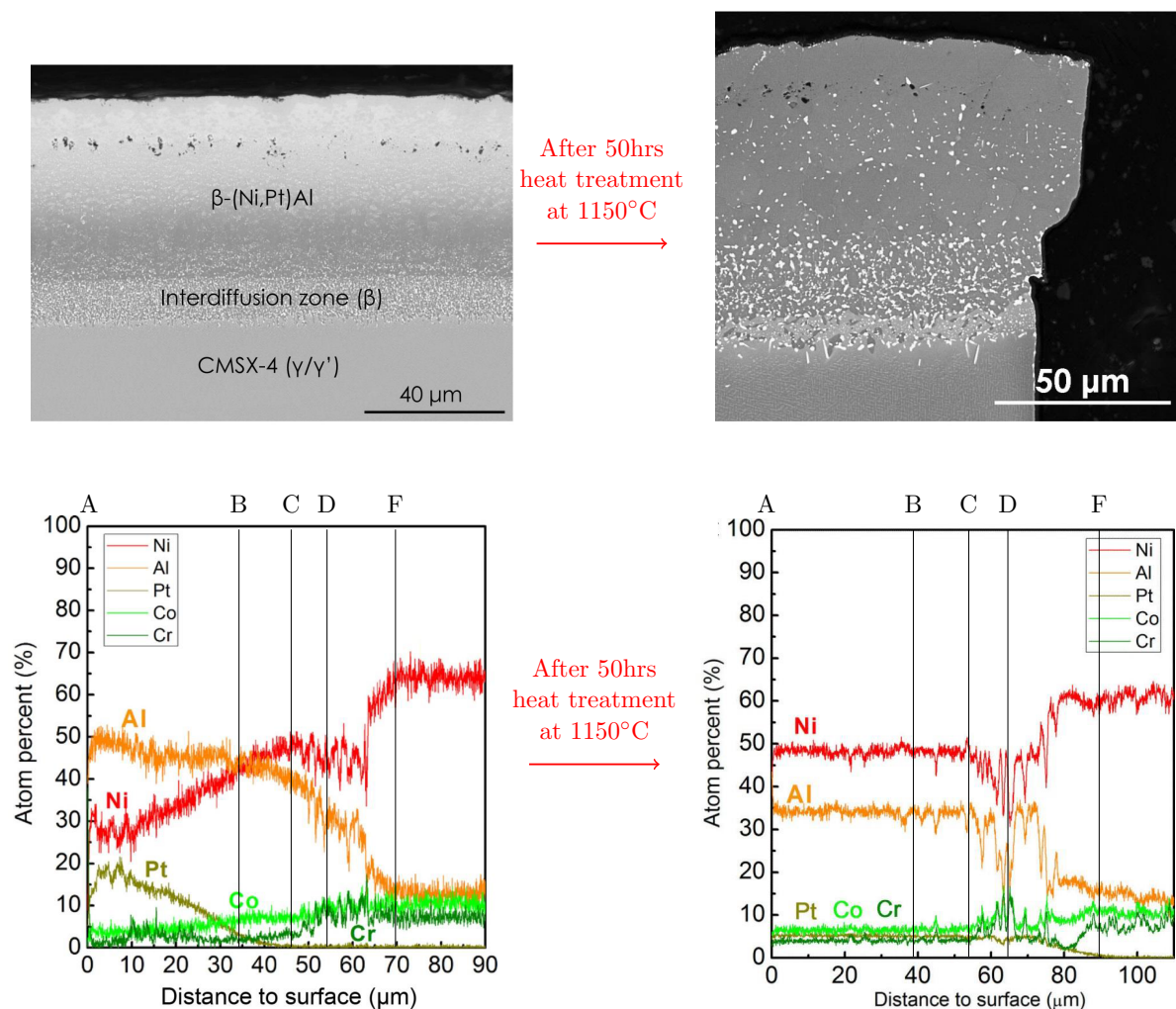


Figure 3.16: **Top:** The image of the system under study before and after the experiment. **Bottom:** The composition of the layers in the system before and after the experiment. These images are taken from personal contact with Chen *et al.* Please note the A to F labels here are added manually based on the middle plot in Figure 3.2.

The second and more important reason is the compositional change of the layers and sections during the experiment, i.e. Figure 3.16. It is clear from Figure 3.16 that the distribution of Ni, Al,

and other elements is not uniform and does not change uniformly across the inter-diffusion and bond coat thicknesses. In previous studies it has been suggested that the non-uniform diffusion of Ni and Al can lead to formation of topologically closed-packed phases or secondary reaction zone; as a results, there are parts of the layers that can swell more or less than the others.

Given that swelling is a product of Ni diffusing into the bond coat and Al into the substrate, the amount of Ni/Al in each layer at any point in time can affect the swelling of that layer. Therefore, as a guidance, the A to F sections are used together with the composition change results from Chen *et al.*, as shown in Figure 3.16, to create the four-layered coating model which will be explained in more details here.

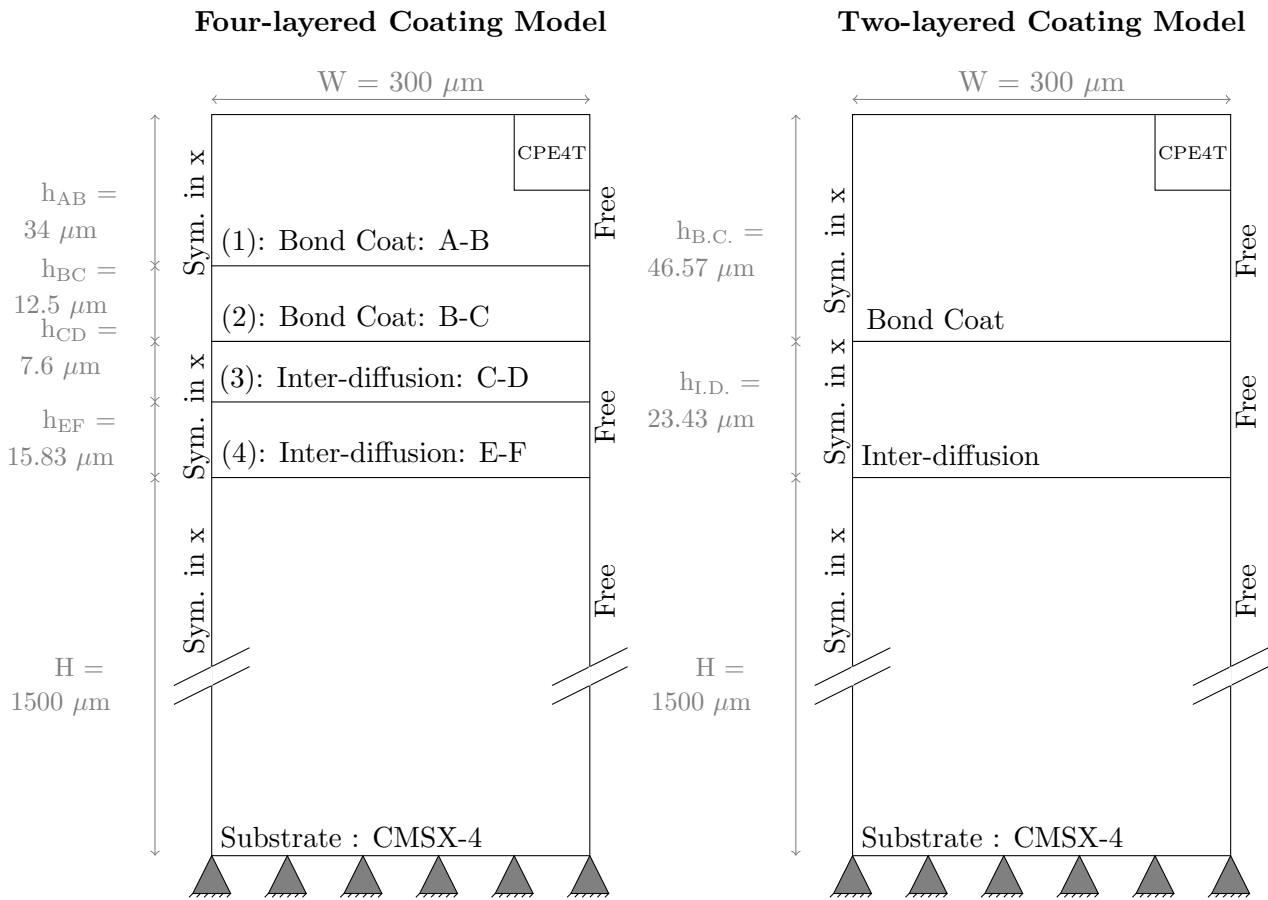


Figure 3.17: The dimensions and boundary conditions of the two-layered and four-layered models of the coating system. (Not to scale)

The four-layered model of the coating system consists of one substrate layer, two inter-diffusion layers, and two bond coat layers where the bond coat is labelled from A to C and the inter-diffusion layer is labeled from C to F, as shown in Figure 3.17. In this figure the geometrical definition of the two-layered coating model is also shown as a comparison. In the two-layered model the initial thickness of each layer is taken from Table 3.1; the same applies to the four-layered model, however, in the latter case each of the coating layers, i.e. inter-diffusion and bond coat, are divided into two

layers. To define the initial thickness of each layer in the four-layered model, a combination of the thicknesses given in Table 3.1 and the ratios of the A to F sections from Figure 3.2 is used.

For example, for the A-B section or the top layer of the bond coat, $38\mu\text{m}$ is its thickness after 50 hours isothermal heat treatment over $52\mu\text{m}$ which is the total thickness of the bond coat layer, i.e. A-C section; all of this information is taken from the middle plot in Figure 3.2. Therefore, assuming that the ratio of A-B over A-C stays as $38/52$ throughout the experiment, the initial height of the A-B layer can be approximated as $h_{AB} = \frac{46.57}{52} \times 38 = 34\mu\text{m}$ where $46.57\mu\text{m}$ is the initial thickness of the bond coat layer from Table 3.1. The same technique is applied to all the other layers and their results are shown in Figure 3.17. The boundary conditions for the four-layered model is the same as the two-layered model; in other words, while the substrate is fixed on the bottom surface, all the layers are free to move laterally, as indicated in Figure 3.17. The element and step type used for the four-layered model stays the same as before, i.e. CPE4T and coupled temperature-displacement.

Having defined the thickness of each layer, as shown in Figure 3.17, the next important step is defining the material properties of each layer in the four-layered coating model; these properties include creep, elastic and swelling properties. The material properties for these layers are chosen based on the change in their composition as shown in Figure 3.16, and the comparison in the BSE images of the coating before and after the experiment, as shown in the same figure. Table 3.5 shows the choice of material properties for each layer, and here the reasons for these choices are given:

- **Layer A-B:** Looking at composition of the A-B layer in Figure 3.16, it is clear that before the heat treatment the Al content is higher than Ni; after 50 hours of annealing, however, because of Ni diffusion from the substrate into the bond coat and Al diffusion from the bond coat into the substrate, Ni level rises significantly while the Al level decreases. This significant raise in the Ni content can be the reason for this layer swelling more than others. Additionally, the Ni and Al contents in the A-B section are not uniform across the thickness which can explain the non-uniform lateral distribution of the A-B layer. The material properties chosen for this layer are the properties that have been given for the bond coat layer through out this chapter, a summary of that can be found in Table 3.5.
- **Layer B-C:** As shown in Figure 3.16, unlike the A-B layer the Ni content is higher than the Al one, except at the B interface where the Al and Ni content seem to be equal. After 50 hours of isothermal heat treatment there is a small increase in the Ni level and a significant decrease in the Al content which leads to a final uniform distribution of Ni and Al across the thickness of B-C and A-B layers. Faster diffusion of Ni from the substrate into the coating layers is known as the primary reason for swelling in TBC systems, therefore, given that the Ni level close to

interface B has raised a lot while the Al level at the same location has dropped can explain the higher swelling closer to the B interface. Whereas at the C interface the Ni content has not changed much while a small drop has occurred for the Al content which can explain the negligible swelling at this interface. Therefore, the swelling property of this layer is chosen to be half of the value reported in Table 3.1 for the bond coat. Additionally, given that not much change of Ni/Al content has occurred in this layer while a lot has changed in the A-B layer, one can argue that in this layer diffusion of Ni and Al have been well accommodated, i.e. a higher creep deformation than A-B section. This argument is supported by the statement that presence of Cr in a layer decreases its creep strength, [4], and the fact that Cr content has increased in the B-C layer. This is why when defining the material properties for this layer, creep properties are chosen such that it allows for higher diffusion rate.

- **Layer C-D:** Before the annealing process as shown in Figure 3.16, the level of Ni is higher than Al, while for both components there is a noticeable fluctuation near the D interface. After 50 hours, while level of Ni is still higher than Al but now the amplitude of fluctuations has increased significantly, particularly, at the D interface where the level of Ni and Al have been reduced compared to the initial composition. This reduction in the Ni level at the D interface can be responsible for the dip in the lateral displacement at the D-E location. Given that the Ni level has not changed significantly in this layer, it is understandable if the swelling is small compared to the bond coat, however, given that the fluctuations in the Ni content have increased, it could be argued that they are responsible for part of the swelling reported in Table 3.1. The creep properties chosen for this layer is based on the postulation that was put forward at the beginning of this chapter, i.e. faster in-plane stress relaxation, less lateral growth.
- **Layer D-F:** Finally, the last layer is D-F which is the closest layer to the substrate; looking at the composition of this layer in Figure 3.16, a clear division in the way that the Ni and Al content are distributed is observed. The region closest to the F interface has a much bigger gap between the Ni and Al content than the region close to the D interface. This can be the reason why using the elastic properties of the CMSX-4 for the inter-diffusion layer in the sensitivity study, produced a better result than using the elastic properties of (Ni,Al)Pt. After the annealing process, while the gap between the Ni and Al content close to the F interface is still large but the overall level of Ni has decreased and level of Al has increased in that vicinity. At the same time the level of fluctuations close to the D interface has raised and the gap between the Ni and Al content has reduced at the D interface. Given the significant changes that occurred within the inter-diffusion layer, it is valid to say that swelling of this layer is not uniform across its thickness, particularly in the D-F layer. Additionally, as can be seen from Figure 3.16, the overall amount of Ni in this layer has decreased close to the F interface, while increased closer

to the D interface; it seems that part of the reduction in the Ni level at the F interface has gone into increase in the Ni level close to D interface. Therefore, the swelling property for this layer is taken to be a fraction of the reported swelling for the inter-diffusion layer. While the reference creep temperature, and reference creep stress and strain of this layer are kept the same as C-D layer, the creep exponent of it is changed to the value for CMSX-4 (taken from [23]) because until exact experimental values are found, this is a good approximation.

Table 3.5: The elastic, creep and swelling properties of each layer used in my two Abaqus models. The column ‘‘Swell’’ gives the material from which the swelling data was used. This table needs to be read together with Figure 3.17.

Layer’s Name	E(MPa)	ν	CTE	$\dot{\epsilon}_0(\text{s}^{-1})$	n	$T_R(\text{K})$	$\sigma_R(\text{MPa})$	Swell
Two-Layers								
Bond Coat	$E_{(\text{Ni,Al})\text{Pt}}$	0.27	$\alpha_{(\text{Ni,Al})\text{Pt}}$	0.2	4	15000	25	(Ni,Al)Pt
Inter-diffusion	$E_{\text{CMSX-4}}$	$\nu_{\text{CMSX-4}}$	$\alpha_{\text{CMSX-4}}$	10	1	15000	25	Inter-diffusion
Substrate: CMSX-4	$E_{\text{CMSX-4}}$	$\nu_{\text{CMSX-4}}$	$\alpha_{\text{CMSX-4}}$	N/A	N/A	N/A	N/A	None
Four-Layers								
Bond Coat: A-B	$E_{(\text{Ni,Al})\text{Pt}}$	0.27	$\alpha_{(\text{Ni,Al})\text{Pt}}$	0.2	4	15000	25	(Ni,Al)Pt
Bond Coat: B-C	$E_{(\text{Ni,Al})\text{Pt}}$	0.27	$\alpha_{(\text{Ni,Al})\text{Pt}}$	2.6	2	11000	15	$0.5 \times (\text{Ni,Al})\text{Pt}$
Inter-diffusion: C-D	$E_{\text{CMSX-4}}$	$\nu_{\text{CMSX-4}}$	$\alpha_{\text{CMSX-4}}$	2.2	2	15000	20	Inter-diffusion
Inter-diffusion: D-F	$E_{\text{CMSX-4}}$	$\nu_{\text{CMSX-4}}$	$\alpha_{\text{CMSX-4}}$	2.2	8.8	15000	20	$0.25 \times \text{Inter-diffusion}$
Substrate: CMSX-4	$E_{\text{CMSX-4}}$	$\nu_{\text{CMSX-4}}$	$\alpha_{\text{CMSX-4}}$	N/A	N/A	N/A	N/A	None

3.3 Results & Discussion

Using the developed four-layered model of the coating system in Abaqus together with the data from Table 3.5, the edge profile of the bond coat/inter-diffusion layers is produced, as shown in Figure 3.18. In this figure also the result from the two-layered coating model is shown for comparison.

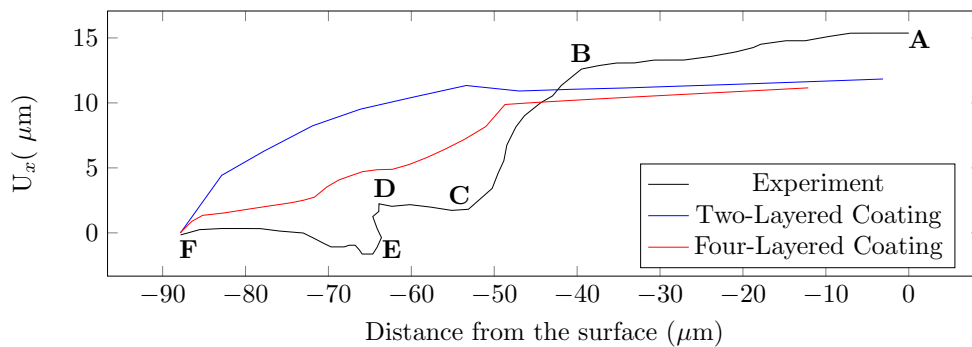


Figure 3.18: Comparison of the right edge profile of the inter-diffusion and bond coat layers when the two-layered and four-layered coating models are used.

As is clear from Figure 3.18, the four-layered coating model qualitatively captures the characteristics of the edge profile obtained from the experiment. In other words the edge profile produced from the four-layered model has captured the large lateral swelling of the A-B part of the bond coat

compared to the small lateral growth of the inter-diffusion layer; it also has captured the small bump in the D-C layer.

This outcome shows that defining the material properties of each layer, particularly swelling, in the four-layered coating model based on the compositions in Figure 3.16 has been the correct approach, however, that information alone is not enough to give the exact material property of each layer. Since there are not enough experimental information available for the elastic or creep properties of the inter-diffusion layer, in addition to the swelling behaviour of each layer in the four-layered approach, there is a variety of material property combinations that can lead to the correct edge profile, and Table 3.5 only shows one example. To obtain a more accurate edge profile from this model, requires experimental measurements of the swelling for each of these four layers, and information regarding the elastic and creep properties of the inter-diffusion layer.

The important point to take away from this model and its outcome is the fact that the two-layered coating model is not detailed enough to capture the edge profile of this system because of the non-uniform diffusion of Ni/Al and other elements through its thickness. Whereas, the four-layered model provides the tool for producing and understanding the lateral growth behaviour of this system while taking into account its other mechanical properties such as creep. As seen in this study, the non-uniform swelling across the thickness of the coating has a significant effect on the behaviour of the system. Given that the rumpling effect is highly sensitive to swelling, particularly at regions close to the TGO, it is essential to improve the existing rumpling models to take into account the multi-layered nature of the bond coat. For example, one can implement the multi-layered nature of the bond coat in the analytical model of rumpling and use that to more accurately model this damage mechanism.

3.4 Conclusion

Chen *et al.* in their experimental work on measuring the lateral growth of the bond coat/inter-diffusion layers of TBC system after 50 hours of isothermal heat treatment at 1150°C, came across a puzzling result. Their results showed a large lateral deformation for the bond coat and almost none for the inter-diffusion layer. This was surprising because swelling effect which is a volumetric phenomenon, was observed in both layers, hence, it should have led to lateral swelling for the inter-diffusion layer as well. As a collaboration with Chen *et al.*, a postulation was put forward; given the relationship between the creep deformation and in-plane stresses, it is possible for the inter-diffusion layer to have a lower creep strength than the bond coat which leads to higher stress relaxation and so less lateral growth. In order to test the postulation and reproduce the experimental results first an analytical model of the stress in the layers, including swelling, was created where it was shown that lower creep

strength indeed leads to less in-plane stresses in the layer. To test this postulation for the coating system under the experimental conditions, the analytical model of the swelling strain rate and creep strain rate were implemented in a finite element model of the system.

Initially a two-layered model of the coating system was created in finite element which corresponded to the swelling information taken from Chen *et al.*. Given the limited information about the properties of the inter-diffusion layer, a sensitivity study was carried out on the elastic and creep properties of this layer using this two-layered model. While the outcome of this sensitivity study confirmed the proposed postulation but there was no reasonable combination of material properties that produced the experimental edge profile. This showed that a two-layered model of the coating system is not detailed enough to capture the true lateral behaviour of this system, mainly because the Ni/Al diffusion which are responsible for swelling, are not uniformly distributed across the coating thickness. This is why a four-layered coating model of the system was suggested where the boundaries of each layer were defined based on the experimental edge profile and their properties were approximated based on the compositional map of the layers and how they changed during the heat treatment.

This four layered model of the coating system produced a qualitative match with the experimental results, which captured the main characteristics of the experimental edge profile. This outcome showed that the proposed four-layered coating model gives the tool for understanding the mechanical behaviour of the materials involved in this system. However, given that some of the material properties used in this model were based on the qualitative understanding of the compositional change in the layer, in order to get a more accurate result from this model, experimental data regarding the swelling of each layer in the four-layered coating model is required. Once this information is available, one can use the four-layered coating model to capture the experimental results for the lateral expansion of the bond coat and inter-diffusion layers more accurately. In addition to the insight into the material property of the layers, the four-layered coating model highlights the importance of the multi-layered nature of the bond coat on its swelling behaviour. Given the high sensitivity of rumpling growth on the swelling behaviour of the bond coat particularly at the region near the TGO, the fact that bond coat is found to be multi-layered in nature is very important. Therefore, it is clear that in order to model rumpling more accurately, one needs to develop a multi-layered model (analytical or others) of the bond coat layer.

3.5 Table of variables

Table 3.6: Variables and terms used in this chapter and their definitions.

TGO	Thermally grown oxide
TBC	Thermal barrier coating
IDZ	Inter-diffusion zone
I.D.	Inter-diffusion zone
B.C.	Bond coat
CTE	Coefficient of thermal expansion
T	Temperature of the system
T_R	The creep reference temperature of the layer
\dot{T}	Temperature rate of the system
W_{BC}	Stored strain energy of the bond coat
W_{TGO}	Stored strain energy of the TGO
V_{BC}	Volume of the bond coat layer.
V_{TGO}	Volume of the TGO layer.
h	Current height of the layer
h_0	Initial height of the layer
\dot{h}	Rate of thickening of the layer
t	Time
Δt	Time step
a	Constant to be found from experimental results for Equation 3.5
b	Constant to be found from experimental results for Equation 3.5
c	Constant to be found from experimental results for Equation 3.5
$\varepsilon_{(ij)}^{(k)}$	Strain term of the k^{th} layer in the ij direction, where i & j change between 1, 2 and 3
$\dot{\varepsilon}_{(ij)}^{eng}$	Engineering strain rate of the layer in the ij direction, where i & j change between 1, 2 and 3
$\dot{\varepsilon}_{creep,ij}$	Creep strain rate of the layer in the ij direction, where i & j change between 1, 2 and 3
$\dot{\varepsilon}_{(ij)}^{(k)}$	True strain rate of the k^{th} layer in the ij direction, where i & j change between 1, 2 and 3
$\nu^{(k)}$	Poisson ratio of the k^{th} layer
$E^{(k)}$	Young's modulus of the k^{th} layer
$\alpha^{(k)}$	Coefficient of thermal expansion of the k^{th} layer
$\nu_{Mat. name}^{(k)}$	Poisson ratio of the k^{th} layer using the property of the named material
$E_{Mat. name}^{(k)}$	Young's modulus of the k^{th} layer using the property of the named material
$\alpha_{Mat. name}^{(k)}$	Coefficient of thermal expansion of the k^{th} layer using the property of the named material
n	The creep exponent of the layer
δ_{ij}	Kronecker delta
$\square^{(2)}$	Properties and variables related to the IDZ
$\square^{(3)}$	Properties and variables related to the bond coat
A	The constant defined by the user
\tilde{q}	The uniaxial equivalent deviatoric stress
$\dot{\varepsilon}_0$	The creep reference strain rate of the layer
$\dot{\varepsilon}^{cr}$	The uniaxial equivalent creep strain rate
$\dot{\varepsilon}_P$	Strain rate of the layer due to phase transformation
$\dot{\varepsilon}_S$	Strain rate of the layer due to swelling

ε_S^m	Strain term of the layer due to swelling in the time increment m
$\sigma_{ij}^{(k)}$	Stress term of the k^{th} layer in the ij direction, where i & j change between 1, 2 and 3
$\dot{\sigma}_{ij}^{(k)}$	Stress rate of the k^{th} layer in the ij direction, where i & j change between 1, 2 and 3
$s_{ij}^{(k)}$	k^{th} layer deviatoric stress in the ij direction, where i & j change between 1, 2 and 3
σ_R	The creep reference stress of the layer
σ_e	Effective stress in the layer
m	Time exponent
W	Width of the system
H	Height of the substrate

3.6 Bibliography

- [1] C.M.F. Rae, M.S.A. Karunaratne, C.J. Small, R.W. Broomfield, C.N. Jones, and R.C. Reed. Topologically Close Packed Phases in an Experimental Rhenium-Containing Single Crystal Superalloy. *Superalloys 2000 (Ninth International Symposium)*, pages 767–776, 2000.
- [2] Henderson. Investigation into the properties of titanium based films deposited using pulsed magnetron sputtering. *Surface and Coatings Technology*, 174 -175:720–724, 2003.
- [3] Z. Bai, D. Li, H. Peng, J. Wang, H. Guo, and S. Gong. Suppressing the formation of SRZ in a Ni-based single crystal superalloy by RuNiAl diffusion barrier. *Progress in Natural Science: Materials International*, 22(2):146–152, 2012.
- [4] Ali Dad Chandio. *Processing, Characterisation and Oxidation Study of the Nickel Aluminides (β NiAl) for Thermal Barrier Coating Applications*. PhD thesis, University of Manchester, 2015.
- [5] A.D. Chandio, X. Zhao, Y. Chen, M. Bai, and P. Xiao. β NiAl Bondcoat Deposited onto CMSX-4 Superalloy for Thermal Barrier Applications. In W. M Kriven, J. Wang, D. Zhu, and T. Fischer, editors, *Developments in Strategic Ceramic Materials*, page 215. John Wiley and Sons, 2015.
- [6] V K Tolpygo and D R Clarke. On the rumpling mechanism in nickel-aluminide coatings Part II : characterization of surface undulations and bond coat swelling. *Acta Materialia*, 52:5129–5141, 2004.
- [7] R V Hillery, B.H. Plisner, R.L. McKnight, T.S. Cook, and M.S. Hartie. Thermal Barrier Coating Model Development Final Report. Technical report, NASA, 1988.
- [8] W S Walston, J C Schaeffer, and W H Murphy. A New Type of Microstructural Instability in Superalloys- SRZ. *The Minerals, Metals and Materials Society*, 1996.
- [9] J. H. Chen and J. A. Little. Degradation of the platinum aluminide coating on cmsx4 at 1100C. *Surface and Coatings Technology*, 92(1-2):69–77, 1997.

- [10] B. Tryon, Q. Feng, R.G. Wellman, K.S. Murphy, J. Yang, C.G. Levi, J.R. Nicholls, and T.M. Pollock. Multi-layered Ruthenium-modified Bond Coats for Thermal Barrier Coatings. *Metallurgical and Materials Transactions A*, 37(11):3347–3358, 2006.
- [11] Dipak K. Das, Kenneth S. Murphy, Shuwei Ma, and Tresa M. Pollock. Formation of secondary reaction zones in diffusion aluminide-coated Ni-base single-crystal superalloys containing ruthenium. *Metallurgical and Materials Transactions A: Physical Metallurgy and Materials Science*, 39(7):1647–1657, 2008.
- [12] T. Pollock, D. Widrevitz, R. Pong, F. Cao, and B. Tryon. Intermetallic B2 Bond Coats: Systems Compatibility and Platinum-Group Metal Additions. *2008 MRS Fall Meeting*, 2008.
- [13] M.-P. Bacos, J.-M. Dorvaux, R. Mévrel O. Lavigne, C. Rio M. Poulain, and M.-H. Vidal-Sétif. Performance and Degradation Mechanisms of Thermal Barrier Coatings for Turbine Blades : a Review of Onera Activities. *Journal Aerospace Lab*, (3):1–11, 2011.
- [14] R Darolia. Thermal barrier coatings technology : critical review , progress update , remaining challenges and prospects. *International Materials Reviews*, 58(6):315–348, 2013.
- [15] D. K. Das. Microstructure and high temperature oxidation behavior of Pt-modified aluminide bond coats on Ni-base superalloys. *Progress in Materials Science*, 58(2):151–182, 2013.
- [16] Ashok K Sinha. TOPOLOGICALLY CLOSE-PACKED STRUCTURES OF TRANSITION METAL ALLOYS. *Progress in Materials Science*, pages 79–185, 1972.
- [17] G. W. Goward and D. H. Boone. Mechanisms of formation of diffusion aluminide coatings on nickel-base superalloys. *Oxidation of Metals*, 3(5):475–495, 1971.
- [18] D. Dye, K.T. Conlon, P.D. Lee, R.B. Rogge, and R.C. Reed. Welding of Single Crystal Superalloy CMSX-4: Experiments and Modeling. *Superalloys 2004*, pages 485–491, 2004.
- [19] M Zielińska, M Yavorska, M Poręba, and J Sieniawski. Thermal properties of cast nickel based superalloys. *Archives of Materials Science and Engineering*, 44(1):35–38, 2010.
- [20] D. Pan, M. W. Chen, P. K. Wright, and K. J. Hemker. Evolution of a diffusion aluminide bond coat for thermal barrier coatings during thermal cycling. *Acta Materialia*, 51(8):2205–2217, may 2003.
- [21] D S Balint, S Kim, Yu-fu Liu, R Kitazawa, Y Kagawa, and A G Evans. Anisotropic TGO rumpling in EB-PVD thermal barrier coatings under in-phase thermomechanical loading. *Acta Materialia*, 59(6):2544–2555, 2011.

- [22] J. A. Haynes, B. A. Pint, W. D. Porter, and I. G. Wright. Comparison of thermal expansion and oxidation behavior of various high-temperature coating materials and superalloys. *Materials at High Temperatures*, 21(2):87–94, 2004.
- [23] W. Schneider, H. Mughrabi, and J. Hammer. Creep deformation and rupture behavior of the monocrystalline superalloy CMSX-4–A comparison with the alloy SRR 99. *Superalloys 1992*, pages 589–598, 1992.
- [24] M. P. Taylor, H. E. Evans, E. P. Busso, and Z. Q. Qian. Creep properties of a Pt-aluminide coating. *Acta Materialia*, 54(12):3241–3252, 2006.

3.A Appendix

In Figure 3.19 an example of the UEXPAN subroutine used for a simplified model of swelling in Abaqus is shown.

```

C
C
SUBROUTINE UEXPAN(EXPAN,DEXPANDT,TEMP,TIME,DTIME,PREDEF,
1 DPRED,STATEV,CMNAME,NSTATV,NOEL)
C
INCLUDE 'ABA.PARAM.INC'
C
CHARACTER*80 CMNAME
C
DIMENSION EXPAN(*),DEXPANDT(*),TEMP(2),TIME(2),PREDEF(*),
1 DPRED(*),STATEV(NSTATV)

REAL*8 A,B,C,EXPDATA

C----- User defined constants
A = 4.053
B = 0.405
C = 23.43

C----- Experimental strain rate for thickening
EXPDATA = (A*B/3600.00*((TIME(2)+720)/3600.0)**(B-1.0))/
1 (A*((TIME(2)+720)/3600.0)**B+C)

C----- Swelling for the symmetrical cube
IF (TIME(2).EQ.DTIME)THEN
! Initial swelling strain rate
EXPDATA = (A*B/3600.00*((720)/3600.0)**(B-1.0))/C
EXPAN(1) = EXPDATA *DTIME

ELSE
EXPAN(1) = DTIME*EXPDATA

ENDIF

RETURN
END

```

Figure 3.19: The Abaqus UEXPAN subroutine written for the simplified swelling strain rate of the freely expanding cube.

In this subroutine $TIME(2)$ is the total time of the simulation in seconds, and $DTIME$ is the time increment. Please note, while $TIME(2)$ starts at zero, 720s is added to it in the equation for the swelling strain rate or $EXPDATA$; this is because at time zero, $EXPDATA$, becomes infinite, and in order to avoid this, it is assumed that the calculations starts from 720s or 0.2 hr. To compensate for the swelling in the first 720s an initial strain rate is defined.

Figure 3.20 shows a clear outline of the equations and the subroutines used for the Abaqus model of complete swelling model.

```

C
C
SUBROUTINE USDFLD(FIELD,STATEV,PNEWDT,DIRECT,T,CELENT,
1 TIME,DTIME,CMNAME,ORNAME,NFIELD,NSTATV,NOEL,NPT,LAYER,
2 KSPT,KSTEP,KINC,NDI,NSHR,COORD,JMAC,JMATYP,MATLAYO,
3 LACCFLA)

INCLUDE 'ABA.PARAM.INC'

CHARACTER*80 CMNAME,ORNAME
CHARACTER*3 FLGRAY(15)
DIMENSION FIELD(NFIELD),STATEV(NSTATV),DIRECT(3,3),
1 T(3,3),TIME(2)
DIMENSION ARRAY(15),JARRAY(15),JMAC(*),JMATYP(*),
1 COORD(*)

REAL*8 SXX,SYY,SZZ

C----- Value of current stress taken from the simulation
CALL GETVRM('S',ARRAY,JARRAY,FLGRAY,JRCD,JMAC,JMATYP,
1 MATLAYO,LACCFLA)

SXX = ARRAY(1)
SYY = ARRAY(2)
SZZ = ARRAY(3)

STATEV(1) = SXX
STATEV(2) = SYY
STATEV(3) = SZZ

RETURN
END

C
C
SUBROUTINE UEXPAN(EXPAN,DEXPANDT,TEMP,TIME,DTIME,PREDEF,
1 DPRED,STATEV,CMNAME,NSTATV,NOEL)

INCLUDE 'ABA.PARAM.INC'

CHARACTER*80 CMNAME

DIMENSION EXPAN(*),DEXPANDT(*),TEMP(2),TIME(2),PREDEF(*),
1 DPRED(*),STATEV(NSTATV)

REAL*8 A,B,C,P1,P2 ! User defined constants
REAL *8 Nu,E-2, e-0_dot ,TR,Sig-R ! Material Properties
INTEGER n-2 ! Creep exponent
REAL *8 S-11,S-22,S-33,Sig-e ! Deviatoric and equivalent stresses
REAL *8 Sig11_dot , Sig22_dot ,Sig33_dot ! Stress rates
REAL *8 EXPDATA ! Experimental swelling strain rate
REAL *8 e-crp-1 ,e-crp-2 ,e-crp-3 ! Creep strain rate
REAL *8 e-dot-s ! The swelling strain rate

```

```

C----- Defining the user defined constants and Material properties
A = 4.053
B = 0.405
C = 23.43
P1 = 0.0028936
P2 = 12.729
Nu = 0.270
E_2 = 90400.0
e_0_dot = 2.2
n_2 = 3
Sig_R = 25
TR = 15000

C----- Swelling for the symmetrical cube
IF (TIME(2).lt.720)THEN ! ----- Before the start of swelling
EXPAN(1)= 0.0

ELSEIF (TIME(2).eq.720)THEN ! ----- Initialisation
EXPDATA = (A*((720)/3600.0)**(B))/C
EXPAN(1) = EXPDATA

C----- Deviatoric stresses
S_11 = STATEV(1) - 1.0/3.0*(STATEV(1)+STATEV(3))
S_22 = - 1.0/3.0*(STATEV(1)+STATEV(3))
S_33 = STATEV(3) - 1.0/3.0*(STATEV(1)+STATEV(3))

STATEV(4) = S_11
STATEV(5) = S_22
STATEV(6) = S_33

STATEV(7) = 0.0 ! Sig11_dot
STATEV(8) = 0.0 ! Sig22_dot
STATEV(9) = 0.0 ! Sig33_dot

ELSE ! ----- Start of swelling

C----- Equivalent Stress
Sig_e = SQRT(1.50*(STATEV(4)*STATEV(4)+STATEV(5)*STATEV(5)+
1 STATEV(6)*STATEV(6)))

C----- Creep strain rates
e_crp_1 = 1.50*e_0_dot*(Sig_e/Sig_R)**(n_2-1)*
1 exp(-TR/TEMP(1))*(STATEV(4)/Sig_R)

e_crp_2 = 1.50*e_0_dot*(Sig_e/Sig_R)**(n_2-1)*
1 exp(-TR/TEMP(1))*(STATEV(5)/Sig_R)

e_crp_3 = 1.50*e_0_dot*(Sig_e/Sig_R)**(n_2-1)*
1 exp(-TR/TEMP(1))*(STATEV(6)/Sig_R)

C----- Experimental strain rate for swelling
EXPDATA = (A*B/3600.00*((TIME(2))/3600.0)**(B-1.0))/
1 (A*((TIME(2))/3600.0)**B+C)

C----- Swelling strain increment of the symmetric cube
C- 0.5 factor in EXPAN(1) is to take into account the fact that Abaqus calls UEXPAN
C- twice per increment for coupled temperature-displacement
EXPAN(1) = DTIME*( EXPDATA + Nu/E_2 *(STATEV(7)+STATEV(8)+STATEV(9)) -
1 1.50*e_0_dot*(Sig_e/Sig_R)**(n_2-1)*exp(-TR/TEMP(1))*(STATEV(5)/Sig_R)-
2 (1+Nu)/E_2*STATEV(8))* 0.5

```

```

C————— Current Swelling strain rate
C— 0.5 factor is to take into account the fact that Abaqus calls UEXPAN twice per
C— increment for coupled temperature–displacement
  e_dot_s = EXPAN(1)/DTIME *0.50

C————— Current value of stress rates
  Sig22_dot = (EXPDATA-e_dot_s-e_crp_2)/((1+Nu)/E_2-Nu/(1+Nu)*
1      (2*e_crp_2-e_crp_1-e_crp_3)+3*Nu/E_2)

  Sig11_dot = Sig22_dot +E_2/(1+Nu)*( e_crp_2 - e_crp_1)
  Sig33_dot = Sig22_dot +E_2/(1+Nu)*( e_crp_2 - e_crp_3)

C————— Deviatoric stresses
  S_11 = STATEV(1) - 1.0/3.0*(STATEV(1)+STATEV(3))
  S_22 = - 1.0/3.0*(STATEV(1)+STATEV(3))
  S_33 = STATEV(3) - 1.0/3.0*(STATEV(1)+STATEV(3))

C————— Storing the deviatoric and stress rates for the next increment
  STATEV(4) = S_11
  STATEV(5) = S_22
  STATEV(6) = S_33

  STATEV(7) = Sig11_dot
  STATEV(8) = Sig22_dot
  STATEV(9) = Sig33_dot

  ENDIF

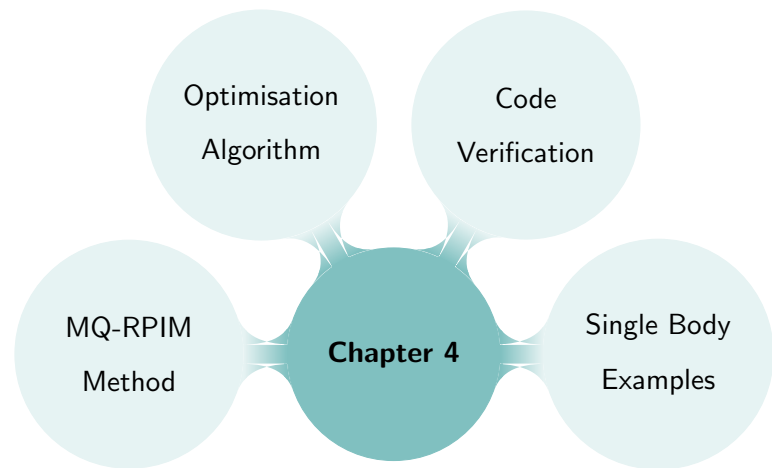
  RETURN
  END

```

Figure 3.20: The Abaqus USDFLD and UEXPAN subroutines written for the complete swelling strain rate model of the freely expanding cube.

In the above figure the way to exchange variables between USDFLD and UEXPAN is through the state variables, STATEV. In order to define how many state variables are used, the “Depvar” option needs to be defined in the Abaqus material property.

4



MQ-RPIM Optimisation for Engineering Single Body Problems

4.1 Introduction

While the Finite element method (FEM) is a well known and well-developed concept that is being used in many modelling applications, its high dependency on quality meshing makes it difficult to accurately and efficiently model complex geometries such as woven composites. For example, Bacarreza *et al.*, [1], highlighted the issues in modelling the yarn-matrix interface of a representative volume element (RVE) of a 3D woven composite using FEM. The computation of the shape functions and relevant integrations in FEM are element based and will be affected by the distorted elements. Because of this issue meshfree methods are good alternatives to FEM for modelling complex geometries such as woven composites. As the name suggests, meshfree or meshless methods do not require meshing or elements to define the problem domain; instead, the problem domain is defined using field nodes. Use of field nodes allows for easier modelling of complex geometries, eliminates the element distortion problems and removes the inefficient remeshing issues. This is in addition to the fact that it is possible to add more field nodes to a required region easily and without the need for remeshing.

Meshfree is the name for a large collection of methods that do not require meshes for the numerical calculations. One of the most popular meshfree methods is radial point interpolation method or RPIM. This method was first introduced by Liu *et al.*, [2], where the radial basis functions were used for the shape function calculations instead of moving least square, which was used in element-free Galerkin (EFG). The advantages of RPIM over EFG are that i) the essential boundary conditions

can be applied exactly, ii) accurate results can still be achieved by non-uniform distribution of the field nodes, and iii) RPIM is easily implemented in two- and three- dimensional problems. RPIM requires background cells for integration purposes, however, it still has the advantages of meshfree methods in modelling complex geometries and addition of extra nodes at the desired location in the problem domain. In RPIM the shape functions are computed during the main calculations, which may reduce the overall computational speed for simple geometries compared to FEM but at the same time convergence can be obtained with much less field nodes which can lead to less computation time at the end; this quality of RPIM will be discussed in this chapter. These advantages of the RPIM method make it one the most popular meshfree methods used in the literature, and the method used in this project for modelling woven composites.

In spite of all the advantages, one of the problems with RPIM method is that the shape parameters involved in the shape function calculations strongly affect the accuracy of the results, therefore, it is important to choose them sensibly. Multi-quadric radial point interpolation method (MQ-RPIM) is one of the RPIM methods which is used in this project; MQ-RPIM has two shape parameters in its definition which makes choosing them more difficult. There are ad-hoc approaches in the literature for choosing these parameters for some given conditions, which means that most likely sub-optimum or inefficient choices are being made, and they are not applicable to all problems; this will be discussed later in the literature review. Therefore, there is not a general optimisation procedure for these parameters that applies to all problems. This chapter is aimed at developing a detailed step-by-step procedure to making the optimum choice of MQ-RPIM shape parameters for single body problems and small displacement applications, which later in the next chapter is also applied to a frictionless Hertzian contact problem.

In the rest of this chapter, first a literature review is given on the meshfree methods and the optimisation work carried out on the MQ-RPIM method, so the objective for this chapter can be placed in relation to the work of others. In order for the reader to understand the objective of this chapter, it is required to know about the MQ-RPIM method, therefore, the MQ-RPIM method is presented after the objective section with a description of the algorithm that is introduced in this work. Following the theory on the MQ-RPIM, the results of applying the introduced algorithm to three solid mechanics examples are shown and discussed. At the end a summary of the findings and concluding points are given.

4.1.1 Literature Review

The idea of meshfree methods has been around since 1977, when Gingold *et al.* [3] introduced the smoothed particle hydrodynamics method to find the analytical relation between the physical vari-

ables and a known distribution of fluid particles in the field of astronomy. Later in 1992, Nayroles *et al.*, [4], introduced the diffuse element method where instead of elements, the Galerkin equations were determined using a distribution of nodes in the problem domain with a set of defined boundary conditions. The interpolation of the field variables in this method was carried out using polynomials fitted to the data from the field nodes via the least-squares approximation. The idea of moving least squares, itself, as interpolants was previously introduced and studied by McLain in 1971 [5], Barnhill in 1977 [6], Gordon and Wixom in 1978 [7] and Lancaster *et al.* in 1981 [8].

Meshfree methods are a vast field with a wide range of different approaches, most of which fall under one of the following categories: i) global weak-form, ii) local weak-form and iii) collocation method [9–11]. For example, collocation method uses the strong-form of partial differential equations, which is simple and computationally efficient, however, because of its instability and low accuracy, is not a suitable method for solid mechanics applications with natural or Neumann boundary conditions [12]. Weak-form methods, on the other hand, are known to be robust with high accuracy. However, because of their need for numerical integration they can be computationally expensive. Global weak-form is based on the Galerkin weak-form, [13], defined over the whole problem domain which requires background cells for its numerical integration, as a result, it is not truly meshfree. Local weak-form, on the other hand, is truly meshfree and follows the meshless local Petrov-Galerkin method [14]. This method carries out the integrations over a local quadrature domain for the field node, which is very demanding and the system matrix is usually non-symmetric [15]. Therefore, global weak-form method, which is stable, reasonably accurate and gives a good control over the measure of errors, is the method used in this project.

The most common form of global weak-form method is the element-free Galerkin method or EFG, which was first introduced by Belytschko *et al.* [13]. EFG uses a combination of moving least squares interpolants and background cells to solve the Galerkin equations for the problem domain. EFG is popular because it is easy to implement, there is no more volume locking, there is a faster convergence rate compared to FE, and high resolutions can be achieved for the localised sharp gradients. In spite of all the advantages, EFG shape functions are not unity at the field nodes, which makes it difficult to apply the essential boundary conditions. Therefore, to overcome the unity problem, a number of different methods for shape function calculations were introduced, which includes methods such as moving Kriging, [16], point interpolation method (PIM), [17, 18], and radial point interpolation method (RPIM) [2, 19–21] .

Moving Kriging is a modified version of the moving least squares which produces unity shape functions at the field nodes. PIM method, which was first introduced by Liu *et al.* [17] for stress

analysis of 2D solids, uses polynomial interpolants to compute the displacements and stresses at a given point in the problem domain with delta function property at the field nodes. In spite of the unity property at the field nodes, the PIM matrices can be singular for some situations, therefore, RPIM, which uses the radial base function for the shape function calculations, was introduced as a solution to the singularity problem. In addition to solving the singularity issues, RPIM has stable functions which makes it suitable for irregular node distributions and easily transferable from two- to three-dimensional problems. This is why it is a suitable method in development of a model for the woven composite unit cell. RPIM shape functions can be more computationally expensive than the PIM ones but with the right choice of parameters, both accuracy and efficiency of the RPIM method can be increased.

Convergence and optimum shape parameters of the meshfree methods have been a subject of study for a lot of researchers. The RPIM method requires background cells and Gauss quadrature points in order to carry out the integration, which is believed to lead to errors when the background cells do not coincide with the shape function supports. One of the key issues in the Galerkin weak-form method is the choice of a suitable quadrature scheme for the domain integration because not only can the domain integration affect the accuracy of the solution and its convergence rate but also the presence of instability can change as the choice of quadrature schemes changes [22]. Several algorithms have been suggested to improve these misalignment errors; for example, building cells which align with the compact supports in the domain improves the accuracy due to integration significantly, [23], or a tree-based cover construction method which increases the efficiency, [24], or building a support integration method which is similar to the truly meshfree cases but much faster because only two or three quadrature points are required [25].

There also have been a few methods introduced to achieve the optimum convergence rates; for example, a nodal integration method based on addition of the square of residuals of the equilibrium equation to the potential energy functional, [26], or an iterative correction method of nodal integration together with the least square stabilisation, [27], or a strain-smoothing stabilisation method, [28], and many more [23, 29–31].

RPIM methods use a combination of radial basis functions and polynomial terms for the shape function calculations. There are different definitions used for the radial basis functions in the RPIM method; some of these definitions include multi-quadric (MQ), inverse multi-quadric (IMQ), Gaussian (EXP), thin plate spline (TPS) and logarithmic. The most common definitions used are MQ, IMQ and EXP which have shape parameters included in their formulation, affecting their performance. Therefore, to have an accurate solution, it is important to choose the right values for these shape

parameters.

According to the work of Franke [32] who compared a large number of interpolant algorithms, Hardy's multi-quadrics method, [33], gives the most accurate results which has a general form of $(r^2 + (\alpha_c d_c)^2)^q$. Accuracy of the MQ method is strongly influenced by the shape parameters, which in this case are $\alpha_c d_c$ and q , therefore, defining the right values of $\alpha_c d_c$ and q is an important research topic. For example, if q is fixed at 0.5, as $\alpha_c d_c$ increases the accuracy increases, but up to a point above which the accuracy becomes worse [34].

In 2011 Boyd *et al.*, [35], carried out an examination of the condition number for the interpolation matrix of different RBF methods on uniform grids which was the basis of the later work by Zhang *et al.* [34]. [34] introduced an effective condition number depending on both the \mathbf{A} matrix and \mathbf{b} vector in an equation $\mathbf{Ax}=\mathbf{b}$. According to their work, the effective condition number only depends on α_c and total number of field nodes, i.e. N_{FN} , where the effect of α_c is stronger than N_{FN} . It was shown that the optimum shape parameter corresponds to the early stage oscillations of the condition number, therefore, for a finite precision, the upper limit of the condition number and so an optimum shape parameter can be determined. While their method finds the optimum α_c based on condition number, it does not show any relationship between those values and the accuracy of any real problems.

Most of the optimisation work on the MQ shape parameters in the literature focuses on finding the optimum value of $\alpha_c d_c$ when q is fixed at 0.5 or -0.5 because in a lot of the literature, MQ, method is known as when $q = 0.5$ and IMQ when $q = -0.5$. There have been a number of strategies and numerical suggestion for what these shape parameters should be [11, 36–44]; for example Hardy in 1977 [45] suggested $\alpha_c d_c = 0.815d$ where d is the grid spacing of the nodes, or Franke [46] used $\alpha_c d_c = 1.25D/\sqrt{N_{\text{FN}}}$ where D is the diameter of the supporting domain around the point of interest, or Fasshauer [47], who suggested a multilevel Newton iteration with $\alpha_c d_c = 2/\sqrt{N_{\text{FN}}}$. Mongillo [48] in his work on choosing shape parameters for the RBF methods showed that the most accurate results are obtained for small values of $\frac{1}{\alpha_c d_c}$, however, at the same time instability may be reached. This conflict between the accuracy and stability is referred to as the trade-off principle. The strategy they used is minimisation of the predictor function which represents the interpolation error. While all of these approaches offer an optimisation of the MQ-RBF shape parameter, they have not been tested for applicational problems and are only for the cases when $q = 0.5$ or -0.5 .

Xiang *et al.* [49] proposed a trigonometric variable shape parameter and exponent strategy for generalised MQ functions, when q can take any value, however, it is not tested in the context of applicational problems where the problem is ill-defined. Chenoweth *et al.* [50] carried out a number of numerical experiments on the general MQ method in order to understand its optimisation process.

They concluded that for an optimum choice of shape parameter the condition number of the matrix has to be in a critical range of 10^{15} to 10^{17} .

G.R. Liu in his work on Local RPIM method, [2], investigated the effect of $\alpha_c d_c$ and q on the accuracy of the general MQ-RBF shape functions when used in modelling free vibration problems of a two-dimensional beam, showing that the effect of q on the accuracy is higher than effect of $\alpha_c d_c$. For the examples that they used in their work, it was shown that the best options are $q = 1.03$ and $\alpha_c = 1.0$. They also investigated the effect of the size of local support domain, α_s on the accuracy which led to the conclusion that a too small support domain (<0.5) is unacceptable because it becomes more similar to the strong form formulation which is less accurate than the weak integral form. But also a too large support domain can lead to a computationally expensive simulation without much accuracy to gain, therefore, they recommended an economic choice of $\alpha_s = 2.0$.

In 2002 Wang *et al.* [20] carried out an optimisation study on the general MQ-RBF shape parameters, i.e. α_c and q in the context of two two-dimensional solid mechanic examples; a cantilever beam and a circular hole in the plate. In these studies no polynomial terms were added to the shape function calculations. It was found that condition number of the matrices involved, which is heavily affected by the shape parameters, has a significant influence on the accuracy of the interpolation. It was shown while the condition number increases with increasing $\alpha_c d_c$, the accuracy of the results becomes high and independent of $\alpha_c d_c$ when q is near 1.0, whereas, when $q = 0.5$, the accuracy becomes very sensitive to $\alpha_c d_c$. $q = 1.0$ is not a viable choice because the matrix becomes singular at this value. Therefore, the optimum choice of shape parameters independent of node density, node distribution and problem was suggested to be $q = 1.03$ and $\alpha_c d_c = 1.42$. It was also stated that addition of the linear polynomial terms to the shape function calculations increases the accuracy significantly.

Later in 2005 Liu *et al.* [21] introduced the three-dimensional version of the RPIM method where a brief sensitivity study on the MQ-RBF shape parameters was also carried out on the examples of cantilever beam and axletree base. It was found that for the three dimensional models of the mentioned examples, the best results is obtained when q is between 1.0 and 3.0 while α_c and α_s are fixed. It was concluded that the RBF shape functions have a good convergence, while $q = 1.03$ and $\alpha_c = 4.0$ are a robust choice.

These two papers, i.e. [20, 21] form the starting point for this chapter because while they suggest a general optimum value for the MQ-RBF shape parameters and size of the support domain, these values are not applicable to all different solid mechanic problems; this was also stated by Chenoweth *et al.* [50] when they disproved the previous claims of one optimum q for all problems because the

choice of q is problem dependent.

4.1.2 Objective

Most of the work in the literature have focused on finding the best values for a subset of the variables involved in the RPIM method (e.g. quadrature point, α_c while $q = 0.5$ and etc.), or are mainly centred around the RPIM method itself, not its application to engineering problems. Therefore, in this chapter the objective is finding a systematic algorithm that is applicable to any given application or engineering problem while considering all the parameters involved in the RPIM method, i.e. number of field nodes, background cell, quadrature points, support domain size, q , and α_c . Given all of these parameters, a step-by-step algorithm is introduced for finding both the converged solution and optimum values of MQ-RPIM shape parameters for any given application. In order to demonstrate, the introduced algorithm has been applied to three solid mechanics examples in both two- and three-dimensional forms with the optimum values of q and α_c tabulated for each case. Additionally, the algorithm from this chapter is used in the next chapter when modelling frictionless contact with RPIM method.

4.2 Materials and Method

4.2.1 Radial Point Interpolation Method

This section describes the theory behind radial point interpolation method and the work that has gone into its improvement, taken from [15]. Consider an arbitrary problem domain Ω bounded by Γ , as shown in Figure 4.1.

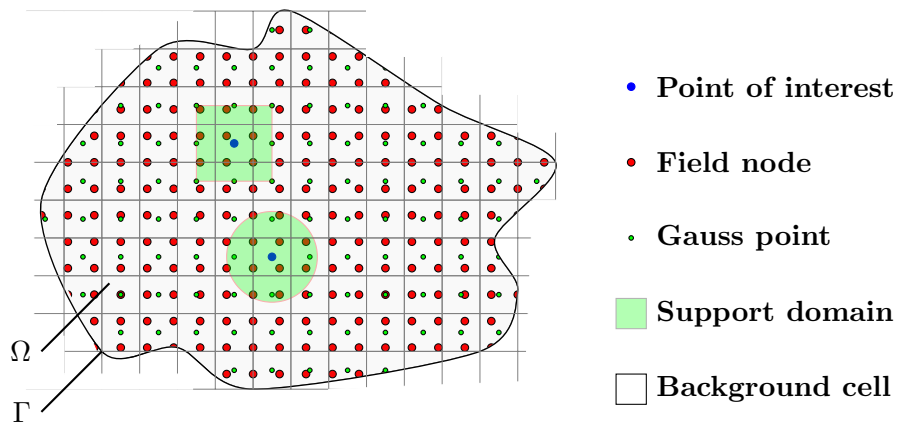


Figure 4.1: Demonstration of the support domain around the point of interest in the problem domain, Ω , bounded by Γ .

The field properties of this domain such as stress and displacement are described with the following differential equation and the boundary conditions:

- Equilibrium equation:

$$\mathbf{L}^T \boldsymbol{\sigma} + \mathbf{F}^b = 0 \quad \text{in } \Omega, \quad (4.1)$$

- Natural boundary condition

$$\boldsymbol{\sigma} \mathbf{n} = \bar{\mathbf{t}} \quad \text{in } \Gamma_t, \quad (4.2)$$

- Essential boundary condition

$$\mathbf{u} = \bar{\mathbf{u}} \quad \text{in } \Gamma_u, \quad (4.3)$$

where \mathbf{n} is the normal vector to the surface, and \mathbf{F}^b , $\bar{\mathbf{t}}$ and $\bar{\mathbf{u}}$ are the body force vector, prescribed surface traction on traction boundaries and applied displacement on displacement boundaries, respectively. \mathbf{L} is the differential operator

$$\mathbf{L}_{(2D)} = \begin{bmatrix} \frac{\partial}{\partial x} & 0 \\ 0 & \frac{\partial}{\partial y} \\ \frac{\partial}{\partial y} & \frac{\partial}{\partial x} \end{bmatrix}, \quad \mathbf{L}_{(3D)} = \begin{bmatrix} \frac{\partial}{\partial x} & 0 & 0 \\ 0 & \frac{\partial}{\partial y} & 0 \\ 0 & 0 & \frac{\partial}{\partial z} \\ 0 & \frac{\partial}{\partial z} & \frac{\partial}{\partial y} \\ \frac{\partial}{\partial z} & 0 & \frac{\partial}{\partial x} \\ \frac{\partial}{\partial y} & \frac{\partial}{\partial x} & 0 \end{bmatrix}, \quad (4.4)$$

and $\boldsymbol{\sigma}$ is the Cauchy stress in Voigt notation.

$$\boldsymbol{\sigma}_{(2D)} = \begin{Bmatrix} \sigma_{xx} \\ \sigma_{yy} \\ \tau_{xy} \end{Bmatrix}, \quad \boldsymbol{\sigma}_{(3D)} = \begin{Bmatrix} \sigma_{xx} \\ \sigma_{yy} \\ \sigma_{zz} \\ \tau_{yz} \\ \tau_{zx} \\ \tau_{xy} \end{Bmatrix}, \quad (4.5)$$

To solve for the stress-strain field, the global weak-form meshfree method is used, which applies the virtual work principle to the whole problem domain, Equation 4.6. The principle of virtual work states that if a virtual displacement, $\delta \mathbf{u}$, is applied to the domain, Ω , then sum of the work done by the external forces (i.e. the last two integrals in Equation 4.6) equals the work done by internal forces (i.e. the first integral in Equation 4.6).

$$\int_{\Omega} \delta \boldsymbol{\varepsilon}^T \boldsymbol{\sigma} d\Omega - \int_{\Omega} \delta \mathbf{u}^T \mathbf{b} d\Omega - \int_{\Gamma_t} \delta \mathbf{u}^T \bar{\mathbf{t}} d\Gamma = 0$$

$$\int_{\Omega} \delta(\mathbf{Lu})^T \mathbf{D}(\mathbf{Lu}) d\Omega - \int_{\Omega} \delta \mathbf{u}^T \mathbf{b} d\Omega - \int_{\Gamma_t} \delta \mathbf{u}^T \bar{\mathbf{t}} d\Gamma = 0 \quad (4.6)$$

where \mathbf{Lu} is the strain vector, written in the Voigt notation

$$\mathbf{Lu} = \boldsymbol{\varepsilon}_{(2D)} = \begin{Bmatrix} \varepsilon_{xx} \\ \varepsilon_{yy} \\ \gamma_{xy} \end{Bmatrix}, \quad \mathbf{Lu} = \boldsymbol{\varepsilon}_{(3D)} = \begin{Bmatrix} \varepsilon_{xx} \\ \varepsilon_{yy} \\ \varepsilon_{zz} \\ \gamma_{yz} \\ \gamma_{zx} \\ \gamma_{xy} \end{Bmatrix}, \quad (4.7)$$

and \mathbf{D} is the material constant matrix. For an isotropic material

$$\mathbf{D}_{(2D)}^{\text{Plane Strain}} = \frac{E}{(1+\nu)(1-2\nu)} \begin{bmatrix} (1-\nu) & \nu & \nu \\ \nu & (1-\nu) & \nu \\ 0 & 0 & (1-2\nu)/2 \end{bmatrix} \quad (4.8)$$

$$\mathbf{D}_{(3D)} = \frac{E}{(1+\nu)(1-2\nu)} \begin{bmatrix} (1-\nu) & \nu & \nu & 0 & 0 & 0 \\ \nu & (1-\nu) & \nu & 0 & 0 & 0 \\ \nu & \nu & (1-\nu) & 0 & 0 & 0 \\ 0 & 0 & 0 & (1-2\nu)/2 & 0 & 0 \\ 0 & 0 & 0 & 0 & (1-2\nu)/2 & 0 \\ 0 & 0 & 0 & 0 & 0 & (1-2\nu)/2 \end{bmatrix} \quad (4.9)$$

4.2.1.1 Gaussian Approximation

In order to evaluate the integrals in Equation 4.6 over the problem domain, the Gaussian quadrature approximation, as shown by Equation 4.10 and Equation 4.11, is used. In this approximation the whole problem domain is divided into non-overlapping background cells, containing quadrature points (or Gauss points), Figure 4.1. These background cells are then mapped into the parent space, Figure 4.2, where the Gaussian quadrature approximation is carried out using

$$I_{P(2D)} = \int_{-1}^1 \int_{-1}^1 f(s_1, s_2) ds_1 ds_2 \approx \sum_{p=1}^{n_{gp}} \sum_{k=1}^{n_{gp}} w_p w_k f(\xi_p, \xi_k), \quad (4.10)$$

$$I_{P(3D)} = \int_{-1}^1 \int_{-1}^1 \int_{-1}^1 f(s_1, s_2, s_3) ds_1 ds_2 ds_3 \approx \sum_{p=1}^{n_{gp}} \sum_{k=1}^{n_{gp}} \sum_{h=1}^{n_{gp}} w_p w_k w_h f(\xi_p, \xi_k, \xi_h), \quad (4.11)$$

where I_P is the integral in the parent domain. Here I_P is shown for both two- and three-dimensions. $f(s_1, s_2)$ and $f(s_1, s_2, s_3)$ are the integrands as a function of parent space parameters, i.e. s_1, s_2 and

s_3 ; n_{gp} is the number of Gauss points in every background cell in every direction; ξ_p , ξ_k and ξ_h are the s_1 , s_2 and s_3 coordinates of Gauss points in the parent space, respectively; and w_p , w_k and w_h are their corresponding weight factors. Depending on n_{gp} , values of ξ_p , ξ_k , ξ_h , w_p , w_k and w_h will change, which can be found from the literature [51].

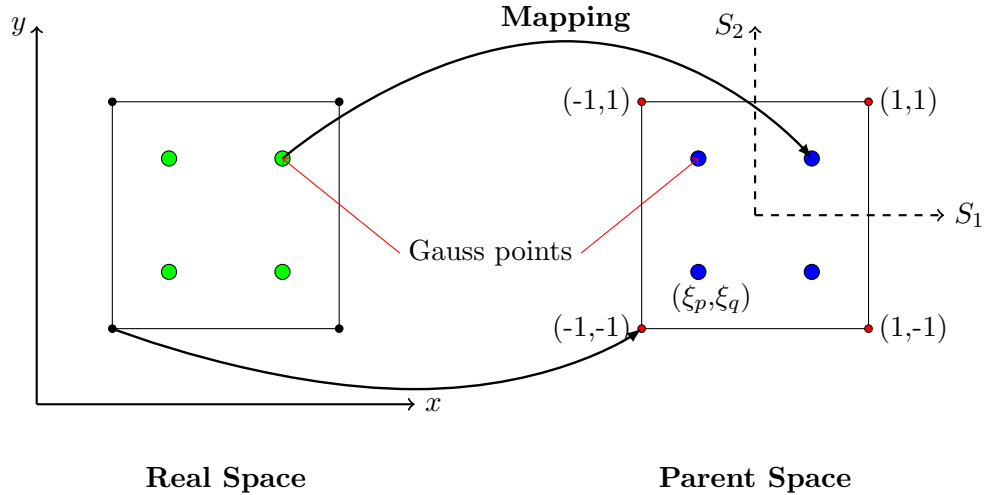


Figure 4.2: Mapping between the real (left figure) and parent (right figure) space for the Gauss points and the background cell in two-dimensions.

Once the integral in the parent domain, I_P , is computed, the result is mapped back into the real space to find the real integral, I_R using

$$I_{R(2D)} = \int_x \int_y f(x, y) dx dy = J I_{P(2D)} = \int_{s_1} \int_{s_2} f(s_1, s_2) J(s_1, s_2) ds_1 ds_2 \quad (4.12)$$

$$I_{R(3D)} = \int_x \int_y \int_z f(x, y, z) dx dy dz = J I_{P(3D)} = \int_{s_1} \int_{s_2} \int_{s_3} f(s_1, s_2, s_3) J(s_1, s_2, s_3) ds_1 ds_2 ds_3 \quad (4.13)$$

In order to map the results back into the real space, the Jacobian, J , is required. J is the determinant of the Jacobian matrix, J_{ij} , derived from the mapping between the parent and real space. J_{ij} is computed for every Gauss point as

$$J_{ij} = \frac{\partial x_i}{\partial s_j} = \frac{\partial}{\partial s_j} \left(\sum_{a=1}^M N_a X_i^a \right) = \sum_{a=1}^M N_{a,j} X_i^a, \quad (4.14)$$

where M is the total number of nodes forming the corresponding background cell; X_i^a is the value of the independent variable x at the background cell node a ; and N_a is the shape function, interpolating the independent variable x at the Gauss point using the node a of the background cell.

4.2.1.2 Radial Basis Function

In order to use the Gaussian quadrature approximation for the integrals in Equation 4.6, the displacement field, $u(\mathbf{x})$, at the Gauss point is needed. To compute $u(\mathbf{x})$ at the Gauss point, an interpolation

function (or shape function), ϕ_i , is required which is computed at n field nodes in a compact region around \mathbf{x} . Results of which is used in

$$u(\mathbf{x}) = \sum_{i=1}^n \phi_i(\mathbf{x})u_i, \quad (4.15)$$

to approximate the displacement at point \mathbf{x} , where u_i is the displacement at the i_{th} node in the compact region. Please note the shape function used for this approximation is different from the one used previously in Equation 4.14.

The compact region around \mathbf{x} is known as the support domain for that \mathbf{x} . Only the field nodes that fall in the support domain are used for the interpolation of displacement at that \mathbf{x} . The characteristic dimension of this domain is d_s , which is defined as

$$d_s = \alpha_s d_c, \quad (4.16)$$

where α_s is a dimensionless coefficient for defining the size of the support domain, and d_c is a characteristic length proportional to the nodal spacing near the point of interest. Liu *et al.*, [15, 25], recommended α_s to be $\sim 2.0 - 3.0$ for a good result. Support domains can have any shape but the most commonly used shapes are rectangle (or cuboid in 3D) and circle (or sphere in 3D), Figure 4.1. In meshfree methods, unlike finite element methods, there is no restriction on the overlap of support domains. Therefore, it is possible for \mathbf{x} values close to each other have overlapping support domains which leads to a smoother stress calculations compared to FEM.

There are a number of meshfree methods used for computing the shape function in Equation 4.15 such as moving least square, [5–8, 13], moving Kriging, [16], polynomial basis, [17], and radial basis, [2, 18, 20]. Radial basis function is the chosen method for the shape function calculations in this study because RBF shape functions are positive definite, stable and flexible for arbitrary nodal distribution. These functions also have the delta function property, which makes the application of essential boundary conditions much easier. In radial point interpolation method a combination of radial and polynomial basis functions are used for the shape function calculations which changes Equation 4.15 to

$$u(\mathbf{x}) = \sum_{i=1}^n R_i(\mathbf{x})a_i + \sum_{j=1}^m p_j(\mathbf{x})b_j, \quad (4.17)$$

where $R_i(\mathbf{x})$ is the radial basis matrix and $p_j(\mathbf{x})$ is the monomial in the space coordinate $\mathbf{x}^T = [x, y, z]$, m is the number of polynomial basis function, and a_i and b_j are constants to be found.

Within radial basis function there are a number of different methods used for computing $R_i(\mathbf{x})$ such as i) multi-quadrics (MQ), ii) inverse multi-quadrics (IMQ) iii) Gaussian (EXP), iv) Thin plate

spline (TPS) and v) Logarithmic. The main variable used in all the radial basis function methods is $r_i = \sqrt{(x - x_i)^2 + (y - y_i)^2 + (z - z_i)^2}$, which is real-valued and based on the distance between the point of interested and the field nodes in the support domain. MQ and IMQ are the chosen methods for this study because it is shown to be one of the most accurate methods when compared to other interpolation algorithms [32, 34]. General MQ has the form of

$$R_i(x, y) = (r_i^2 + (\alpha_c d_c)^2)^q, \quad (4.18)$$

where q and α_c are the shape parameters for this method. In MQ method q is positive and in IMQ method q is negative. To find a_i and b_i in Equation 4.17, $u(\mathbf{x})$ is forced to satisfy the n field nodes in the support domain, leading to the following linear equation

$$\mathbf{U}_s = \mathbf{R}_0 \mathbf{a} + \mathbf{P}_m \mathbf{c}, \quad (4.19)$$

where \mathbf{U}_s is the displacement vector, \mathbf{R}_0 is the moment matrixes of radial basis functions for the n field nodes in the support domain,

$$\mathbf{R}_0 = \begin{bmatrix} R_1(r_1) & R_2(r_1) & \dots & R_n(r_1) \\ R_1(r_2) & R_2(r_2) & \dots & R_n(r_2) \\ \dots & \dots & \dots & \dots \\ R_1(r_n) & R_2(r_n) & \dots & R_n(r_n) \end{bmatrix}_{n \times n}, \quad (4.20)$$

and \mathbf{P}_m is the polynomial moment matrix of m polynomial basis,

$$\mathbf{P}_m^T = \begin{bmatrix} 1 & 1 & \dots & 1 \\ x_1 & x_2 & \dots & x_n \\ y_1 & y_2 & \dots & y_n \\ \dots & \dots & \dots & \dots \\ p_m(\mathbf{x}_1) & p_m(\mathbf{x}_2) & \dots & p_m(\mathbf{x}_n) \end{bmatrix}_{m \times n} \quad (4.21)$$

While \mathbf{R}_0 is for n variables, the linear Equation 4.19 is for $n+m$ variables, therefore, the constraints

$$\sum_{i=1}^n p_j(\mathbf{x}_i) a_i = 0 \quad j = 1, 2, \dots, m, \quad (4.22)$$

are added to include the additional m equations. Addition of the m constraint equations changes Equation 4.19 to

$$\tilde{\mathbf{U}}_s = \begin{bmatrix} \mathbf{U}_s \\ \mathbf{0} \end{bmatrix} = \underbrace{\begin{bmatrix} \mathbf{R}_0 & \mathbf{P}_m \\ \mathbf{P}_m^T & \mathbf{0} \end{bmatrix}}_{\mathbf{G}} \underbrace{\begin{Bmatrix} \mathbf{a} \\ \mathbf{c} \end{Bmatrix}}_{\mathbf{a}_0} = \mathbf{G} \mathbf{a}_0, \quad (4.23)$$

where

$$\tilde{\mathbf{U}}_s = \{u_1 \ u_2 \ \dots \ u_n \ 0 \ 0 \ \dots \ 0\}, \quad (4.24)$$

and

$$\mathbf{a}_0^T = \{a_1 \ a_2 \ \dots \ a_n \ c_1 \ c_2 \ \dots \ c_m\} \quad (4.25)$$

\mathbf{R}_0 is symmetric and therefore, \mathbf{G} becomes symmetric, which is then used to compute \mathbf{a}_0 ,

$$\mathbf{a}_0 = \mathbf{G}^{-1}\tilde{\mathbf{U}}_s, \quad (4.26)$$

and consequently $u(\mathbf{x})$ by substituting \mathbf{a}_0 back into Equation 4.17 to get

$$\begin{aligned} u(\mathbf{x}) &= \{\mathbf{R}^T(\mathbf{x}) \ \mathbf{p}^T(\mathbf{x})\} \begin{Bmatrix} \mathbf{a} \\ \mathbf{c} \end{Bmatrix} \\ &= \{\mathbf{R}^T(\mathbf{x}) \ \mathbf{p}^T(\mathbf{x})\} \mathbf{G}^{-1}\tilde{\mathbf{U}}_s \\ &= \tilde{\Phi}(\mathbf{x})\tilde{\mathbf{U}}_s \end{aligned} \quad (4.27)$$

where $\tilde{\Phi}(\mathbf{x})$ is the matrix of radial basis, RBF, shape functions including the polynomial basis.

4.2.1.3 System of Linear Equations

Having computed the displacement, $u(\mathbf{x})$, at the Gauss points using the RBF shape functions, the nodal stiffness, \mathbf{K}_{ij} , can be approximated using Gaussian integration.

$$\mathbf{K}_{ij} = \int_{\Omega} \mathbf{B}_i^T \mathbf{D} \mathbf{B}_j d\Omega \approx \sum_{i=1}^n \sum_{j=1}^n \mathbf{B}_i^T \mathbf{D} \mathbf{B}_j w_j J, \quad (4.28)$$

where, \mathbf{B} represents the first derivative of the shape function, i.e. $\mathbf{L}\Phi$; w is the corresponding Gaussian weight factor, $w_p w_k w_h$; and n is the total number of field nodes in the support domain. Using the nodal stiffness equation, the first term in Equation 4.6 can be rewritten for the global calculations as

$$\int_{\Omega} \delta(\mathbf{L}\mathbf{u})^T \mathbf{D}(\mathbf{L}\mathbf{u}) d\Omega \approx \sum_{I=1}^{N_{\text{FN}}} \sum_{J=1}^{N_{\text{FN}}} \delta \mathbf{u}_I^T \underbrace{\left(\int_{\Omega} \mathbf{B}_I^T \mathbf{D} \mathbf{B}_J d\Omega \right)}_{\mathbf{K}_{IJ}} \mathbf{u}_J = \delta \mathbf{U}^T \mathbf{K} \mathbf{U}, \quad (4.29)$$

where N_{FN} is the total number of field nodes in the problem domain and \mathbf{K}_{IJ} is the nodal stiffness of size 2×2 (3×3 for 3D). \mathbf{K}_{IJ} becomes zero if nodes I and J are not in the same support domain for the same quadrature point. \mathbf{K} in Equation 4.29 is the global stiffness matrix with a size of $2N_{\text{FN}} \times 2N_{\text{FN}}$ ($3N_{\text{FN}} \times 3N_{\text{FN}}$ for 3D) and \mathbf{U} is the global displacement vector, which has a size of $2N \times 1$ ($3N \times 1$ for 3D) and contains the nodal displacement of all the field nodes.

A similar analysis to the Global stiffness can be carried out on the body force and traction force, i.e. the second and third terms in Equation 4.6. By substitution of Equation 4.27 into the second and third terms of Equation 4.6, the following results can be obtained

$$\int_{\Omega} \delta \mathbf{u}^T \mathbf{b} \, d\Omega \approx \sum_{I=1}^{N_{\text{FN}}} \delta \mathbf{u}_I^T \left(\int_{\Omega} \Phi_I^T \mathbf{b} \, d\Omega \right) = \sum_{I=1}^{N_{\text{FN}}} \delta \mathbf{u}_I^T \mathbf{F}_I^b = \delta \mathbf{U}^T \mathbf{F}^b, \quad (4.30)$$

and

$$\int_{\Gamma_t} \delta \mathbf{u}^T \bar{\mathbf{t}} \, d\Gamma \approx \sum_{I=1}^{N_{\text{FN}}} \delta \mathbf{u}_I^T \left(\int_{\Gamma_t} \Phi_I^T \bar{\mathbf{t}} \, d\Gamma \right) = \sum_{I=1}^{N_{\text{FN}}} \delta \mathbf{u}_I^T \mathbf{F}_I^{(t)} = \delta \mathbf{U}^T \mathbf{F}^{(t)}, \quad (4.31)$$

where \mathbf{F}^b is the global body force vector and $\mathbf{F}^{(t)}$ is the traction force vector, both with a length of 2N. Substituting Equation 4.29, Equation 4.30 and Equation 4.31 into Equation 4.6 gives

$$\delta \mathbf{U}^T \mathbf{K} \mathbf{U} - \delta \mathbf{U}^T \mathbf{F}^b - \delta \mathbf{U}^T \mathbf{F}^{(t)} = 0 \quad (4.32)$$

and

$$\mathbf{K} \mathbf{U} = \underbrace{\mathbf{F}^b + \mathbf{F}^{(t)}}_{\mathbf{F}} \quad (4.33)$$

where \mathbf{F} is the global force vector. This equation is the discretised system of linear equations that can be solved numerically.

Once the system of equations is formed, the boundary conditions are applied. Natural (force) boundary conditions are applied by changing the relevant terms in the \mathbf{F} vector. The essential (displacement) boundary conditions are applied through the direct method. Penalty method can also be used for applying the essential boundary conditions but it is not used or explained here. To read more about penalty method please refer to [15]. In the direct method, the nodes for the essential boundary condition are forced to satisfy the displacement boundary condition. Therefore, the corresponding rows and columns of the global stiffness matrix are set to zero except the corresponding term on the diagonal, which is set to 1. The global force vector also changes as a result of the application of essential boundary conditions. This change occurs according to

$$F_j \Rightarrow \begin{cases} \bar{u}_i & i = j \\ F_j - K_{ji} \bar{u}_i & i \neq j \end{cases} \quad (4.34)$$

where \bar{u}_i is the applied essential boundary condition for the i^{th} term in \mathbf{U} . Once the boundary conditions are applied, Equation 4.33 is solved numerically to find \mathbf{U} . The computed \mathbf{U} is then used to compute the stress at the field nodes,

$$\sigma_l = \int_{\Omega} \mathbf{D} \mathbf{B} \mathbf{U} \, d\Omega \approx \sum_{i=1}^{n_l} \mathbf{D} \mathbf{B}_i \mathbf{U}_i, \quad (4.35)$$

where i represents the field node number and n_l is the total number of field nodes in the support domain of the l^{th} field node. At this point, unlike before, the shape functions used for \mathbf{B} are calculated for the field nodes and not the Gauss points.

4.2.2 Step-by-Step Optimisation Method

Using the theory described in the previous section, MQ-RPIM is written into a Fortran 90 code for both two- and three-dimensional problems, a description of which is given in Appendix A. An important part of any numerical method is convergence of its solution. In MQ-RPIM, there are a number of factors that affect its accuracy and convergence, such as number of field nodes, integration points, size of the support domain and MQ-RPIM shape parameters. In order to have a systematic understanding of the accuracy, speed, convergence, and optimisation of the shape parameters, a step-by-step approach is introduced here, i.e. Figure 4.3, that can be used for any problem. Please note, for convenience, from now on RPIM refers to MQ-RPIM.

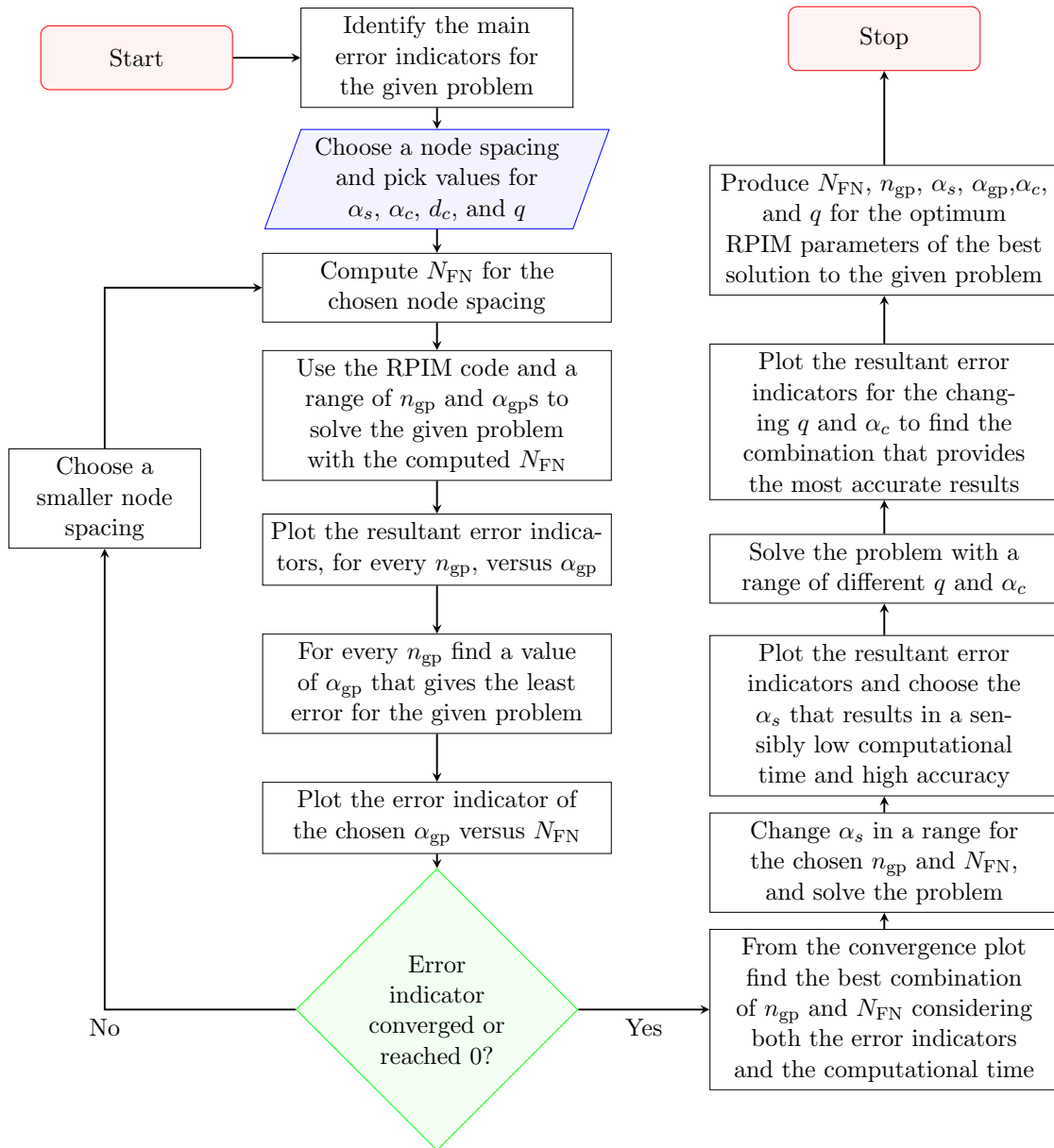


Figure 4.3: An overview of the convergence and optimisation method introduced here.

The method introduced here consists of three parts, i) identification of error indicators, ii) convergence, and iii) optimisation of the RPIM shape parameters, i.e. α_c and q from Equation 4.18. In order to carry out this step-by-step process, it is important to define variables or measures that can be used as indicators of the accuracy of the solution; these variables are called “error indicators”. Error indicators are error variables defined based on the available information, and importance of a particular solution.

Using the defined error indicators, the convergence study on a given problem is carried out where the smallest number of required field nodes and background cells for a reasonably accurate solution is found. Please note convergence can be obtained for both regular and irregular distributions of nodes, [15], however, for this chapter only a regular distribution is shown. Readers can refer to [15] or other references mentioned in this chapter for further information on a non-uniform distribution of nodes. Additionally, in this part, effect of the support domain size on the accuracy and speed of the simulation is also studied. The obtained combination of field nodes, background cells, and support domain size from the convergence part is used in the optimisation part to find the best combination of α_c and q for obtaining the minimum error. In this work, this process is carried out for three different examples in two- and three-dimensions, in order to test the introduced step-by-step optimisation method under different conditions.

4.2.2.1 Error Indicators

In any numerical calculations, the accuracy and efficiency of the method determines whether it is good for a given problem. Depending on the problem, there are different variables that can be used for error analysis and as the error indicator. For problems such as the cantilever beam, where the analytical solution is known for the whole problem domain, energy error, e_E , can be used. Energy error is an average error variable and is one of the common methods used in the literature [15, 20]. This error indicator is defined as

$$e_E = \frac{1}{V} \left[\int_{\Omega} (\varepsilon^{\text{RPIM}} - \varepsilon^{\text{Exact}})^T : (\sigma^{\text{RPIM}} - \sigma^{\text{Exact}}) d\Omega \right]^{1/2}, \quad (4.36)$$

where V is the volume of the problem domain or the area for a 2D problem. $\varepsilon^{\text{RPIM}}$ is the strain computed by the RPIM method and $\varepsilon^{\text{Exact}}$ is the exact strain value, similarly for the stress terms. The advantage of energy error is that it takes into account the accuracy of the solution for every point in the problem domain. However, it can only be used for problems where the exact value for every point of the problem domain or the domain of interest is known.

For problems where an analytical solution or experimental value is only known for a given location or as an average value, percentage error or e_x is used, which is defined as

$$e_x = \frac{(x^{\text{Exact}} - x^{\text{RPIM}}) \times 100}{x^{\text{Exact}}}, \quad (4.37)$$

where x is the chosen variable used to compute the percentage error. Energy error has an average form, therefore, for problems where solutions for a specific part of the domain is important, percentage error is used. There are other methods of error analysis such as residual error and convergence of the solution at a given point in the problem domain. Residual error is a measure of the equilibrium reached by the computed solution and is computed by substituting the computed \mathbf{U} back into the equilibrium Equation 4.1, as shown here:

$$\mathbf{Res} = \mathbf{L}^T (\mathbf{DLU}) - \mathbf{KU} \quad (4.38)$$

Here \mathbf{KU} is the same as the force vector, i.e. F , which is computed with the new U and the initial stiffness matrix, K , before application of essential boundary conditions. The smaller the norm of the residual error, $\|\mathbf{Res}\|$, the more accurate the solution. This error analysis can be done over the whole domain or on parts of it as required. The advantage of this error analysis is that there is no need for the exact solution, however, it is only valuable for parametric or optimisation studies because the solution needs to converge before using it. Please note, the explanation for the residual error is given here for completeness, however, in the following examples the energy error and the percentage error analysis are only used as the error indicators.

4.2.2.2 Convergence

In this part, α_c and q are fixed while the number of field nodes, background cells and the size of the support domain are changed to find the most accurate solution with the minimum running time. To carry out the convergence process, first the total number of field nodes, N_{FN} , and size of the support domain, α_s , are fixed, while the total number of integration points (or background cells) is varied within a given range. For each choice of integration points the relevant error indicators are computed; the choice that gives the minimum indicated error is picked and its simulation time is recorded. This process is carried out for four values of N_{FN} , in the ascending order. The minimum error and their corresponding simulation times are then plotted against the total number of field nodes which forms the convergence plot. At this point the obtained converged solution and rate of convergence are compared to FE for the same problem.

By comparing the minimum errors and their corresponding computational times in the convergence plot, the best choice of N_{FN} and number of integration points is made. In the final step of the convergence process, size of the support domain is changed and its corresponding computational time and error indicator values are computed. Taking into account both the simulation time and the error

indicator, the best support domain size is chosen.

The complexity in the convergence study of RPIM comes from the need for background cells. Keeping the number of integration points (or background cells) fixed while increasing the field nodes does not lead to a converged solution. Therefore, it is important to change the background cells accordingly. Total number of integration points is varied both by changing the number of Gauss points per background cell, and by changing the total number of background cells. According to the book by Liu *et al.* [15], on page 157, a suitable number of integration points in a two-dimensional problem domain is about $3 \sim 9$ times the number of unfixed field nodes. If this factor is called α_{gp} , then for a single dimension, a good approximation of this factor would be $\sqrt{\alpha_{gp}}$. Therefore, for a three-dimensional problem this factor can be estimated as $(\sqrt{\alpha_{gp}})^3$.

Using this guideline with the given number of integration points per background cell, i.e. n_{gp}^3 , an estimating algorithm is written for choosing the number of background cells, (Please note the power 3 for n_{gp} corresponds to the dimension of the problem; for two-dimensional problems it will be 2 and so on). For a problem domain with characteristic lengths of L_x , L_y and L_z , and filled with N_{FN} field nodes, the total number of integration points in the problem domain, N_{gp} , becomes

$$N_{gp} = n_{gp}^3 N_{BC} = \alpha_{gp}^{3/2} N_{FN}, \quad (4.39)$$

where N_{BC} is the total number of background cells computed as

$$N_{BC} = n_{BCx} \cdot n_{BCy} \cdot n_{BCz} = n_{BCx}^3 \left(1 \cdot \frac{L_y}{L_x} \cdot \frac{L_z}{L_x} \right) \quad (4.40)$$

In this equation n_{BCx} , n_{BCy} and n_{BCz} are positive integers representing the number of background cells in the x, y and z directions, respectively, where $n_{BCy} = (L_y/L_x)n_{BCx}$ and $n_{BCz} = (L_z/L_x)n_{BCx}$. By substituting Equation 4.40 into Equation 4.39 and rearranging, the number of background cells in the x-direction for a given n_{gp} is found as

$$n_{BCx} = \text{Ceil} \left[\frac{\sqrt{\alpha_{gp}}}{n_{gp}} \left(\frac{N_{FN} L_x^2}{L_y L_z} \right)^{1/3} \right] \quad (4.41)$$

For a given problem domain and N_{FN} , n_{BCx} is computed for a range of n_{gp} and α_{gp} values, using Equation 4.41; these values are $n_{gp} \in \{2, 3, 4\}$, and $\alpha_{gp} \in \{2, 3, 4, \dots, 14, 15\}$.

As an initial value for the convergence study, MQ-RBF shape parameters are fixed at $q = 1.03$, $\alpha_c = 0.71$, which were suggested by [20], however, later in the optimisation part of this chapter these values will change depending on the combination that provides the best solution. d_c which is multiplied by

α_c in Equation 4.18 is taken to be 2.0; this choice is arbitrary but the value is fixed so when it comes to optimisation process the solution is only affected by q and α_c .

4.2.2.3 Optimisation

An optimisation study is carried out to find the effect of RPIM shape parameters, α_c and q , on the accuracy of the RPIM method for different single body problems. In the optimisation process number of the field nodes, number of integration points and size of the support domain are taken from the convergence part of the study. While those parameters are fixed, values of α_c and q are changed to understand their effect on the accuracy of the results. It is called optimisation, because the purpose is to find a combination of α_c and q that gives the minimum error, and to check if it is a universal optimum. Therefore, once the optimisation process is carried out for three very different single body examples, the obtained shape parameters are compared to see if there is a universal choice.

During the optimisation process, α_c is changed between 0.25 and 2.0, and q is changed between -0.7 and 1.5. The simulations incorporating these changes run in sequence; for a given α_c , simulations run for different qs ; then α_c is changed to the next value and the simulations run for different qs with the new α_c . This process repeats until all the combinations of α_c and q are included.

The indicated error approach used in the convergence part is also used for the optimisation study. The error values obtained from simulations with different combinations of α_c and q are plotted against q for every value of α_c . The combination of α_c and q that gives the minimum error is considered as the optimum choice of the RPIM shape parameters for the corresponding problem; at the end a conclusion is drawn based on the optimum values obtained for different examples.

In addition to the RPIM shape parameters, the polynomial terms in the RPIM shape function calculations play an important role in the accuracy of the results. Therefore, for producing a complete picture of the optimisation and all the parameters that affect the RPIM accuracy, optimisation is carried out in two parts. i) no polynomial terms included in the shape function calculations and ii) linear polynomial term is added to the shape function calculations.

4.2.3 Single Body Examples

As mentioned previously, the convergence and optimisation studies are carried out for three different examples. These examples include: i) a cantilever beam, Figure 4.4, which is chosen for consistency with the literature [2, 13, 17, 19–21, 26, 28, 30]; ii) a cube under uniform compression, Figure 4.5; iii) and a cylinder under line compression, Figure 4.6. These examples are chosen because they cover a range of problems with different stress and strain distributions. The cantilever beam example tests

the RPIM code for a changing stress and displacement domain, the cube example looks at the uniform stress and strain distributions, and the cylinder example is concerned with stress concentration and circular geometry. These examples are modelled in both two- and three-dimensions so both versions of the RPIM code can be tested and verified, but also it can be shown that the step-by-step approach introduced in this chapter is applicable to both two- and three-dimensional problems.

One of the questions that can be answered at the end of this chapter is that whether, there is a universal optimum choice for α_c and q for every problem. But also one can use the optimisation results from the cube and cylinder in this chapter to compare with the optimisation results of the frictionless Hertzian contact in the next chapter to see if there is a relationship between the optimisation of individual bodies and when they are in contact.

4.2.3.1 Cantilever Beam Bending

The cantilever beam used in this study is the same as the one used in [20], as shown in Figure 4.4, which undergoes a vertical parabolic traction on the right end of the beam with the boundary conditions shown in the figure.

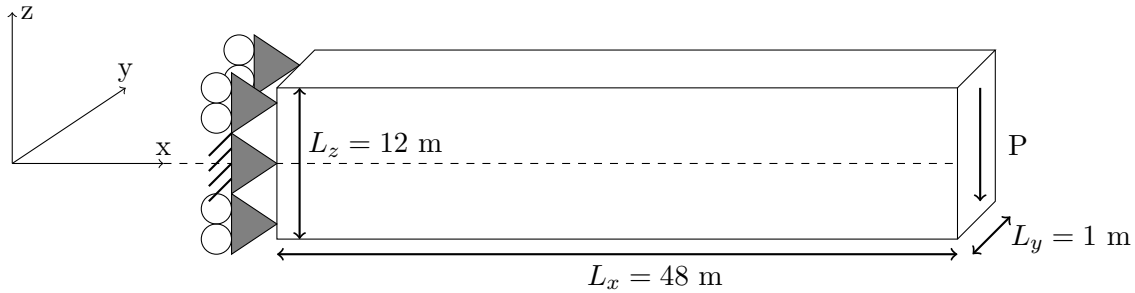


Figure 4.4: The three-dimensional cantilever beam used for verifications.

The applied traction on the right face of the beam, τ_{xz} , is given as

$$\tau_{xz} |_{x=L_x} = \frac{P}{2I} \left[\frac{L_z^2}{4} - z^2 \right] \quad (4.42)$$

where $P = -1000\text{kN}$ is the value of the applied load and I is the second moment of area; for a rectangular cross section I is equal to $\frac{L_y L_z^3}{12}$. The Young's modulus, E , of the beam is 30 GPa and its Poisson's ratio, ν , is 0.3. The analytical solution for the x and z displacements of the beam are given as

$$u(x, z) = -\frac{Pz}{6EI} \left[(6L_x - 3x)x + (2 + \nu) \left(z^2 - \frac{L_z^2}{4} \right) \right] \quad (4.43)$$

and

$$w(x, z) = \frac{P}{6EI} \left[3\nu z^2 (L_x - x) + (4 + 5\nu) \frac{L_z^2 x}{4} + (3L_x - x)x^2 \right] \quad (4.44)$$

The corresponding stresses for these displacements are

$$\sigma_{xx} = -\frac{P(L_x - x)z}{I}, \quad (4.45)$$

$$\sigma_{zz} = \sigma_{yy} = 0, \quad (4.46)$$

where the shear stress in the xz direction is the same as τ_{xz} in Equation 4.42, and for yz and yx directions is taken to be zero. Please note, the analytical solutions used for the two- and three-dimensional versions of the beam example are the same. For the error analysis of this example, energy error is used as the first error indicator because both stress and deflection are known for the whole problem domain. Additionally, the maximum percentage error in the shear stress across the thickness at the mid-length of the beam, and the maximum percentage error in the computed deflection of the beam are used as the other two error indicators for this problem.

4.2.3.2 Uniform Compression on a Cube

This example is one of the simplest problems to solve. For a cube of size $L = 10\mu\text{m}$ and a uniform applied compressive strain of $\varepsilon_{zz} = -0.1$, the stress in the z direction becomes $\sigma_{zz} = E \varepsilon_{zz}$, while the other faces are free to deform, i.e. $\sigma_{xx} = \sigma_{yy} = 0$. Using the Young's modulus of 207GPa, the analytical value of σ_{zz} throughout the cube becomes -2070MPa. The boundary condition of the two- and three-dimensional versions of this example are shown in Figure 4.5.

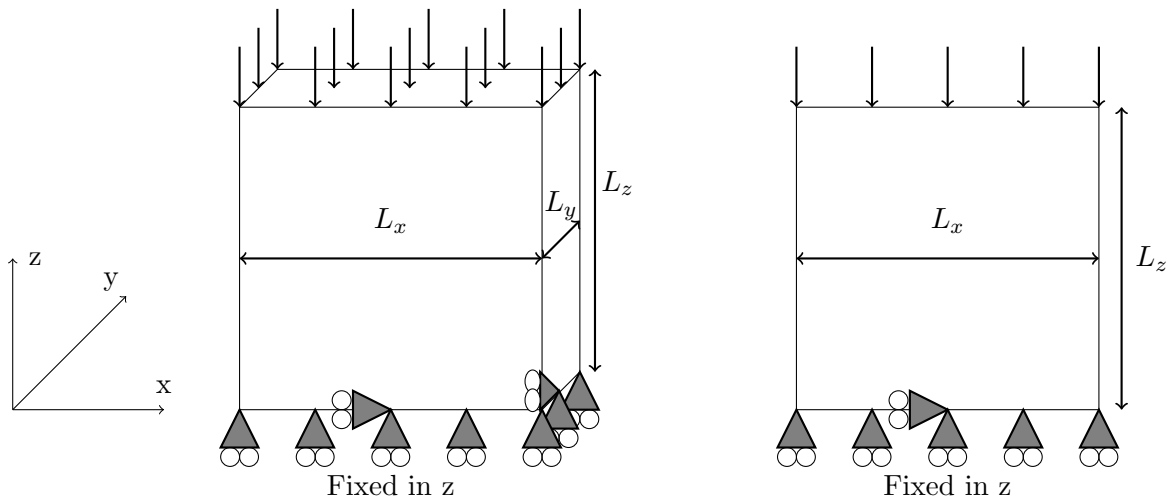


Figure 4.5: The boundary conditions for the two- and three-dimensional examples of the cube.

For the convergence and optimisation studies of the two- and three-dimensional RPIM models of the cube, energy error, maximum percentage error in σ_{zz} , and maximum percentage error in the vertical displacement, u_z , are used as error indicators for this problem.

4.2.3.3 Line Compression on a Cylinder

This is an example of a cylinder with radius R placed under a uniform compressive line force in the three-dimensional case or a point compressive force on the two-dimensional case. The force is applied while the cylinder is fixed in the y -direction at one point on the bottom surface, Figure 4.6, and is fixed in the x -direction at the centre and bottom to prevent rotation and rigid body motion. Here $R = 20\text{m}$ and $L_z = 10\text{m}$ with an applied load of $P = -5000\text{N/m}$ where the Young's Modulus and Poisson ratio are 207GPa and 0.3 , respectively.

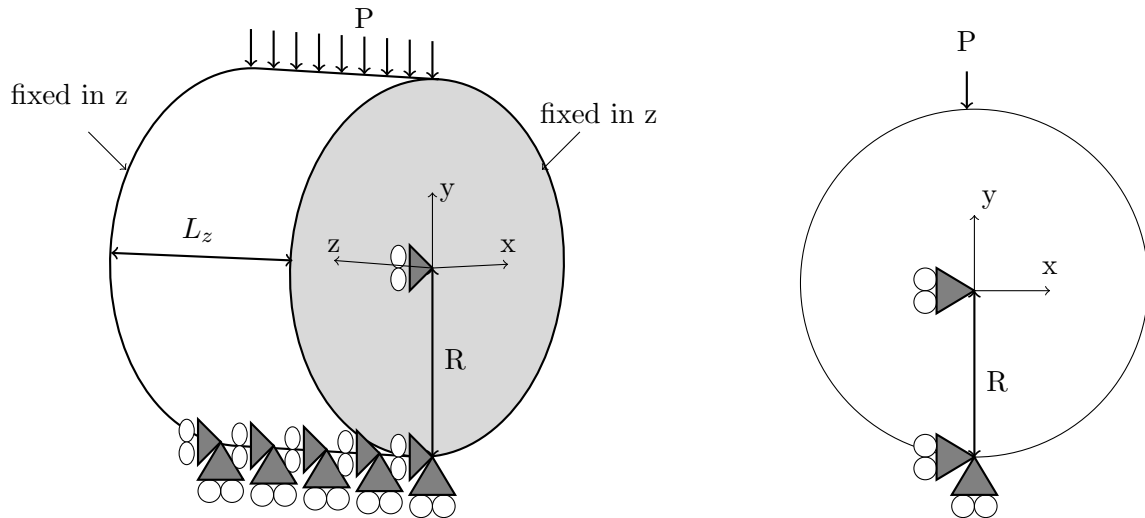


Figure 4.6: The boundary conditions for the two- and three-dimensional examples of the cylinder.

There is no analytical solution available for this example, therefore, in order to define suitable error indicators, the theoretical reaction force, the difference between the top and bottom forces, and a finite element model are used. The first error indicator is the percentage error of the computed reaction force on the bottom of the cylinder using the resultant stresses from the RPIM code, i.e. $F_R = \sum^{n_R} \sigma_{yy}(x)^{(n_R)} \Delta x(x)$. Here n_R is the number of nodes on the bottom surface of the cylinder used to compute the reaction force, $\sigma_{yy}^{(n_R)}$ is the vertical stress of the node n_R , and $\Delta x(x)$ is the x -spacing between the nodes which changes with the location along the surface; for the three dimensional case this spacing becomes an area of $\Delta x(x)\Delta z$. Theoretically the magnitude of the reaction force has to equal to the applied load, i.e. 5000N .

The second error indicator is the percentage difference between the computed force on the top and bottom surface of the cylinder using the resultant stresses from the RPIM code. The difference between the first and second error indicators is that in the first one the reaction force is checked against the theoretical value of the reaction force, whereas, in the second one the difference between the computed forces on the top and bottom of the cylinder are considered as a measure of equilibrium. For the final error indicator, the vertical stress value, σ_{yy} , at the centre of the cylinder computed by the RPIM model is compared to the solution from a finite element model created in Abaqus 6.14. For

the three-dimensional model of the cylinder, average values of the error indicators across the length of the cylinder are used.

4.3 Results & Discussion

In this section, the results obtained from the two- and three-dimensional RPIM codes for the three examples, are presented and discussed. For each example, first the process and results of the convergence study are discussed, then the approach in finding the optimum RPIM shape parameter is shown.

4.3.1 Verification - Cantilever Beam

In the convergence part of this example, first effect of the number of integration points, background cells and field nodes on error indicators are shown; then the results from the RPIM code is compared to the FE results (Using Abaqus) in terms of accuracy, computation time and convergence. Once the best combination of integration points, background cells and field nodes is found, effect of the support domain size on the accuracy and computation time of the RPIM method is shown. Finally, in the optimisation part, variation of the energy error and percentage errors with α_c and q are shown.

4.3.1.1 Convergence

Results of the convergence study is presented in a few steps for both two- and three-dimensional versions of the beam example. In the first step, effect of the number integration points on the energy error, e_E , for a given N_{FN} is shown, Figure 4.7 & Figure 4.8. In these figures α_{gp} from Equation 4.41 is used as the representative of the total number of integration points. In addition to the effect of α_{gp} , effect of integration point distribution per background cell is also shown in Figure 4.7 & Figure 4.8 by changing n_{gp} . In this step, for every combination of N_{FN} and n_{gp} , the value of α_{gp} that gives the lowest error is chosen. This step is named “background cell finder” because in this step the best choice of background cells and distribution of integration points per cell can be found for a given number of field nodes.

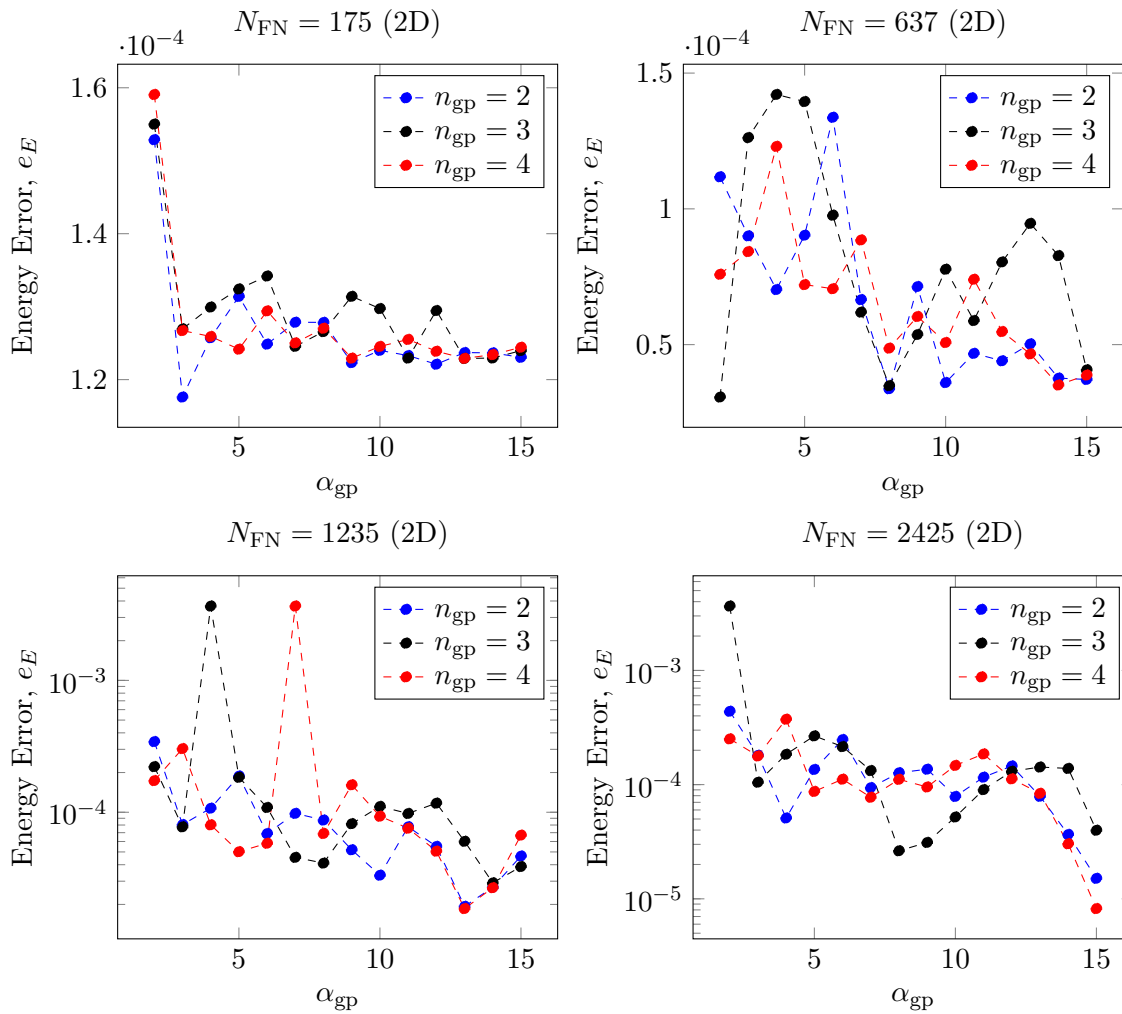


Figure 4.7: In each plot the computed energy error from the results of the RPIM code for the two-dimensional version of the beam is shown versus the α_{gp} factor from Equation 4.41. These plots show how increasing N_{FN} and changing the distribution of integration points per background cell, i.e. n_{gp} , affect the energy error. For these calculations $\alpha_s = 3.0$, $\alpha_c = 0.71$ and $q = 1.03$.

The plots in Figure 4.7, show change of the energy error for the two-dimensional beam as a result of changing α_{gp} for a given number of N_{FN} and n_{gp} . As can be seen in these plots, there is a clear fluctuation in the energy error with changing α_{gp} , which seems to become stronger with increasing the number of field nodes in the problem domain. For a fixed number of field nodes and support domain size, increasing the number of integration points affects the relative position of those points to the field nodes which in turn affects the RPIM shape functions. This can be a reason behind these fluctuations; as [23] have shown in their work, when the background cells do not coincide with the shape function supports, using the Gauss quadrature rules leads to integration errors. Finding the exact influence of this relative position is not the main focus and is not investigated here.

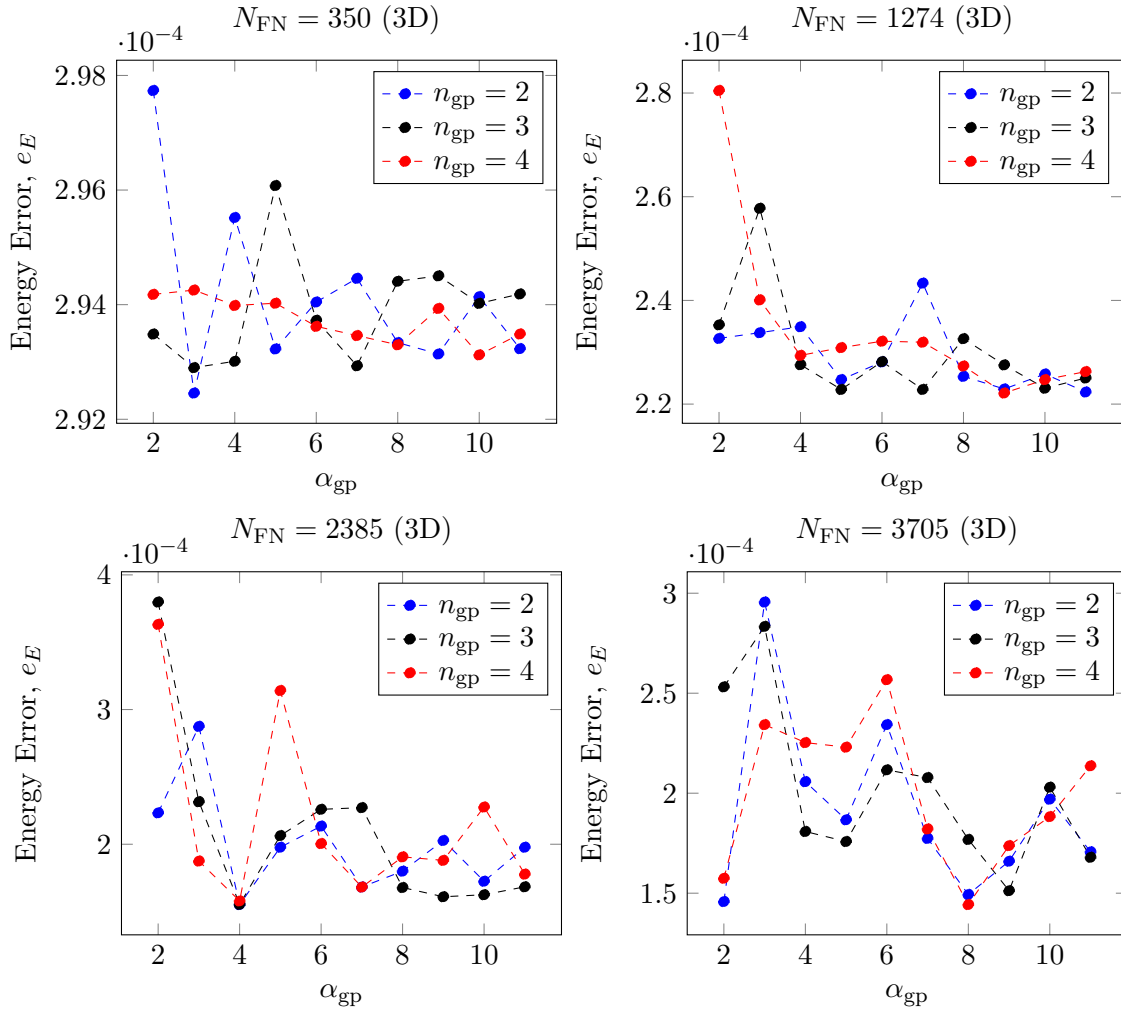


Figure 4.8: In each plot the computed energy error from the results of the RPIM code for the three-dimensional version of the beam is shown versus the α_{gp} factor from Equation 4.41. These plots show how increasing N_{FN} and changing the distribution of integration points per background cell, i.e. n_{gp} , affect the energy error. For these calculations $\alpha_s = 3.0$, $\alpha_c = 0.71$ and $q = 1.03$.

Similar to the example of the two-dimensional beam, Figure 4.8 shows the change of the energy error for the three-dimensional beam as a result of changing α_{gp} for a given number of N_{FN} and n_{gp} . A similar fluctuation as the two-dimensional case is also observed here where the fluctuations become stronger by increasing the number of field nodes. Similar to the two-dimensional case these fluctuations can be due to the change in relative position of field nodes and integration points. The main and most obvious difference between the two- and three-dimensional results is the overall energy error. As can be seen from the numerical comparison between Figure 4.7 & Figure 4.8, the overall energy error is higher for the three-dimensional model. This is because of the additional uncertainties and numerical errors are introduced through the third dimension.

In spite of the fluctuations in Figure 4.7 & Figure 4.8, there is a very mild reduction in the average energy error as α_{gp} increases, which suggests a better accuracy with larger number of integration points within the given range of α_{gps} . However, since fluctuations are high, it is not a clear trend,

therefore, the best option would be the one with the minimum error. Additionally, as α_{gp} increases, the simulation time increases as well, therefore, this must be taken into account when choosing α_{gp} .

In order to find the best choice of α_{gp} for a given number of field nodes from the results in Figure 4.7 & Figure 4.8, the minimum energy error for every N_{FN} and n_{gp} is considered. However, this is not sufficient to ensure the complete accuracy of the solution because energy error calculation is an average error indicator and may not flag the error at an important part of the problem domain. Therefore, to ensure that the best value of α_{gp} is chosen, two additional criteria had to be met; the energy error must be a minimum while i) the deflection profile at the neutral axis, and ii) the shear stress at the mid-length of the beam have to best match their corresponding analytical solutions. Using these criteria for every N_{FN} and n_{gp} , the best values of α_{gp} are chosen, a summary of which is shown in Table 4.1.

Table 4.1: The best choice of α_{gp} for a given N_{FN} and n_{gp} in the two- and three- dimensional beam.

2D Beam	$n_{gp} \backslash N_{FN}$	175	637	1235	2425
	2	3	8	13	15
	3	13	2	14	8
	4	13	14	13	15
3D Beam	$n_{gp} \backslash N_{FN}$	350	1274	2385	3705
	2	3	11	4	2
	3	3	5	4	9
	4	10	9	4	8

Comparing the minimum energy errors corresponding to the α_{gps} in Table 4.1, it becomes clear that the minima in energy error decreases with increasing the number of field nodes which means the error is converging. This is shown more clearly in the next part of the convergence study, i.e. Figure 4.10 for the two-dimensional beam and Figure 4.12 for three-dimensional beam. Please note that for all the convergence studies carried out here, linear polynomial terms are included in the shape function calculations; because as the effect of linear polynomial terms on the pattern of energy error with changing α_{gp} and n_{gp} was investigated, it was found that while linear polynomial terms increase the overall accuracy, the pattern of the energy error changing with α_{gp} and n_{gp} does not change, Figure 4.9. Therefore, a linear polynomial was included in all convergence calculations. While the polynomial term does not affect the convergence pattern but it has a strong influence on the optimisation of RPIM shape parameters which will be discussed in more detail in the optimisation section.

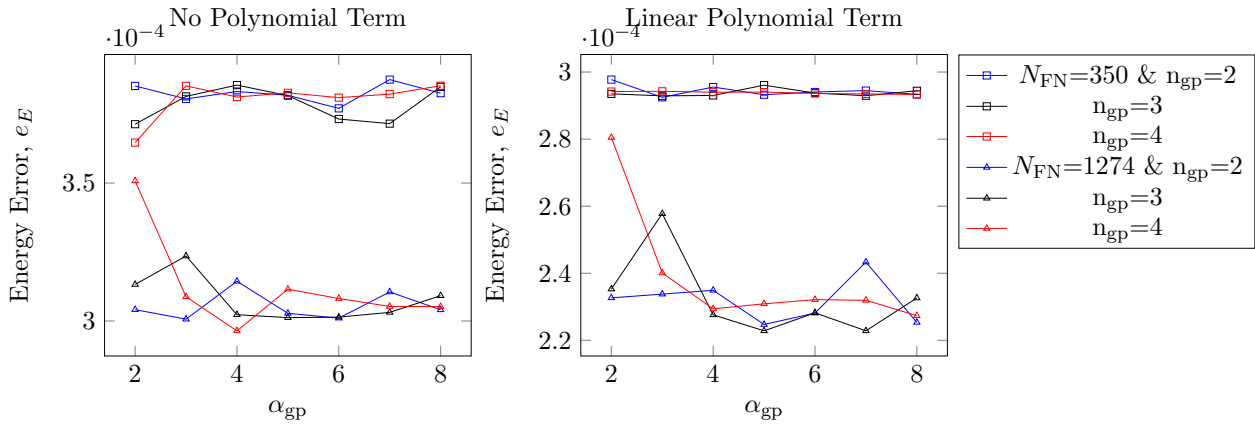


Figure 4.9: The plot on the left shows the change of energy error with α_{gp} when the linear polynomial term is not included in the RPIM shape function calculations, for two cases of N_{FN} . The right plot shows the same data as the left plot except that now for the calculations linear polynomial terms are included in the RPIM shape function calculations.

In the second step of the convergence study, the results of the chosen α_{gps} for every N_{FN} and n_{gp} from Table 4.1 are used to create the convergence plots for the energy error, maximum percentage error in deflection and maximum percentage error in the shear stress at the mid-length of the beam, i.e. Figure 4.10 & Figure 4.12.

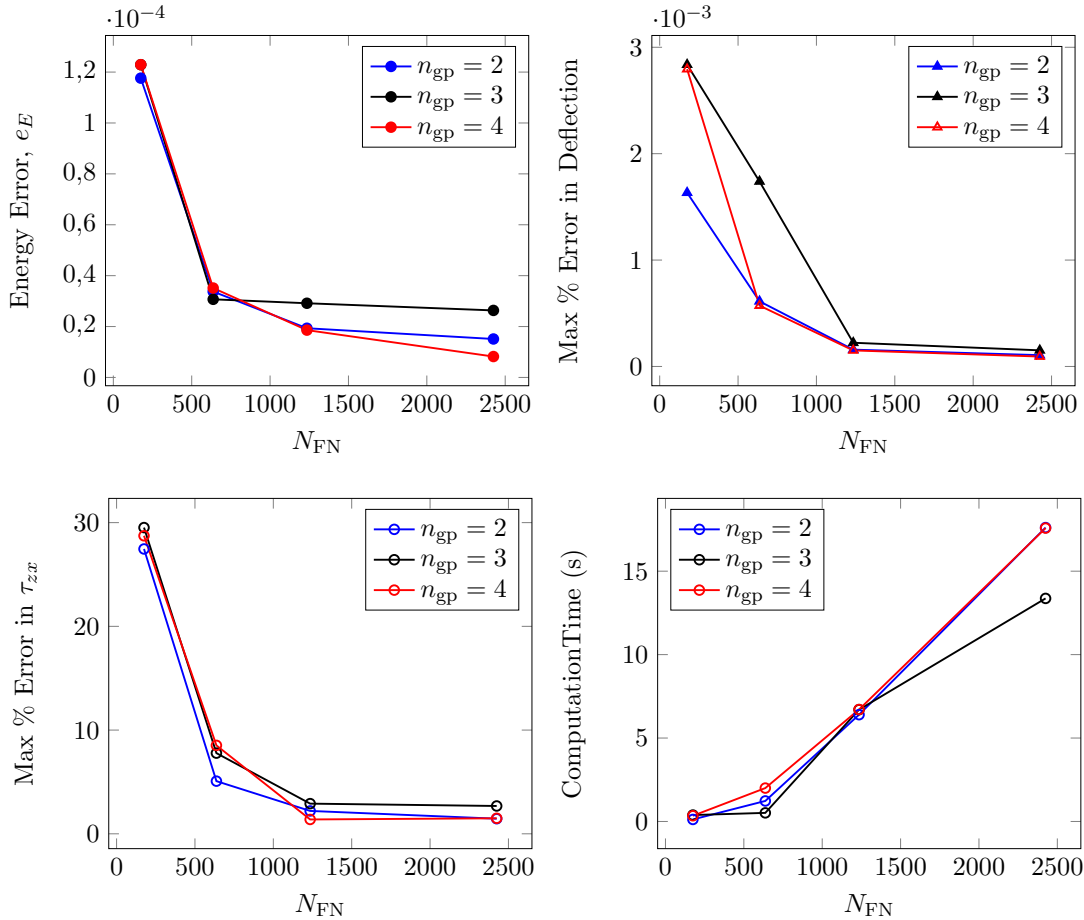


Figure 4.10: The convergence plots of the two-dimensional RPIM model of the beam using the energy error, maximum percentage error in deflection and maximum percentage error in the shear stress, τ_{zx} , at the mid-length of the beam. The bottom right plot shows the corresponding cpu times.

The plots in Figure 4.10 & Figure 4.12 show the overall convergence of the error indicators for this problem and their corresponding computational time. Thus, when choosing the converged solution both the accuracy and computational time can be taken into account.

As can be seen in the plots of Figure 4.10, for the two-dimensional model of the beam, convergence is obtained at $N_{\text{FN}} = 1235$ for all the n_{gp} s. This convergence is true for the maximum percentage error in τ_{zx} , maximum percentage error in deflection, and energy error. Additionally, the corresponding computation time for this choices of N_{FN} is about 7s. While choosing the best choice of N_{FN} is obvious from the plots, choosing the best value of n_{gp} is not as clear. $n_{\text{gp}} = 3$ has the worst accuracy in comparison to $n_{\text{gp}} = 2$ and 4, which eliminates it from the selection but $n_{\text{gp}} = 2$ and 4 both have very similar effects, therefore, either of them can be chosen. One might expect the accuracy to increase monotonically with increase in the number of Gauss points, but given the nature of RPIM and support domain, different number of Gauss points leads to different relative position between the field nodes and the Gauss point, which affects the accuracy of the integration.

In summary, for the two-dimensional RPIM model of the beam where $\alpha_s = 3.0$, $\alpha_c = 0.71$, $q = 1.03$ and $d_c = 2.0$, the best choice of field nodes and integration points are found to be $N_{\text{FN}} = 1235$, $n_{\text{gp}} = 4$ and $\alpha_{\text{gp}} = 13$. Figure 4.11 shows the computed displacement and shear stress profile of the two-dimensional beam with the chosen parameters for the RPIM code. For completing the verification process of the 2D-RPIM code, the shear stress at the mid-length of the beam, and the beam deflection at the neutral axis are plotted against the analytical solution in Figure 4.14.

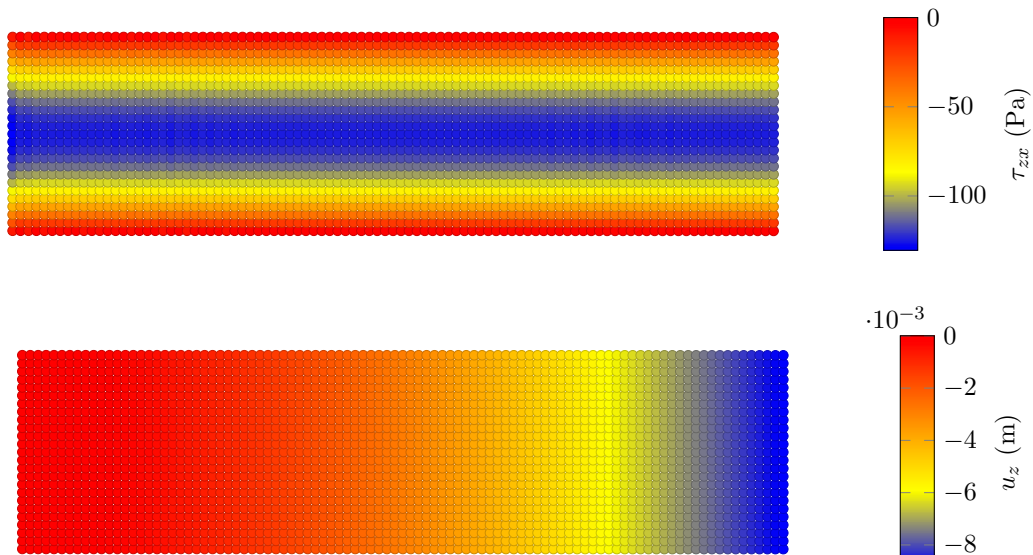


Figure 4.11: The deflection and the shear stress profiles of the two-dimensional beam for the converged case in the RPIM code.

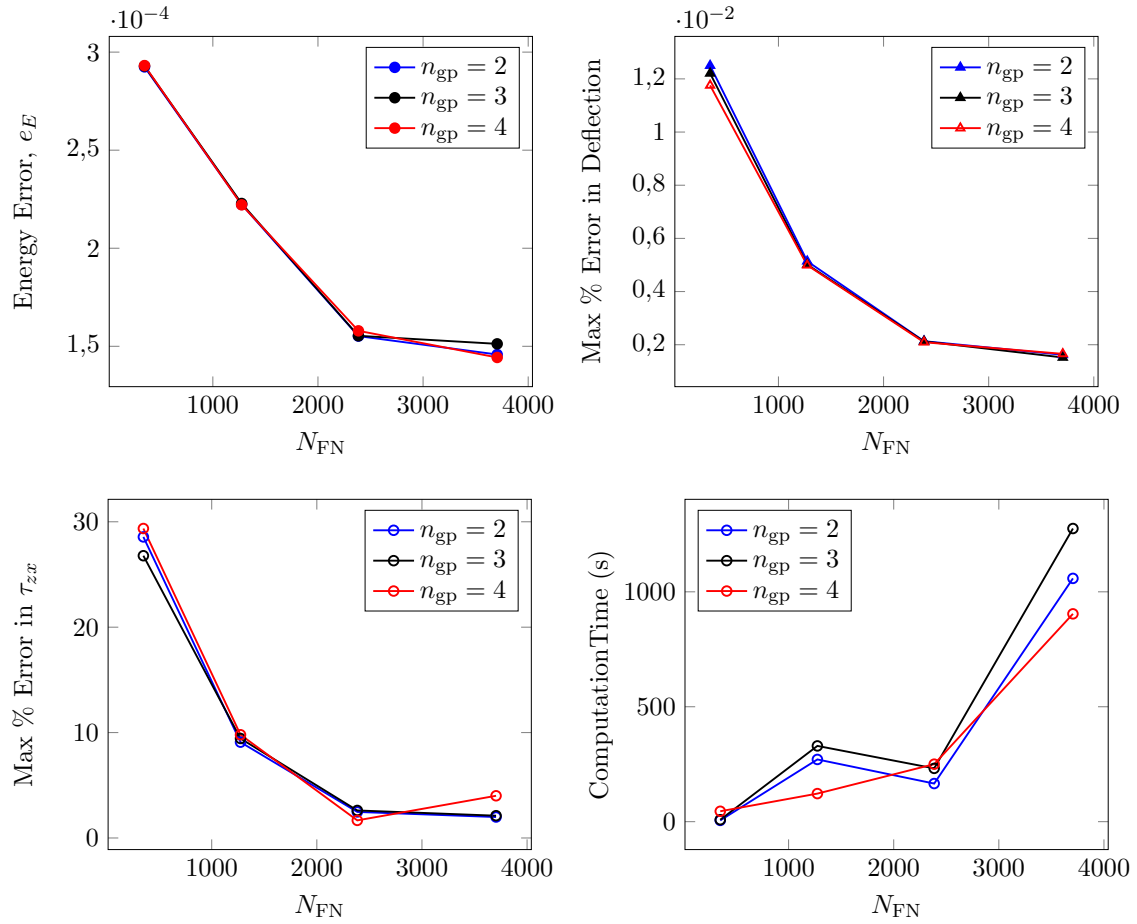


Figure 4.12: The convergence plots of the three-dimensional RPIM model of the beam using the energy error, maximum percentage error in deflection and maximum percentage error in the shear stress, τ_{zx} , at the mid-length of the beam. The bottom right plot shows the corresponding cpu times.

Similar to the 2D beam, for the three-dimensional version of the beam the best choice of N_{FN} and n_{gp} were made from the convergence plots, i.e. Figure 4.12. From the plots in Figure 4.12, it is clear that convergence for all the solutions is reached at $N_{FN} = 2385$ where the computational time is about 200s. Clearly, the simulation time is high for the three dimensional beam compared to two-dimensional version and an equivalent finite element model; this is because of the additional dimension and the fact that the shape functions are calculated as part of the simulation, unlike FEM. The convergence behaviour of all the error indicators looks almost the same for different n_{gp} s. However, for $n_{gp} = 3$ the computational time is higher compared to the other two n_{gp} s, therefore, $n_{gp} = 3$ is eliminated. Similar to the two-dimensional case, not much difference is observed between $n_{gp} = 2$ and 4. However, when looking at the shear stress profile at the mid-length of the beam, $n_{gp} = 4$ showed a better match, therefore, it is the chosen value for n_{gp} .

In summary, for the three-dimensional beam shown here where $\alpha_s = 3.0$, $\alpha_c = 0.71$, $q = 1.03$ and $d_c = 2.0$, the best choice of number of field nodes and integration points are $N_{FN} = 2385$, $n_{gp} = 4$ and $\alpha_{gp} = 4$. The computed deflection and shear stress profile of the three-dimensional beam with these

choice of parameters are shown in Figure 4.13. Same as before, for completing the verification process of the 3D-RPIM code, the shear stress at the mid-length of the beam, and the beam deflection at the neutral axis are plotted against the analytical solution in Figure 4.14.

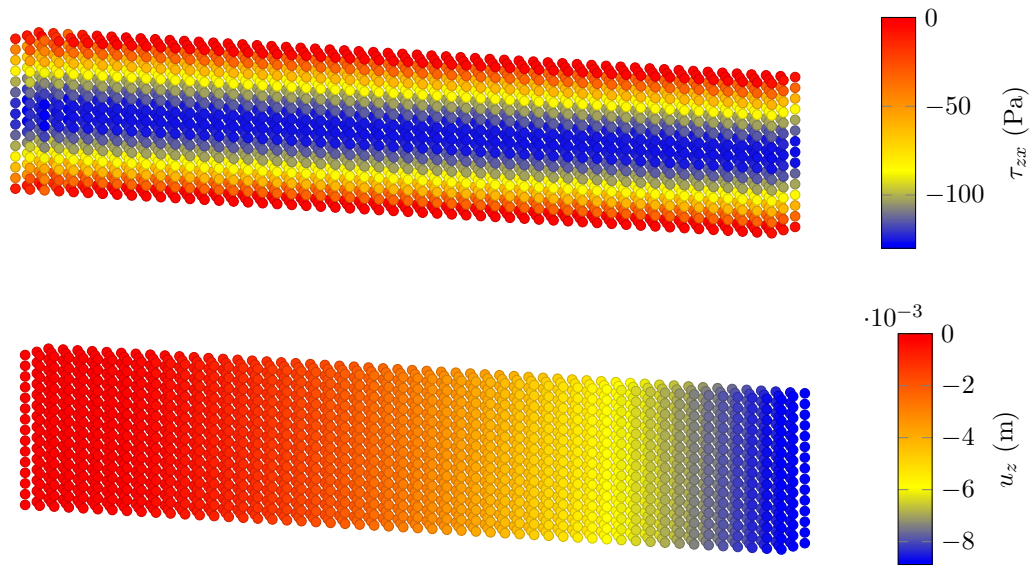


Figure 4.13: The deflection and the shear stress profiles of the three-dimensional beam for the converged case in my RPIM code.

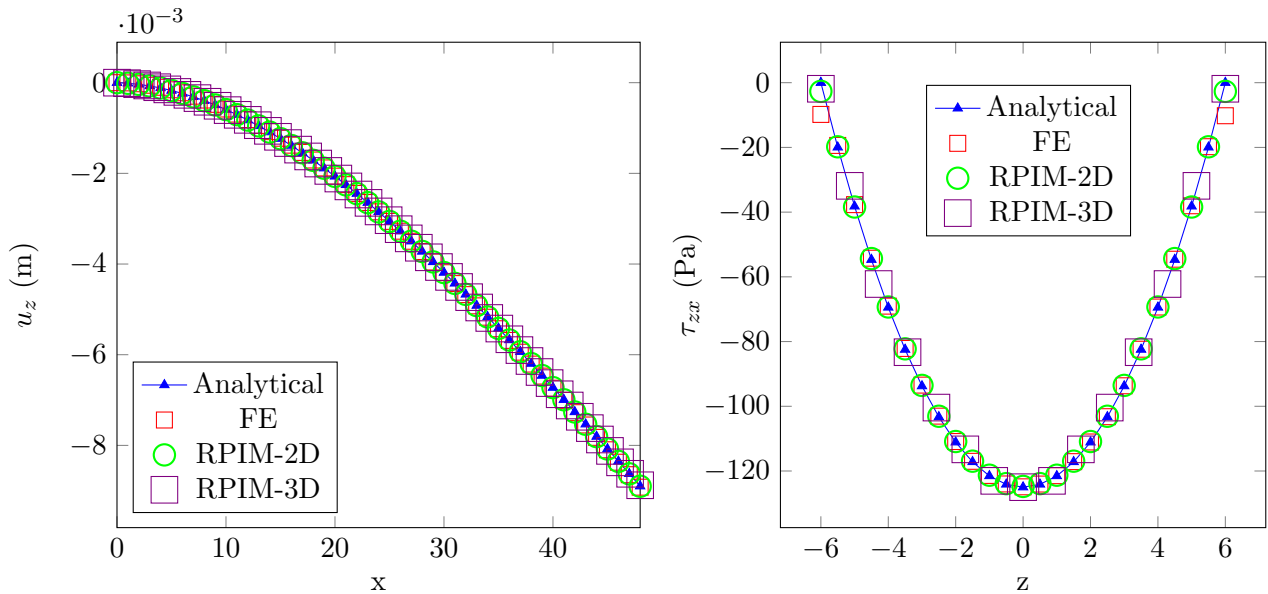


Figure 4.14: The deflection of the beam at the neutral axis and the shear stress at the mid-length of the beam computed by two-dimensional RPIM, three-dimensional RPIM, three-dimensional FE and analytical models.

At this point the convergence, computational time and accuracy of the RPIM method is compared to the ones from finite element method. In order to do that, the same 3D beam example as here is modelled using Abaqus 6.14 with linear solid elements. Figure 4.15 shows the comparison between RPIM and FE methods in terms of convergence rate, computational time and accuracy of the converged solution. The comparison in terms of accuracy is also apparent in Figure 4.14 where the deflection

of the beam at the neutral axis and the shear stress at the mid-length of the beam computed by three-dimensional FE is compared to the solutions from two-dimensional RPIM, three-dimensional RPIM, and the analytical models.

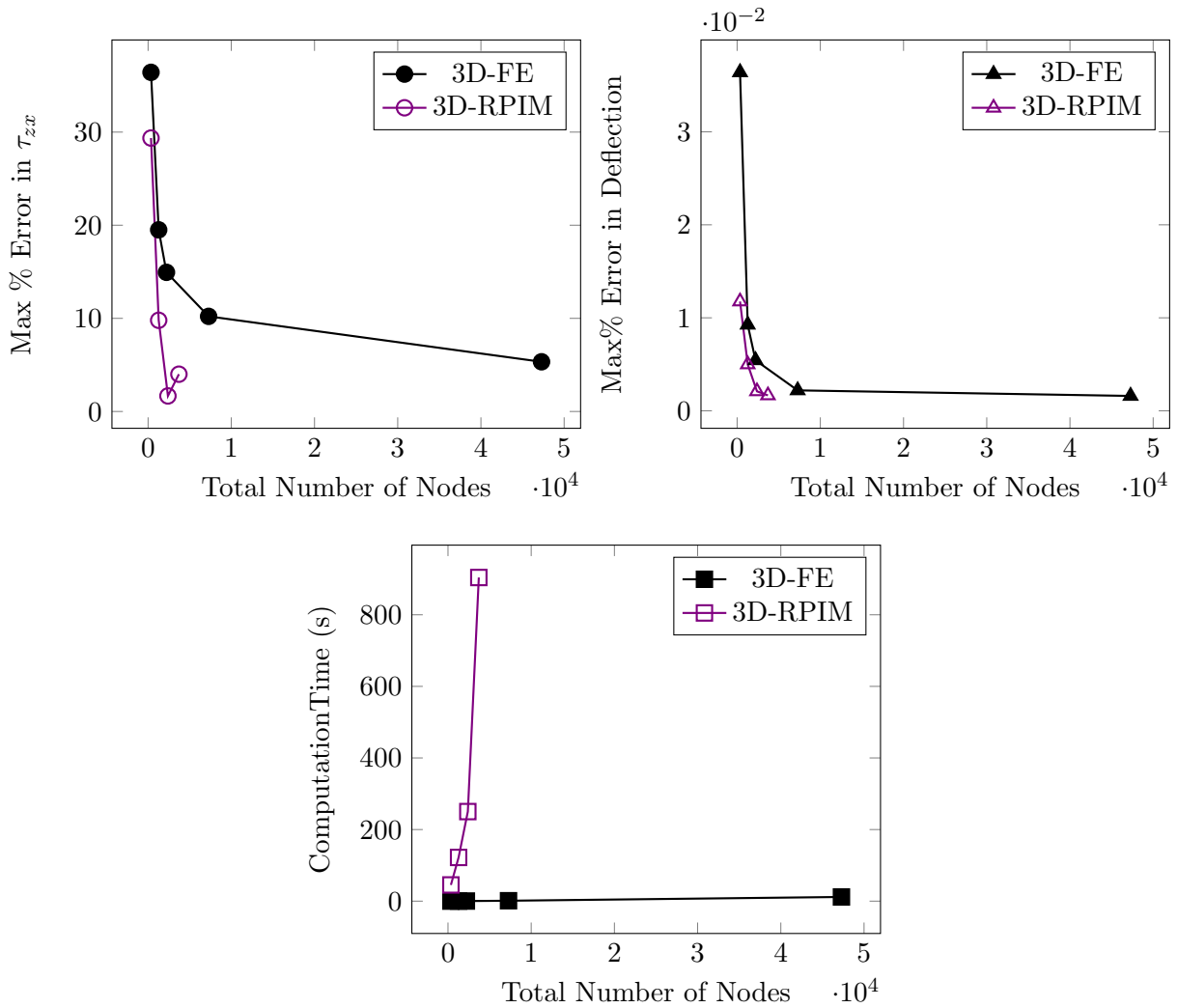


Figure 4.15: The plots here show the effect of total number of nodes on maximum percentage error in beam deflection, shear stress at the mid-length of the beam, and computational time for the 3D-FE and 3D-RPIM models.

There are three obvious outcomes from the convergence plots in Figure 4.15; i) 3D-RPIM reaches convergence at a much faster rate and with much less nodes than FE, ii) the converged accuracy of the RPIM is higher than FE, and iii) the time taken for the simulation is much higher for RPIM than FE. The longer simulation time for RPIM is because the shape functions are computed as part of the simulation, whereas, in Finite element, the shape functions are defined prior to the simulation. While being slower than FEM for the same number of nodes is a shortcoming of RPIM but reaching convergence with less nodes can compensate for that. For the RPIM code developed for single body problems in this work direct solver is used, which makes the simulations slower; one can make a use of iterative solvers to speed up the calculations in RPIM.

In FE, the convergence is obtained for 7275 nodes (4608 elements) with a node spacing of 0.5m, whereas, for 3D-RPIM the convergence is reached for 2385 nodes with a node spacing of 0.92cm. Therefore, it is clear that RPIM method converges much faster compared to FE. Additionally, for a similar spacing between the nodes, RPIM gives a more accurate solution compared to FE. This is apparent from Figure 4.14, where the deflection and shear stress of the beam are computed with 2D-RPIM, 3D-RPIM, and FE models with similar node spacings. In Figure 4.14, while all the methods give a perfect match for the beam deflection, only the two RPIM results give the exact solution for the shear stress at the edges of the beam. It will be possible to reach the perfect solution with the FE model but that requires using more elements. Therefore, having a much faster convergence rate, and more smooth stress results are two of the important advantages of RPIM compared to FE, as shown here.

While RPIM method has these advantages, the time taken for the converged 3D-RPIM is 164.3 s and for FE is 11.3s. In addition to the discussion above for the speed of simulation in RPIM models, there are other ways of improving the speed of the RPIM simulations; for example using the smallest possible support domain, making a use of speed optimisation techniques for running the simulations, using faster solvers, or for problems with the same geometries, defining and storing the stiffness matrix once and using it for different boundary conditions. The last three suggestions are for future work and are worth exploring, the first suggestion, on the other hand, is the last step of the convergence study. In the this step α_s from Equation 4.16 is changed in order to investigate its effects on accuracy and computational time of both the two- and three-dimensional RPIM models.

Figure 4.16 presents the effect of support domain size or α_s on energy error, maximum percentage error in deflection, maximum percentage error in shear stress at the mid-length of the beam, and the computational time for the two- and three-dimensional beams. Looking at the 2D-RPIM results, it can be seen that the most accurate result is obtained when $\alpha_s = 3.0$, however, the corresponding computational time is the highest which is 8s. 8s is not a very significant time for this problem, given that the best accuracy is obtained for all cases of energy error, deflection and shear stress. Therefore, for the two-dimensional beam, $\alpha_s = 3.0$ is chosen and used for the optimisation section. Please note that for other problems, the computational time may vary significantly by changing α_s , therefore, a sensible compromise between accuracy and computational time may be required.

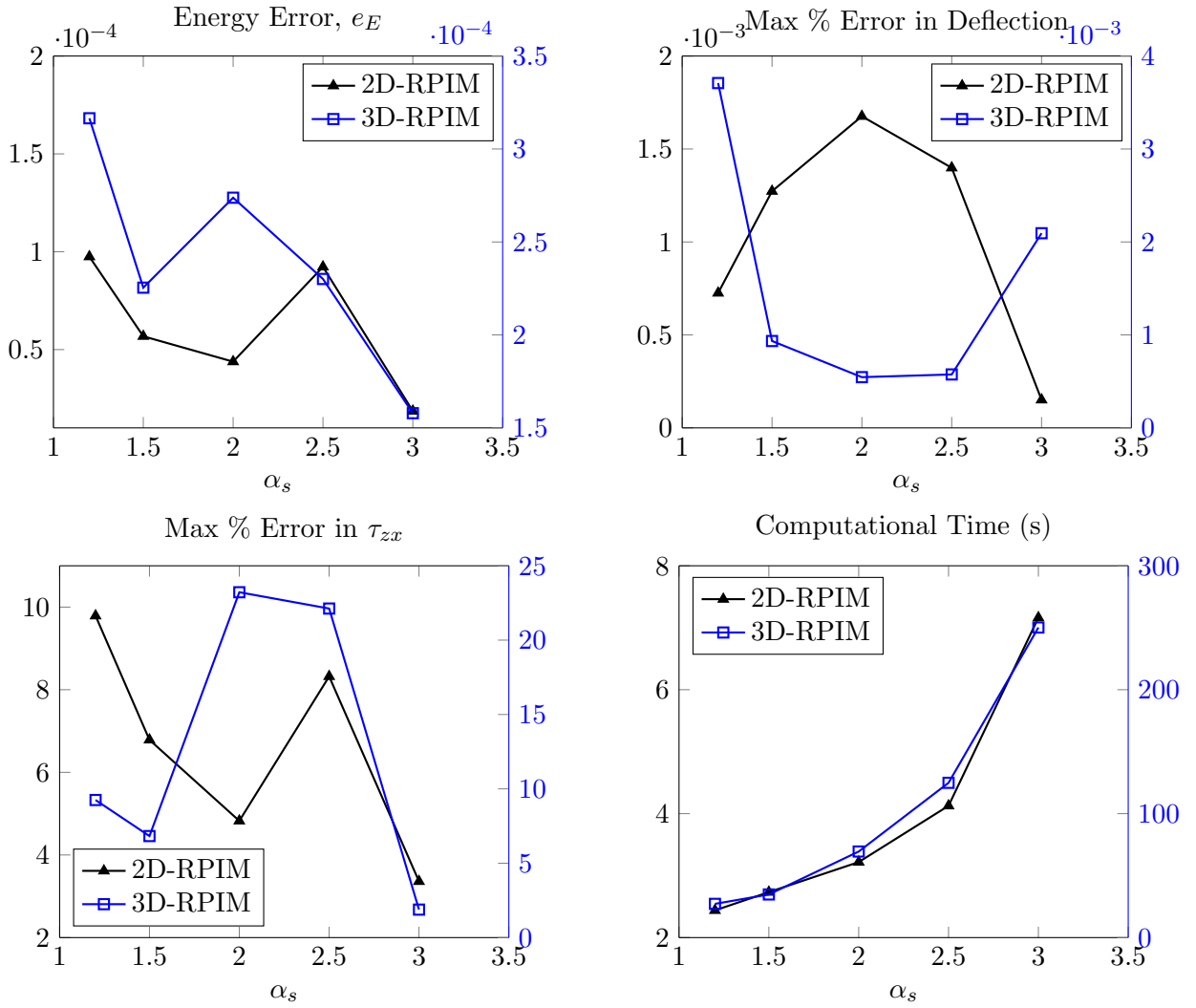


Figure 4.16: These plots show effect of α_s on energy error, maximum percentage error in deflection, maximum percentage error in shear stress at the mid-length of the beam, and the computational time for two- and three-dimensional RPIM models. The parameters other than α_s for the 2D model are $N_{FN} = 1235$, $n_{gp} = 4$, $\alpha_c = 0.71$, $q = 1.03$, $d_c = 2.0$ and $\alpha_{gp} = 13$, and for the 3D model are $N_{FN} = 2385$, $n_{gp} = 4$, $\alpha_c = 0.71$, $q = 1.03$, $d_c = 2.0$ and $\alpha_{gp} = 4$.

Similarly as before, $\alpha_s = 3.0$ for the 3D-RPIM gives the most accurate results, however, the computational time for it is near 250s which is too costly for a simple problem. Therefore, looking at both the computational time and accuracy, the next best option is $\alpha_s = 1.5$ with a running time of 34.7s and a maximum percentage error in shear stress below 5%. As a result, for the optimisation section of the three-dimensional beam $\alpha_s = 1.5$ is chosen and used for the optimisation section.

4.3.1.2 Optimisation

In this section, parameters of the converged case from previous section are used for the optimisation study where values of the RPIM shape parameters, i.e. α_c and q , are varied to find the combination that gives the lowest error. This process is carried out for two cases; i) when linear polynomial terms are included in the RPIM shape function calculations, and ii) when no polynomial terms are included.

As mentioned previously, Figure 4.9 , adding the linear polynomial term does not affect the convergence pattern but it has a significant effect on the optimisation which becomes apparent in this part. The error indicators used for the optimisation are the same as the convergence study, i.e. energy error, maximum percentage error in deflection, and maximum percentage error in τ_{zx} .

Two-dimensional Beam

Plots in Figure 4.17 show the results used to find the optimum combination of RPIM shape parameters for the two-dimensional beam example. As can be seen, when no polynomial term is used in the shape function calculations, as α_c increases up to 1.5, the energy error and maximum deflection error decrease for any given q . Additionally, for every α_c there is a q around 1 (but not at 1 itself because the matrix becomes singular [20]) that gives the minimum error for all the error indicators. This results is in accordance with the work of Wang *et al.* [20] who carried out the same optimisation study on the same two-dimensional beam without the use of polynomial terms in the shape function calculations. Therefore, when modelling a two-dimensional cantilever beam using the RPIM method without polynomial terms, the optimum choice of RPIM shape parameters would be $q = 0.98$ and $\alpha_c = 1.5$.

On the other hand, as can be seen in Figure 4.17, when the linear polynomial terms are included in the shape function calculations, choosing the optimum α_c and q is not as clear as before. While the overall accuracy has increased by using the linear polynomial terms, the clear pattern for the choosing the optimum combination of α_c and q from before is distorted. For example, when using energy error and maximum percentage error in τ_{zx} as error indicators, the optimum choice of α_c and q does not match the optimum choice when considering the maximum percentage error in deflections. Therefore, extra care must be taken when choosing α_c and q for this case.

Looking at the values of error indicators, it is clear that the highest overall error is for the maximum percentage error in τ_{zx} , therefore, a sensible choice of α_c and q would be the one that gives a minimum in percentage error in τ_{zx} , i.e. $\alpha_c = 0.85$ and $q = 1.5$. Nevertheless, this choice can also be altered by the importance of each error indicator. For example if the beam was representing a sensor that depends on the deflection of the beam, the optimum α_c and q should be based on the maximum percentage error in deflection rather than stress.

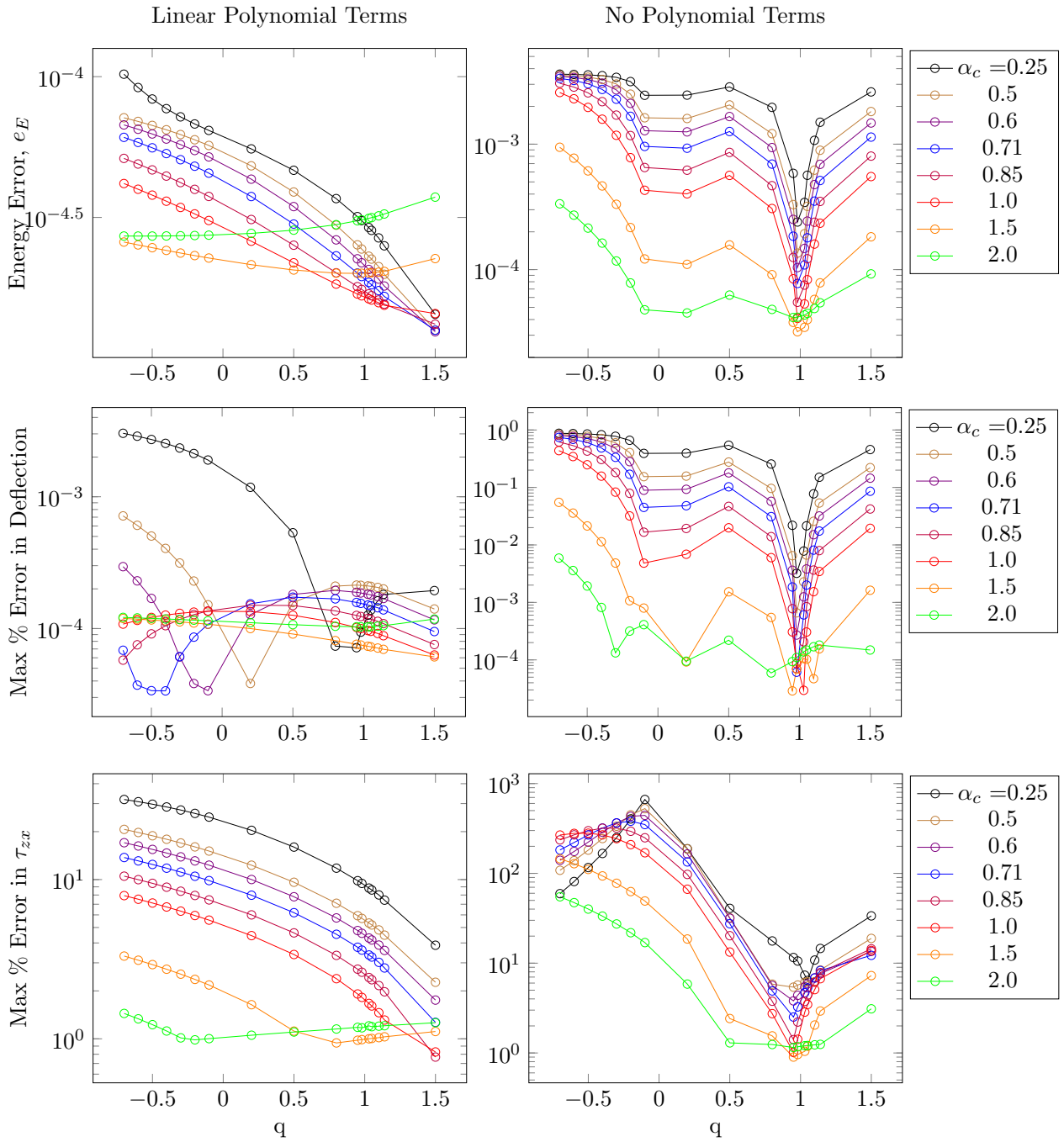


Figure 4.17: The plots here show the effect of α_c and q on the energy error, maximum percentage error in deflection, and maximum percentage error in τ_{zx} of the two-dimensional beam. The left plots are for the case with linear polynomial included and the right plots are for when no polynomial is included. Here, $N_{FN} = 1235$, $n_{gp} = 4$, $\alpha_s = 3.0$, $d_c = 2.0$, and $\alpha_{gp} = 13$.

Three-dimensional Beam

For the example of three-dimensional beam without polynomial terms in the shape function calculations, there is an overall reduction in the energy error and maximum percentage error in deflection by increasing α_c , similar to the two-dimensional case. However, for the maximum percentage error in τ_{zx} , where the overall errors are very high, only the error at the minima decreases with increasing

α_c , therefore, $\alpha_c = 2.0$ seem to be the optimum choice. Looking at the overall pattern of the error indicators changing with q and α_c , two minimums can be seen for each error indicator; one near $q = 0$ and one near $q = 1$. For the energy error the minimum error near $q = 0$ is stronger than the other one, whereas for the other two the minimum near $q = 1$ is slightly stronger. Given that the error in τ_{zx} is higher than the other two error indicators, it is sensible to choose $q = 1.03$ for the optimum value.

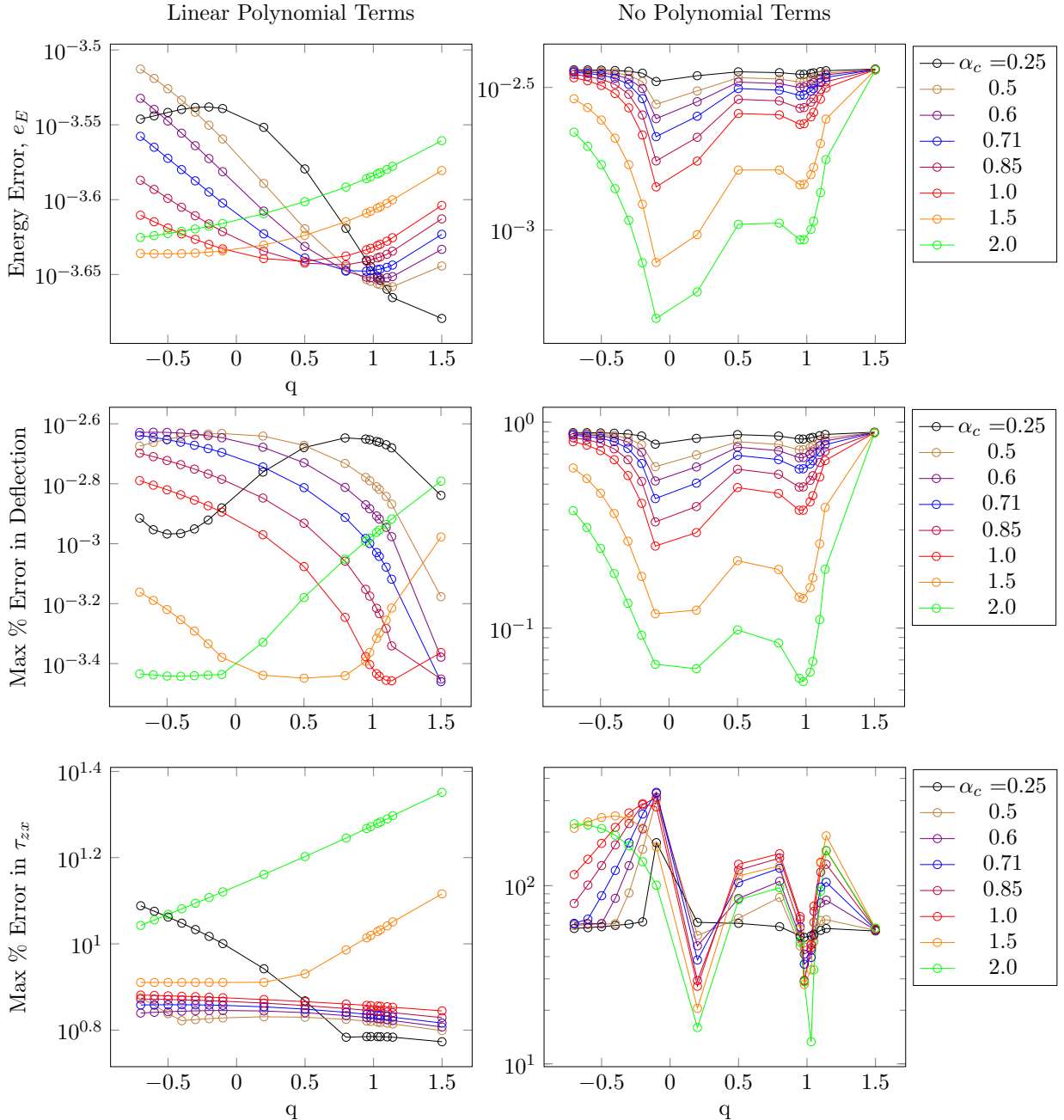


Figure 4.18: The plots here show the effect of α_c and q on the energy error, maximum percentage error in deflection, and maximum percentage error in τ_{zx} of the three-dimensional beam. The left plots are for the case with linear polynomial included and the right plots are for when no polynomial is included. Here, $N_{FN} = 2385$, $n_{gp} = 4$, $\alpha_s = 1.5$, $d_c = 2.0$, and $\alpha_{gp} = 4$.

$q = 1.03$ for all choices of α_c is the same outcome as the two-dimensional RPIM model of the

beam without polynomial terms in the shape function. As a result, there can be a common optimum choice of q and α_c between the two- and three-dimensional models of the beam. However, as can be seen from the plot for the maximum percentage error of the shear stress, the errors are very high, therefore, modelling the three-dimensional beam using RPIM without polynomial terms is not suitable for stress calculations. Similar to the two-dimensional beam, as soon as the linear polynomial terms are added into the shape function calculations, the overall accuracy of all the error indicators has increased, especially for τ_{zx} . However, at the same time the clear pattern obtained from before is distorted, therefore, in order to choose a sensible optimum value of q and α_c for the three-dimensional beam, given that error in τ_{zx} has the highest overall value, the minimum error from the τ_{zx} plot is considered. This choosing process leads to $\alpha_c = 0.25$ and $q > 0.7$.

Comparing the optimum values of q and α_c between the two- and three-dimensional RPIM models of the beam with the use of linear polynomial terms, it is clear that there is no general choice for α_c and q . Hence the choice of optimum value for q and α_c depends on the dimension of the problem and use of polynomial terms in the shape function calculations. In order to see how the change of boundary conditions and geometry affects the optimum values of RPIM shape parameters, the convergence and optimisation processes introduced here are applied to the next two examples, i.e. cube under uniform compression and cylinder under line compression.

4.3.2 Square/Cube

The next example for which the introduced optimisation algorithm is tested is the cube under uniform compression. The results in this section follow the same structure as the beam example; first the convergence study is discussed, and then the optimisation of the RPIM shape parameters for the two- and three-dimensional models of the cube.

4.3.2.1 Convergence

Similar to the beam example, in the first step of the convergence study, effect of the number of background cells and integration points, α_{gp} on the energy error is presented for ascending values of N_{FN} , Figure 4.19 & Figure 4.20. While N_{FN} , α_{gp} and n_{gp} are changing in the convergence part, other RPIM parameters are fixed at $\alpha_c = 0.71$, $q = 1.03$, $d_c = 2.0$, and $\alpha_s = 2.0$.

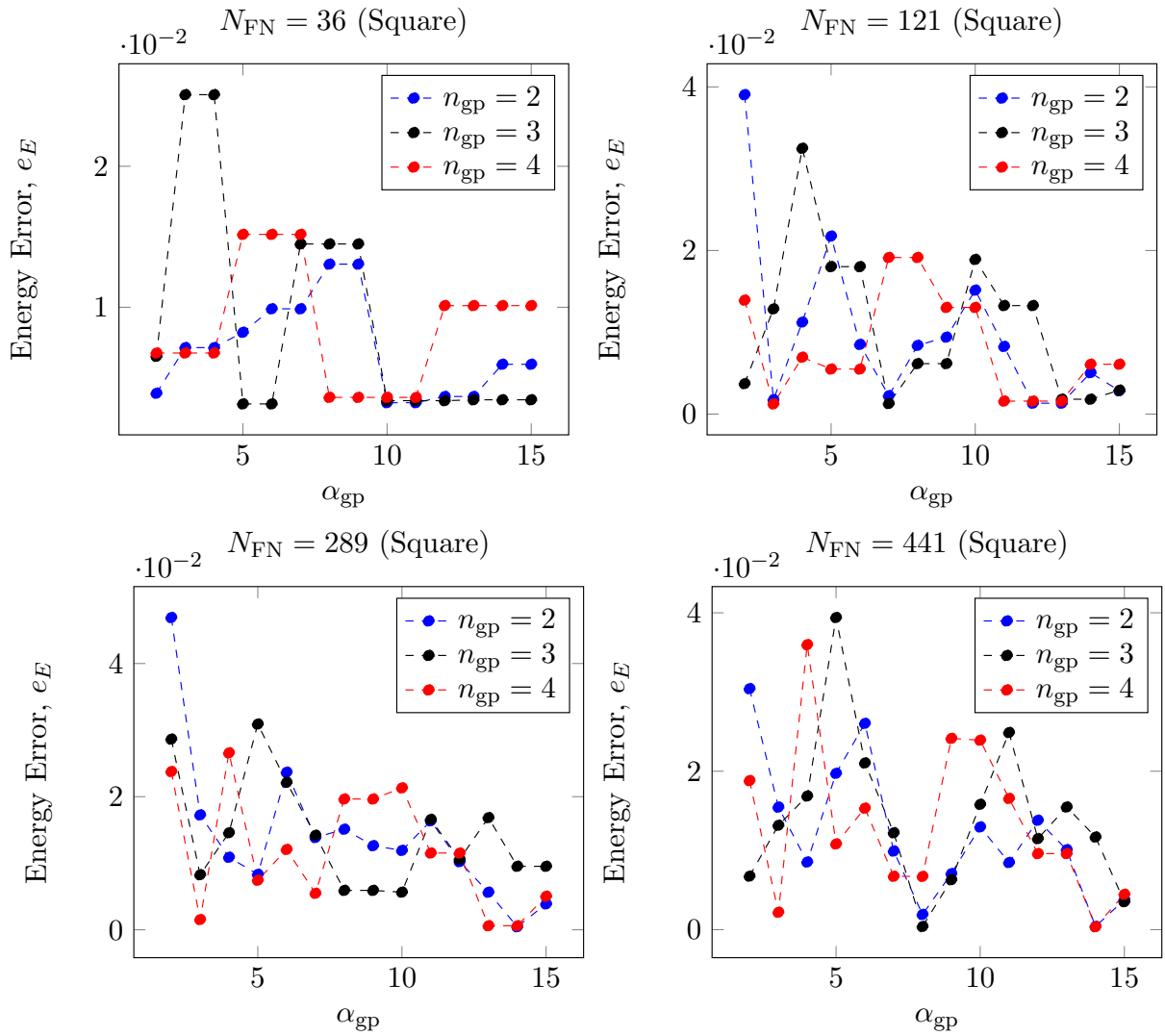


Figure 4.19: Computed energy error, e_E , from my 2D RPIM code for the square example versus the α_{gp} factor from Equation 4.41. The plots in this figure also show the effect of N_{FN} and n_{gp} on e_E .

As can be seen from Figure 4.19 & Figure 4.20, there are fluctuations in the energy error by changing α_{gp} , similar to the beam example; additionally, increasing N_{FN} leads to a stronger fluctuation with slightly higher error range, especially for the three-dimensional version of the cube example.

For $N_{FN} = 36$ and 121 in Figure 4.19, and all N_{FN} s in Figure 4.20, there are parts where the error does not change with α_{gp} . This is because in this case total number of field nodes is small enough for Equation 4.41 to round them up to the same number of integration points. As you can see in Figure 4.19 & Figure 4.20, the higher the value of N_{FN} the less constant error patches occurring.

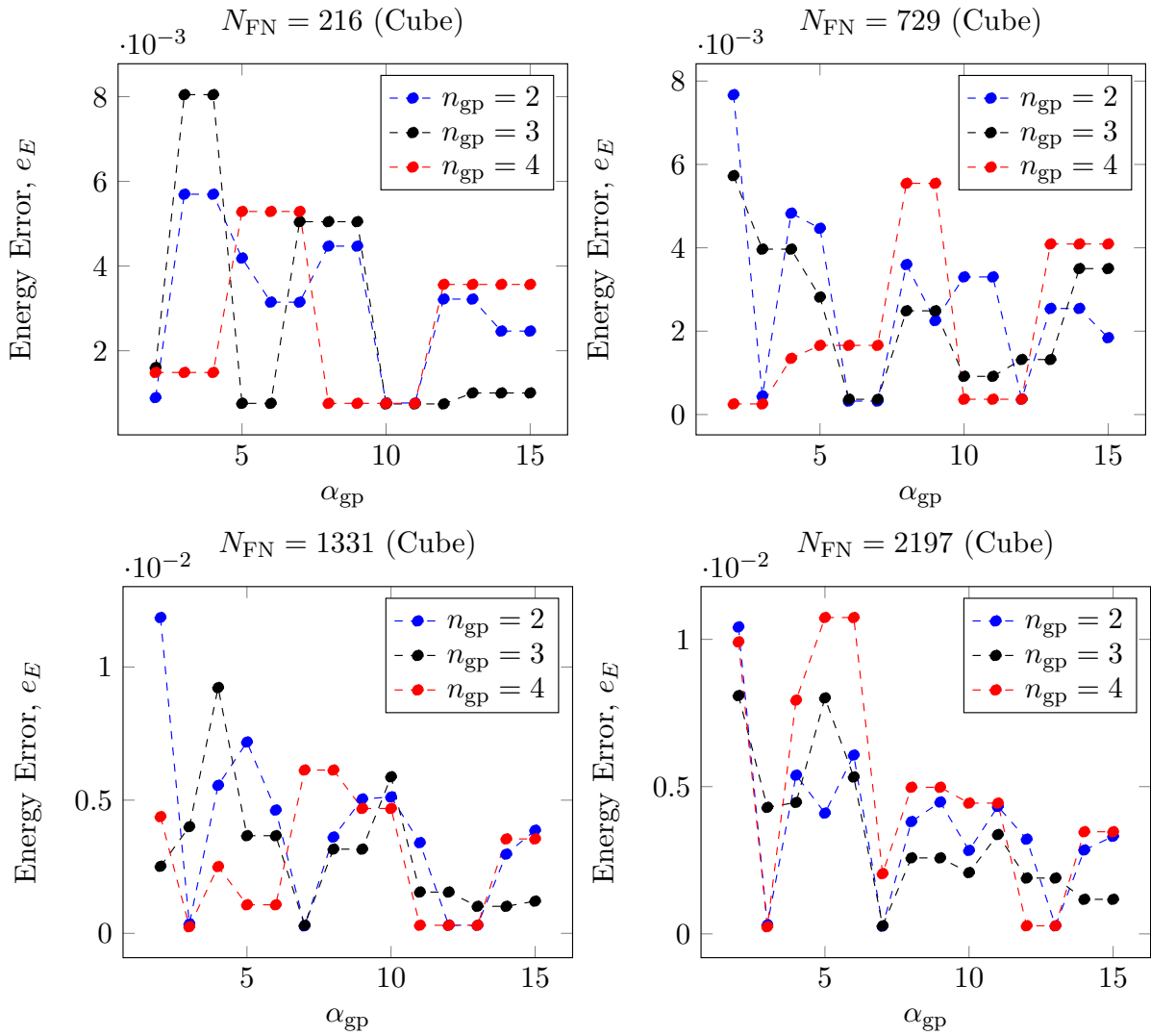


Figure 4.20: Computed energy error, e_E , from my 2D RPIM code for the cube example versus the α_{gp} factor from Equation 4.41. The plots in this figure also show the effect of N_{FN} and n_{gp} on e_E .

In order to choose the best α_{gp} for every N_{FN} and n_{gp} , three criteria had to be met; i) e_E has to be a minimum, while ii) the stress is uniform in all the problem domain, and iii) displacement at a random part of the problem domain matches the analytical one. The reason for adding the two additional conditions is that energy error is an average error indicator for the whole problem domain and does not necessarily flag the error at parts that could be important. However, it is still important to calculate so the quality of the results at the bigger picture can be monitored. Table 4.2 shows a summary of the best α_{gp} that are chosen for both the two- and three-dimensional model of the cube under compression based on these criteria.

Table 4.2: The best choice of α_{gp} for a given N_{FN} and n_{gp} in the square and cube examples.

Square	$n_{gp} \backslash N_{FN}$	36	121	289	441
		2	10	12	14
	3	5	7	10	8
	4	8	3	13	14

Cube	$n_{gp} \backslash N_{FN}$	216	729	1331	2197
		2	10	6	7
	3	10	6	7	7
	4	8	2	3	3

Figure 4.21 shows the converging plots for the energy error, maximum percentage error in the vertical displacement, u_z , the maximum percentage error in the vertical stress, σ_{zz} , and their corresponding simulation time for the two-dimensional cube (or square). The value of error indicators in this figure are based on the chosen α_{gp} s from Table 4.2.

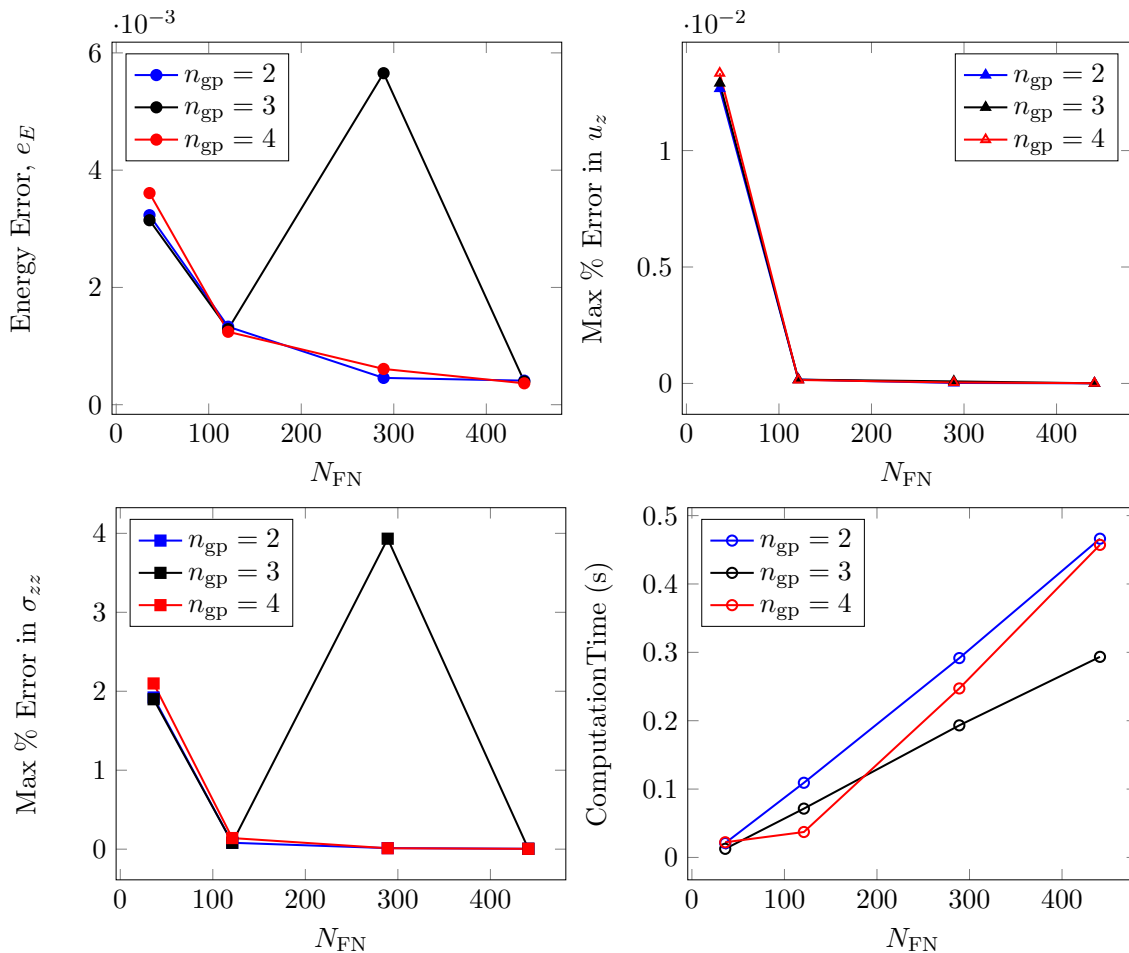


Figure 4.21: The plots here show convergence of the RPIM model of the square using e_E , maximum percentage error in u_z , and maximum percentage error in σ_{zz} for every n_{gp} . The bottom right plot shows their corresponding cpu time.

As can be seen from Figure 4.21 for the two-dimensional cube, the N_{FN} for which all the error indicators have converged is 289 with a computation time range of about 0.18 - 0.3s. Looking at the

effect of n_{gp} on convergence, it is very clear that $n_{gp} = 3$ is not the right choice for this example, therefore, it is eliminated. The other two n_{gp} cases have almost the same outcome, however, given that the time taken for $n_{gp} = 4$ is slightly less than $n_{gp} = 2$, the former is chosen. The computed vertical displacement and stress profile of the square for the converged case are shown in Figure 4.22.

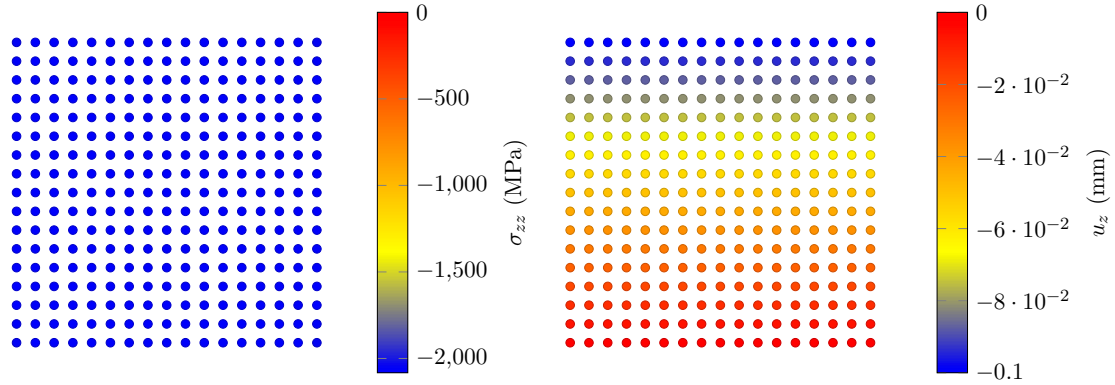


Figure 4.22: The vertical displacement and stress profiles of the two-dimensional cube for the converged case in the RPIM code.

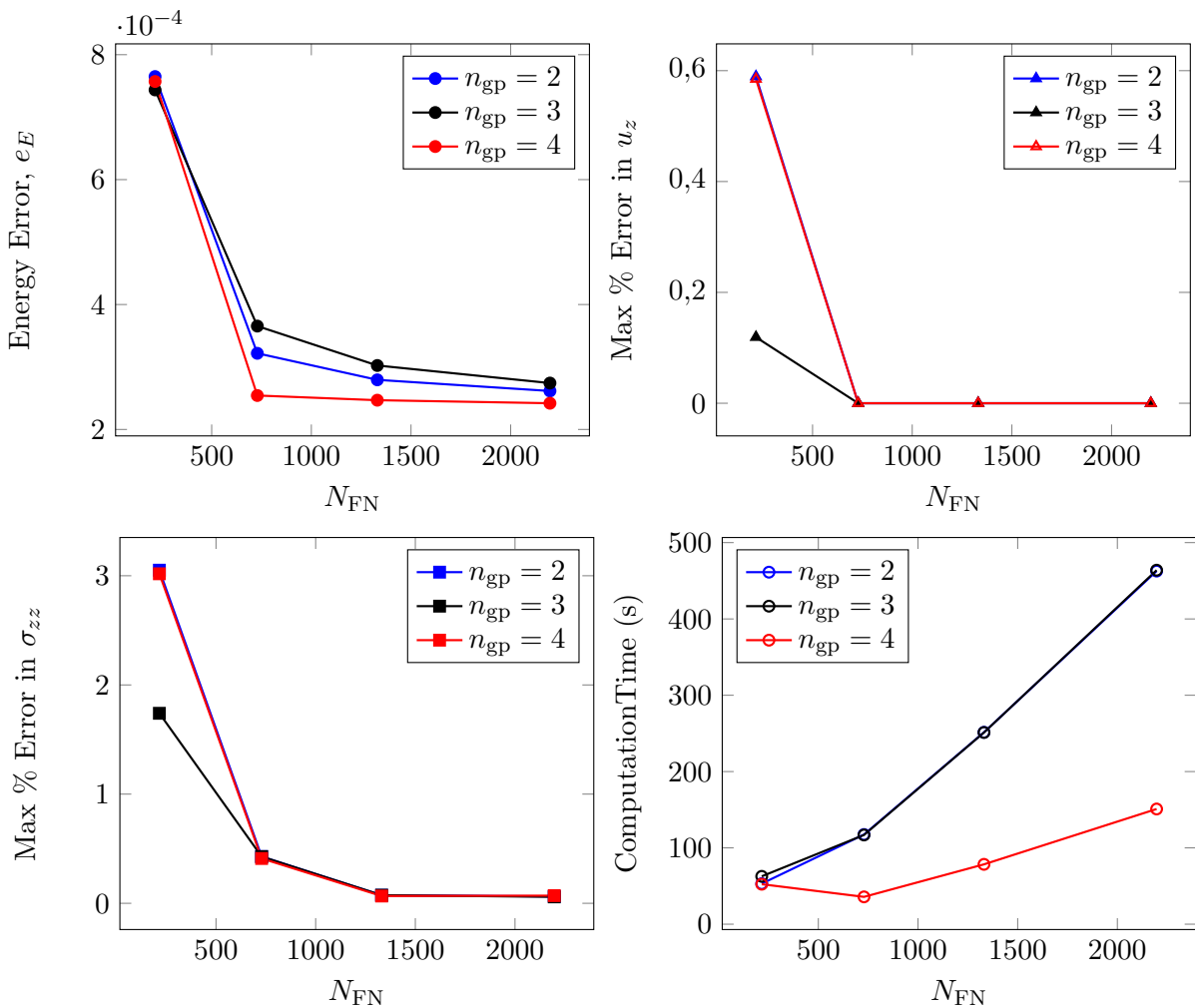


Figure 4.23: The plots here show convergence of my RPIM model of the cube using e_E , maximum percentage error in u_z , and maximum percentage error in σ_{zz} for every n_{gp} . The bottom right plot shows their corresponding cpu time.

Figure 4.23 shows the convergence plots of the three-dimensional cube under compression for different n_{gp} s. As can be seen from the energy error plot and the computational time, the results for $n_{gp} = 4$ is much better than $n_{gp} = 2$ & 3, hence it is chosen for the converged solution. For $n_{gp} = 4$ it is clear that the energy error and maximum percentage error in u_z have converged for $N_{FN} = 729$, whereas, for the maximum percentage error in σ_{zz} the convergence is reached at $N_{FN} = 1331$. However, given that the computational time for $N_{FN} = 729$ is less than $N_{FN} = 1331$ while the error in maximum percentage error in σ_{zz} is much less than 1%, $N_{FN} = 729$ is a sensible choice for the converged solution.

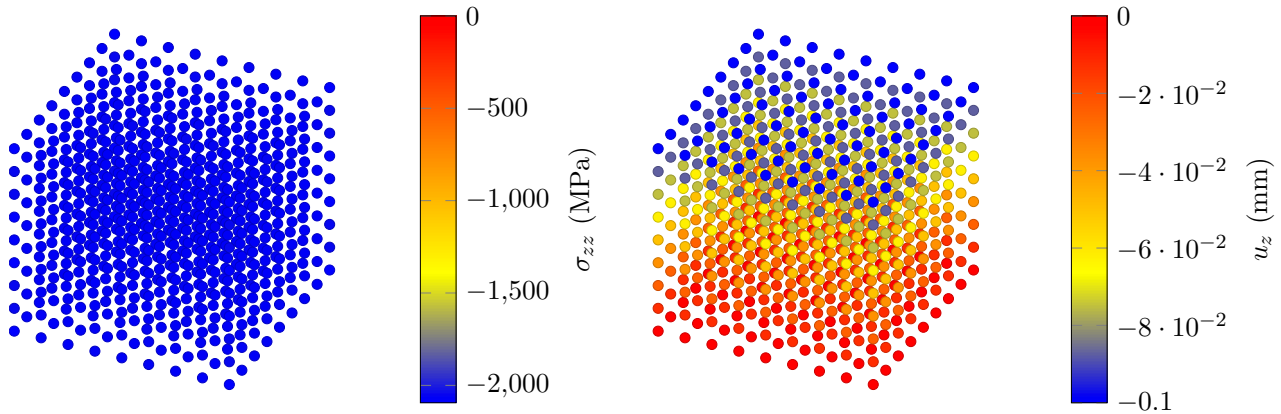


Figure 4.24: The vertical displacement and stress profiles of the three-dimensional cube for the converged case in the RPIM code.

Once the converged solution for the two- and three-dimensional versions of the cube under uniform compression is obtained, the last part of the convergence study is carried out where effect of the support domain size, i.e. α_s , on the error indicators and the computational time is investigated, Figure 4.25.

As can be seen in Figure 4.25, for the two-dimensional cube, i.e. the black line, the best choice for α_s is 1.2. Not only $\alpha_s = 1.2$ gives the minimum error (almost zero) in all the error indicators but also the computational time for it is the lowest. Hence 1.2 is the best choice for α_s for the two-dimensional cube. For the three-dimensional cube, on the other hand, $\alpha_s = 1.2$ gives one of the highest errors. The best choice of α_s for the three dimensional cube is 2 which is the one already used in the calculations so far. $\alpha_s = 2.0$ gives the lowest error in all the error indicators with a relatively low computational time. As a summary for the convergence study, for the two-dimensional model of the cube under uniform compression the best converging parameters are found to be $\alpha_{gp} = 13$, $N_{FN} = 289$, $n_{gp} = 4$, and $\alpha_s = 1.2$, and for the three-dimensional version of the cube example these parameters are $\alpha_{gp} = 2$, $N_{FN} = 729$, $n_{gp} = 4$, and $\alpha_s = 2.0$.

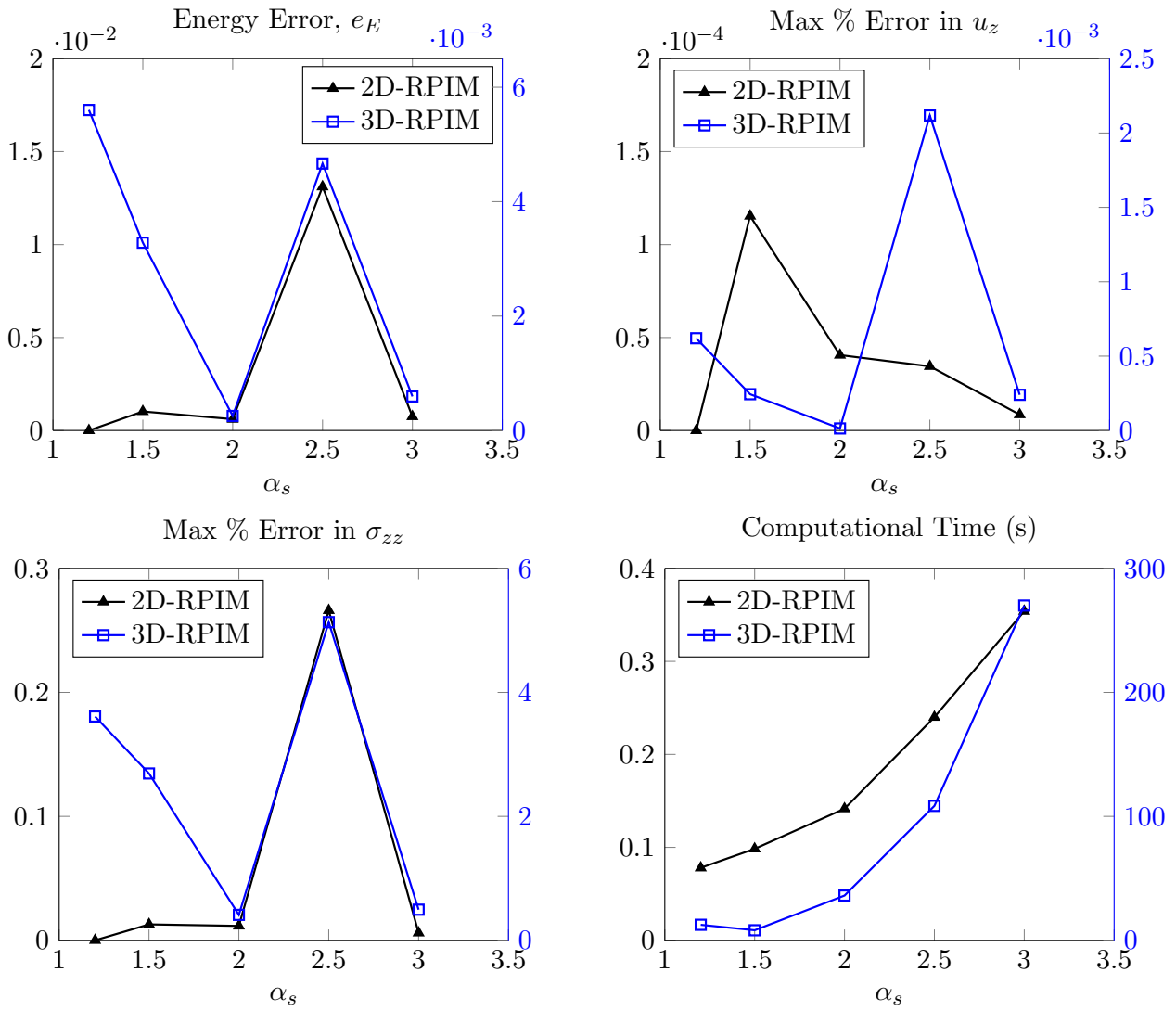


Figure 4.25: These plots show effect of α_s on energy error, maximum percentage error in u_z , maximum percentage error in σ_{zz} , and the computational time for two- and three-dimensional RPIM models of the cube. The parameters other than α_s for the square are $N_{\text{FN}} = 289$, $n_{\text{gp}} = 4$, $\alpha_c = 0.71$, $q = 1.03$, $d_c = 2.0$ and $\alpha_{\text{gp}} = 13$, and for the cube are $N_{\text{FN}} = 729$, $n_{\text{gp}} = 4$, $\alpha_c = 0.71$, $q = 1.03$, $d_c = 2.0$ and $\alpha_{\text{gp}} = 2$.

4.3.2.2 Optimisation

The converged cases of the two- and three-dimensional models of the cube, from the previous part, are used in the optimisation study here where the RPIM shape parameters, i.e. α_c and q are changed to find the combination that gives the most accurate solution for each of the converged cases.

Two-dimensional Cube

For the two-dimensional model of the cube under uniform compression, Figure 4.26 shows the change of error indicators with changing α_c and q for both when polynomial terms are and are not included in the RPIM shape function calculations.

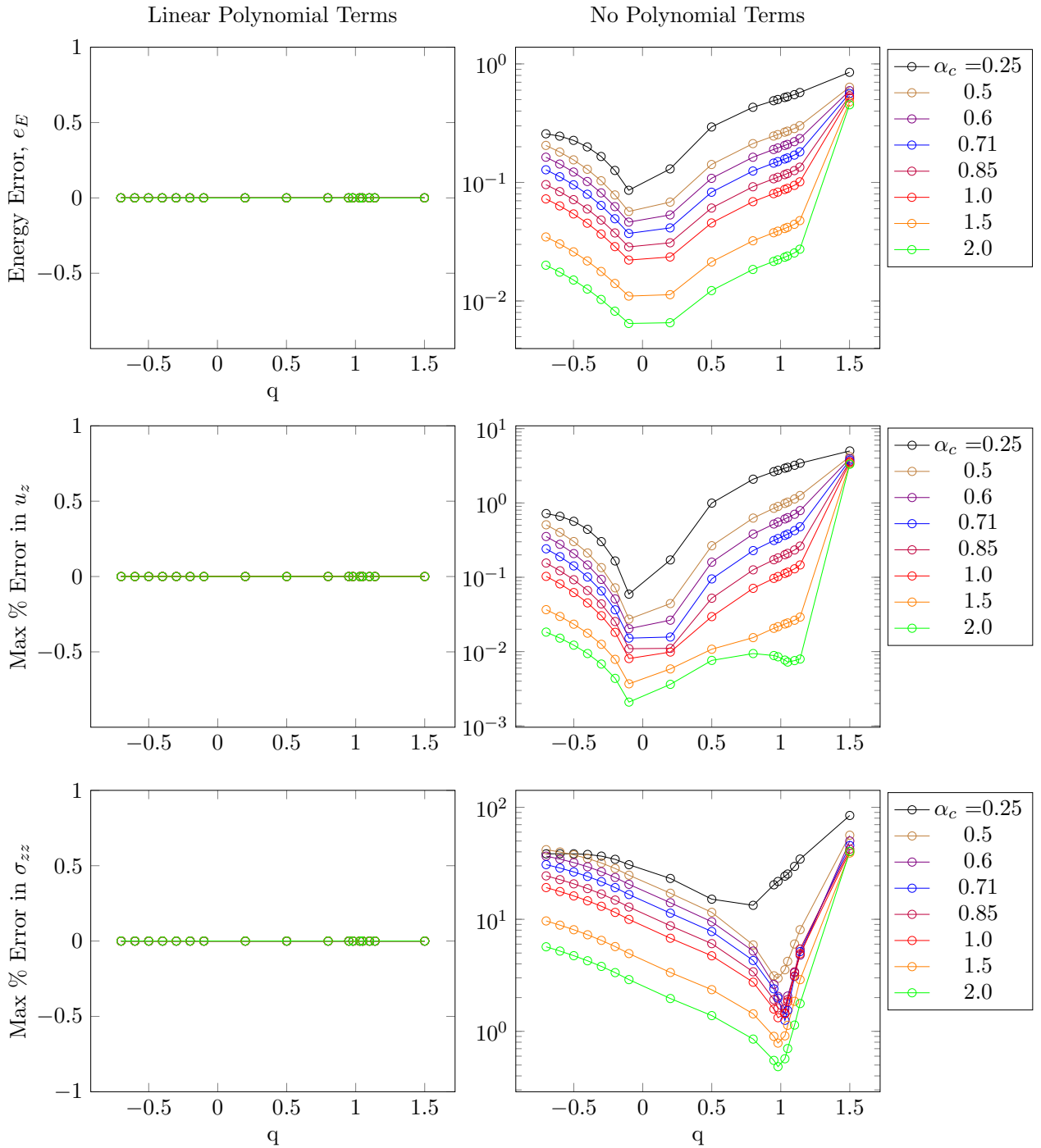


Figure 4.26: The effect of α_c and q on the energy error, maximum percentage error in u_z , and maximum percentage error in σ_{zz} of the two-dimensional version of the cube. The left plots are for the case with linear polynomial included and the right plots are for when no polynomial is included in the RPIM shape function calculations. Here, $N_{FN} = 289$, $n_{gp} = 4$, $\alpha_s = 1.2$, $d_c = 2.0$, and $\alpha_{gp} = 13$.

As can be seen in Figure 4.26, the error indicators on the left plots are zero, where linear polynomial terms are included in the shape function calculations. This means that 100% accuracy is reached for the two-dimensional model of the cube for any combination of α_c and q , as long as linear polynomial terms are used in the shape function calculations. For the plots on the right hand side of Figure 4.26, on the other hand, 100% accuracy is not reached and patterns of error changing with q and α_c can be seen. For example for the energy error plot on the top right, it is clear that increasing α_c

increases the overall accuracy; this is true for maximum percentage error in u_z and σ_{zz} as well. In addition to that, a clear minimum error can be seen for every α_c in each of the plots on the right hand side.

While a minimum error exists for each of the error indicators on the right plots of Figure 4.26, but values of q for the minima in the energy error and maximum percentage error in u_z do not match the one in the maximum percentage error in σ_{zz} . For the energy error and maximum percentage error in u_z , $q = -0.1$ gives the minimum error value, whereas, for the maximum percentage error in σ_{zz} , $q = 0.98$ gives the minimum error value. In order to make the best choice for q , the minimum for the error indicator that has the highest overall error is used, i.e. $q = 0.98$.

Three-dimensional Cube

The next optimisation analysis is carried out for the three-dimensional cube under uniform compression where the results are presented in Figure 4.27. The outline of this figure is similar to all the previous optimisation figures so far. In other words there are two columns where the left one shows the change of error indicators by the RPIM shape parameters for when linear polynomial terms are included in the shape function calculations, and the right column shows the ones for which no polynomial terms are included in the shape function calculations.

Looking at the plots in the right column of Figure 4.27, it can be seen that for the energy error and maximum percentage error in σ_{zz} as α_c increases from 0.25 to 2.0, the error decreases, except when q is near the minimum error. Near the region of the minimum error, i.e. $q = 0.98$, the error decreases as α_c goes from 0.25 to 0.71 and then it increases as α_c goes from 0.71 to 2.0, therefore, for these two error indicators, the minimum error is reached at $\alpha_c = 0.71$ and $q = 0.98$. For the maximum percentage error in u_z , the error continuously decreases as α_c increases from 0.25 to 2.0, and as is clear from the plot, there is a minimum at $q = 0.98$. While the optimum choice of q matches between all the error indicators on the right plots of Figure 4.27, their optimum choice of α_c does not match, however, given that the overall error in σ_{zz} is higher, the optimum α_c for this set of results is chosen to be 0.71.

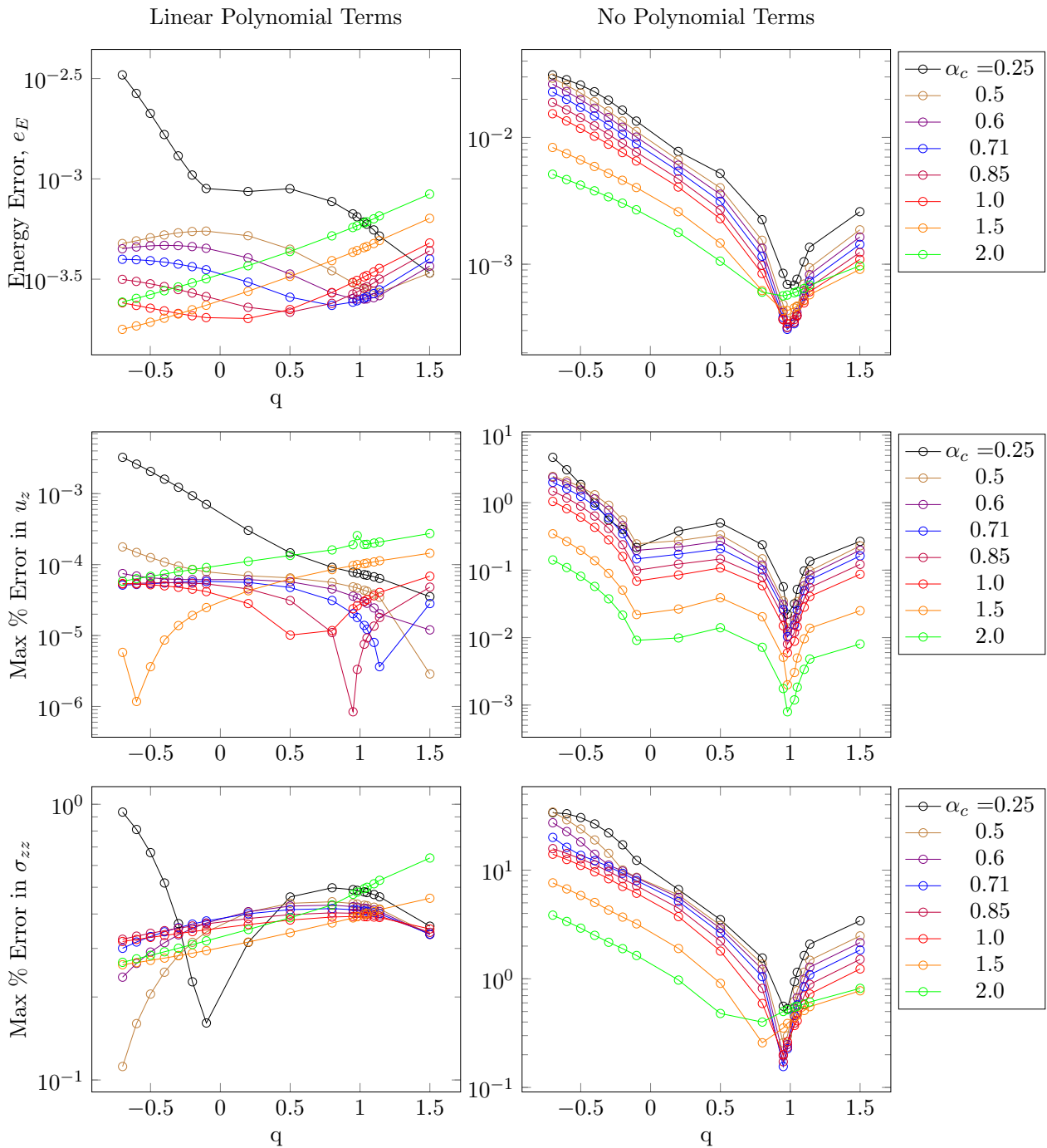


Figure 4.27: The effect of α_c and q on the energy error, maximum percentage error in u_z , and maximum percentage error in σ_{zz} of the three-dimensional version of the cube. The left plots are for the case with linear polynomial included and the right plots are for when no polynomial is included in the RPIM shape function calculations. Here, $N_{\text{FN}} = 729$, $n_{\text{gp}} = 4$, $\alpha_s = 2.0$, $d_c = 2.0$, and $\alpha_{\text{gp}} = 2$.

The next discussion about Figure 4.27 is on the left column of plots, where linear polynomial terms are included in the RPIM shape function calculations. Comparing the vertical axis of the left and right plots of this figure, it is clear that addition of the polynomial terms increases the accuracy of the solutions, however, at the same time the clear pattern observed on the right plots is distorted. This distortion removes the unique choice of q for all the values of α_c ; now the optimum choice has to be done case by case. For example for the energy error, as α_c changes the value of q that provides the

minimum error changes as well, and the trend by which it changes is not the same as the ones for the other two error indicators. Therefore, to choose a sensible combination of α_c and q , the error indicator with the higher overall value is chosen, i.e. the maximum percentage error in σ_{zz} , which leads to the choice of $q = -0.6$ and $\alpha_c = 0.5$.

Comparing the optimisation results from the cube example to the beam example, some similarities in terms of RPIM optimum shape parameters can be seen when no polynomial terms are included, however, when the linear polynomial terms are added, no similarities are found except the fact that overall accuracy increases.

4.3.3 Circle/Cylinder

The cylinder under a uniform compressive line force is the last example of this chapter, where the introduced optimisation algorithm for the RPIM codes is applied.

4.3.3.1 Convergence

The first set of plots for the two- and three-dimensional models of the cylinder are shown in Figure 4.28 and Figure 4.29 where the effect of α_{gp} , n_{gp} , and N_{FN} on the percentage error of reaction force is presented. Here, while N_{FN} , α_{gp} and n_{gp} are changing, the other RPIM parameters are fixed at $\alpha_c = 0.71$, $q = 1.03$, $d_c = 2.0$, and $\alpha_s = 2.0$ because as explained in subsection 4.2.2.2, value of α_c , q , and α_s are taken from [20], as a starting value, which later will be changed in the optimisation process; and the value of d_c is fixed at 2.0 so the accuracy of the solution based on Equation 4.18 becomes dependent on α_c and q only.

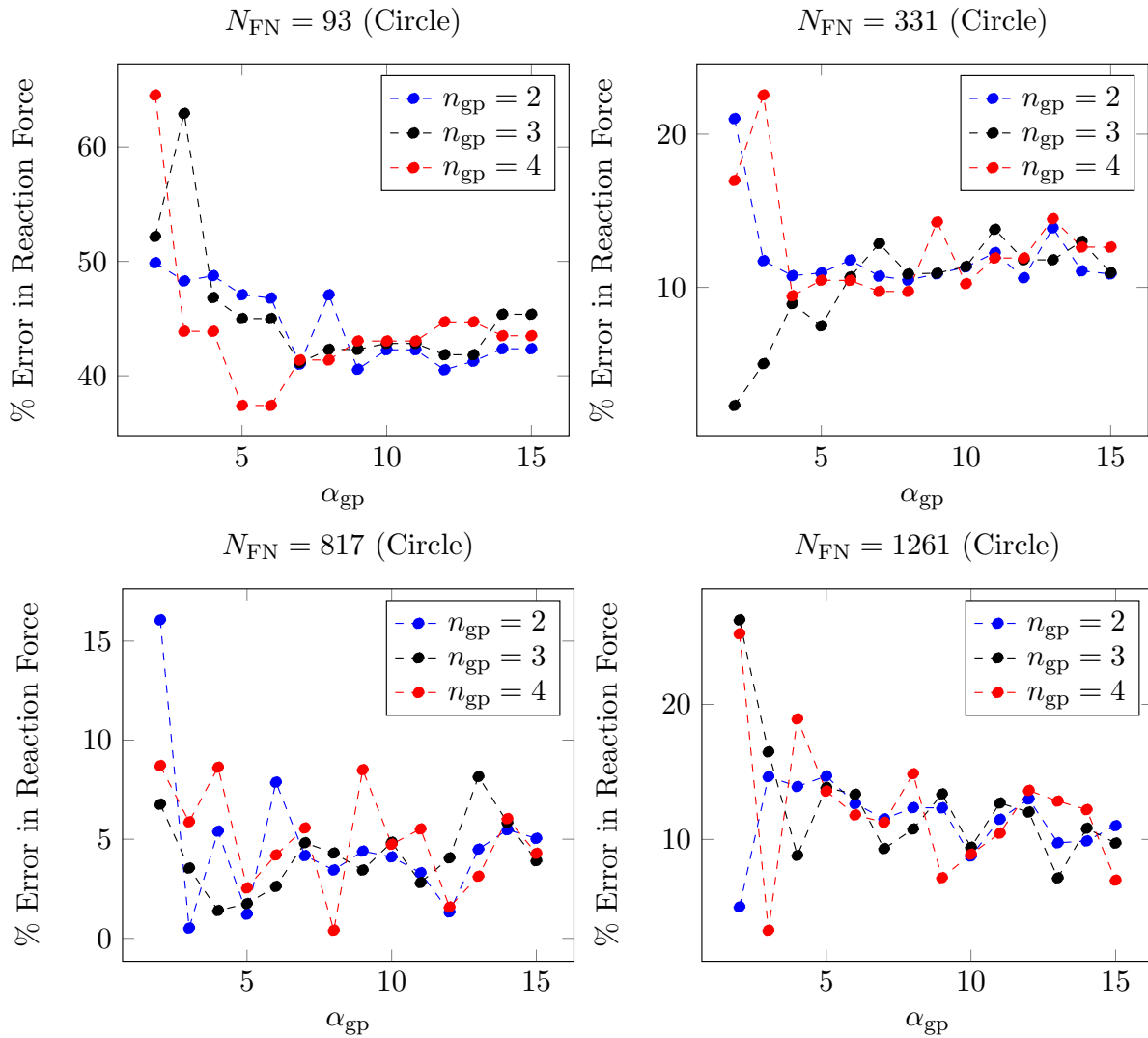


Figure 4.28: Percentage error of the computed reaction force from the 2D RPIM code for the circle example versus the α_{gp} factor from Equation 4.41. The plots in this figure also show the effect of N_{FN} and n_{gp} on the percentage error.

Similar to the cube and beam examples, the error indicator in Figure 4.28 & Figure 4.29 show fluctuations for every N_{FN} and n_{gp} as α_{gp} changes. Here the fluctuations reduce as the value of α_{gp} increases but increase as N_{FN} increases. The presence of the fluctuations in the error by changing α_{gp} , and increase in the strength of the fluctuations by increasing the total number of field nodes for all three examples seem to indicate that relative location of the field nodes and the integration points have a significant influence on the accuracy of the RPIM method. Please note this is a different argument from the uniform or non-uniform distribution of the field nodes because in all the examples here the nodes are distributed uniformly. The method discussed in this chapter focuses on finding the best RPIM parameters for any given problem using a step-by-step approach, not the relationship between the relative positions of the integration points and the field nodes with the error; this can be a future work on this method.

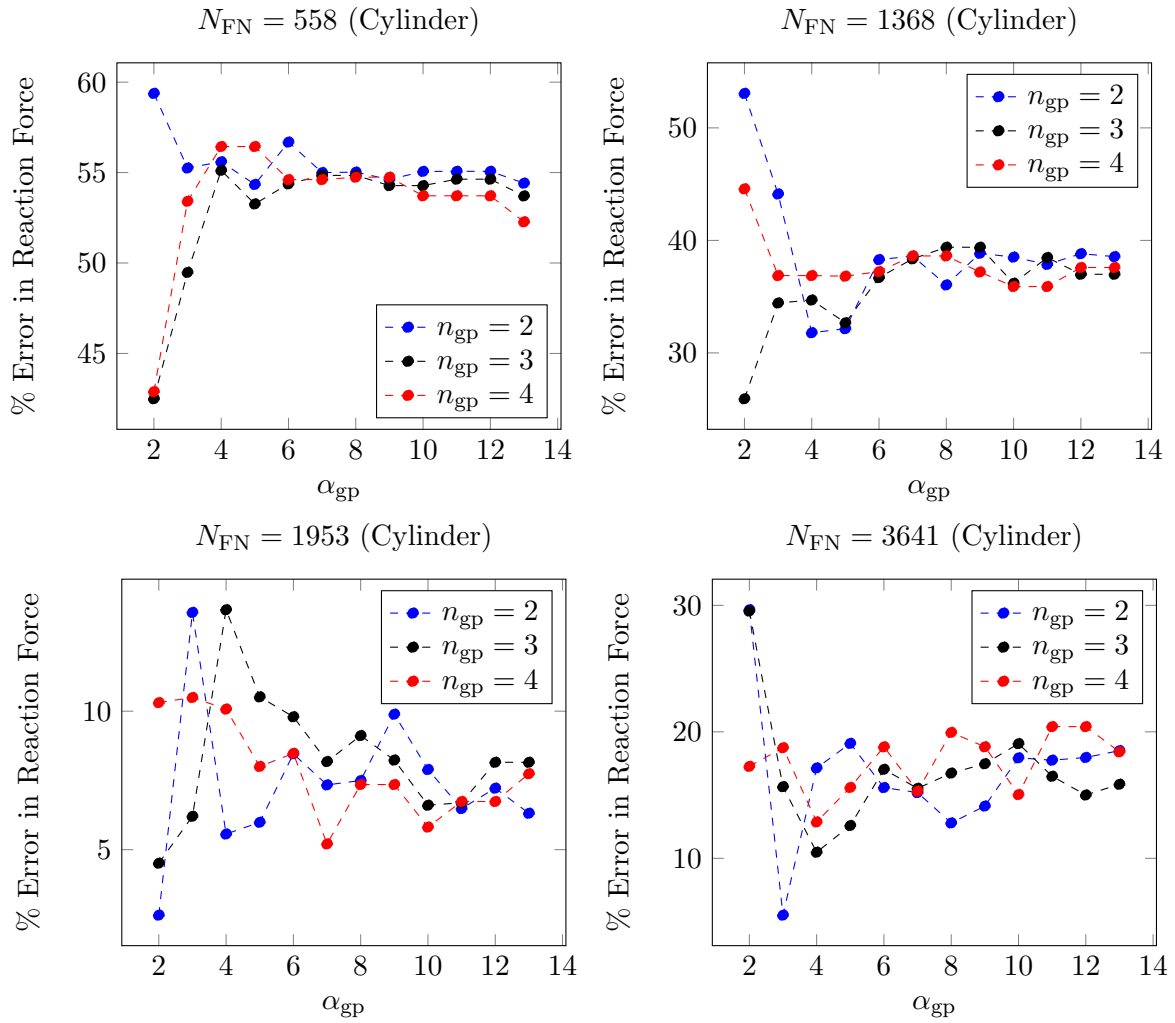


Figure 4.29: Percentage error of the computed reaction force from the 3D RPIM code for the cylinder example versus the α_{gp} factor from Equation 4.41. The plots in this figure also show the effect of N_{FN} and n_{gp} on the percentage error.

The criteria used here to choose the best value of α_{gp} for every N_{FN} and n_{gp} are i) the one that gives the minimum percentage error in reaction force, while ii) best matches the results from FE. A summary of the best choices of α_{gp} for each N_{FN} and n_{gp} is given in Table 4.3 and shown in Figure 4.30 & Figure 4.32.

Table 4.3: The best choice of α_{gp} for a given N_{FN} and n_{gp} for the circle and cylinder example.

Circle	$n_{gp} \backslash N_{FN}$	93	331	817	1261	
		2	12	8	3	2
	3	7	2	4	13	
	4	5	4	8	3	
Cylinder	$n_{gp} \backslash N_{FN}$	558	1368	1953	3641	
		2	5	4	2	3
		3	2	2	2	4
		4	2	10	7	4

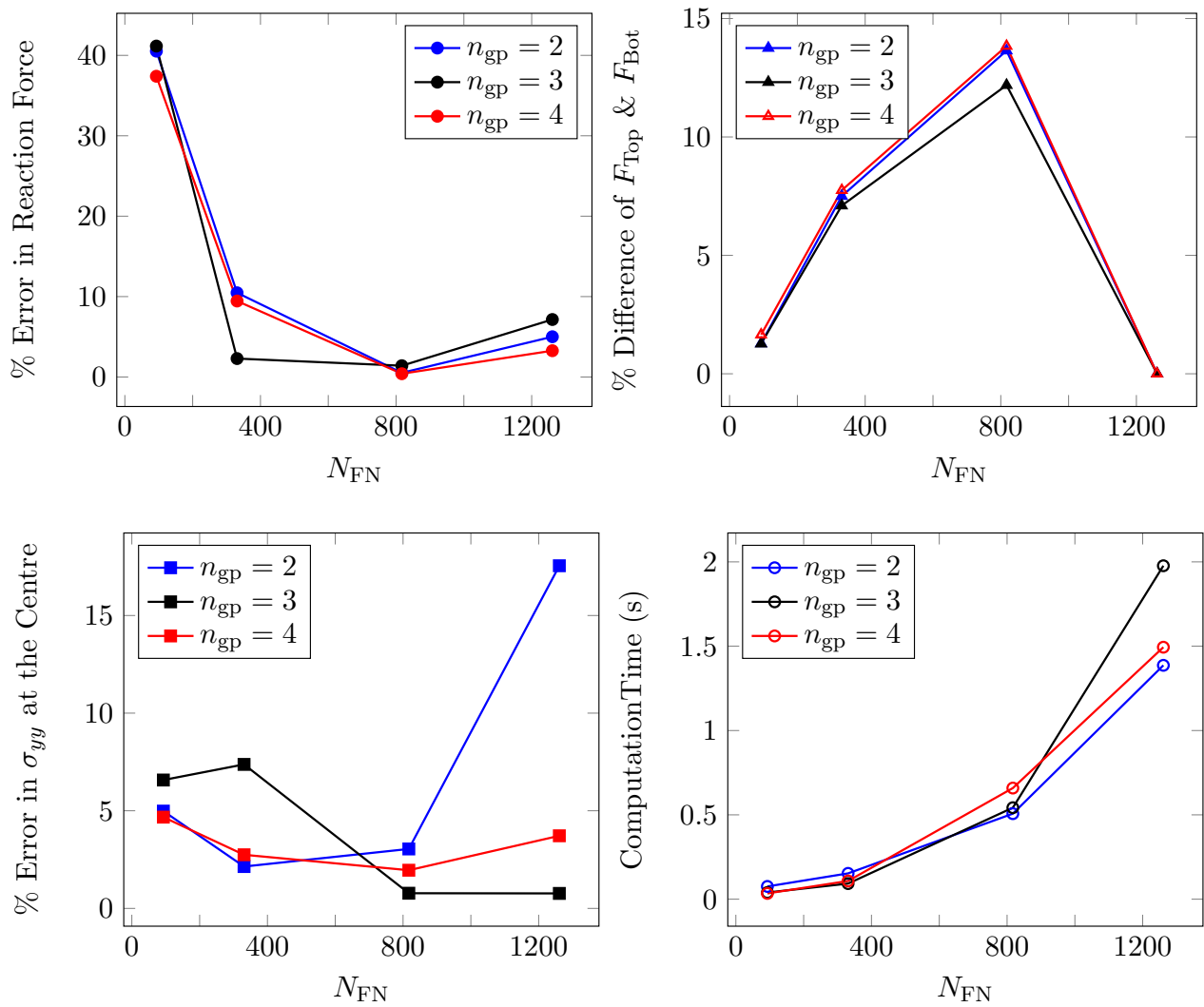


Figure 4.30: The plots show convergence of the RPIM model of the circle using the percentage error in the reaction force, percentage difference between the top and bottom forces and the percentage error in σ_{yy} at the centre of the circle for every n_{gp} . The bottom right plot shows the corresponding cpu time.

The plots here in Figure 4.30 show the results used for the convergence study of the circle under the compressive point load. It is clear from the plot of the percentage error in the reaction force that for all of the n_{gps} convergence is reached at $N_{FN} = 817$. Looking at the percentage error in σ_{yy} at the centre of the circle based on the results from FE, a convergence at about $N_{FN} = 817$ for $n_{gp} = 3$ and 4 is observed but not for $n_{gp} = 2$ which eliminates it from further consideration. However, for the percentage difference between the top and bottom forces, only at $N_{FN} = 1261$ the minimum error is reached. Therefore, given that at $N_{FN} = 1261$ in addition to convergence of the reaction force and σ_{yy} , the best match between the computed top and bottom forces is also achieved, $N_{FN} = 1261$ is chosen as the converged solution. The best choice of n_{gp} for the converged solution is 4 because the simulation time for it is less than for $n_{gp} = 3$.

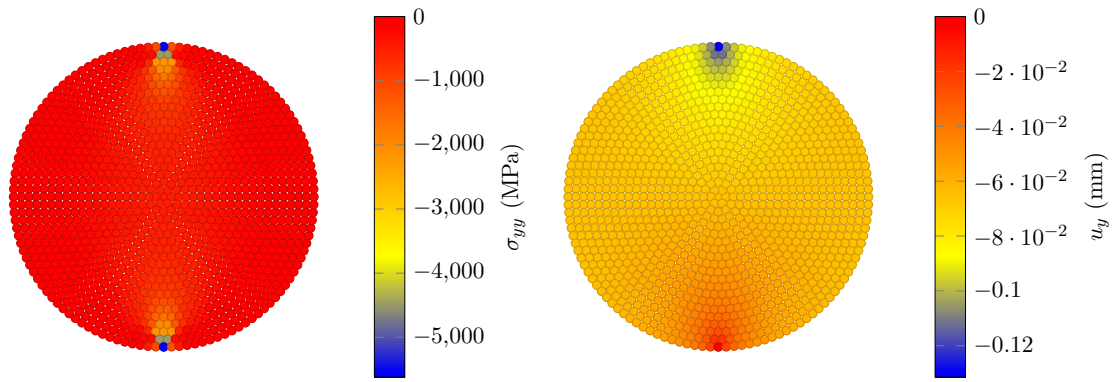


Figure 4.31: The vertical displacement and stress profiles of the two-dimensional circle for the converged case in the RPIM code.

Figure 4.31 shows the vertical stress and displacement distribution of the converged solution for the circle. As expected, in addition to the symmetry there are two stress concentration points on the top and bottom surfaces of the circle at the location of the applied and reaction forces.

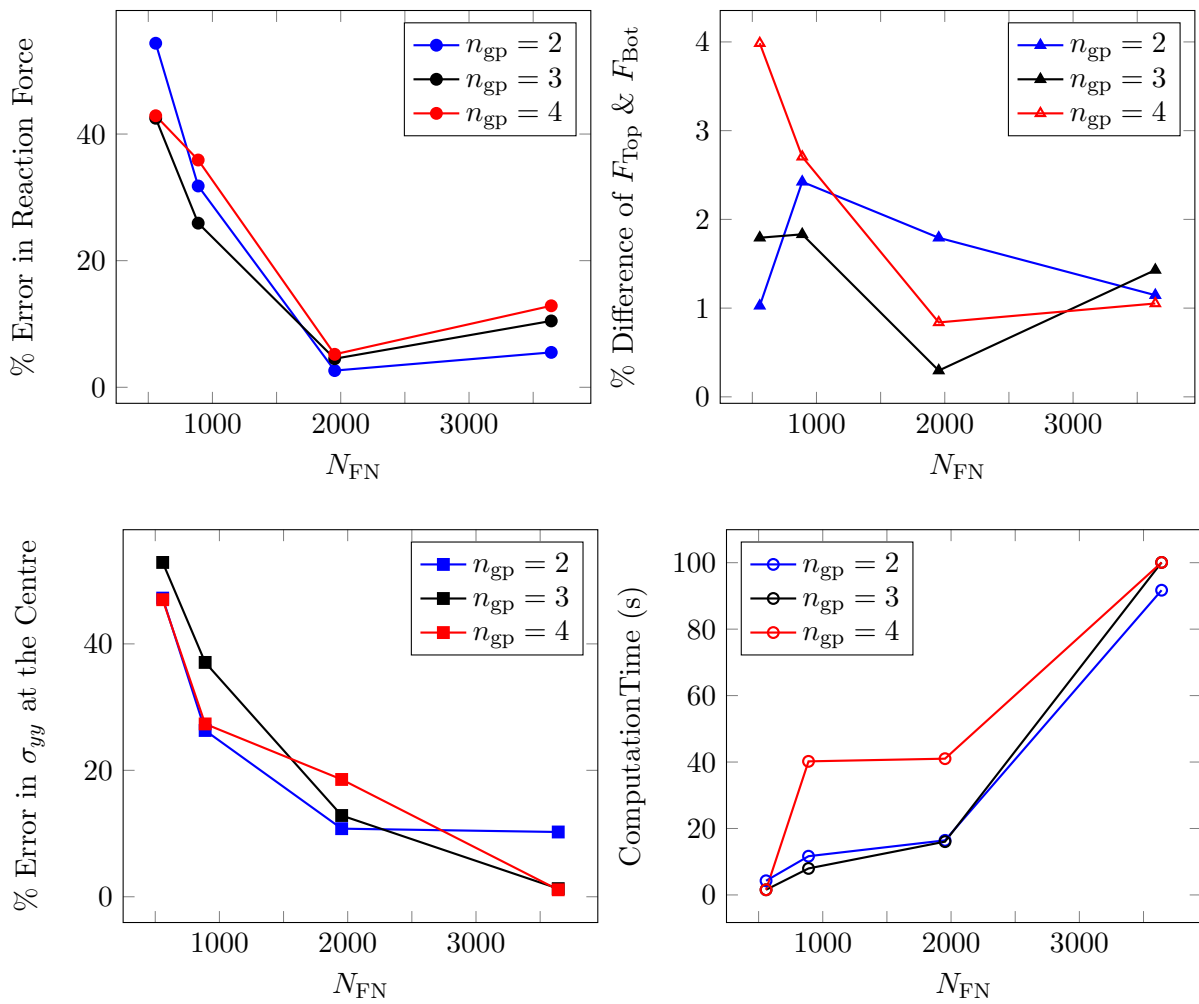


Figure 4.32: The plots show convergence of the RPIM model of the cylinder using the percentage error in the reaction force, percentage difference between the top and bottom forces and the percentage error in σ_{yy} at the centre of the circle for every n_{gp} . The bottom right plot shows the corresponding cpu time.

For $n_{gp} = 2$ in Figure 4.32, the percentage error in the reaction force has converged at $N_{FN} = 1953$, however, at this N_{FN} the percentage error in σ_{yy} is above 10% which is accompanied with percentage difference of 2% between the top and bottom forces. Looking at $N_{FN} = 3641$, while the difference between the top and bottom forces is reduced to about 1% but the percentage error in σ_{yy} has stayed above 10%, therefore, $n_{gp} = 2$ is eliminated from further consideration.

For $n_{gp} = 3$ and 4, a convergence is reached at about $N_{FN} = 1953$ where the percentage difference between the top and bottom forces is less than or equal to 1%. However, for the percentage error in σ_{yy} at the centre of the cylinder, the error at $N_{FN} = 1953$ is above 10%. At $N_{FN} = 3641$ on the other hand, the percentage error in σ_{yy} at the centre of the cylinder reaches almost 0% while the percentage difference between the top and bottom forces becomes 1% for $n_{gp} = 4$ and 1.5% for $n_{gp} = 3$. The percentage error in the reaction force at $N_{FN} = 3641$ is slightly higher than $N_{FN} = 1953$, however, it is acceptable because the increase in the reaction force error is much less than the decrease in the σ_{yy} error.

The difference between $n_{gp} = 3$ and 4 for $N_{FN} = 3641$ is very small, however, because $n_{gp} = 4$ gives a lower percentage error in the difference between the top and bottom forces, it is the chosen one. Even though the simulation time for $N_{FN} = 3641$ is much higher than $N_{FN} = 1953$ but the error in σ_{yy} cannot be ignored. The corresponding vertical stress and displacement profile of the cylinder for the chosen case are shown in Figure 4.33.

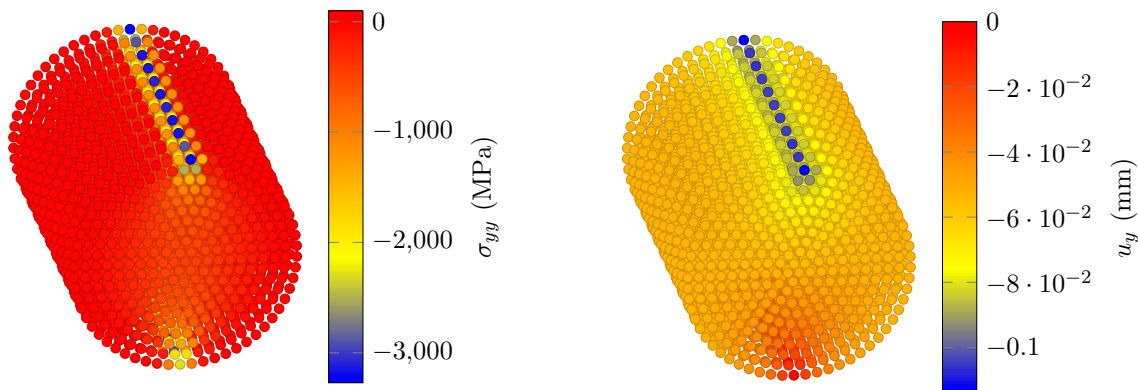


Figure 4.33: The vertical displacement and stress profiles of the three-dimensional cylinder for the converged case in the RPIM code.

Once the converged solution is found for the two- and three-dimensional cylinders, size of the support domain, i.e. α_s , is varied in order to investigate its effect on the accuracy of the solution and the computational time. Figure 4.34 shows variation of the error indicators and the computational time with change in α_s for both the two- and three-dimensional RPIM models of the cylinder.

Looking at the results for the two-dimensional model of the cylinder first, i.e. the black lines

in Figure 4.34, it seems that the best value of α_s from each error indicator does not match. For instance, in the plot for the percentage error in the reaction force, $\alpha_s = 1.5$ gives the minimum error which is in agreement with the percentage difference between the top and bottom forces, however, for the percentage error in σ_{yy} , $\alpha_s = 1.5$ gives the highest error. Hence, taking into account all of these differences, the best choice of α_s would be 2.0 because it provides a similar error in both reaction force and σ_{yy} while having a percentage difference between the top and bottom forces of less than 0.02%. As a summary for the convergence study of the two-dimensional model of the cylinder (or the circle), the best solution is obtained for $N_{FN} = 1261$, $n_{gp} = 4$, $\alpha_s = 2.0$ and $\alpha_{gp} = 3$ which is later used in the optimisation study of this example.

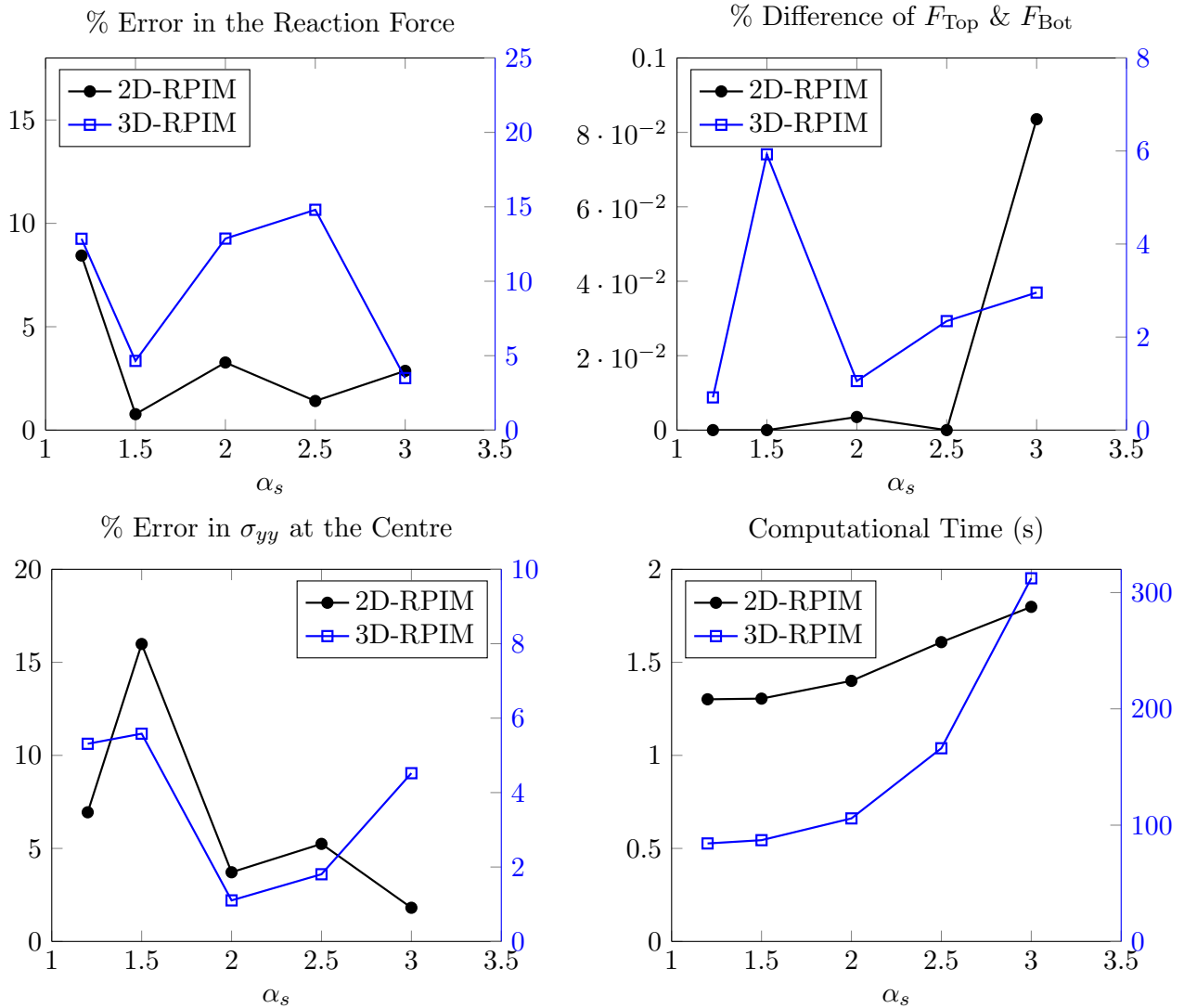


Figure 4.34: These plots show effect of α_s on the percentage error in the reaction force, percentage difference between the top and bottom forces, percentage error in σ_{yy} at the centre of the cylinder, and the computational time for two- and three-dimensional RPIM models of the cylinder. The parameters other than α_s for the circle are $N_{FN} = 1261$, $n_{gp} = 4$, $\alpha_c = 0.71$, $q = 1.03$, $d_c = 2.0$ and $\alpha_{gp} = 3$, and for the cylinder are $N_{FN} = 3641$, $n_{gp} = 4$, $\alpha_c = 0.71$, $q = 1.03$, $d_c = 2.0$ and $\alpha_{gp} = 4$.

For the three-dimensional model of the cylinder, i.e. the blue lines in Figure 4.34, the best choice of α_s for each error indicator does not match, similar to the two-dimensional model of the cylinder.

Comparing all the error indicators, it can be seen while $\alpha_s = 3.0$ gives an error of less than 5% for all the error indicators but the simulation time for it is above 300s which makes it very inefficient. Therefore, considering the simulation time, the next best option is $\alpha_s = 1.5$ because even though it has the highest percentage error in σ_{yy} and difference between the top and bottom forces, in all the cases the error value is around 6%. Whereas for $\alpha_s = 1.2, 2.0,$ and 2.5 the maximum error reached is near 15%. Therefore, given the consistency in the error and the low simulation time, $\alpha_s = 1.5$ is the best choice. Additionally, as it becomes more apparent later on, changing the RPIM shape parameters improves the accuracy significantly. In summary, for the three-dimensional model of the cylinder the converged solution parameters are $N_{FN} = 3641, n_{gp} = 4, \alpha_s = 1.5,$ and $\alpha_{gp} = 4$ which will be used for the optimisation study of this example.

4.3.3.2 Optimisation

Figure 4.35 & Figure 4.36 show how the three error indicators used for the example of the cylinder change with changing the RPIM shape parameters. These figures also show the effect of using linear polynomial terms in the shape function calculations on the accuracy of the results.

Two-dimensional Cylinder

Plot of the percentage error in the reaction force on the right side of Figure 4.35 shows two outstanding minima for $\alpha_c = 1.5$ at $q = -0.4$ and -0.1 . Given that percentage error in the reaction force at $q = -0.1$ and $\alpha_c = 1.5$ is the minimum ($\sim 0.16\%$) it is the optimum choice for this error indicator, however, for the other two error indicators the same outcome is not true. For example, for the percentage difference between the top and bottom forces on the right hand side, the optimum choice of α_c and q are 2.0 and 0.98, respectively, or for the percentage error in σ_{yy} the optimum α_c and q are 0.5 and 0.98. Given the difference in the behaviour of the error indicators with change of RPIM shape parameters, a compromise has to be made when choosing the optimum values of α_c and q for this case. The choice that satisfies all the error indicators for the case when no polynomial term is included, is $\alpha_c = 1.0$ and $q = 1.03$ with the corresponding error indicators as i) error in reaction force $\approx 3.5\%$, ii) percentage difference between the top and bottom forces $\approx 0.16\%$, and iii) percentage error in $\sigma_{yy} \approx 1.6\%$.

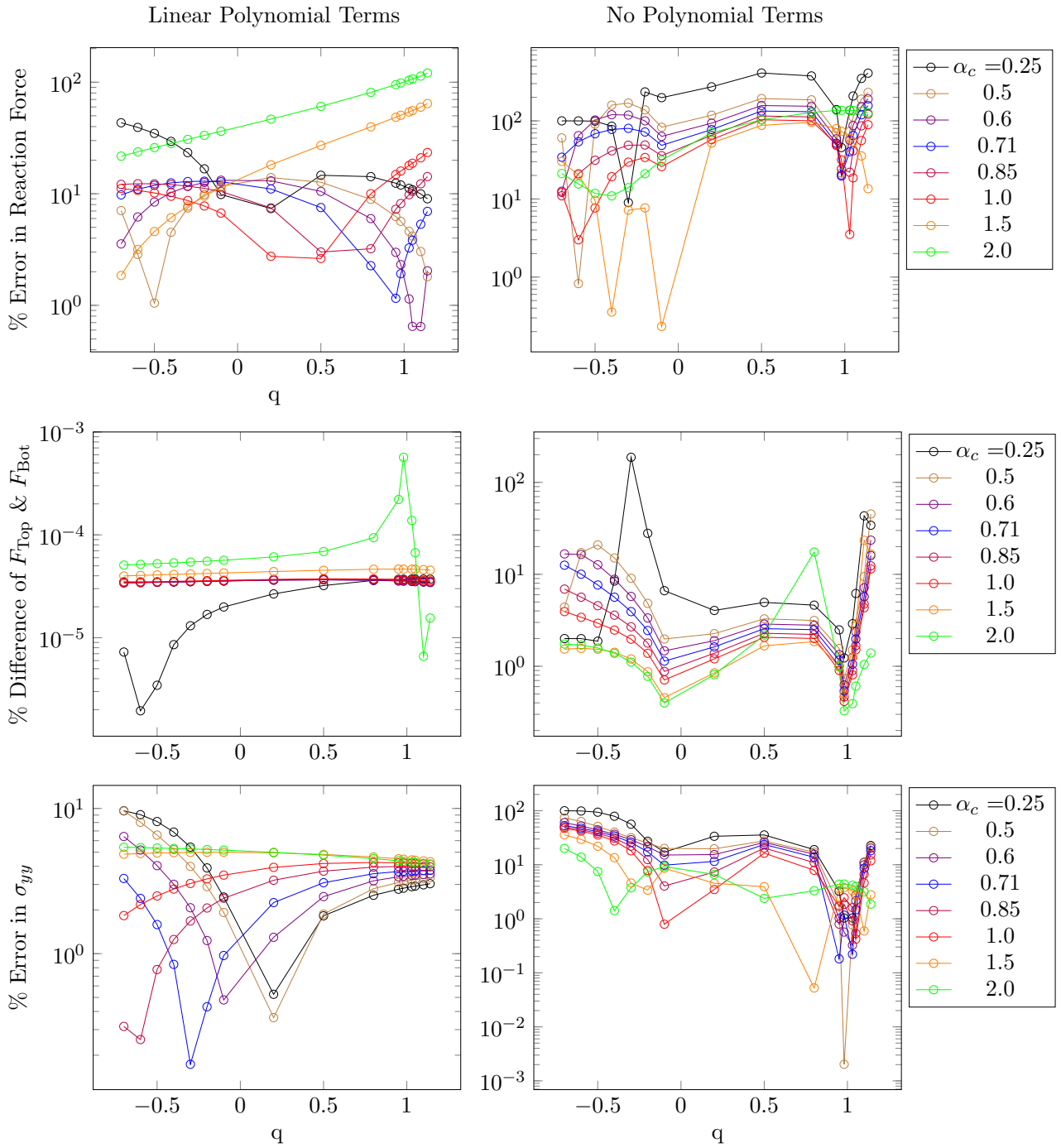


Figure 4.35: The plots here show the effect of α_c and q on the percentage error in the reaction force, percentage difference between the top and bottom forces, and the percentage error in σ_{yy} at the centre of the two-dimensional model of the cylinder. The left plots are for the case with linear polynomial included and the right plots are for when no polynomial is included in the RPIM shape function calculations. Here, $N_{\text{FN}} = 1261$, $n_{\text{gp}} = 4$, $\alpha_s = 2.0$, $d_c = 2.0$, and $\alpha_{\text{gp}} = 3$.

As can be seen from the comparison of the plots on the left and right columns of Figure 4.35, when linear polynomial terms are added to the shape function calculations, the overall accuracy of the results has noticeably increased. For the percentage difference between the top and bottom forces, except for $\alpha_c = 0.25$ and 2.0, the error does not change with q for all the other α_c s, and its value is around 0.000018%. Even the maximum percentage difference between the top and bottom forces

is less than 0.001% which makes any combination of α_c and q acceptable for this error indicator, therefore, to choose the best combination of α_c and q the other two error indicators are considered. Looking at the percentage error in σ_{yy} , it is clear that to obtain an error below 1%, α_c has to be less than or equal to 0.85 while q is less than 0.5. For the reaction force, on the other hand, the error is below 1% for when q is near 1.0, except for when $\alpha_c = 0.5$ and $q = -0.5$, however, at this point the error in σ_{yy} becomes about 10% which discards this combination. Considering all the possible cases, $\alpha_c = 0.6$ and $q = 1.03$ is the chosen combination, not only percentage difference between the top and bottom forces, and percentage error in the reaction force are below 1% but also the corresponding percentage error in σ_{yy} is less than 4%.

Three-dimensional Cylinder

The plots for the three-dimensional model of the cylinder, Figure 4.36, are very different to the ones from the two-dimensional case, Figure 4.35; not only the errors are higher (because of the numerical errors in the third dimension) but also the patterns are different.

Looking at the plots on the right side of Figure 4.36, it is clear that all the error indicators have a minimum near $q = 1.0$, however, for the percentage error in σ_{yy} this minimum only exists for α_c s from 0.25 to 0.71. Considering that $\alpha_c = 1.5$ and 2.0 for $q = 1.03$ are the only viable combinations for the percentage difference between the top and bottom forces, the combination with the lowest error in this error indicator is the chosen ones for when no polynomial terms are included, i.e. $\alpha_c = 2.0$ and $q = 1.03$. Even though at this combination the percentage error in reaction force and σ_{yy} are about 4% and 10%, respectively, but since the difference between the top and bottom is a measure of equilibrium, it is very important for its error to be low.

As has been shown in all the previous examples, addition of linear polynomial terms in the shape function calculations improves the accuracy of the solutions significantly which is also apparent here in Figure 4.36. Comparison of the patterns in the error indicators on the left side of Figure 4.36 shows an increase in the overall error as α_c increases, however, for the reaction force and σ_{yy} there are a number of minima which appear as q becomes more negative. In order to keep all the error indicators in the vicinity or less than 1%, the best combination of the RPIM shape parameters are $\alpha_c = 0.6$ and $q = -0.7$ which leads to i) error in reaction force $\approx 0.28\%$, ii) percentage difference between the top and bottom forces $\approx 1.5\%$, and iii) percentage error in $\sigma_{yy} \approx 1.0\%$.

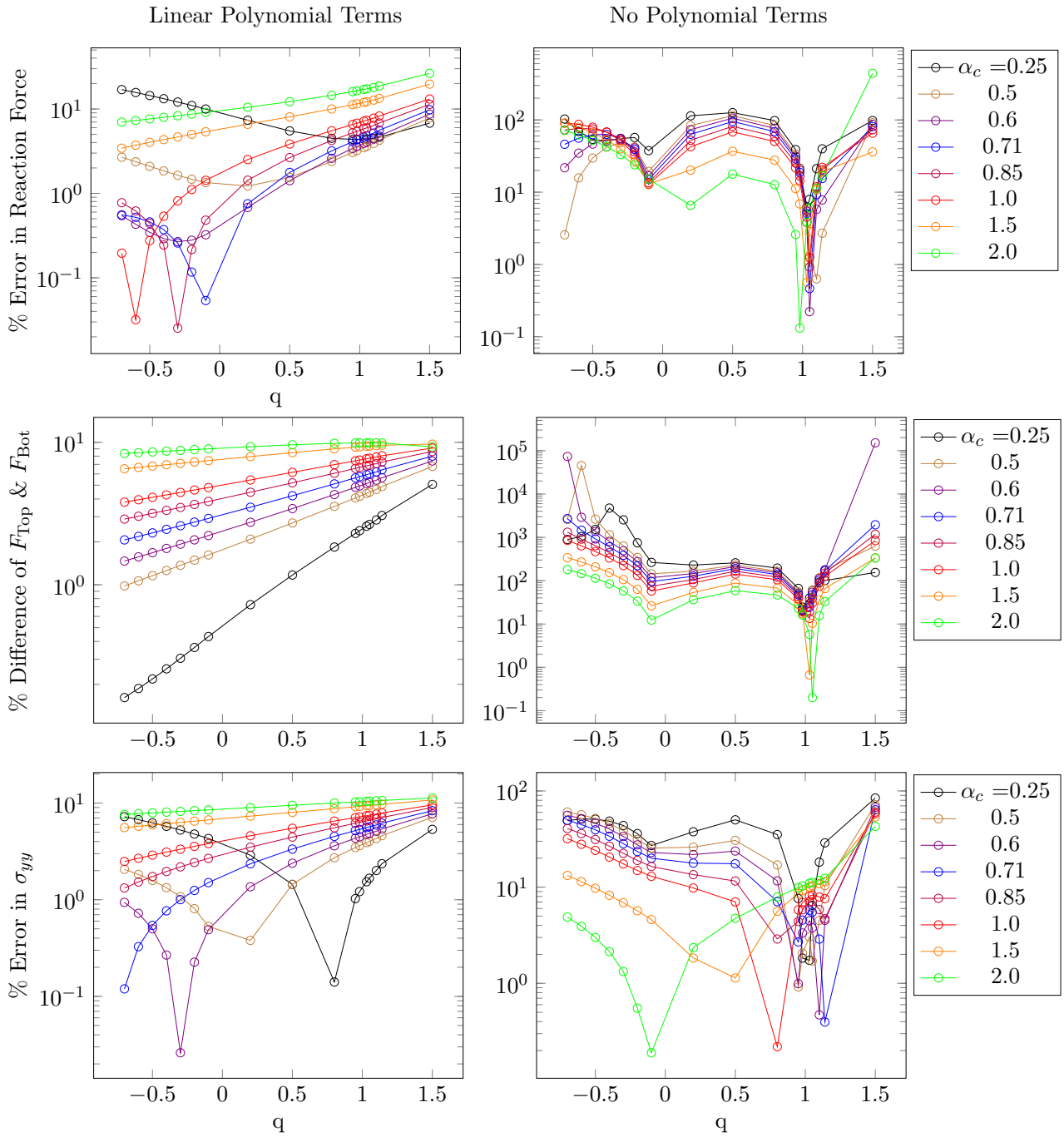


Figure 4.36: The plots here show the effect of α_c and q on the percentage error in the reaction force, percentage difference between the top and bottom forces, and the percentage error in σ_{yy} at the centre of the three-dimensional model of the cylinder. The left plots are for the case with linear polynomial included and the right plots are for when no polynomial is included in the RPIM shape function calculations. Here, $N_{FN} = 3641$, $n_{gp} = 4$, $\alpha_s = 1.5$, $d_c = 2.0$, and $\alpha_{gp} = 4$.

4.4 Conclusion

In summary, in this chapter a step-by-step method for finding the converged solution and optimum shape parameters of the general MQ-RPIM method was introduced, which is applicable to different engineering single body problems, even if the analytical solution is not known. The flow chart

in Figure 4.3 gives an overview of the method introduced here which was successfully applied to three examples in both two- and three-dimensional forms. A summary of the optimum choices of MQ-RPIM shape parameters, i.e. α_c and q is shown in Table 4.4. As is clear from these results, there is no universal optimum for the MQ-RPIM shape parameters, so the need for the introduced convergence/optimisation algorithm is clearly felt.

Table 4.4: The summary of optimum RPIM shape parameters for the examples in this chapter.

With Linear Polynomial	Shape Parameters	2D-Beam	3D-Beam	Square	Cube	Circle	Cylinder
	α_c	0.85	0.25	all	0.5	0.6	0.6
	q	1.5	> 0.7	all	-0.6	1.03	-0.7
Without Polynomial Terms	Shape Parameters	2D-Beam	3D-Beam	Square	Cube	Circle	Cylinder
	α_c	1.5	2.0	2.0	0.71	1.0	2.0
	q	0.98	1.03	0.98	0.98	1.03	1.03

While the results from this chapter show the way that the introduced algorithm works for a range of different problems, a number of general conclusions are drawn about the MQ-RPIM method, which agrees with the literature findings:

- RPIM method is slower than finite element method for the same number of nodes, however, it reaches convergence in a much faster rate than finite element method, compensating for its slowness.
- RPIM method is more flexible in modelling complex geometries and non-uniform node distribution.
- Use of linear polynomial terms in the shape function calculations is very important because they give a much better accuracy for all the cases.
- In accordance with the previous works on MQ-RPIM [2, 20, 21], value of q near 1 for any given α_c produces the best solution, provided that no polynomial terms are included in the MQ-RPIM shape function calculations. However, when linear polynomial terms are included, the optimum value of q becomes problem dependent, hence requiring the algorithm that was developed here.
- The optimum choice of α_c and q differs between the two- and three-dimensional versions of the same problem, therefore, it has to be taken into account when choosing optimum shape parameters for MQ-RPIM method.

4.5 Table of variables

Table 4.5: Variables and terms used in this chapter and their definitions.

EFG	Element free Galerkin
RPIM	Radial point interpolation method
RVE	Representative volume element
FEM	Finite element method
MQ-	Multi-quadric
IMQ-	Inverse multi-quadric
EXP	Gaussian
TPS	Thin plate spline
r	Radial distance between two points
α_s	A coefficient to define the size of support domain
α_c	MQ-RPIM shape parameter
α_{gp}	Factor for estimating the number of background cells
e_E	Energy error
e_x	Percentage error in x
q	MQ-RPIM shape parameter
d_c	A characteristic length proportional to the nodal spacing near the point of interest
d_s	The characteristic dimension of this domain
Ω	Problem domain
Γ	Boundary of the problem domain
L	Differential operator
σ	Cauchy stress
F^b	Body force vector
\bar{t} and $F^{(t)}$	Surface traction
\bar{u}	Applied displacement
n	Normal vector
ε	Strain vector
D	Material constant matrix
U_s	Displacement vector
R_0	Radial moment matrix
Res	Residual vector
P_m	Polynomial moment matrix
Φ	Matrix of radial basis shape functions
K_{ij}	Noda stiffness matrix
K_{IJ}	Global stiffness matrix
U_J	Global displacement vector
F_I	Global force vector
B	Derivatives of the shape function matrix

N_{FN}	Total number of field nodes in the problem domain
N_{BC}	Total number of background cells in the problem domain
N_{gp}	Total number of quadrature points in the problem domain
ν	Poisson ratio
E	Young's modulus
I_P	The Gaussian approximation of the integral of function f
s_i	Coordinates of the parent space
n_{gp}	Number of quadrature points per direction per background cell
n_{bc_i}	Number of background cells per direction i
L_i	Characteristic length of the problem domain in the i direction
w	Weight values used for the quadrature integration
ζ	Coordinate of the quadrature points in the parent space
J_{ij}	Jacobian matrix
J	Determinant of the Jacobian matrix, i.e. Jacobian
M	Total number of nodes forming the background cell
N_a	Shape function, interpolating x at the Gauss point using the node a of the background cell
X_i^a	the value of x at the background cell node a
$u(\mathbf{x})$	Displacement at \mathbf{x}
n	Number of field nodes in the support domain
ϕ_i	MQ-RPIM shape function of field node i
$R_i(\mathbf{x})$	The radial basis matrix
$p_i(\mathbf{x})$	The monomial in the space coordinate $\mathbf{x}^T = [x, y, z]$
\mathbf{a}, \mathbf{c}	Vector of constants to be determined
P	Applied load in the examples
I	Second moment of area
τ_{xz}	Shear stress in the beam
F_R	Reaction force in the cylinder example
n_R	Number of nodes in the bottom surface of the cylinder

4.6 Bibliography

- [1] O. Bacarreza, D. Abe, M. H. Aliabadi, and N. Kopula Ragavan. Micromechanical modeling of advanced composites. *Journal of Multiscale Modelling*, 04(02):1250005 – (1–20), jun 2012.
- [2] G.R. Liu and Y. T. Gu. A local radial point interpolation method (LRPIM) for free vibration analyses of 2-D solids. *Journal of Sound and Vibration*, 246(1):29–46, 2001.
- [3] R.A. Gingold and J. J. Monaghan. Smoothed particle hydrodynamics: theory and application to non-spherical stars. *Royal Astronomical Society*, 181:375–389, 1977.
- [4] B Nayroles, G Touzot, and P Villon. Generalizing the finite element method : Diffuse approximation and diffuse elements. *Computational Mechanics*, 10:307–318, 1992.

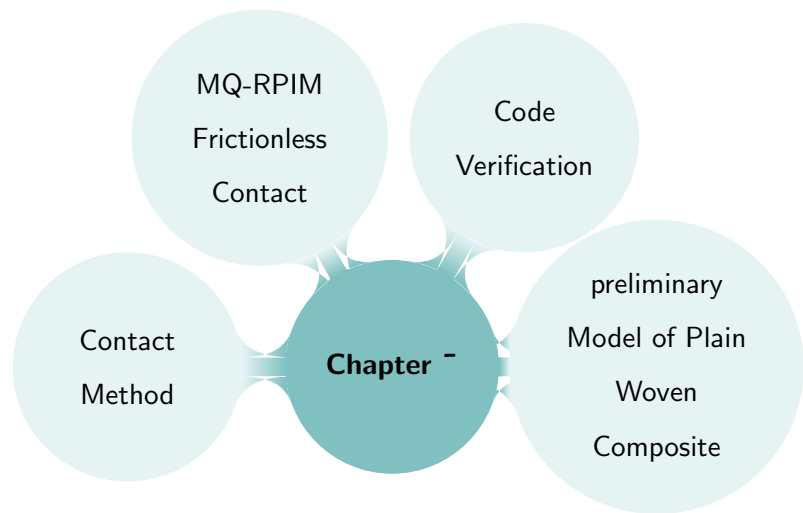
- [5] D.H. McLain. Drawing contours from arbitrary data points. *The Computer Journal*, 17(4):318–324, 1971.
- [6] R.E. Barnhill. Representation and approximation of surfaces. *Mathematical Software III*, 1977.
- [7] By William J Gordon and James A Wixom. Shepard’s method of ”metric interpolation” to bivariate and multivariate interpolation. *Mathematics of Computation*, 32(141):253–264, 1978.
- [8] P. Lancaster and K. Salkauskas. Surfaces generated by moving least squares methods. *Mathematics of Computation*, 37(155):141–158, jul 1981.
- [9] Alexandre Joel Chorin. Numerical study of slightly viscous flow. *Journal of Fluid Mechanics*, 57:785–796, 1973.
- [10] Eugenio Onate. Derivation of stabilized equations for numerical solution of advective-diffusive transport and fluid flow problems. *Computer Methods in Applied Mechanics and Engineering*, 151(97):233–265, 1998.
- [11] E.J. Kansa. Multiquadratics-a scattered data approximation scheme with applications to computational fluid-dynamics-II: solutions to parabolic, hyperbolic and elliptic partial differential equations. *Computers Math. Applic.*, 19(8):147–161, 1990.
- [12] G. R. LIU and Y.T. Gua. A meshfree weak-strong-form (MWS) method for solid and fluid mechanics. *International Journal for Numerical Methods in Fluids*, 46:1025–1047, 2004.
- [13] T Belytschko, YY Lu, and L Gu. Element-free Galerkin methods. *International Journal for Numerical Methods in Engineering*, 37:229–256, 1994.
- [14] Satya N Atluri and Shengping Shen. The meshless Local Petrov-Galerkin (MLPG) method: a simple & less-costly alternative to the finite element and boundary element methods. *CMES*, 3(1):11–51, 2002.
- [15] G. R. LIU and Y. T. GU. *An Introduction to Meshfree Methods and Their Programming*. Springer-Verlag, Berlin/Heidelberg, 2005.
- [16] Lei Gu. Moving Kriging interpolation and element-free Galerkin Method. *International Journal for Numerical Methods in Engineering*, 56(1):1–11, jan 2003.
- [17] G R Liu and Y T Gu. A point interpolation method for two-dimensional solids. *International Journal for Numerical Methods in Engineering*, 50:937–951, 2001.
- [18] J.G. Wang, G.R. Liu, and Y.G. Wu. A point interpolation method for simulating dissipation process of consolidation. *Computer Methods in Applied Mechanics and Engineering*, 190(45):5907–5922, aug 2000.

-
- [19] J G Wang and G R Liu. A point interpolation meshless method based on radial basis functions. *International Journal for Numerical Methods in Engineering*, 54(November 1999):1623–1648, 2002.
- [20] J G Wang and G R Liu. On the optimal shape parameters of radial basis functions used for 2-D meshless methods. *Comput. Methods Appl. Mech. Engrg*, 191:2611–2630, 2002.
- [21] G.R. Liu, G.Y. Zhang, Y.T. Gu, and Y.Y. Wang. A meshfree radial point interpolation method (RPIM) for three-dimensional solids. *Comput Mech*, 36:421–430, 2005.
- [22] Jiun-Shyan Chen, Michael Hillman, and Sheng-Wei Chi. Meshfree methods: progress made after 20 years. *Journal of Engineering Mechanics*, 143(4):04017001–(1–38), 2017.
- [23] John Dolbow and Ted Belytschko. Numerical integration of the Galerkin weak form in meshfree methods. *Computational Mechanics*, 23(3):219–230, 1999.
- [24] Michael Griebel and Marc Alexander Schweitzer. A particle-partition of unity method–part II: efficient cover construction and reliable integration. *SIAM J. Sci. Comput.*, 23(5):1655–1682, 2002.
- [25] Yan Liu and Ted Belytschko. A new support integration scheme for the weakform in mesh-free methods. *International Journal for Numerical Methods in Engineering*, 82(November):699–715, 2009.
- [26] Stephen Beissel and Ted Belytschko. Nodal integration of the element-free Galerkin method. *Computer Methods in Applied Mechanics and Engineering*, 139(1):49–74, 1996.
- [27] J. Bonet and S. Kulasegaram. Correction and stabilization of smooth particle hydrodynamics methods with applications in metal forming simulations. *International Journal for Numerical Methods in Engineering*, 47(6):1189–1214, 2000.
- [28] Jiun Shyan Chen, Sangpil Yoon, Cheng Tang Wu, and Yang You. A stabilized conforming nodal integration for Galerkin mesh-free methods. *International Journal for Numerical Methods in Engineering*, 50:435–466, 2001.
- [29] Ivo Babuska, Uday Banerjee, John E. Osborn, and Qiaoluan Li. Quadrature for meshless methods. *International Journal for Numerical Methods in Engineering*, 76(June):1434–1470, 2008.
- [30] Sheng-Wei Chi, Jiun-Shyan Chen, Hsin-Yun Hu, and Judy P. Yang. A gradient reproducing kernel collocation method for boundary value problems. *International Journal for Numerical Methods in Engineering*, 93(January):1381–1402, 2013.
- [31] Christian Peco, Daniel Millán, Adrian Rosolen, and Marino Arroyo. Efficient implementation of Galerkin meshfree methods for large-scale problems with an emphasis on maximum entropy approximants. *Computers and Structures*, 150:52–62, 2015.
-

- [32] Richard Franke. Scattered data interpolation: tests of some methods. *Mathematics of Computation*, 38(157):181–200, 1982.
- [33] Rolland L. Hardy. Multiquadric equations of topography and other irregular surfaces. *Journal of Geophysical Research*, 76(8):1905–1915, 1971.
- [34] Huaqing Zhang, Chunxian Guo, Xiangfeng Su, and Lin Chen. Shape parameter selection for multi-quadrics function method in solving electromagnetic boundary value problems. *The international journal for computation and mathematics in electrical and electronic engineering*, 35(1):64–79, 2016.
- [35] John P. Boyd and Kenneth W. Gildersleeve. Numerical experiments on the condition number of the interpolation matrices for radial basis functions. *Applied Numerical Mathematics*, 61(4):443–459, 2011.
- [36] E. J. Kansa. Multiquadrics-a scattered data approximation scheme with applications to computational fluid-dynamics-I: surface approximations and partial derivative estimates. *Computers and Mathematics with Applications*, 19(8-9):127–145, 1990.
- [37] W. R. Madych. Miscellaneous error bounds for multiquadric and related interpolators. *Computers and Mathematics with Applications*, 24(12):121–138, 1992.
- [38] Shmuel Rippa. An algorithm for selecting a good value for the parameter c in radial basis function interpolation. *Advances in Computational Mathematics*, 11:193–210, 1999.
- [39] B. Fornberg and G. Wright. Stable computation of multiquadric interpolants for all values of the shape parameter. *Computers and Mathematics with Applications*, 48(5-6):853–867, 2004.
- [40] J. Wertz, E. J. Kansa, and L. Ling. The role of the multiquadric shape parameters in solving elliptic partial differential equations. *Computers and Mathematics with Applications*, 51:1335–1348, 2006.
- [41] Scott A Sarra and Edward J Kansa. Multiquadric radial basis function approximation methods for the numerical solution of partial differential equations. *Advances in Computational Mechanics*, 2:2009, 2009.
- [42] S.A. Sarra and D. Sturgill. A random variable shape parameter strategy for radial basis function approximation methods. *Engineering Analysis with Boundary Elements*, 33(11), 2009.
- [43] Michael Scheuerer. An alternative procedure for selecting a good value for the parameter c in RBF-interpolation. *Advances in Computational Mathematics*, 34(1):105–126, 2011.

- [44] Victor Bayona, Miguel Moscoso, and Manuel Kindelan. Optimal constant shape parameter for multiquadric based RBF-FD method. *Journal of Computational Physics*, 230(6):7384–7399, 2011.
- [45] Rolland L. Hardy. Least squares prediction. *Photogrammetric Engineering & Remote Sensing*, 43(4):475–492, 1977.
- [46] Richard Franke. A Critical Comparison of Some Methods for Interpolation of Scattered Data. Technical report, Calhoun, 1979.
- [47] G E Fasshauer. Newton iteration with multiquadratics for the solution of nonlinear PDEs. *Computer and Mathematics with Applications*, 43:423–438, 2002.
- [48] Michael Mongillo. Choosing basis functions and shape parameters for radial basis function methods. *SIAM Undergraduate Research Online*, pages 190–209, 2011.
- [49] Song Xiang, Ke ming Wang, Yan ting Ai, Yun dong Sha, and Hong Shi. Trigonometric variable shape parameter and exponent strategy for generalized multiquadric radial basis function approximation. *Applied Mathematical Modelling*, 36(5):1931–1938, 2012.
- [50] Maggie E Chenoweth and Scott A Sarra. A numerical study of generalized multiquadric radial basis function interpolation. *SIAM Undergraduate Research Online*, pages 58–70, 2009.
- [51] M.P. Kamermans. Gaussian quadrature weights and abscissae, 2011.
- [52] P. W. Randles and L. D. Libersky. Normalized SPH with stress points. *International Journal for Numerical Methods in Engineering*, 48(10):1445–1462, 2000.

5



MQ-RPIM Model of Plain Woven Composite with Frictionless Contact

5.1 Introduction

One method of increasing the efficiency in jet engines of an airplane is increasing the running temperature of the engine, however, the highest temperature that can be reached is limited by the materials that are used in the hot sections of the jet engine. The current materials used for the high temperature components of the jet engine are cobalt or nickel based alloys, which usually run close to or in excess of their melting temperatures, ($\sim 1100^{\circ}\text{C}$) [1]. Therefore, using these materials there is no room to increase the combustion temperature, thus increasing the efficiency, without significantly reducing the lifetime and functionality of the components.

One of the ways to increase the engine's efficiency while preventing this issue, is the use of materials with higher melting temperatures and better high temperature properties. One such a material is silicon carbide (SiC), which was accidentally discovered in 1890 by Edward G. Acheson when he was running an experiment on synthesis of diamonds. SiC is created through a reaction between silicon and carbon at high temperatures, which forms covalent bonds between the Si and C atoms [2]. Because of its covalent bonded nature it has a melting temperature of about 2650°C , [3], and is particularly suitable for high temperature applications due to its high thermal conductivity, high creep resistance and excellent mechanical properties at high temperatures [1,4]. Not only does SiC have these outstanding properties, but it also reduces the CO/NO_x emissions [1,5], complexity in component design [1] and

weight of the components [1,4], which are attractive qualities for the material used in jet engine design.

In spite of all the excellent properties that SiC has, it is a very brittle material and using it in its natural form is not suitable for high stress and impact applications of a jet engine. One solution to this problem is to manufacture this material in the form of a woven composite, because at a high enough stress or during the manufacturing process, micro-cracks form at the interface of the fibres and the matrix. These micro-cracks allow for yielding and more strain energy absorption in the system, i.e. higher toughness which reduces the brittleness issue of SiC. A study on the fracture toughness of woven SiC/SiC composite showed that higher density of matrix micro-cracks and a strong yarn-matrix interface lead to a higher fracture toughness [6], therefore, having these micro-cracks is an advantage for SiC/SiC woven composite.

Modelling these micro-cracks and computing their effect on the overall behaviour of the composite material, is an important research question which if answered, can be of significant help to the design of future engines. There have been a number of different theoretical works in the literature attempting to model this behaviour of the SiC/SiC woven composite using finite element, however, it was reported that using finite element for modelling woven composite has element distortion issues which is why an alternative method is needed, such as radial point interpolation method which is used here.

In the rest of this chapter first a literature review on the topics of woven composite and contact in meshfree is given, then the chapter goes to explain the contact theory and algorithm used in the RPIM codes for both two- and three-dimensional cases; where for each case two examples of Hertzian contact are used for verification purposes. In this verification section the algorithm introduced in chapter 4 is used to find the optimum RPIM parameters for the given Hertzian problems. Once the contact implementation is verified, an example of the plain woven unit cell for two cases of full stick and full slip at the yarn-matrix interface are shown and compared to the results from finite element. The chapter is then concluded with the findings from this work, and the future works required to complete the explicit delamination model of yarn-matrix interface for woven SiC/SiC composite with frictional contact.

5.1.1 Literature Review

5.1.1.1 Woven Composites

Composite materials are formed as a combination of two or more materials that result in better properties than the individual components involved, while maintaining their individual chemical, physical and mechanical properties. One of the modern descriptions of composites is a matrix material that is reinforced by fibres; typically the fibre material has higher strength than the matrix because its

purpose is reinforcing it. The key parameters defining the property of a composite are volume fraction of the fibres, the mechanical properties of the fibres, their orientation within the matrix and their interface properties with the matrix; this is why understanding these parameters is of great interest. The main advantages of composites are the high specific strength (strength/density), specific modulus (modulus/density), high fatigue life, and corrosion resistance, which is very desirable in aircraft industry [7, 8].

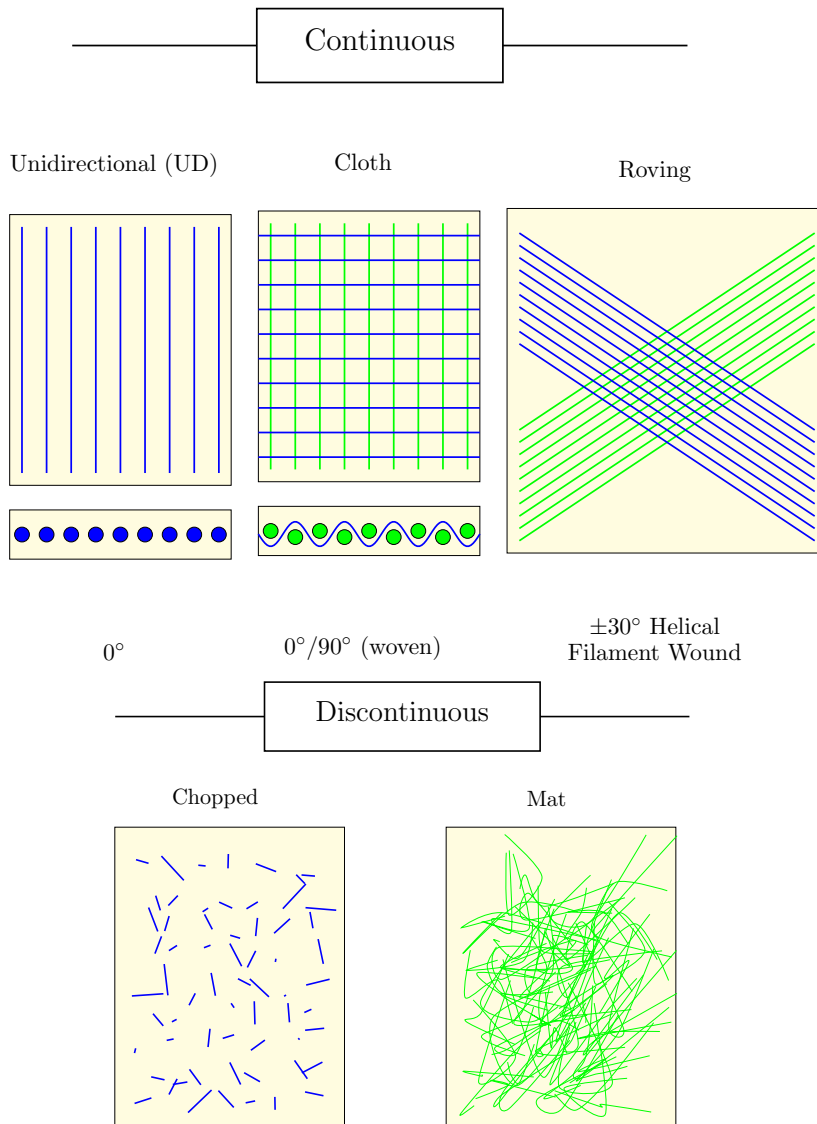


Figure 5.1: Different types of composite, showing various combinations of fibres and matrix, (Images are drawn based on the infographic taken from [8]).

There are two major types of composites; continuous and discontinuous, Figure 5.1; discontinuous composites are formed of short and randomly oriented fibres, whereas, continuous ones are formed of long and continuous fibres. The former composites tend to have lower strength and modulus because of the random orientation of the fibres, which is why latter composites are more suitable for high strength applications such as turbine blades [8]. One example of these continuous composites are

woven composites which are the most commonly used branch of textile composites. This popularity is because of their very good conformability and easy handling, which makes their manufacturing, especially for complex geometries, easier than other types of composite [9].

In woven composites, groups of fibres bundle to form yarns, and yarns are weaved to create different patterns in the x , y and z directions such as the ones shown in Figure 5.2, which are then surrounded by the matrix material. Because of these weave patterns the matrix material can be reinforced in multiple directions within a single layer. Woven composites can be two-dimensional with the weaves in the x and y direction only or three-dimensional with an additional weave in the z direction that interlocks multiple layers of 2D woven; three-dimensional woven composites tend to have better through thickness properties. Figure 5.2 shows a few examples of woven composites and their corresponding properties; from this figure it can be seen that on average twill and satin composites have better properties. However, the choice of the woven architecture will depend on the application and the importance of each property for that application. A common finding in the literature suggests that the mechanical properties of woven composites rely strongly on parameters such as the weave pattern, yarn-matrix interface strength, yarn size, fibre material, fibre orientation and their corresponding volume fraction [6, 8, 10–14]. For the purpose of this project plain woven is being studied due to its simplicity, symmetry, good balance and high stability, nevertheless, the model developed here can be extended to twill and satin architectures as required.

	Plain	Twill	Satin	Basket
Good Stability	****	***	**	**
Good Drape	**	****	*****	***
Low Porosity	***	****	*****	**
Smoothness	**	***	*****	**
Balance	****	****	**	*****
Symmetrical	*****	***	*	***
Low Crimp	**	***	*****	**

Figure 5.2: A few different architectures of 2D woven composites and their properties, (the images are drawn based on the infographic taken from [15]).

Some of the common woven composite materials are carbon/epoxy, graphite/epoxy, carbon/carbon and SiC/SiC where the first material in the name is the fibre and the second one is the matrix. The composite of interest for this project, however, is woven SiC/SiC composite whose macro-scale properties are influenced by the micro-cracks at its yarn-matrix interface. Therefore, the literature search here is pivoted around the topic of modelling damage growth in woven composites and their homogenised properties; particularly for the woven SiC/SiC composites.

Given the advantages of woven composites in terms of material property and manufacturing, currently considerable amount of research have gone into understanding their properties and failure mechanisms, out of which use of the finite element method is the most common, but not the only, approach, [16–24]. In 1993 Blackketter *et al.*, [25], introduced a method of describing the damage propagation in woven composites under tension or shear; this method was then used in an incremental iterating FE model of the woven composite, capturing response of the system to the load as damage progressed. Their work was followed by the constitutive model of anisotropic damage in any fibre-reinforced composites introduced by Matzenmille, [26], which later became the inspiration for the continuum damage mechanics meshfree model of damage in plain woven composite by Wen and Aliabadi [27]. In 1998, Vandeurzen *et al.*, [28], used a multilevel decomposition scheme to compute the stress concentration factors of woven composites under three-dimensional mechanical loads. In this process, the unit cell was divided into matrix and yarn cells, where the link between external load and internal stresses was formed through a multi-step homogenisation process.

Later in year 2000, Camus, [29], used continuum damage mechanics to study the behaviour of woven SiC/SiC under multi-axial loading, modelling the damage process through four simplified state variables; one total imposed stress and three internal damage variables. This model was able to describe the non-linear behaviour of the material under various on- and off-axis loadings, however, an important issue that remained to be investigated was the hysteretic effects of the frictional sliding [29]. In another study from the same year, Ismar *et al.* [30], computed the mechanical properties of a two-dimensional woven SiC/SiC composite under tensile loading using finite element methods. The model consisted of yarns, the matrix between yarns and the inter-yarn matrix, where the yarns were modelled as being homogeneous with properties of the fibres. The separation of the yarn-matrix interface was modelled through reduction of the elastic coefficients in the finite element model based on the fracture criterion of the components.

Ten years later Couégnat *et al.*, [31], used the idea of damage parameters based on crack density and debonding area to form a discrete micro damage (DMD) model of woven composites in finite element. In this model the effective elastic stiffness of a damaged unit cell was computed through

the introduced parameters, including damage modes such as (i) intra-yarn matrix micro-cracking, (ii) fibre breakage at the micro-scale, (iii) inter-yarn matrix cracking and (iv) transverse yarns cracking at the mesoscale. Taking a different approach in modelling the damage of woven composites, Kulkarni and Gao [21], used the Tsai-Wu failure criterion together with a two-parameter Weibull distribution to incorporate the change in strength of the material because of the increase in the specimen volume. The results showed a decrease in the strength of the material with an increase in the volume which is a result of increase in the probability of the critical defects; as a defect forms the elastic properties of the local nodes will reduce according to a material degradation model. Finite element was used to carry out the homogenisation analysis of this model and to predict its progressive failure behaviour under uni-axial tensile loading. In this study the yarns and the matrix material were modelled as separated bodies which were assemble together, however, a perfect bonding condition was assumed between them, hence a discrete model of delamination was not possible.

In most of the works carried out on modelling the damage in woven composites, particularly SiC/SiC, different damage parameters have been defined which become active once a threshold or limiting stress or strain is reached; activation of these parameters affects the homogenised elastic property of the composite and this is how the damage is incorporated. While this approach is easier to model the complex system of damage in woven composite, it is an approximation and does not capture the exact effect of delamination and damage growth. In 2013 Duan *et al.*, [32], introduced a meso-scale finite element model of damage in the two-dimensional woven C/SiC composite, where the unit cell was represented with three material parts; fibre, matrix and the yarn-matrix interface material. To capture the damage at the yarn-matrix interface which has a key role in the mechanical behaviour of the composite, cohesive elements and maximum stress criterion were used; as maximum stresses were reached the relevant elements in the yarn-matrix interface became inactive representing the damage progress. The results of this study showed that damage in the matrix was initiated at the thinnest regions close to the yarn; the interface damage was initiated at the weaving edge of the interface around the yarn in the longitudinal direction and then spread in the other directions.

While being a very popular method, finite element has issues when it comes to modelling complex geometries or highly non-linear problems; such reported issues are element distortion for large deformation problems and complex geometries, or remeshing issues for modelling crack growth and large stress gradient regions [33–37]. With the advancement in the field of computing and numerical methods, other numerical methods than finite element have gained the attention of researchers when modelling woven composite [38–41]. For example Barbieri *et al.* in 2009, [38], created a two-dimensional meshfree model of delamination in composites using Reproducing Kernel Particle Method modelling the composite layers as two-dimensional cantilever beams connected through cohesive con-

straints. They showed that the implemented meshfree method, unlike FE, treated the contact between the parts effectively and without the need for elements or conforming meshes. Or later in 2012 Potter *et al.* [40] used the voxel meshing method to overcome the issues with finite element when modelling woven composite, however, given the 90° corners of the voxel mesh, a smoothing algorithm such as the one from Boyd and Muller, [42], was needed at the yarn-matrix interface to produce a reasonable result for elastic stiffness but not for the failure initiation.

Meshfree methods are a good alternative to finite element method for complex geometries such as woven composites, particularly if damage and crack growth are involved. Because in meshfree methods no element is required, it is easier to add nodes for regions of high stress gradient or errors without the need of remeshing the whole problem domain.

One of the early works of modelling woven composites using meshfree methods was the work of Wen and Aliabadi [39] who made a use of radial point interpolation method for modelling woven composites. Using radial point interpolation method, not only the issues with FE method were eliminated but also a good agreement with the results from literature for elastic constants of E-glass/epoxy, glass/epoxy and graphite/epoxy woven composites was obtained. Later Li and Aliabadi, [43, 44], extended the use of radial point interpolation to modelling micro-mechanical continuum damage analysis of woven composites, showing the accuracy and effectiveness of this method for modelling plain woven composite.

Given that application of meshfree methods for modelling woven composites and their damage is relatively new, as far as the author of this work is aware, there are not many works available in this area; particularly, there is no meshfree model of the explicit debonding at the yarns-matrix interface of the woven SiC/SiC composite. This is why developing this explicit debonding meshfree model for the yarn-matrix interface became the objective for this chapter. The idea is to treat the yarns and the matrix as separate bodies which are in contact; when an external load is applied to the unit cell, at locations where the interfacial forces between the yarn and matrix overcome the frictional or normal contact forces, a delamination forms. The information about the unit cell after the deformation and delamination happen can be used to compute effective properties of the unit cell. This is why modelling contact with meshfree method formed the next part of this literature review.

5.1.1.2 Meshfree Contact Modelling

Modelling contact is a vast and complex area of research, for which many methods have been developed over the years; this range of methods include analytical (e.g. [45]), finite element (e.g. [46]), meshfree, and other approaches [47–49]. However, given that aim of this project is around the use of meshfree methods, therefore, the review search is narrowed down to the use of meshfree methods

in contact modelling. Advantage of using meshfree methods for contact modelling compared to other methods is also discussed here.

The idea of meshfree method was first introduced in 1977 when Gingold *et al.* [50] introduced the smoothed particle hydrodynamics method. Since then, many more meshfree methods have been developed such as Reproducing Kernel Particle Method (RKPM), Element Free Galerkin (EFG), Radial Point Interpolation Method (RPIM) and many more. Meshfree methods are known to be flexible in modelling complex geometries and non-linear problems while providing a smooth stress solution compared to FE, therefore, using meshfree methods for modelling contact, which is non-linear in nature, is a suitable choice. The particular meshfree method used in this project is RPIM, because of its ability to provide accurate solutions for irregular node distribution, its simplicity to implement for three-dimensional problems and having Kronecker delta property for application of essential boundary conditions. Please note a detailed discussion on the meshfree method and RPIM is given in chapter 4.

Not only contact modelling is a vast field on its own, but even when the search is narrowed down to meshfree methods, there are plenty of methods and works dedicated to it. The two most common meshfree methods used in the literature for contact modelling are element-free Galerkin (EFG), [33, 51–56], and Reproducing Kernel Particle method (RKPM) [34, 35, 57–62]. Nevertheless, other methods of meshfree such as collocation method, [63, 64], local Petrov-Galerkin method, [65], first-order least-squares formulation without background cells, [66], meshfree B-Spline finite element, [67], and maximum-entropy meshfree with iso-geometric analysis on the boundary, [68], have also been used in contact modelling. To learn about all these different methods, the reader can refer to the references in this section, however, the rest of this review is pivoted around application of EFG, RKPM and RPIM in contact modelling, given that they are the most popular of the meshfree methods.

One of the earliest works on contact modelling using meshfree methods is that of Belytschko *et al.* in 1995, [51], when they modelled crack growth in a static problem using EFG. It was shown that when using EFG, accurate results for the stress intensity factor can be obtained, not only with irregular distribution of nodes but also without the need for enrichment of the displacement field at the crack tip. When they compared their approach to the boundary element method, they found EFG to have more well-conditioned, sparse, banded and symmetric system of equations which also makes this method suitable for modelling anisotropic materials. Later, in 1999, Belytschko *et al.*, [52], developed an enriched form of the EFG method for modelling contact on the crack surface with the assumption of small displacement. For every point from the first body that came into contact with the second body, a local coordinate was defined; this local coordinate was then used to avoid penetration of points into each other. The results of their work suggested that using this method not only decreases the number

of unknowns but also multiple cracks can be modelled with little increase in the computational expense.

Two of the most complicated and time consuming contact problems in the literature are large deformation followed by self-contact, and high speed impact; this is why a lot of the meshfree contact modelling papers in the literature are focused on these topics. For example, Li *et al.*, [57], introduced the use of window function based meshfree interpolants for computing very smooth shape functions in three-dimensions when modelling large deformations and self-contact. One of their outcomes was comparison between a range of different methods for modelling large deformation in shell structures; methods such as shell theory and degenerate continuum approach, which resulted in three-dimensional meshfree continuum model being the simplest one in both implementation and formulation. Following [57], Li and Belytschko in 2001, [33], introduced an element-free Galerkin model for contact-impact problems with large deformation, where they showed element free methods to be very effective in solving problems with large deformation and material distortion, especially, for modelling the motion of work piece around the corners compared to FEM. Another useful outcome of their work was the use of stress points in the integration process leading to elimination of the background cells, which are typically needed for EFG method.

In other works on large deformation, self-contact and high speed impact Li *et al.*, [58], introduced a contact-detection algorithm based on the moment matrix of Kernel particle method; Li *et al.*, [34], developed an adaptive meshfree method for large mechanical deformation and contacts where additional nodes are automatically inserted to the locations with large errors in mechanical stress; Bokar *et al.*, [35], who showed the effectiveness of RKPM in modelling contact by creating a two-dimensional contact model; and a few more recent works showing the advantages of meshfree approach for modelling impact and large deformation compared to FE [69–71].

Having discovered the advantages of meshfree methods in modelling non-linear and complex problems such as large deformation, self-contact and high speed impact, in the more recent years, the span of contact modelling with meshfree method has expanded to include frictional contact problems, [61], elastic fracture mechanics, [72], metal forming, [62], and more general contact problems [73–75]. For example, Chi *et al.*, [61], used semi-Lagrangian RKPM together with an elasto-plastic layer to model Coulomb friction in their contact model; or Wang *et al.*, [62], who used RKPM to produce a smooth contact model for metal forming, and showed that use of nodes for the surface representation allows for continuum-based contact formulations, which is difficult to implement in FEM, and has a significantly improved rate of convergence.

Given that the need for background cells in integration process of radial point interpolation method can be computationally expensive, as far as the author of this works is aware, this method has not been

used in large deformation and high speed impact problems. However, given its simplicity in implementation for two- and three-dimensional problems, and its accuracy for irregular distribution of node, use of radial basis function is an attractive method for contact modelling of static or small displacement problems. One of such cases is the work of Xiao *et al.* in 2005, [73], who developed a subdomain variational inequality and its meshless complementary formulations for two-dimensional contact problems. The complementary meshless method used in this work was meshless local Petrov-Galerkin (MLPG) which is based on local weighted residual method with Heaviside step function as weighting function over a local subdomain, and radial basis function as a trial function for interpolation. The result of this work showed that the use of multi-quadrics (MQ) radial basis function provides the best accuracy but is sensitive to node spacing. In another work, Li. *et al.* , [74], showed that linearly conforming radial point interpolation method (LC-RPIM) with the nodal integration techniques can very well simulate the non-linear behaviour of contact. This method was tested on two-dimensional examples such as contact of an elastic body with a rigid body, and frictionless contact of an elastic cylinder on a rigid body.

One of the most recent works in the area of contact modelling with RPIM method is the work of Qian *et al.* in 2014, [75], where they produced a general 3D contact smoothing method based on the meshfree RPIM, to improve the simulation of contact problems through reproduction of smooth surfaces, even for models with coarse meshes. While this method applies the RPIM method at the contact surface, the whole simulation is not carried out with RPIM method. As far as the author of this work is aware, there is no three-dimensional RPIM model of contact available in the literature, therefore, given that this is the chosen method for modelling small displacement and delamination of the woven SiC/SiC composite unit cell, as part of the work here, a three-dimensional RPIM contact code was developed from scratch.

5.1.2 Objective

Having considered the works done in the literature and the need for modelling delaminations at the yarn-matrix interface of woven SiC/SiC composite, the objectives for this project formed. In order to model these delaminations, it was proposed to model the yarns and the matrix as separate bodies that are in frictional contact within the unit cell. As an external load is applied to the unit cell, internal stresses will form within the unit cell and at the interface of yarns and matrix; given the coulomb frictional constrains, parts of the interface will move or separate, leading to delamination. This way the micro-cracks in the unit cell can be modelled explicitly; Figure 5.3 shows a demonstration of the individual bodies involved in the unit cell and possibilities of discrete delaminations. From the resultant stress and strain profiles of the unit cell, the effective property of the unit cell can be computed using Hill-Mandle, [76, 77], homogenisation method.

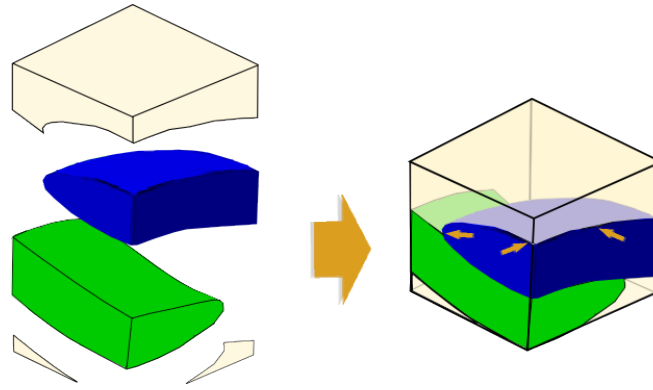


Figure 5.3: Demonstration of the proposed idea for modelling the micro-crack at the yarn-matrix interface when each part is considered as an individual body.

As discussed in the literature review, meshfree methods can be very efficient for modelling complex geometries such as woven composite and non-linear problems such as contact. From all the available meshfree methods, radial point interpolation or RPIM is chosen because this method gives accurate solutions for non-uniform distribution of nodes, has easy transferability from two- to three-dimensional modelling, and it has high capability in modelling complex geometries. The two downfalls of this method are i) the dependency of the accuracy on multiple parameters such as radial basis shape parameters, and ii) the long simulations times, especially for three-dimensional cases compared to FEM. For the first issue, an algorithm was introduced in chapter 4, where through a systematic series of steps these parameters can be found for any given problem. The second issue still remains, but given that convergence can be reached with low number of field nodes, it is still advantageous to use this method for problems such as woven composites. Using parallel programming could be beneficial in decreasing the simulation time but that is not in the scope of this work.

Given that there is no three-dimensional RPIM contact code available in the literature to use, as part of this project, a RPIM contact code was developed from scratch. As the development process of a code from scratch goes, in order to obtain the final model, there are a number of simpler steps that needs to be taken and verified before the final model is formed; the verification and completion of each step gives more confidence in the reliability of the final model. The main and simplified steps needed to complete the proposed idea for modelling the delamination at the yarn-matrix interface using RPIM method are shown in Figure 5.4.

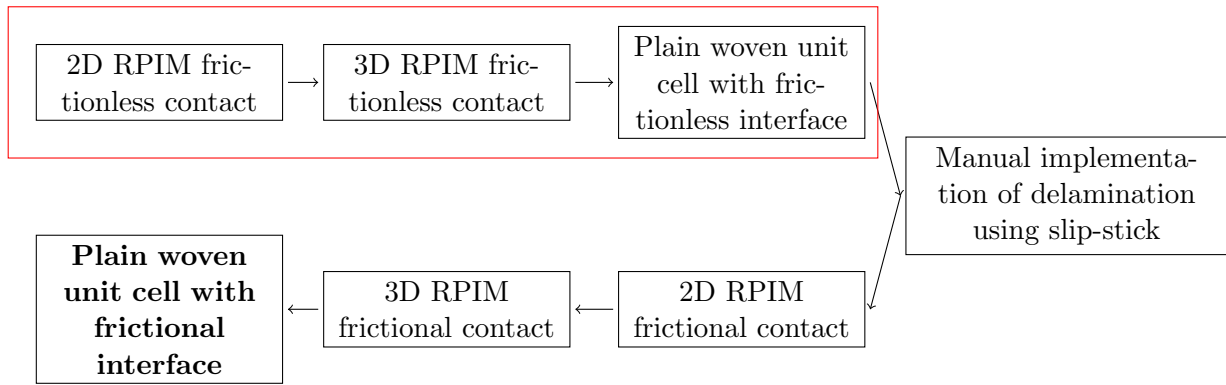


Figure 5.4: Required simplified steps for obtaining the final model of the woven unit cell with delaminations at the yarn-matrix interface.

Developing a RPIM code from scratch for all of the steps shown in Figure 5.4 is a long process which is beyond the scope of a PhD, therefore, in this work the first three steps are completed, creating the building blocks of the main model. For the woven composite model developed in this chapter, the solid materials and component are assumed to be isotropic in order to verify the RPIM contact model developed here. In reality for these woven composites the mechanical properties for the fibre bundles are anisotropic, therefore, this needs to be taken into account for future analysis and completion of the steps in Figure 5.4.

This chapter outlines the details and results of the first three steps taken in the path for achieving the final model of the delaminations at the yarn-matrix interface in woven SiC/SiC composite. As discussed previously, there are not any three-dimensional RPIM contact codes available in the literature, therefore, the novelty of this work not only lies on writing the first three-dimensional RPIM code for modelling frictionless contact, but also creating the first preliminary model of the plain woven unit cell in meshfree with possibility of contact at the yarn-matrix interface.

5.2 Materials & Methods

The meshfree method used for numerical computation of the contact code is RPIM (Radial Point Interpolation Method) which is fully explained in chapter 4. In this section only the contact theory and algorithm used for both the two- and three-dimensional RPIM contact codes are discussed, which are applied to two two- and three-dimensional frictionless contact examples for verification. At the end, application of the developed frictionless contact code for modelling the example of a plain woven composite unit cell is discussed. The optimisation algorithm introduced in chapter 4 is used for choosing the best combination of RPIM parameters when using the frictionless contact model for Hertzian contact problems.

Please note for the contact theory, as described in this chapter, I partly used the information from

the book of “Computational Methods in Contact Mechanics”, [78], but had the full on support from Prof. A. Salehzadeh Nobari for understanding the contact theory and implementing it into my RPIM codes.

5.2.1 Contact Theory

There are two common methods of implementing contact into numerical computations; one is by Lagrange multipliers, and the other through penalty method. The latter method, has a fixed size matrix, which makes it faster and ideal for dynamic and impact contact problems, however, it is an approximation and its accuracy is dependent on the choice of penalty factor. The Lagrange multiplier method, on the other hand, is exact but matrix size increases with the growth of the contact region, therefore, it can be slow; because of this characteristics this method is mostly used for stationary and small strain contact problems [79]. For the contact models in this project Lagrange multiplier method is used because small deformation can be assumed when modelling the contact in plain woven composite under quasi-static load.

In the Lagrange multiplier method, contact between the two bodies is implemented through Lagrange constraints which consist of two parts, and are defined for every node that is involved in the contact region. This is the reason for why matrix size increases in Lagrange multiplier method by increase in the contact region. For every node there is one normal and one tangential constraint; the normal constraint is introduced to prevent the bodies from penetrating into each other, and the tangential constrains is to check if a contact node has slipped or stuck at its original position. The slip or stick condition of a contact node occurs because of the friction coefficient, i.e. μ .

When modelling contact between two bodies, it is important to define the target and the contactor; contactor is the body that comes into contact with the target body. Usually choice of the contactor and target is arbitrary but there are some guidelines in making the most suitable choice. For example, contactor is usually taken to be the body with the most movement and least rigidity, while the target is taken to be the most stationary and rigid body. For a given problem, once the contactor and the target bodies are defined, the energy state of the whole system, Π , can be written as

$$\begin{aligned} \Pi = & \frac{1}{2}[\mathbf{u}_C]^T[\mathbf{k}_C][\mathbf{u}_C] + \frac{1}{2}[\mathbf{u}_T]^T[\mathbf{k}_T][\mathbf{u}_T] + \lambda_n [([\mathbf{u}_C] - [\mathbf{u}_I]) \cdot [\mathbf{n}] - g_n] + \lambda_t [([\mathbf{u}_C] - [\mathbf{u}_I]) \cdot [\mathbf{t}] - g_t] \\ & - [\mathbf{F}_C][\mathbf{u}_C] - [\mathbf{F}_T][\mathbf{u}_T], \end{aligned} \tag{5.1}$$

where subscripts C and T represent contactor and target bodies, respectively; $[\mathbf{k}_C]$ and $[\mathbf{k}_T]$ are the stiffness matrices for the contactor and target bodies, while their corresponding displacement vectors are given by $[\mathbf{u}_C]$ and $[\mathbf{u}_T]$; $[\mathbf{n}]$ represents the unit normal and $[\mathbf{t}]$ represents the unit tangential vectors

to the contact surface; λ_n and λ_t are the normal and tangential contact forces; g_n and g_t are the initial normal and tangential gaps between the two nodes that come into contact, computed as

$$\begin{aligned} g_n &= ([\mathbf{u}_C] - [\mathbf{u}_I]) \cdot [\mathbf{n}], \\ g_t &= ([\mathbf{u}_C] - [\mathbf{u}_I]) \cdot [\mathbf{t}]; \end{aligned} \quad (5.2)$$

and finally $[\mathbf{F}_C][\mathbf{u}_C]$ and $[\mathbf{F}_T][\mathbf{u}_T]$ are the work done associated with the external loads applied to the contactor and the target bodies, respectively. Equation 5.1 can also be written in the index format as

$$\Pi = \frac{1}{2}k_{C_{j_i}}u_{C_i}^2 + \frac{1}{2}k_{T_{j_i}}u_{T_i}^2 + \lambda_n [(u_{C_i} - u_{I_i})n_i - g_n] + \lambda_t [(u_{C_i} - u_{I_i})t_i - g_t] - F_{C_i}u_{C_i} - F_{T_i}u_{T_i}, \quad (5.3)$$

where i is the directional index which equals to 1 and 2 for two-dimensional and 1,2 and 3 for three-dimensional cases. $[\mathbf{u}_I]$ in Equation 5.1, or u_{I_i} in Equation 5.3 are the displacement vector of the intersection points between the contactor and target bodies placed on the target body, which is found as the simulation runs. Given that the intersection point is defined on the target body, using the RPIM method, the displacement for this point is approximated as

$$u_I(\mathbf{x}) = \sum_{i=1}^N \phi_i(\mathbf{x})u_{T_i} = [\Phi] \cdot [\mathbf{u}_T], \quad (5.4)$$

where $\phi_i(\mathbf{x})$ is the RPIM shape function used to approximate u_I at position \mathbf{x} ; u_{T_i} is the displacement vector of the target field nodes that fall in the support domain for position \mathbf{x} ; and finally, N is the total number of target field nodes that fall in the support domain of $u_I(\mathbf{x})$. In addition to the building of \mathbf{K} matrices for each body, this is where the RPIM method is directly used for the contact constraint implementation.

The first two terms of Π in Equation 5.1 describe the energy states of the two bodies, and the last two terms describes the work done by the external loads to the system. The stiffness matrix and applied boundary conditions of each individual body using the RPIM method is explained in chapter 4. It is through the third and fourth terms of the equation that contact constraints are implemented; the third term of Π implements the normal contact constraints to prevent penetration of the bodies into each other. This term computes the normal contact forces, λ_n , required to stop the penetrations from happening, given an initial normal gap of g_n . In other words, for every contractor node that reaches the target, in order to stop the penetration, the two nodes will have to move together in the normal direction with a normal force between them, which means that the difference between their normal displacements, $([\mathbf{u}_C] - [\mathbf{u}_T]) \cdot [\mathbf{n}]$, remains as g_n .

Once λ_n is computed, it is important to check for its sign because when two nodes are in contact, the natural tendency for each node is to move the other one in the direction of its own movement, however, the other node is opposing this movement and exerting an opposite force, i.e. a compressive force between the two nodes; this is why the normal contact force has to be negative. Following this, if during the calculations λ_n is computed to be positive, this means that the node corresponding to this force is not actually in contact and has to be released.

The fourth term of Π corresponds to the tangential constraints of the contact process which deals with friction or slip and stick conditions. When modelling the tangential constraint part of the contact, initially in the simulation, it is safe to assume that all the contactor nodes that contact the target surface stick to it with their corresponding difference in the tangential displacement equal to the initial tangential gap, i.e. $([\mathbf{u}_C] - [\mathbf{u}_T]) \cdot [\mathbf{t}] = g_t$. However, as the simulation goes on, if the tangential force (i.e. λ_t), exceeds the limiting Coulomb friction force (i.e. $\mu\lambda_n$), then slip occurs leading to a constant tangential force from the friction, i.e. $|\lambda_t| = \mu\lambda_n$, and if not, the stick assumption stays in place. In other words

$$\lambda_t = \begin{cases} \pm\mu\lambda_n & \lambda_t \geq \mu\lambda_n & \text{Slip} \\ \lambda_t & \lambda_t < \mu\lambda_n & \text{Stick,} \end{cases} \quad (5.5)$$

therefore, in order to know if stick or slip has occurred, the parameter that is required to be computed is λ_t . Incorporating these information into the energy equation, two sets of system of equations form for the contact constraints; i) stick and ii) slip.

Stick: Starting from Equation 5.1, which undergoes the Lagrange multiplier differential procedure, the system of equations are found, as shown here

$$\frac{\partial \Pi}{\partial [\mathbf{u}_C]} = [\mathbf{k}_C][\mathbf{u}_C] + \lambda_n[\mathbf{n}] + \lambda_t[\mathbf{t}] - [\mathbf{F}_C] = 0, \quad (5.6)$$

$$\frac{\partial \Pi}{\partial [\mathbf{u}_T]} = [\mathbf{k}_T][\mathbf{u}_T] - \lambda_n[\mathbf{\Phi}] \cdot [\mathbf{n}] - \lambda_t[\mathbf{\Phi}] \cdot [\mathbf{t}] - [\mathbf{F}_T] = 0, \quad (5.7)$$

$$\frac{\partial \Pi}{\partial \lambda_n} = ([[\mathbf{u}_C] - [\mathbf{\Phi}] \cdot [\mathbf{u}_T]] \cdot [\mathbf{n}] - g_n) = 0, \quad (5.8)$$

$$\frac{\partial \Pi}{\partial \lambda_t} = ([[\mathbf{u}_C] - [\mathbf{\Phi}] \cdot [\mathbf{u}_T]] \cdot [\mathbf{t}] - g_t) = 0, \quad (5.9)$$

leading to the final system of equations for the stick case written in a matrix format,

$$\begin{bmatrix} [\mathbf{k}_C] & [0] & [\mathbf{n}] & [\mathbf{t}] \\ [0] & [\mathbf{k}_T] & -[\Phi][\mathbf{n}] & -[\Phi][\mathbf{t}] \\ [\mathbf{n}] & -[\Phi][\mathbf{n}] & [0] & [0] \\ [\mathbf{t}] & -[\Phi][\mathbf{t}] & [0] & [0] \end{bmatrix} \begin{bmatrix} [\mathbf{u}_C] \\ [\mathbf{u}_T] \\ \lambda_n \\ \lambda_t \end{bmatrix} = \begin{bmatrix} [\mathbf{F}_C] \\ [\mathbf{F}_T] \\ g_n \\ g_t \end{bmatrix} \quad (5.10)$$

Slip: However, if the computed contact forces lead to $\lambda_t \geq \mu\lambda_n$ then slip occurs and λ_t in Equation 5.3 changes to $\pm\mu\lambda_n$, depending on the direction of movement. Please note, here $\mu\lambda_n$ is constant which leads to the following system of equations for when slip occurs,

$$\begin{bmatrix} [\mathbf{k}_C] & [0] & [\mathbf{n}] \\ [0] & [\mathbf{k}_T] & -[\Phi][\mathbf{n}] \\ [\mathbf{n}] & -[\Phi][\mathbf{n}] & [0] \end{bmatrix} \begin{bmatrix} [\mathbf{u}_C] \\ [\mathbf{u}_T] \\ \lambda_n \end{bmatrix} = \begin{bmatrix} [\mathbf{F}_C] \\ [\mathbf{F}_T] \\ g_n \end{bmatrix} \quad (5.11)$$

Equation 5.10 shows a system of equations for two bodies that are in contact with all the contactor nodes sticking to the target surface, whereas, Equation 5.11 shows the case when all the contactor nodes slip over the target surface. These two equations are for the two extreme cases, whereas, in reality always a combination of the two happens, hence, the corresponding system of equations will become a combination as well. Please note, all the terms that relate to each individual bodies, i.e. $[\mathbf{k}_C]$, $[\mathbf{k}_T]$, $[\mathbf{u}_C]$, $[\mathbf{u}_T]$, $[\mathbf{F}_C]$, and $[\mathbf{F}_T]$, including the boundary conditions, are computed using the RPIM method as explained in chapter 4.

5.2.2 Contact Algorithm

Up to this point the contact theory used for this project was discussed, but in this section the focus is on the algorithm used to implement this theory into the RPIM codes and solve the system of equations. This algorithm consists of three main steps; i) pre-contact search, ii) contact detection and iii) post-contact calculations; pre-contact search deals with finding the contactor nodes that have the possibility of coming into contact with a segment of the target body and forming test-pairs. One test-pair consists of a single contactor node and a segment of the target surface which have a possibility of coming into contact with each other; once the load is applied, in the contact detection step, this pair is tested for occurrence of contact, hence the name “test-pair”.

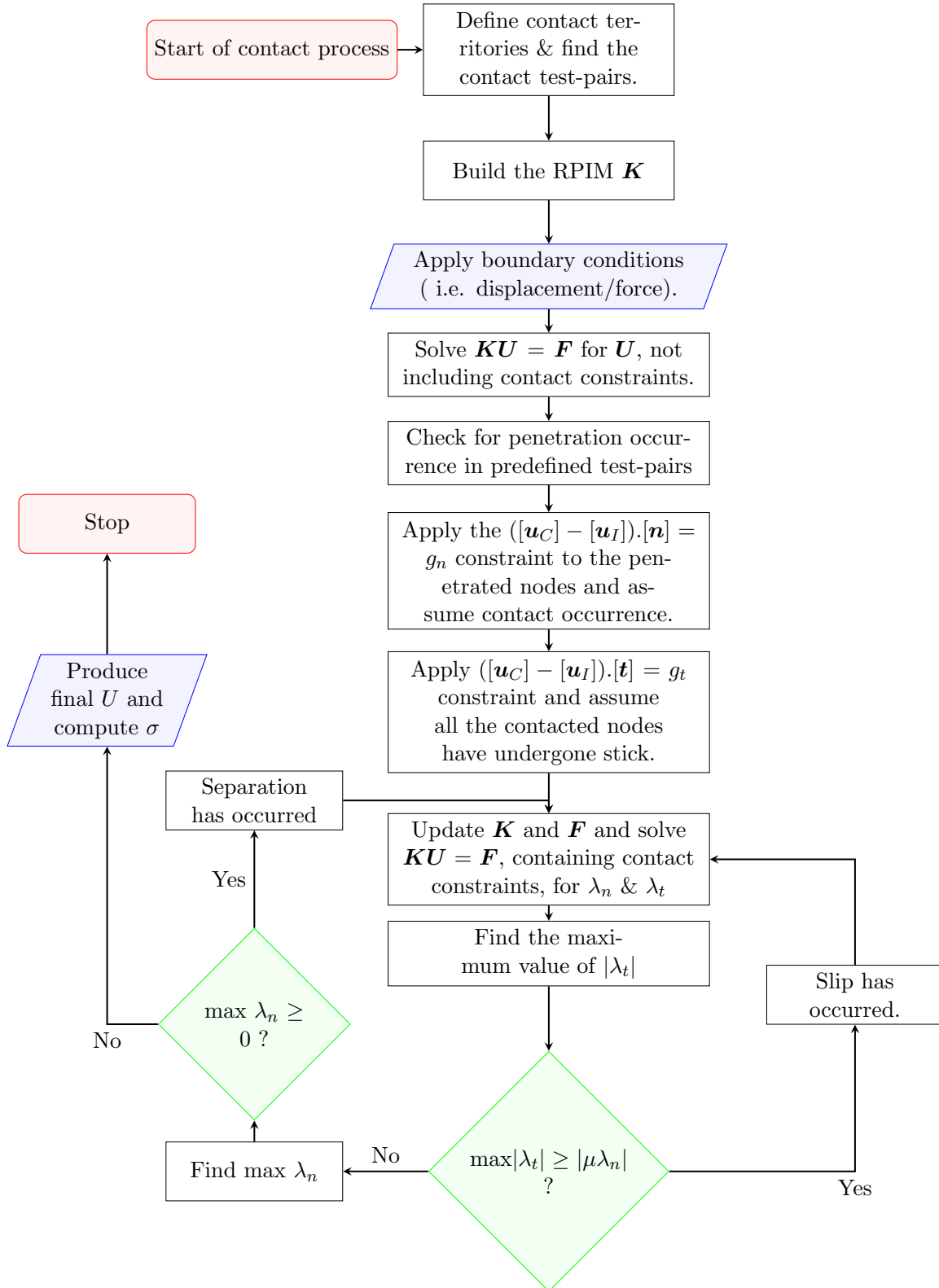


Figure 5.5: Frictionless contact algorithm flow chart used in the RPIM codes.

The final step of the contact algorithm takes place after the system of equations has been solved once; in this step the computed contact forces are checked against the tangential and normal constraints, and decision on separation, slip and stick is made accordingly; a summary of the contact

algorithm is shown in Figure 5.5.

Even though the frictionless contact case is being considered but for completeness, the general contact algorithm is shown and discussed here; Figure 5.5 shows the general algorithm for contact computation only in one increment, because when friction is involved, the application of the load has to be broken down into smaller increments. This means after the computation of U at the end of contact procedure, the geometry has to be updated and the whole algorithm needs to repeat until the final load increment is reached.

5.2.2.1 Pre-contact Search

This section of the contact algorithm is based on the paper by Z.H. Zhong and L. Nilsson in 1989 [81], where pre-contact search is done in an hierarchy manner. Firstly, the contact territories around contactor and target bodies are defined; these territories are regions around each body where contact occurrence is possible. For example in Figure 5.6 the contact territory of a disc and a square are shown with red and green lines, respectively. Once the individual contact territory of each body is defined, depending on the distance between the two bodies, the common territory between the two bodies is identified. This common territory is the overlap of each individual contact territory; an example of it is shown in Figure 5.6. The purpose of common contact territory is to help with identifying possible contact candidates; any surface field node from both bodies that fall within the common contact territory is a possible contact candidate. Please note that Figure 5.6 only shows a two-dimensional representation of the territories to help with the description, otherwise the three dimensional cases follow the same principle.

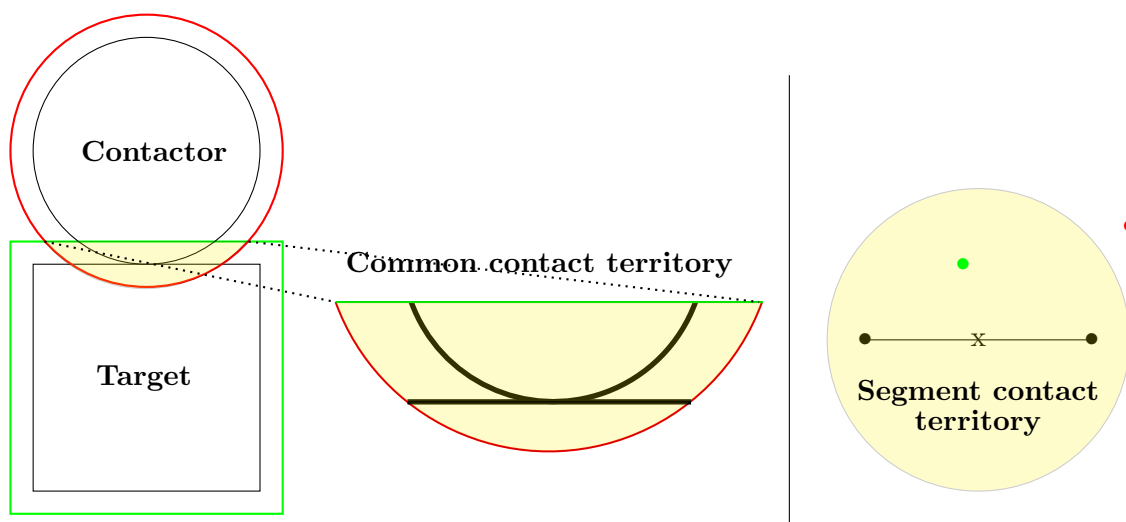


Figure 5.6: **Left diagram:** Red and green lines show the contact territories of the disc and square. The highlighted region shows the common contact territory between these two bodies while the thick black lines show the field nodes regions that fall in the common contact territory. **Right diagram:** Segment contact territory for a two-dimensional target segment. The green contactor node is within the segment contact territory and forms a test-pair with the segment, whereas the red node does not.

Once the field nodes in the common contact territory are identified, the pre-contact search goes to a smaller scale; from the identified field nodes, the nodes that are on the target surface are grouped to form target segments. The target segments in the two-dimensional problems are lines between two nodes, as shown in Figure 5.6, and in the three-dimensional problems are triangles between every three nodes. In the RPIM code developed here, Delaunay triangles functionality of MATLAB is used to find target segments of three-dimensional problems with any given distribution of surface nodes.

For every target segment that is formed, a contact territory is defined around that segment which defines the nodes can form a test-pair with it. Figure 5.6 shows a two-dimensional example of the segment contact territory; the green node which is within the contact territory of the segment forms a test-pair with that segment but the red node cannot. Each test-pair defines the possibility of a contactor node contacting its corresponding target segment, which will be checked later in the “Contact Detection” section of the model. Please note that when forming the test-pairs, there could be more than one contactor node for each target segment and vice versa, however, once the contact occurs, for test-pairs with a common contactor node only one will succeed but the reverse is not true. In other words, a contactor node can only contact one segment whereas one segment can be contacted by multiple contactor nodes.

5.2.2.2 Contact Detection

After the “pre-contact search” step, the load (or displacement) is applied where, initially, no contact constraints is included in the calculations, i.e. penetrations of the bodies can occur. The resultant displacement from the initial calculation is used to check whether the test-pairs have contacted or not; the contactor nodes in the test-pairs that have penetrated through their corresponding segments are recorded as contacted. For every test-pair that has contacted, the intersection point between contactor node and the segment is found. This point is the intersection between the line that connects the initial and final position of the contactor, and the final position of the target segment; Figure 5.7 shows a schematic of this process. If the intersection point lies within the limits of the target segment and the path of the contactor node, then contact has occurred for that pair.

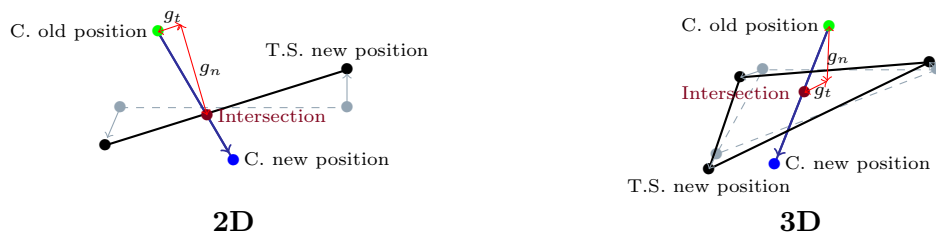


Figure 5.7: Point of intersection (red point) between the contactor, C., and the target segment, T.S., as the contactor node crosses the target segment for both two- and three-dimensional cases. The intersection point must be within the path of the contactor and the limits of the target segment.

Once a test-pair is shown to be contacted, i.e. the contactor node in the test-pair has contacted its corresponding target segment, then all the other test-pairs that include this contactor node are discarded. This process repeats for all the test-pairs until all the contacted nodes are identified; at this point, for every contacted test-pair, the unit normal and tangential vectors to the corresponding target segment are computed. These unit vectors are then used to compute g_n , g_t and the relevant contact terms for the stiffness matrix and the force vector, as shown in Equation 5.10. Once the stiffness matrix and the force vector are updated, the system of equations, i.e. $\mathbf{KU} = \mathbf{F}$, is solved again. At this point in the calculations, it is assumed that all the contactor nodes that have been identified here are in contact with their corresponding target segment (refers to the third term in Π from Equation 5.1), and stuck to where they have contacted (refers to the fourth term in Π from Equation 5.1). In the next step, additional criteria and constraints will be imposed on the results until the final and correct result is produced.

5.2.2.3 Post-Contact Detection

Previously, it was assumed that all the identified contactor nodes are in contact and stuck to their corresponding target segment, however, in reality as a contactor node contacts the target body, it affects the contact conditions of all the other contactor nodes. Therefore, it is important to check the resultant \mathbf{U} and contact forces for validity. The first validity check is for the tangential contact forces, i.e. whether the contacted nodes sticks or slips; the second validity check is for the normal contact forces, i.e. whether they are positive or negative. The tangential force is checked first because for every contactor node that has wrongly assumed to be in contact with the target body, the overall magnitude of all λ_n s will be more than it should be; as a result it can be assured that for any contactor node that $|\lambda_t| \geq |\mu\lambda_n|$ is true, slippage is certainly detected.

For the first validity check, the maximum value of $|\lambda_t|$ and its corresponding contactor node are found; if this value is greater than $|\mu\lambda_n|$, then this node has slipped, and if less than $|\mu\lambda_n|$, then the stick assumption is approved for this node. Once a decision on slip or stick is made, the relevant terms in \mathbf{K} and \mathbf{F} are updated, and $\mathbf{KU} = \mathbf{F}$ is solved again. Updating the terms in \mathbf{K} and \mathbf{F} means that if, for example, slip has occurred, the tangential contact rows and columns of \mathbf{K} and \mathbf{F} are removed, and the normal contact rows and columns of them are changed accordingly, i.e. Equation 5.11. This validity check is carried out for every identified contactor node from the previous step until there is no contactor node for which $|\lambda_t| \geq |\mu\lambda_n|$.

Once the first validity check is complete, the second validity check, i.e. sign of λ_n , is applied where for every contactor node to be in contact with the target body, there must be compressive forces between the two parts at the points of contact. Therefore, for a contactor node to be in contact with

the target body, the normal contact force or λ_n has to be negative. At this point, the maximum value of λ_n is found and checked for its sign; if it is a positive value, then this contactor node is not in contact with the target body which means the assumption made previously does not hold for this node, and if it is a negative value, then the assumption that this contactor node is in contact with the target will hold. According to the findings of the second validity check, \mathbf{K} and \mathbf{F} are updated and $\mathbf{KU} = \mathbf{F}$ is solved again; if the contactor node is not in contact, then the corresponding tangential and normal contact rows and columns are removed from \mathbf{K} and \mathbf{F} , otherwise they are unchanged. This process is carried out for all the contactor nodes identified in the previous step; for every separation that is detected, the first validity check also has to be repeated before the next second validity check takes place. This process continues until all the remaining λ_n s are negative and all the slip or stick cases are identified, then the final values of \mathbf{U} and \mathbf{F} are stored.

5.2.3 Contact Incrementation

Depending on the applied load, it is possible for slip and stick to occur interchangeably for a given contactor node; during different stages of an applied load the contactor node, that is in contact with the target, can slip, stick or even separate which affects the overall contact behaviour of the system. This is why when friction is involved, the problem becomes nonlinear, therefore, to capture the correct slip and stick history, it requires the external load to be applied in small increments. As a result, depending on whether the problem is frictional or frictionless, two different paths can be taken; i) frictionless, where the external load can be applied with a single increment to reach the solution, or ii) frictional, where the external load is applied through a series of small increments. There are two methods of incrementing the applied load; i) full incrementation or ii) pseudo incrementation [82]. Given that the aim of this work is to model frictionless contact for small displacements, there is no need for incrementing the application of the external load. The above discussion is for providing a complete picture on contact modelling; to learn more about this, the reader is encouraged to look at [82].

5.2.4 Contact Verification

Up to this point contact theory and the algorithm by which it was implemented in the code were discussed; in this part the examples by which the code is verified will be described. The contact examples used for this verification are different versions of frictionless Hertzian contact problem, in which a cylinder contacts a plane under applied line force or displacement, Figure 5.8. There are two cases of the Hertzian contact used for this verification; in the first case both bodies are of the same material, whereas, in the second case a deformable cylinder contacts a rigid plane. These examples are solved in both two- and three-dimensional versions of the RPIM contact code.

In the rest of this subsection a description of the analytical solution to the Hertzian contact problems, and a description of their corresponding RPIM models are given. The analytical solution and description for Hertzian contact examples are taken from the book of “Mechanics of Elastic Contacts” [45].

5.2.4.1 Hertzian Contact Model

The well-known Hertzian contact model of a cylinder and a plane is based on the assumption that width of the contact region, i.e. $2a$, is very small in comparison to the radius of the two bodies in contact, therefore, the approach of the contactor nodes in the normal direction to the contact region can be approximated by a parabola given in Equation 5.12.

$$h(x) = C - k \frac{x^2}{2} \quad (5.12)$$

Here, $h(x)$ is the shape of the interpenetration between the two bodies, C is a constant and k is the relative curvature given by

$$k = \frac{1}{R_1} + \frac{1}{R_2}, \quad (5.13)$$

where R_1 and R_2 are the radius of bodies 1 and 2, respectively. For a half-plane the radius is taken to be infinite which means $k = \frac{1}{R}$ where R is the radius of the cylinder.

Similar Bodies

In the case of similar bodies and no friction in Hertzian examples, the pressure distribution at the contact region, i.e. $p(x)$, is computed as

$$p(x) = -p_0 \sqrt{[1 - (x/a)^2]}, \quad (5.14)$$

where p_0 is the maximum contact pressure at the centre of the contact region, computed by

$$p_0 = \frac{ka}{A}, \quad (5.15)$$

and a is the contact semi-width computed as

$$a^2 = \frac{2PA}{\pi k} \quad (5.16)$$

Here P is the magnitude of the applied force per unit length on the cylinder, and A is known as the composite parameter calculated as

$$A = 2 \left(\frac{1 - \nu_1^2}{E_1} + \frac{1 - \nu_2^2}{E_2} \right), \quad (5.17)$$

where E_1 and ν_1 are the elastic properties of body 1, and E_2 and ν_2 are the elastic properties of body 2.

Dissimilar Bodies

In the case of bodies with different elasticities or when friction is present, the pressure distribution at the contact region is computed by

$$p(x) = -p_0 (1 - (x/a))^m (1 + (x/a))^{1-m}, \quad (5.18)$$

where $0 < m < 1$ and is computed from $\tan(m\pi) = \frac{1}{\beta\mu}$. β is another composite parameter and is computed by

$$\beta = \frac{1}{2} \frac{[(1 + \nu_1)(1 - 2\nu_1)]/E_1 - [(1 + \nu_2)(1 - 2\nu_2)]/E_2}{(1 - \nu_1^2)/E_1 + (1 - \nu_2^2)/E_2} \quad (5.19)$$

In the case of two similar bodies β is zero and for the case that one body is rigid, which is the example used here, β will become $\frac{1-2\nu}{2(1-\nu)}$. p_0 in Equation 5.18 is still the central contact pressure but not necessarily the maximum, unless at $m = 1/2$. For dissimilar bodies p_0 is computed as

$$p_0 = \frac{P \sin(m\pi)}{2\pi am(1 - m)} \quad (5.20)$$

where a is still the semi-contact width but now has few additional terms;

$$a^2 = \frac{PA}{2\pi m(1 - m)k} \quad (5.21)$$

5.2.4.2 RPIM Contact Verification

To verify the two- and three-dimensional RPIM contact codes, they are used to run simulations on frictionless Hertzian contact examples for both cases of similar and dissimilar bodies. As a results, there are four set of results produced in the verification of the RPIM contact code; two-dimensional cylinder on a plane (similar bodies), two-dimensional cylinder on a rigid plane (dissimilar bodies), three-dimensional cylinder on a plane (similar bodies), three-dimensional cylinder on a rigid plane (dissimilar bodies).

The dimensions and boundary conditions of the bodies used for this verification are presented in Figure 5.8. For the two two-dimensional cases a load of $P = 5000\text{N/mm}$ has been applied on the cylinder, however, because the structures are halved due to their symmetry, their corresponding applied load is also halved, i.e. $F = P/2 = 2500\text{N/mm}$.

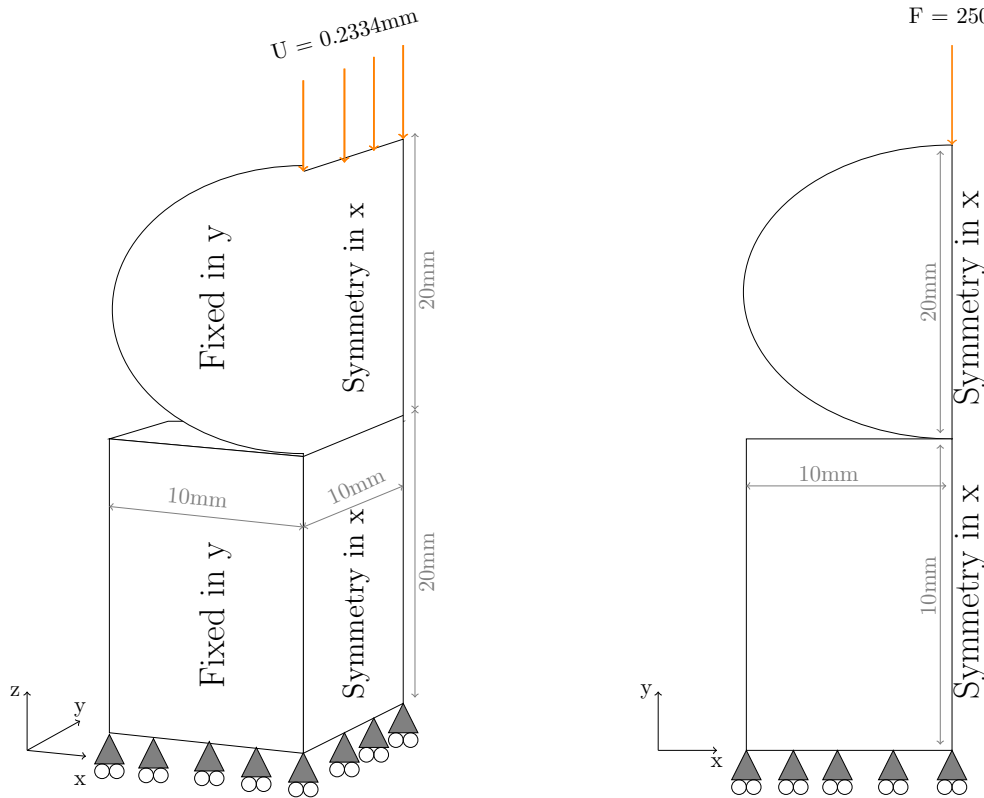


Figure 5.8: The boundary conditions and geometry of the contact models used in this verification for both two- and three-dimensional cases.

For the two three-dimensional cases a line displacement of $U = 0.2334\text{mm}$ is applied on the cylinder, which is not affected by the symmetric nature of the problem. The corresponding load per unit length of $U = 0.2334\text{mm}$ for the case with similar bodies is 6500N/mm , and for the case with rigid plane is 10500N/mm . These loads are used for computing the analytical solutions for the three dimensional cases. When defining the material properties of the bodies in contact, for all the deformable bodies E is set to 207000 MPa and ν to 0.3 , and for the rigid plane E is set to $207000 \times 10000\text{ MPa}$.

Having set the problems for the RPIM contact codes, in order to ensure that the best solution is obtained, the optimisation algorithm introduced in chapter 4 is used here. Figure 4.3 in chapter 4 shows a summary of this algorithm, from which the best choice of number of field nodes (N_{FN}), background cells (α_{gp}), integration points (n_{gp}), support domain size (α_s), and RPIM shape parameters (α_c & q) can be obtained for these contact problems. Given that defining the error indicators is very important in the optimisation process, for the contact problems here the following error indicators are used; i) the percentage error in the half-width contact area, i.e.

$$\epsilon_a = \frac{a^{\text{RPIM}} - a^{\text{Ana}}}{a^{\text{Ana}}}; \quad (5.22)$$

ii) the percentage error in central contact pressure, i.e,

$$\epsilon_{p_0} = \frac{p_0^{\text{RPIM}} - p_0^{\text{Ana}}}{p_0^{\text{Ana}}}; \quad (5.23)$$

and iii) the maximum percentage error in the computed contact pressure or $p(x)$, i.e.

$$\text{Max}(\epsilon_p) = \text{Max} \left(\frac{(p(x)^{\text{RPIM}} + \text{Cons.}) - (p(x)^{\text{Ana}} + \text{Cons.})}{p(x)^{\text{Ana}} + \text{Cons.}} \right) \quad (5.24)$$

The final error indicator represents the accuracy of stress profile in the contact region; the Cons. variable in Equation 5.24 is a shifting constant for the stress so when $p(x)^{\text{Ana}}$ is zero, the error indicator does not become infinite. For convenience Cons. is chosen to be p_0^{Ana} .

In addition to the verification of my RPIM contact code against the analytical solution for the contact region, a comparison of the results with a finite element model, using Abaqus/CAE 6.14-4, has also been carried out; this comparison verifies the stress and displacement profiles of the results from the developed RPIM codes.

5.2.5 Preliminary model of the plain woven composite unit cell

In 1989 J.Aboudi, [83], used the periodic nature of woven composites to introduce the idea of representative volume element or RVE, which is the smallest repetitive unit cell that could be used to reproduce the large scale woven structure without addition of unnecessary information. Additionally, later it was shown by [84] that one can decrease the simulation time by making the use of the symmetry of RVE in geometry and material property to introduce smaller “sub-cells” as shown in Figure 5.9. Given the symmetries in the RVE, when modelling the sub-cell, symmetric boundary conditions need to be applied in the relevant positions; but also if one is going to use the Hill-Mandle approach to compute the homogenised property of the sub-cell, they need to apply the appropriate strain boundary conditions, which is what was carried out in this work.

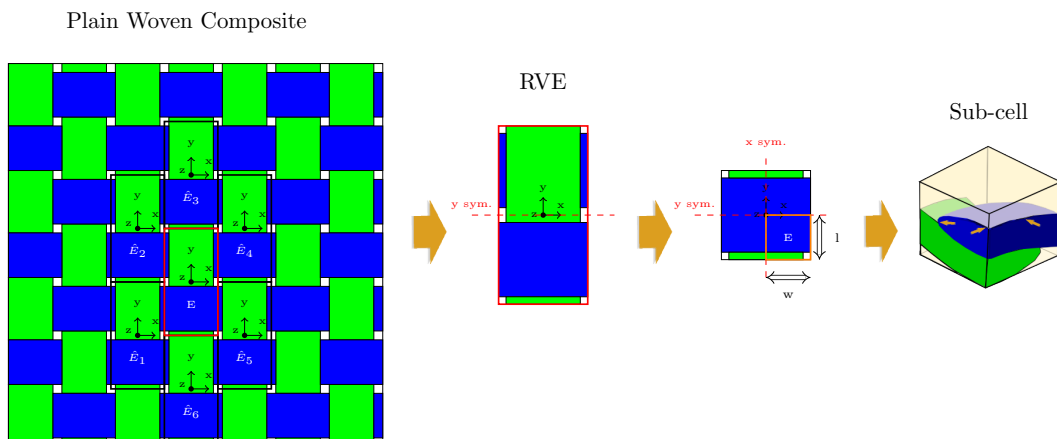


Figure 5.9: Steps taken from the full woven composite material to the smallest cell that can be used to model the property of the whole composite without addition of unnecessary information.

One of the most recent and realistic descriptions of the cross-section of the woven composite sub-cell is given by Wen and Aliabadi, [39], where the cross section of the yarns is defined as the one shown

in Figure 5.10.

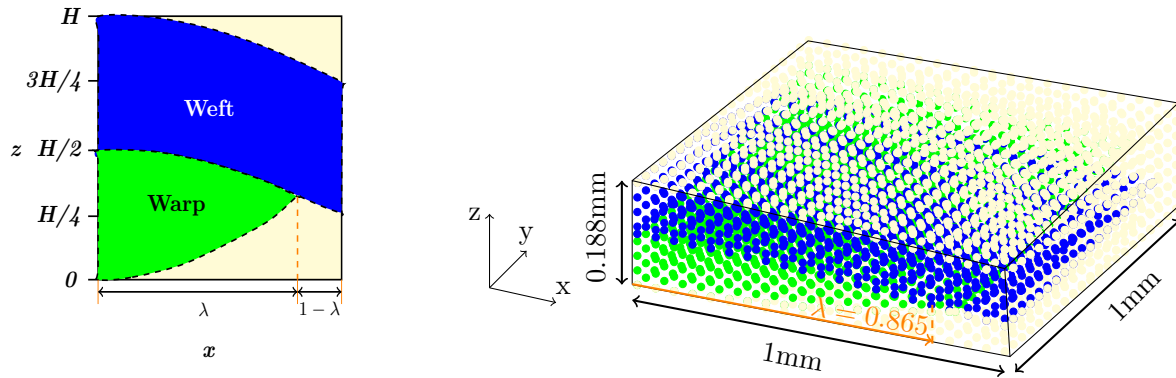


Figure 5.10: **Left:**The smooth definition of the yarn cross section introduced by [39]. (The image is drawn based on the infographic from [39].) **Right:** The dimensions of the plain woven composite sub-cell modelled here.

Shape of the yarns in the warp and weft direction, as shown in Figure 5.10, is defined as

$$z_{top}^{weft}(x, y) = \frac{H}{4} \left(2 + \cos \frac{\pi x}{2} - \cos \frac{\pi y}{2} \right)$$

$$z_{bottom}^{weft}(x, y) = \frac{H}{4} \left(1 - \cos \frac{\pi y}{2} \right) + \alpha x^2 \quad (5.25)$$

$$z_{top}^{warp}(x, y) = H - \alpha y^2 - \frac{H}{4} \left(1 - \cos \frac{\pi x}{2} \right)$$

$$z_{bottom}^{warp}(x, y) = \frac{H}{4} \left(2 + \cos \frac{\pi x}{2} - \cos \frac{\pi y}{2} \right), \quad (5.26)$$

where H is the height of the sub-cell and α is a coefficient dependent on the joint position between the warp and weft yarns, i.e. λ in Figure 5.10.

$$\alpha = \frac{H}{4\lambda^2} \left(1 + \cos \frac{\pi\lambda}{2} \right) \quad (5.27)$$

To find λ , the information regarding the fibre volume fraction, V_y , is required which has to be defined for any woven composite being studied; for the purpose of this preliminary model of the woven composite an arbitrary value of 0.865 is chosen for V_y .

The right image in Figure 5.10 shows dimensions of the woven composite sub-cell that will be used in this study, where both the yarns and matrix are taken to be isotropic and of the same material with Young's modulus and Poisson ratio of 410 GPa and 0.14, respectively. This assumption of isotropic behaviour is only to verify the created RPIM contact model for the simplest case. Given that in reality the material behaviour of the sub-cell is anisotropic, when modelling the complete sub-cell one has to implement the anisotropic nature of the component in the sub-cell.

For simplicity, it is assumed that the two yarns are stuck together and count as a single body which is in contact with the matrix body; in this model, the yarns are taken to be the target, and the

matrix to be the contactor. Having defined the geometry of the sub-cell, the three-dimensional RPIM contact code is used for computation of displacement when a strain of 0.001 is applied to the unit cell in the xx direction, as shown in Figure 5.11, for two limiting cases of full-stick and full-slip. Full-stick is when the yarns and the matrix are fully in stick-contact, and full-slip is when the yarn and matrix are allowed to slip freely with frictionless contact. Using the solutions from a finite element model that was created for the same problem, the accuracy of my RPIM model for the sub-cell in full-stick and full-slip is assessed.

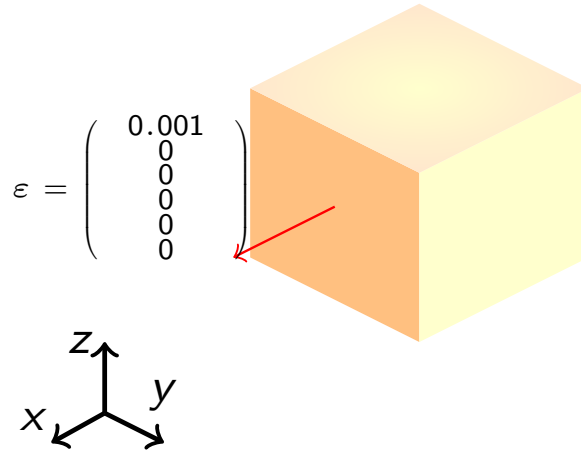


Figure 5.11: The applied strain boundary condition to the preliminary model of the plain woven composite.

5.3 Results & Discussion

The results and discussion section of this chapter consists of two parts; i) verification and optimisation of the developed RPIM frictionless contact code for both two- and three-dimensional cases, and ii) the displacement results of the preliminary model of an isotropic plain woven composite sub-cell for two cases of full-stick and full-slip.

5.3.1 Hertzian Contact - Deformable Cylinder/Rigid Plane

The first set of results considered for the verification of the RPIM contact code, is on the frictionless Hertzian contact between a deformable cylinder and a rigid plane.

5.3.1.1 Convergence

Table 5.1 shows a summary of the best α_{gp} choices for a range of field nodes, i.e. N_{FN} , and integration points, i.e. n_{gp} , for both two- and three-dimensional versions of this example. In order to obtain these values, the first step from the algorithm introduced in chapter 4, i.e. Figure 4.3, is used. In this process for any given number of field nodes, the RPIM simulations ran for a range of α_{gp} s and n_{gp} s,

from which the α_{gp} s that produce the best accuracy are chosen. (For a more detailed explanation of this process please refer to chapter 4.)

Table 5.1: The best choice of α_{gp} for a given N_{FN} and n_{gp} in the two- and three-dimensional versions of the frictionless contact between a deformable cylinder and a rigid plane.

2D	$n_{\text{gp}} \backslash N_{\text{FN}}$	456	970	1993	2531	3D	$n_{\text{gp}} \backslash N_{\text{FN}}$	1491	3159	5588	9126
		2	9	11	6		13		2	14	13
	3	11	15	15	12		3	15	11	11	12
	4	8	14	13	10		4	12	13	11	14
	5	6	11	13	10		5	9	11	14	15

The corresponding convergence plots of Table 5.1 are shown in Figure 5.12 where the three error indicator identified for this example, and their corresponding simulation times are presented for both two- and three-dimensional cases. In each plot the effect of number of integration points per background cell, i.e. n_{gp} is also shown. The results from these plots are used to choose the case with a converged solution.

Considering the two-dimensional case, i.e. the left set of plots in Figure 5.12, it is clear that the green line where $n_{\text{gp}} = 5$, has the lowest percentage error in p_0 and $p(x)$, while showing a very good convergence pattern. For the error in the contact area or a , on the other hand, all the n_{gp} s provide the same error value, which in most cases is more than 10%. This seems to be a large error for a , but given that RPIM method models the contact area with discrete node, it is not possible to capture the exact contact region without high number of nodes and large simulation times. Therefore, as a trade-off between the accuracy and simulation time, these percentage errors for a are considered acceptable.

Looking at the green line in Figure 5.12, the best solution to the two-dimensional version of the problem is for when $N_{\text{FN}} = 1993$. This outcome is additionally approved by plotting the computed stress profile of the contact region against the analytical solution, which is shown in Figure 5.13. It is clear from Figure 5.13 that the RPIM solution matches well with the analytical solution, while due to the discrete nature of RPIM the full contact area is not covered. In order to capture the full contact area more nodes are needed in the contact area which requires longer simulation times. For the purpose of code verification, this outcome is acceptable.

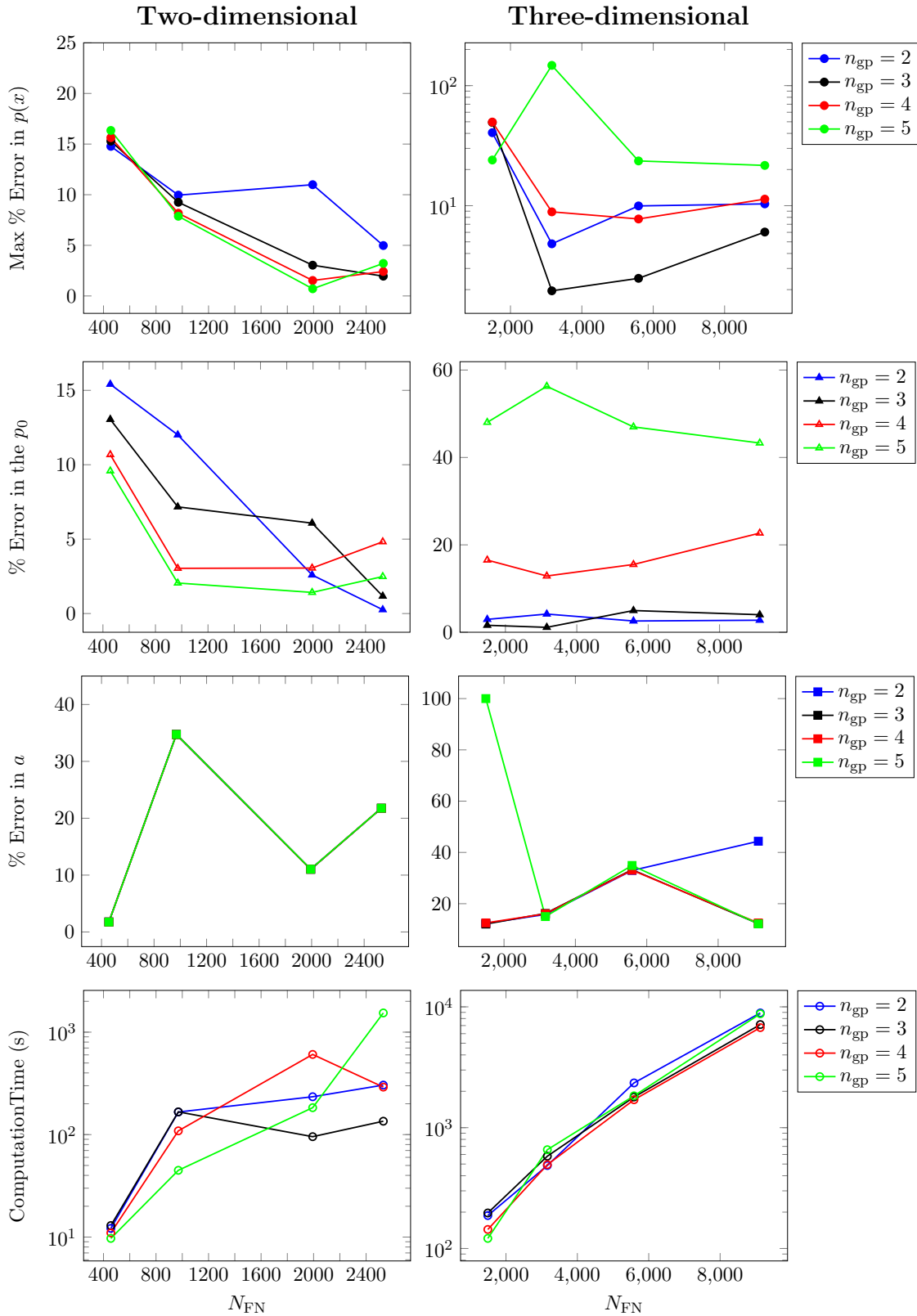


Figure 5.12: The plots here show the convergence results for error indicators of the two- and three-dimensional frictionless Hertzian contact between a deformable cylinder and a rigid plane modelled with the developed RPIM code, and their corresponding simulation times. The first row of plots show the maximum percentage error in the contact stresses, i.e. $p(x)$; the second row of plots show the percentage error in the central contact stress, i.e. p_0 ; the third row of plots show the percentage error in the contact area, i.e. a ; and finally the fourth row of plots show their corresponding computational time.

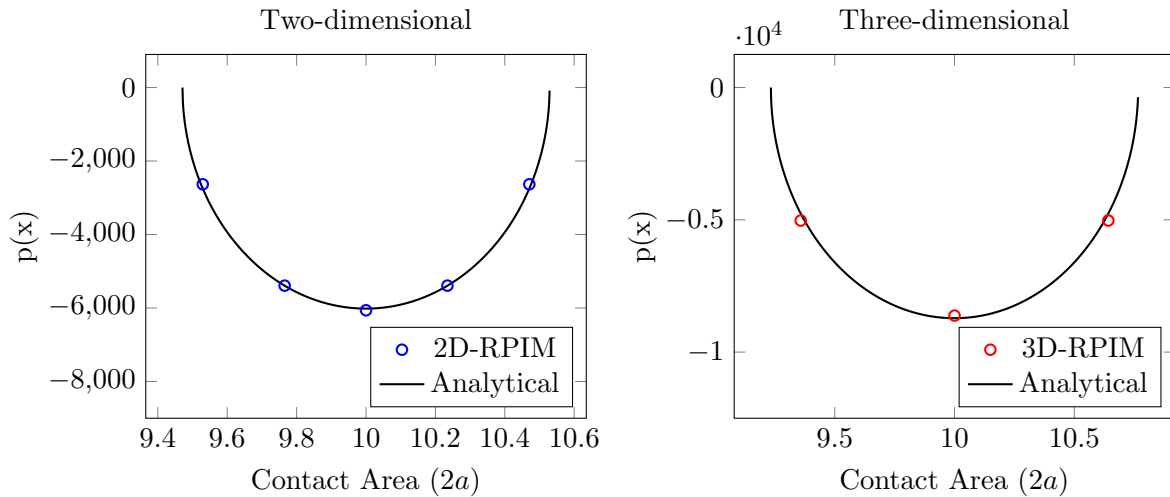


Figure 5.13: The plots here show the converged RPIM stress profile of the contact region against the analytical solution for **left**: two-dimensional, and **right**: three-dimensional contact examples between a deformable cylinder and a rigid plane.

While $n_{\text{gp}} = 5$ gives the best solution for the two-dimensional version of this contact example, for the three-dimensional case the best solution is obtained for when $n_{\text{gp}} = 3$, as can be seen from the black line in the right plots of Figure 5.12. The values used for computation of error indicators in the three-dimensional case are an average value along the length of the cylinder and plane. For the percentage error in the contact area or a , the same argument as the two-dimensional case stands, therefore, a higher level of error compared to stress values is expected. Considering all three error indicators and the simulation time for the three-dimensional case, the converged solution is chosen for when $n_{\text{gp}} = 3$ and $N_{\text{FN}} = 3159$. The right plot in Figure 5.13 also confirms this choice of n_{gp} and N_{FN} for the converged solution of the three-dimensional case.

5.3.1.2 Size of the Support Domain

Once the best choice of field nodes and background cells is obtained, the next step is to find the best support domain size for the given problem. During the convergence process of the two-dimensional example, the variables other than n_{gp} , α_{gp} , and N_{FN} , were fixed as $\alpha_s^{\text{Plane}} = 1.2$, $\alpha_s^{\text{Cylinder}} = 2.0$, $d_c = 2.0$, $\alpha_c = 0.60$ and $q = 1.03$; for the three-dimensional case these variables were fixed as $\alpha_s = 1.5$, $d_c = 2.0$, $\alpha_c = 0.60$ and $q = -0.7$. This initial choice of q and α_c for each example is based on the results from chapter 4.

In the case of the two dimensional examples, an extra investigation for the size of the support domain is carried out; instead of using a single support domain size, i.e. α_s , for both bodies, a separated support domain size is defines for each body, i.e. α_s^{Plane} and $\alpha_s^{\text{Cylinder}}$. For the three-dimensional case, on the other hand, the single support domain size is used for both bodies. This additional comparison of the individual support domain size is introduced to see if it is a good practice to define support

domains of different sizes for different bodies involved in contact problems.

Please note, use of a fixed number of field nodes in every support domain, automatically changes the size of every support domain across the problems domain. This approach is known as influence domain, however, for simple problems use of this method increases the simulation time because at every location that shape functions are calculated, the support domain has to adjust itself to match the required number of field nodes. Defining two separate support domain size for each body, helps reduce the simulation time while considering the different nature of each body.

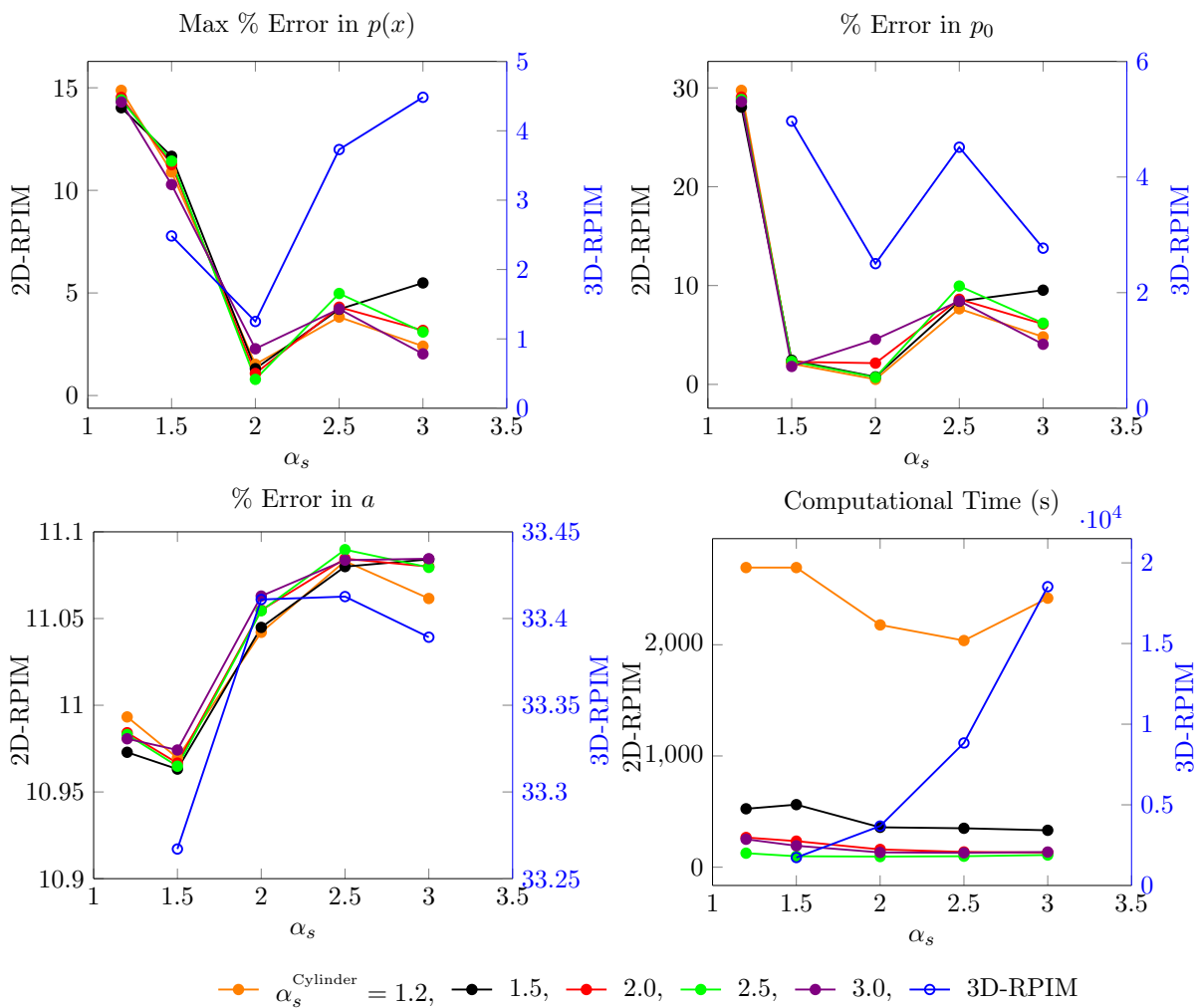


Figure 5.14: The plots here show change of the three error indicators and their corresponding computational time for the two- and three-dimensional versions of the contact between a deformable cylinder and a rigid plane as size of the support domain or α_s changes. The right axis of the plots and the blue line correspond to the three-dimensional case, and the left axis of the plots with all the other coloured lines corresponds to the two-dimensional case.

Figure 5.14, shows the effect of support domain size on the three error indicators defined for the contact between a deformable cylinder and a rigid plane, and their corresponding simulation times. In this figure the results for both two- and three-dimensional cases are presented in the same plots; the blue line and axis in all the plots correspond to the three-dimensional case where the same α_s

is used for both cylinder and the plane. Whereas, for the two-dimensional case, size of the support domain is changed individually for cylinder and the plane. To present these results, the x-axis or α_s is considered as the support domain size of the plane, and the different colours (other than blue) are considered for representing the support domain size of the cylinder or $\alpha_s^{\text{Cylinder}}$.

Considering the two-dimensional results, it is clear that when $\alpha_s^{\text{Plane}} = 2.0$ the best results for $p(x)$ and p_0 are obtained, regardless of $\alpha_s^{\text{Cylinder}}$. For the contact area or a , even though the error for $\alpha_s^{\text{Plane}} = 2.0$ is higher than $\alpha_s^{\text{Plane}} = 1.2$ and 1.5 , but the difference in error is 0.1% which is negligible compared to the low errors obtained in the stress. Therefore, considering all the parameters, the best choice would be $\alpha_s^{\text{Plane}} = 2.0$. At $\alpha_s^{\text{Plane}} = 2.0$, the best choice of $\alpha_s^{\text{Cylinder}}$ is 2.5 because not only for this value the error in $p(x)$ and p_0 is the minimum but also the simulation time is very low.

For the three-dimensional case, as can be seen from the blue lines in Figure 5.14, the lowest error in $p(x)$ and p_0 is for when $\alpha_s = 2.0$, where the simulation time is also on the lower end of the axis. The error in the contact area, on the other hand, is higher than others for this value of α_s but the difference between the lowest and highest error is negligible compared to the over all error value, therefore, $\alpha_s = 2.0$ is accepted at the best choice for this problem.

5.3.1.3 Optimisation

The final step of this process is finding the best choice of RPIM shape parameters, i.e. α_c and q , for both of the two- and three-dimensional contact codes while considering the three error indicators and other relevant information about the problem. Outcome of this sensitivity study is shown in Figure 5.15.

Considering the two-dimensional case, i.e. the left plots in Figure 5.15, it is clear that $\alpha_c = 0.5$ provides the lowest error in p_0 , regardless of q , which also corresponds to the second lowest error in a ; for maximum percentage error in $p(x)$, however, only values of q above 0.5 give low errors. Keeping 0.5 as the best option for α_c , the corresponding best value of q would be 0.98 ; because at this point errors in both $p(x)$ and p_0 are close to 1% . Whereas, if $q = -0.3$ is chosen, the error in $p(x)$ rises to about 4% , even though the error in p_0 drops to 0.1% , therefore, $q = 0.98$ is considered as the best choice for when $\alpha_c = 0.5$. (Please note for the two-dimensional case in Figure 5.15 plots for $\alpha_c = 1.5$ and 2.0 are not included; this is because for these values the errors were significantly high, therefore, there was no advantage in including them.)

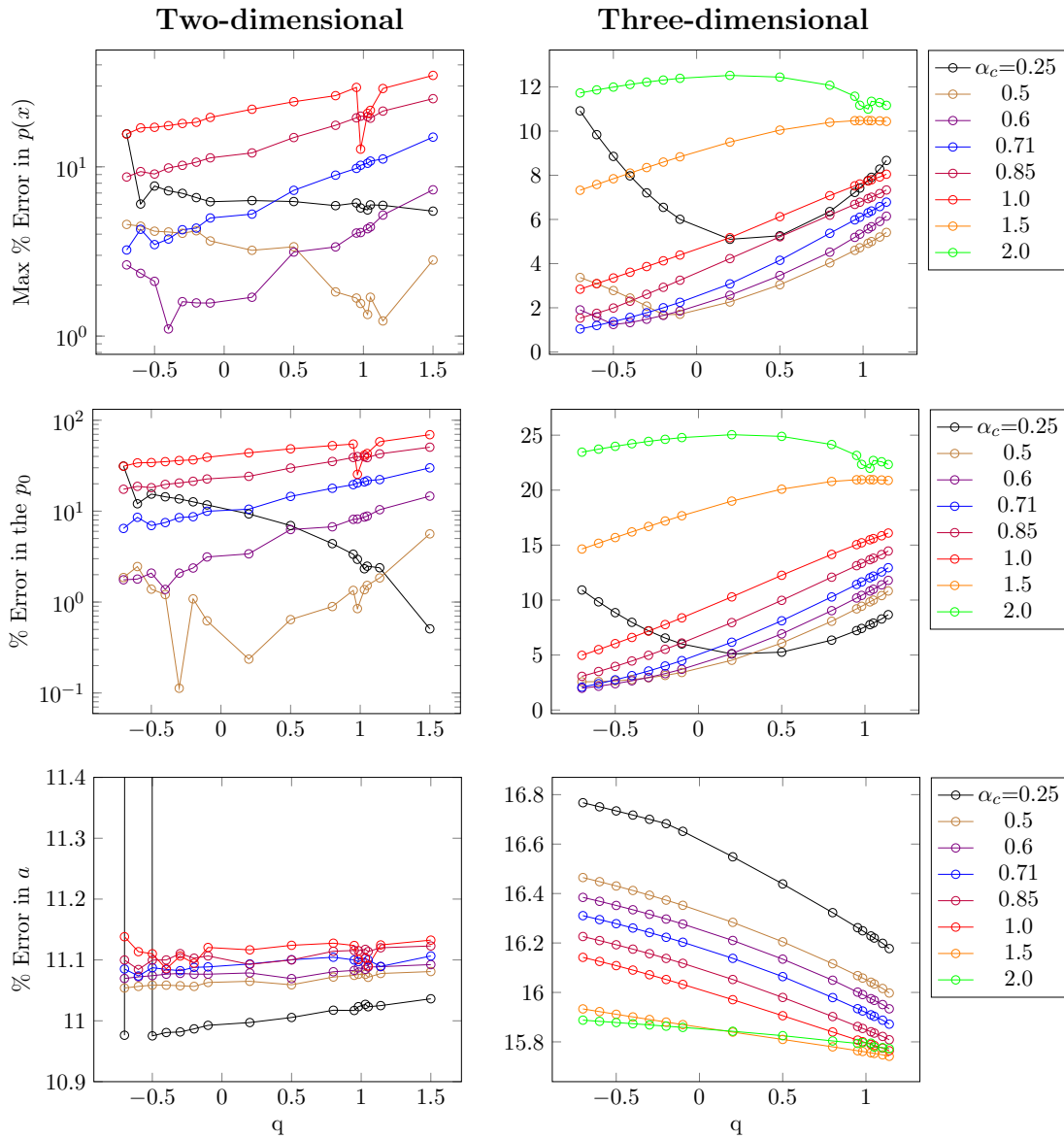


Figure 5.15: The left plots show change of the three error indicators with α_c and q , for the two-dimensional contact between a deformable cylinder and a rigid plane modelled by the developed RPIM code. The right plots show the same information but for the three-dimensional version of this contact example.

Having chosen a sensible combination of α_c and q based on the results in Figure 5.15, there is an additional step for confirmation of this choice. This final check is a comparison between the developed RPIM code and FE for the computed vertical displacement and stress profile in both bodies. The reason for this comparison is that with this RPIM method, it is possible to obtain a correct localised solution while the solution in the rest of the problem domain is wrong. Therefore, to ensure correct solution everywhere, this comparison is carried out. For the choice of $\alpha_c = 0.5$ and $q = 0.98$, this comparison showed a mismatch of stress distribution in parts of the rigid plan, therefore, this choice of RPIM shape parameter is not acceptable. This process of choosing α_c and q , and comparing with FE continues until all the results match. For this two-dimensional example, the choosing process led to $\alpha_c = 0.6$ and $q = -0.3$, where not only the errors in $p(x)$ and p_0 are about 2% but also there is very

good match between the PRIM results and the converged solution from FE, as shown in Figure 5.16.

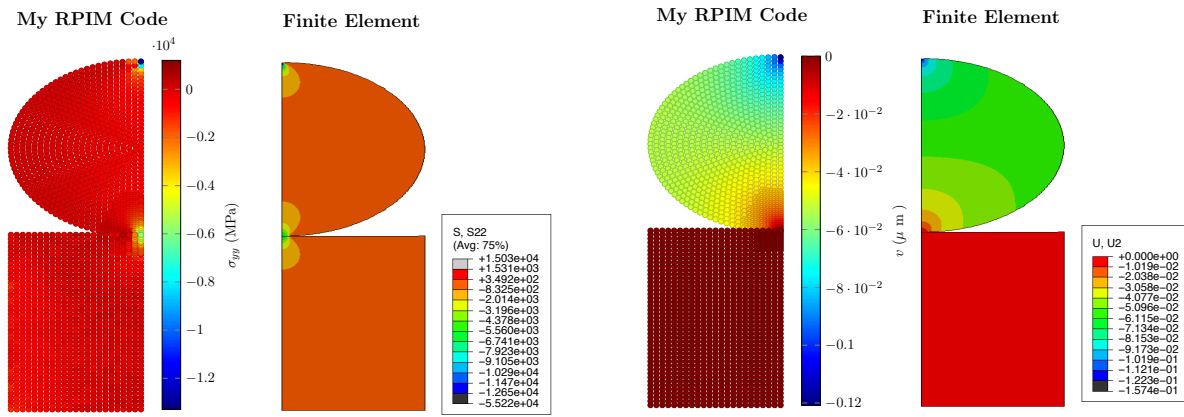


Figure 5.16: The figures here show the comparison between the two-dimensional RPIM contact code and FE (Abaqus/CAE 6.14-4) for the computed vertical stress and displacement profile of the deformable cylinder and the rigid plane. **Left two figures:** the vertical stress (σ_{yy}) profile, and **Right two figures:** the vertical displacement (u_y) profile.

For the three-dimensional case, as can be seen from the right plots in Figure 5.15, a clear trend is observed for the error in $p(x)$ and p_0 as both α_c and q change. For both mentioned error indicators, as α_c increases or as q goes from the negative end to the positive end, the value of error increases, except for when $\alpha_c = 0.25, 0.5$ and 0.6 which all have a minima. For the error in the contact area or a , the exact opposite trend to the one for $p(x)$ and p_0 happens, as α_c increases or as q goes from the negative end to the positive end, the error in a decreases. However, the difference between the maximum and minimum error in a is about 1% compared to 10% or 20% for the $p(x)$ or p_0 , respectively, therefore, choosing according to the errors in $p(x)$ and p_0 is more important.

Considering the errors in $p(x)$ and p_0 , the lowest error is when $\alpha_c = 0.71$ and $q = -0.7$; for this combination, the corresponding error in a is about 16.3% which is only 0.6% more than the minimum error in a . The result from this choice of α_c and q is used when comparing with the FE results, as shown in Figure 5.17. There is a clear match between the finite element results and the ones from the RPIM code; the only difference between them is that the maximum stress in the RPIM code is less than FE. This difference is because of the node spacing in that region. Given that a line displacement is applied on the top of the cylinder, theoretically the stress value along that line is infinite, however, in computational methods a small area is defined in the vicinity of the line to help approximated the stress. This is why the smaller the node spacing in that region the higher the computed stress. For this example, the node spacing for the converged solution of the FE is much smaller than the one for the RPIM code which caused the difference in the maximum stress. This outcome is in accordance with the previous findings in chapter 4 which concluded that RPIM obtains convergence with less nodes than FE.

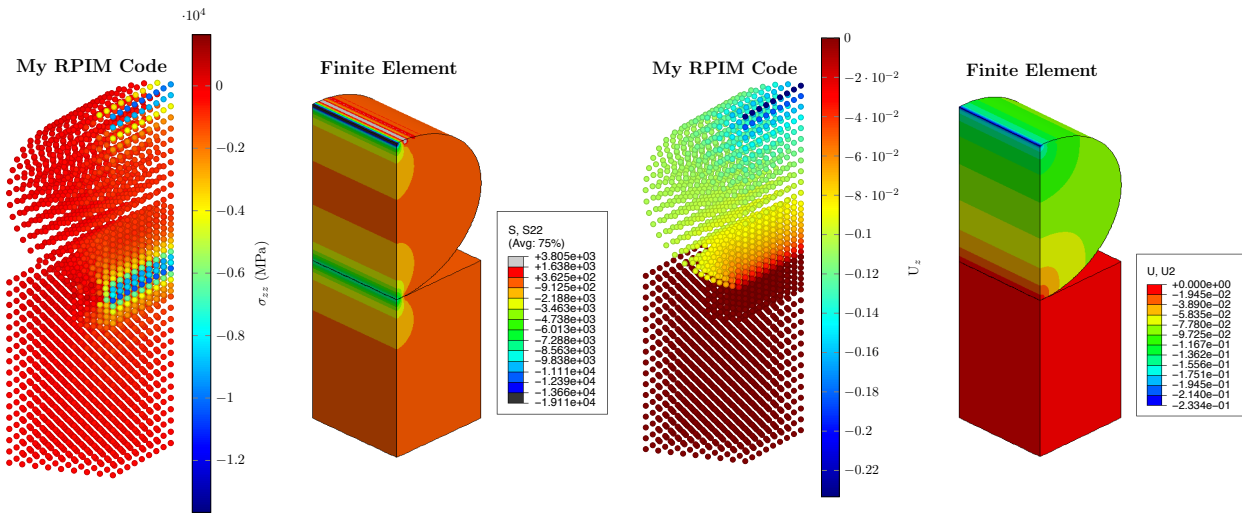


Figure 5.17: The figures here show the comparison between the three-dimensional RPIM contact code and FE (Abaqus/CAE 6.14-4) for the computed vertical stress and displacement profile of the deformable cylinder and the rigid plane. **Left two figures:** the vertical stress (σ_{zz}) profile, and **Right two figures:** the vertical displacement (u_z) profile.

5.3.2 Hertzian Contact - Deformable Cylinder/Deformable Plane

After verifying the two- and three-dimensional versions of the RPIM contact code for the Hertzian contact between a deformable cylinder and a rigid plane, in this part the two codes are used for when both of the bodies are deformable and of the same material. The boundary conditions used for this example are the same as the previous case, i.e. Figure 5.8, and similar to the previous example, for the convergence of the solutions and optimisation of RPIM shape parameters, the algorithm from chapter 4 is used.

5.3.2.1 Convergence

For the first step of the convergence, Table 5.2 shows a summary of the best choice of α_{gp} for a given N_{FN} and n_{gp} for both the two- and three-dimensional versions of this example. Figure 5.18 shows the three error indicators corresponding to these values of α_{gp} .

Table 5.2: The best choice of α_{gp} for a given N_{FN} and n_{gp} in the two- and three-dimensional versions of the frictionless contact between a cylinder and a plane of the same material.

2D	N_{FN}					3D	N_{FN}				
	n_{gp}	456	970	1665	1993		n_{gp}	1491	3159	5588	9126
	2	9	12	6	15		2	9	15	15	14
	3	6	8	9	14		3	12	11	13	14
	4	7	11	14	14		4	12	13	14	12
	5	8	15	14	14		5	9	11	11	13

As can be seen in Figure 5.18 for the two-dimensional case, the overall error in the contact area converges with the increase in N_{FN} for all the values of n_{gp} . For the error in $p(x)$ and p_0 , there is not

such a clear convergence trend, however, considering $N_{\text{FN}} = 970$ where the error in contact area has almost converged, it can be seen that $n_{\text{gp}} = 5$ produces the best error in both $p(x)$ and p_0 . This is in addition to the relatively low simulation time, therefore, for the two-dimensional contact between a deformable cylinder and a deformable plane, the accepted convergence parameters are $N_{\text{FN}} = 970$, $\alpha_{\text{gp}} = 15$ and $n_{\text{gp}} = 5$. The rest of the parameters for this simulation were fixed as $\alpha_s^{\text{Plane}} = 1.5$, $\alpha_s^{\text{Cylinder}} = 1.5$, $d_c = 2.0$, $\alpha_c = 0.60$ and $q = 1.03$.

For the three-dimensional version of this example, the right set of plots in Figure 5.18 are considered where the parameters other than the ones involved in convergence are fixed as $\alpha_s = 1.5$, $d_c = 2.0$, $\alpha_c = 0.60$ and $q = -0.7$. No strong convergence pattern is observed for the three-dimensional case which can be because of two main reasons; i) the initial choice of RPIM shape parameters (i.e. α_c and q) which was based on the results in chapter 4, and ii) because of the slow nature of the three-dimensional RPIM method, it is very time consuming to reduce the node spacing as much as the two-dimensional case. In the later stages of this section the optimum choice of α_c and q for the given combination of N_{FN} , α_{gp} and n_{gp} will be found which can potentially deal with the first reason. However, for the second reason a faster computer and more efficient solver is needed which is not the case here. Nevertheless, from the results in Figure 5.18 a sensible choice can be made for N_{FN} , α_{gp} and n_{gp} , for which the optimum choice of α_c and q can be found later.

Following the discussion about Figure 5.18, the acceptable solution to this problem in three-dimension is for when $N_{\text{FN}} = 3159$, $\alpha_{\text{gp}} = 11$ and $n_{\text{gp}} = 3$; because for this choice not only the error in $p(x)$ and p_0 is very low but also the simulation time is relatively low. The only remaining issue is the error in the contact area, which because of the discrete nature of the RPIM method and low number of field nodes at the contact area, is also acceptable.

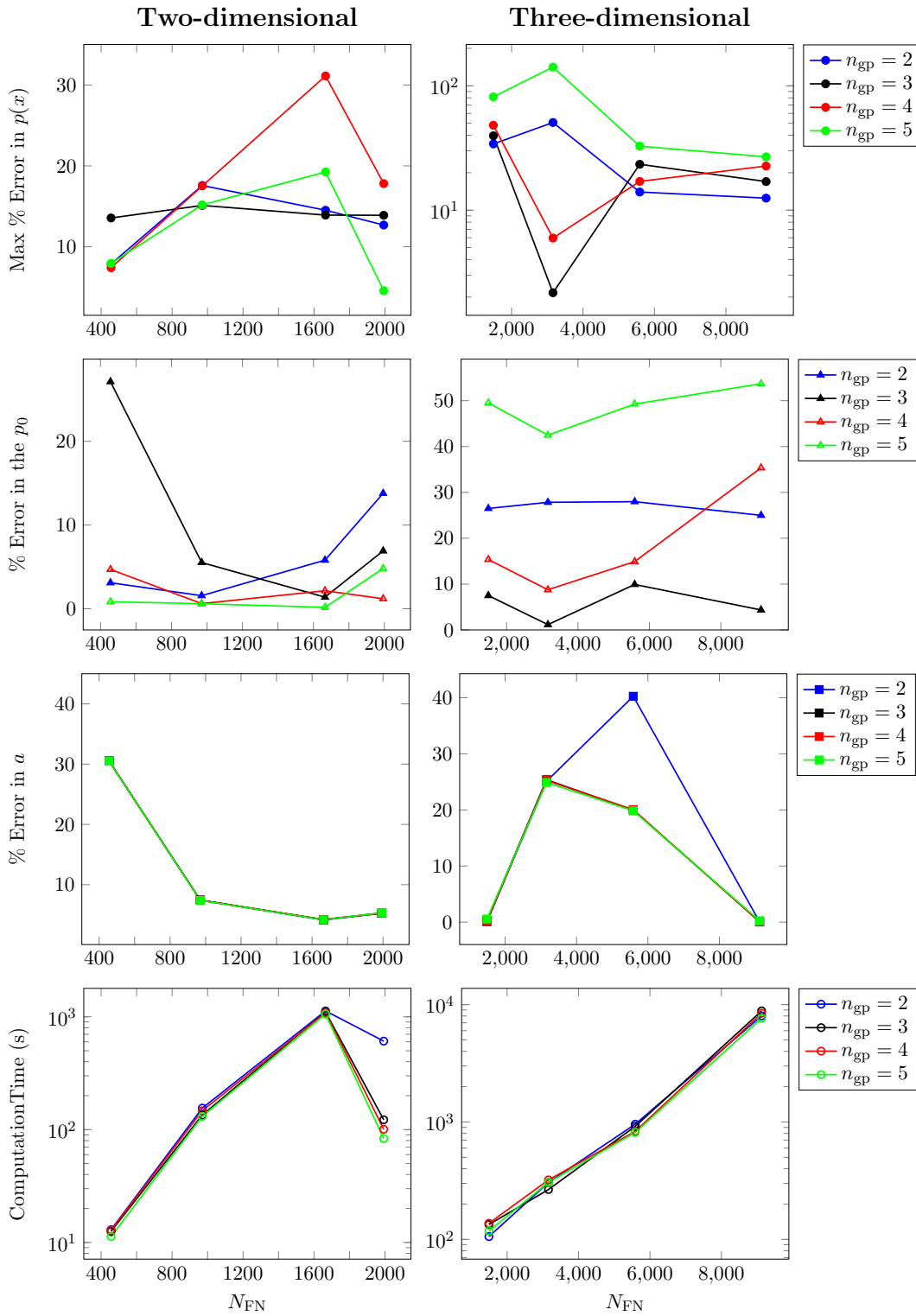


Figure 5.18: The plots here show the convergence results for error indicators of the two- and three-dimensional frictionless Hertzian contact between a cylinder and a plane of the same material modelled with the developed RPIM code, and their corresponding simulation times. The first row of plots show the maximum percentage error in the contact stresses, i.e. $p(x)$; the second row of plots show the percentage error in the central contact stress, i.e. p_0 ; the third row of plots show the percentage error in the contact area, i.e. a ; and finally the fourth row of plots show their corresponding computational time.

Figure 5.19 show the stress profile of the contact region for the chosen converged solution of the two- and three-dimensional examples of the deformable cylinder and plane in contact. It is clear from the left plot that for the two-dimensional contact between the cylinder and plane of the same material there is a good match between the results computed by the RPIM code and the analytical solution for it. Additionally, the contact area covered by the discrete nodes is very close to the analytical one, which is also apparent from the corresponding plot in Figure 5.18.

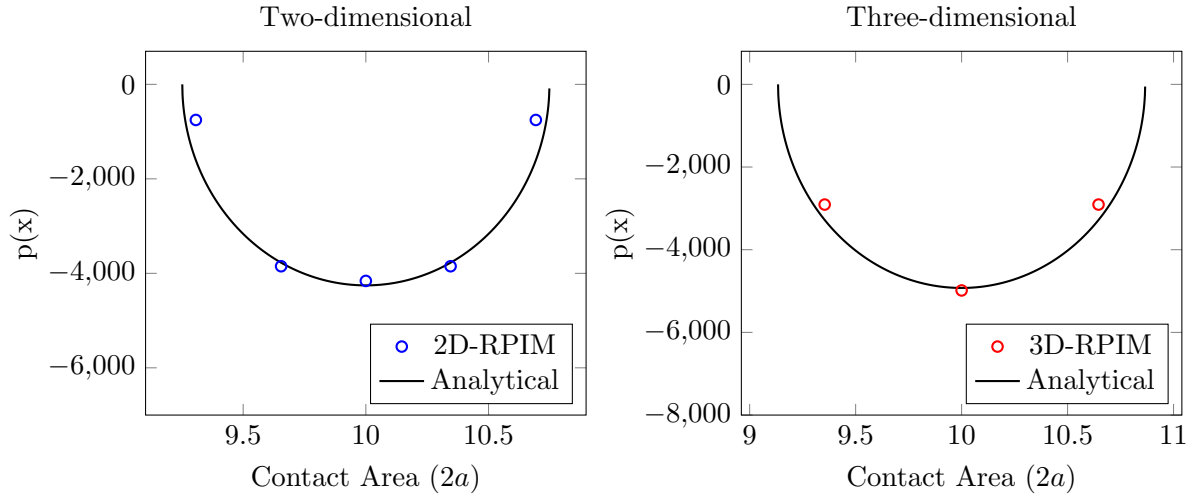


Figure 5.19: The plots here show the converged RPIM stress profile of the contact region against the analytical solution for **left**: two-dimensional, and **right**: three-dimensional contact examples between a deformable cylinder and a deformable plane.

For the three-dimensional stress profile in the contact region, as is clear from Figure 5.19, there is a good match between the computed stress using the RPIM contact code and the analytical solution. However, the contact area captured by the discrete nodes of RPIM is not very close to the actual value; in order to capture that, more nodes are required in the contact region, however, as the nodes increase, the simulation time increases as well, therefore, one can use faster computers together with more field nodes.

5.3.2.2 Size of the Support Domain

Having found the best values of the N_{FN} , α_{gp} and n_{gp} for the two- and three-dimensional examples of contact between a deformable cylinder and a deformable plane, the next step is finding the best support domain size. Similar to the previous case with rigid plane, for the two-dimensional version of the example, the support domain size used for the cylinder and the plane is changed separately which means there are two support domain sizes defined in the code, i.e α_s^{Plane} and $\alpha_s^{\text{Cylinder}}$.

Figure 5.20 shows the effect of α_s^{Plane} and $\alpha_s^{\text{Cylinder}}$ on the three error indicators defined for the examples; the results for the two-dimensional case are shown in the coloured lines except for the blue one. The x-axis labeled as α_s corresponds to α_s^{Plane} for the two dimensional case. Looking at the

percentage error in $p(x)$ and p_0 , it is clear that the black line, i.e. when $\alpha_s^{\text{Cylinder}} = 1.5$, has the lowest errors and simulation times which makes it a very good choice. However, choosing α_s^{Plane} it is not as clear; while for $\alpha_s^{\text{Plane}} \geq 2$ the error in $p(x)$ is very low but at the same time the error in the contact area is more than 50%. Given that with this number of field nodes, it is possible to compute a contact area closer to the analytical one, this outcome is not acceptable. Therefore, the option $\alpha_s^{\text{Plane}} = 1.5$ is chosen; because it has the lowest errors in p_0 and a while at the same time it has a very low simulation time. The percentage error in $p(x)$ is about 15% which is higher than expected, but it is acceptable because this is not the final step of the optimisation process, and lower errors in $p(x)$ could be obtained with change in α_c and q .

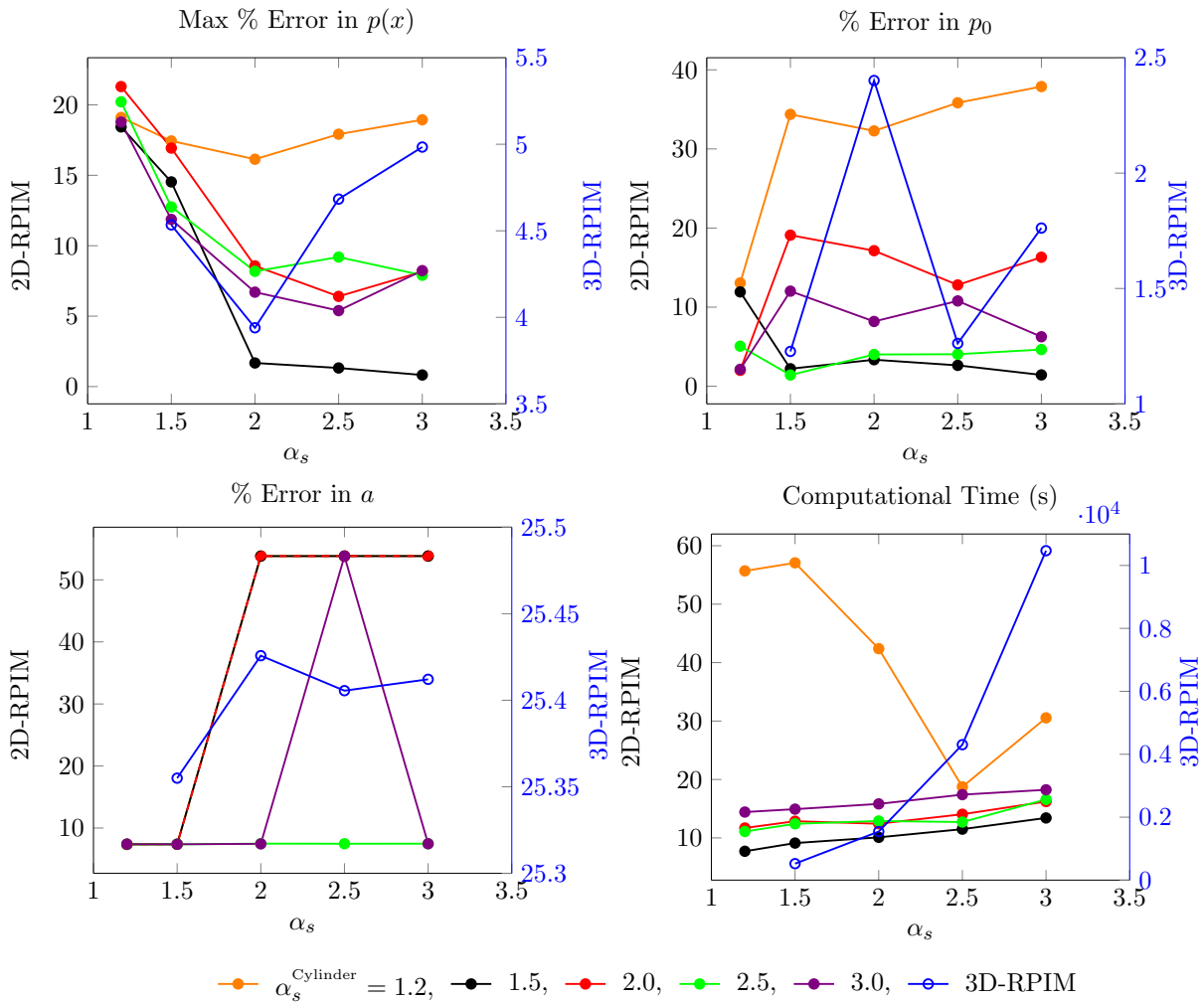


Figure 5.20: The plots here show change of the three error indicators and their corresponding computational time for the two- and three-dimensional versions of the contact between a deformable cylinder and a deformable plane as size of the support domain or α_s changes. The right axis of the plots and the blue line correspond to the three-dimensional case, and the left axis of the plots with all the other coloured lines corresponds to the two-dimensional case.

For finding the best support domain size for the three-dimensional version of this example, also similar to the previous case with the rigid plane, a single support domain size is used for both of the bodies, i.e. α_s . As is clear from the blue lines in Figure 5.20, $\alpha_s = 1.5$ is the best choice; because while

it has the lowest error in both a and p_0 , and the lowest simulation time, but it also has a low error in $p(x)$ relative to the two-dimensional case. $\alpha_s = 2.0$ is not the best choice because at the same time that it has the lowest error in $p(x)$, it has the highest error in a and p_0 . Nevertheless because the difference in the error values is not very significant, depending on what is the most important choosing factor, either of them can be chosen. Given that $\alpha_s = 1.5$ has the lowest simulation time, it is the chosen support domain size for the final optimisation step.

5.3.2.3 Optimisation

The final step for this example is finding the best combination of α_c and q , using the results from Figure 5.21 and the comparison with FE. The process of which is described here.

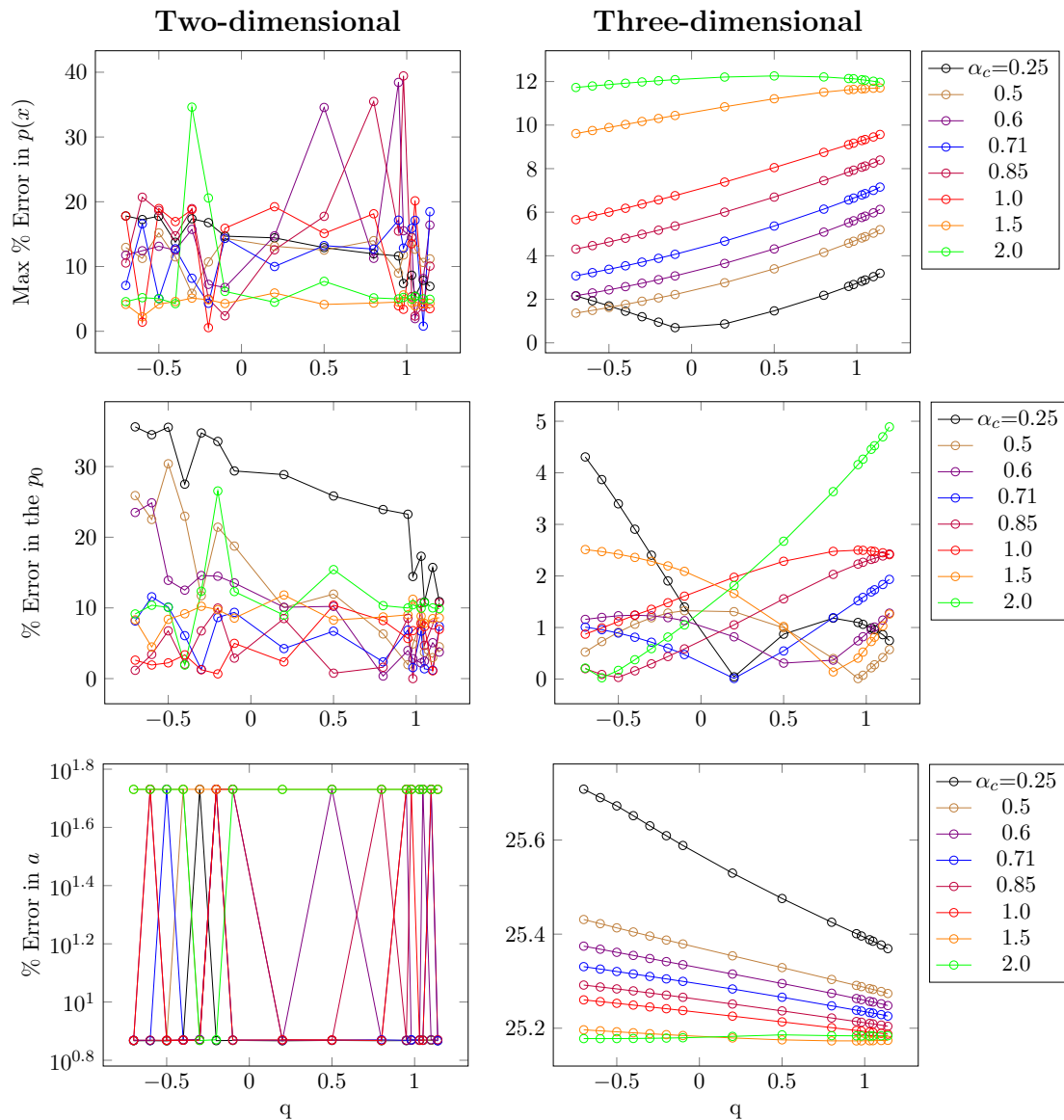


Figure 5.21: The left plots show change of the three error indicators with α_c and q , for the two-dimensional contact between a deformable cylinder and a deformable plane modelled by the RPIM code. The right plots show the same information but for the three-dimensional version of this contact example.

Looking at the results for the two-dimensional in Figure 5.21, it is clear that there are many points where the error in $p(x)$ and p_0 is less than 5%, however, in most of those cases, the error in a is more than 50% which is not acceptable. Therefore, after considering all the error indicators, the combination of RPIM shape parameters that produces the best results is found to be $\alpha_c = 0.71$ and $q = -0.3$. The resultant vertical stress and displacement profile of the cylinder and plane from this choice of α_c and q , is compared to the results from the finite element model as shown in Figure 5.22. In this figure the colour limit for both methods has been set to be the same as the one for my PRIM code so this way a fair comparison can be done. It is clear from this figure that there is a very good agreement between my RPIM code and finite element in both stress and displacement. The only difference is in the maximum value of stress on the top of the cylinder which is because of the smaller node spacing in the finite element model; this reasoning has been discussed previously in section 5.3.1.3.

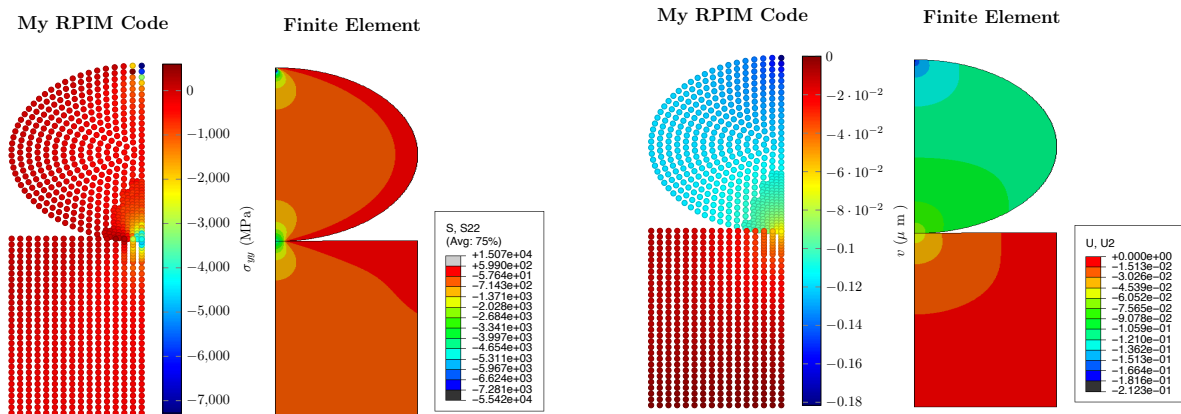


Figure 5.22: The figures here show the comparison between the two-dimensional RPIM contact code and FE (Abaqus/CAE 6.14-4) for the computed vertical stress and displacement profile of the deformable cylinder and the deformable plane. **Left two figures:** the vertical stress (σ_{yy}) profile, and **Right two figures:** the vertical displacement (u_y) profile.

In the final step of the optimisation process for the three-dimensional version of the frictionless contact between a deformable cylinder and plane, the right plots in Figure 5.21 are considered. There is a clear trend in the maximum error in $p(x)$ which shows a decrease in error with decrease in α_c for any value of q . Additionally, as q decreases from the positive end, the value of error in $p(x)$ decreases. For the error in the contact area, the exact opposite is true; in other words, the error increases as α_c decrease, and as q goes from the positive to the negative end. Given that the difference between the maximum and minimum error in a is about 0.5% while this difference in $p(x)$ is about 12%, choosing an α_c and q with lowest error in $p(x)$ becomes more important. In contrast to $p(x)$ and a , there is no clear trend in p_0 , therefore, when choosing the optimum value of α_c and q this has to be taken into account.

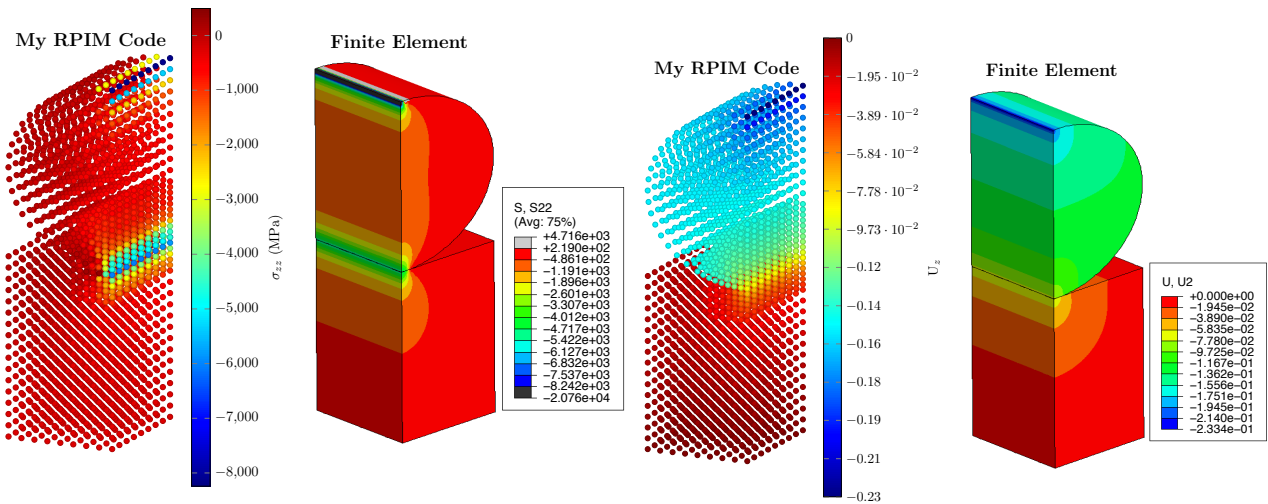


Figure 5.23: The figures here show the comparison between the three-dimensional RPIM contact code and FE (Abaqus/CAE 6.14-4) for the computed vertical stress and displacement profile of the deformable cylinder and the deformable plane. **Left two figures:** the vertical stress (σ_{zz}) profile, and **Right two figures:** the vertical displacement (u_z) profile.

Considering all the error indicators and the comparison with the finite element solution, as shown in Figure 5.23, the best choice is when $\alpha_c = 0.5$ and $q = -0.7$. Figure 5.23 shows the vertical stress and displacement field of the cylinder and the plane for $\alpha_c = 0.5$ and $q = -0.7$, compared to the finite element results of the same problem. It can be seen here that there is very good agreement between the results from the developed RPIM code and the one from finite element.

5.3.3 Preliminary Model of the Woven Unit Cell

Having shown the verification and optimisation process of the two- and three-dimensional RPIM code for frictionless contact using two Hertzian examples, in this section, the results for the preliminary model of the woven composite is shown and discussed; the preliminary model is used for two limiting cases of full-stick and full-slip.

5.3.3.1 Full Stick

In the full-stick case, the yarns are tied to the matrix which together act as a single block of SiC material. This is why it is expected that the yarns and matrix deform with the same displacement as each other; this is apparent from the displacement results of the three-dimensional RPIM code on the left side of Figure 5.24. Additionally, for a more concrete verification of the RPIM model, the results from the developed RPIM code are compared to the ones from a FE model in Abaqus. As is clear from Figure 5.24, the results from the RPIM code is in a very good agreement with the results from FEM, which verifies the use of stick condition in the produced RPIM contact code.

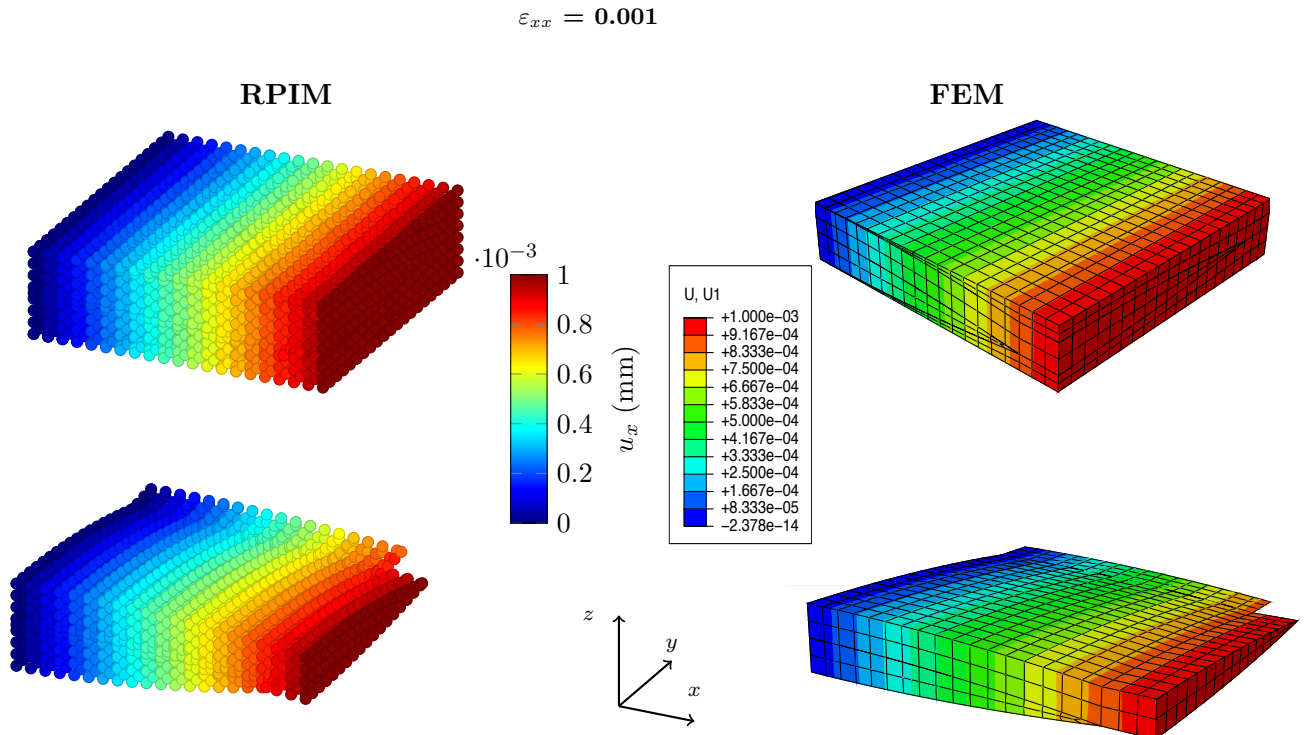


Figure 5.24: Comparison between FEM and the developed RPIM code in computing the displacement profile of the yarns and unit cell for the full-stick condition when a strain is applied in the xx direction.

Figure 5.24 not only shows the resultant displacement in the whole unit cell but also the yarns; the displacement results in the yarns are shown separately in order to give a clearer picture of this verification and how the yarns deform under the stick condition. Please note, given that on each face of the unit cell essential boundary conditions are applied, the contact conditions are removed from those regions to avoid the clash of boundary and contact conditions.

5.3.3.2 Full Slip

The second limiting case for the preliminary model of the woven composite is when the yarns and the matrix are allowed to slip relative to each other with frictionless contact, i.e. full-slip. For this case also the results from the developed RPIM code is compared to that of finite element in Figure 5.25 for verification. As is clear from the figure, there is a very good agreement between the RPIM results and that of finite element which verifies the use of slip conditions in the RPIM contact code. Given that the two parts are free to slip relative to each other, it is expected for the displacement of the matrix have minimal effect on the yarns and vice versa; in other words their displacement profiles should be as if they were separately deformed, which is the case here.

Please note, these two cases are ends of the micro-crack spectrum where full-stick means 0%

delamination and full-slip means 100% delamination at the yarn-matrix interface. While the full-slip case is not realistic but it gives a good understanding of how the developed RPIM frictionless contact code works for the relative slippage in woven composite unit cell.

$$\varepsilon_{xx} = 0.001$$

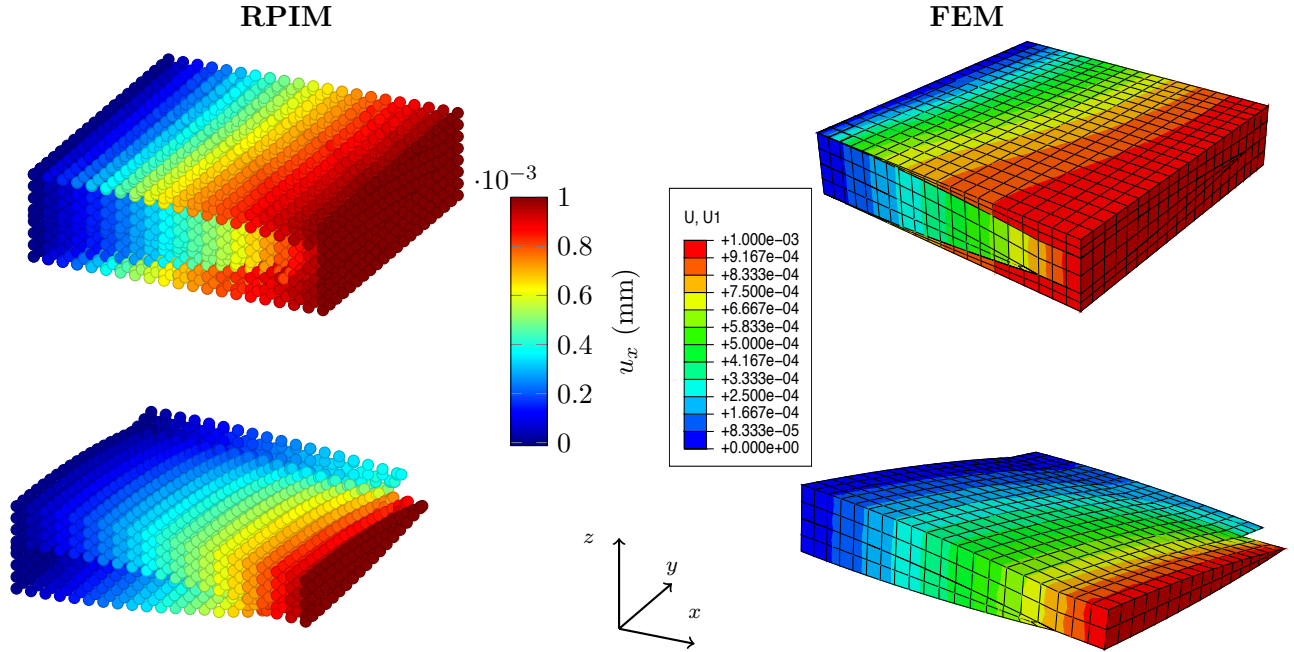


Figure 5.25: The displacement profile of the yarns for the full-slip case when a strain is applied in the xx direction, comparing the RPIM code results with FEM.

Given that this is the beginning stage of developing the meshfree model of a woven $\text{SiC}_f/\text{SiC}_m$ composite, FE method is used for verification of the RPIM results, however, as the geometries and the contact computations become more complex, experimental methods may be required for validation. The most important advantage of the RPIM method over FEM for problems like this is that it gives the flexibility of having non-uniform node distribution and addition of more nodes where required; for example at the sharp edge of the yarns which are in contact with the matrix. In spite of the slow nature of RPIM, the flexibility of this method for complex geometries, its convergence for less nodes than FE and its simple implementation from two- to three-dimensions have been shown and discussed throughout this chapter and the previous one.

5.4 Conclusion

In the process of developing a model for the micro-cracks or delamination at the yarn-matrix interface of a woven $\text{SiC}_f/\text{SiC}_m$ composite using meshfree methods, the first three-dimensional MQ-RPIM frictionless contact code was developed from scratch. The development process in this work included i) implementation of the coulombic contact theory into two- and three-dimensional MQ-RPIM codes using Lagrange multipliers, ii) verification of the MQ-RPIM contact model for two- and three-dimensional

Hertzian examples, and iii) development of the first model of a plain woven composite unit cell where the yarns and matrix are in frictionless contact.

During the verification process of the MQ-RPIM contact model, the optimisation algorithm introduced in chapter 4 was used to find the best set of parameters for the Hertzian contact problems, which included the two- and three-dimensional contact between a cylinder and a plane, where the plane was once rigid and once of the same material as the cylinder. The stress and displacement results obtained from the optimisation process were then verified against the analytical and finite element results. Additionally, the comparison between the RPIM results and FEM confirmed the flexibility of RPIM method in modelling with non-uniform distribution of nodes, particularly at contact regions.

Once verified, the developed frictionless contact code with MQ-RPIM method was successfully applied to the preliminary model of the plain woven composite unit cell. This preliminary model, computed the displacement profile of a plain woven composite unit cell subject to an applied uniform strain under two extreme conditions; i) full-stick (0% delamination) and ii) full-slip (100% delamination). The results from these models were verified against the results from finite element models, showing that the slip and stick conditions used in the developed RPIM model are implemented correctly. Therefore, completing the first building block towards the final model of the woven $\text{SiC}_f/\text{SiC}_m$ composite unit cell with frictional contact at the yarn-matrix interface.

5.5 Table of variables

Table 5.3: Variables and terms used in this chapter and their definitions.

EFG	Element free Galerkin
RPIM	Radial point interpolation method
RKPM	Reproducing Kernel particle method
RVE	Representative volume element
FEM	Finite element method
MQ-	Multi-quadric
IMQ-	Inverse multi-quadric
EXP	Gaussian
Ana	Analytical
μ	Coulumb friction coefficient
Π	Energy of the system
\square_C	Related to the contactor body
\square_T	Related to the target body
\square_I	Related to the point of intersection between two bodies
$[\mathbf{u}_y]$	Displacement vector for the y^{th} body
$[\mathbf{k}_y]$	Stiffness matrix for the y^{th} body
$[\mathbf{F}_y]$	Force vector for the y^{th} body
$[\mathbf{n}]$	Unit normal vector
$[\mathbf{t}]$	Unit tangential vector
g_n	Initial normal gap between the target and contactor body for contacted nodes
g_t	Initial tangential gap between the target and contactor body for contacted nodes
λ_n	The normal force between the target and contactor body at the contacted node
λ_t	The tangential force between the target and contactor body at the contacted node
ϕ_i	MQ-RPIM shape function of field node i
Φ	Matrix of radial basis shape functions
\mathbf{K}	Global stiffness matrix
\mathbf{U}	Global displacement vector
\mathbf{F}	Global force vector
a	Semi-width of the contact area
C	A constant to be found
k	Relative curvature
$h(x)$	Shape of the interpenetration between the two bodies
R_1	Radius of body 1
R_2	Radius of body 2
R	Radius of the cylinder
$p(x)$	Distributed pressure at contact area

p_0	Contact pressure at the centre of the contact area
P	Magnitude of the applied load per length in the examples
F	$P/2$
U	Applied displacement
A and β	Known as composite parameter
ν_y	Poisson ratio for the y^{th} body
E_y	Young's modulus for the y^{th} body
m	A parameter computed from $\tan(m\pi) = \frac{1}{\beta\mu}$
ϵ_a	Percentage error in a
ϵ_{p_0}	Percentage error in p_0
ϵ_p	Percentage error in p
H	Height of the unit cell
α	A coefficient dependent on the joint between the warp and weft yarns
λ	Location of the joint between the warp and weft yarns
V_y	Volume fraction for the fibres
ε	Applied strain vector
N_{FN}	Total number of field nodes in the problem domain
n_{gp}	Number of quadrature points per direction per background cell
α_s	A coefficient to define the size of support domain
α_c	MQ-RPIM shape parameter
α_{gp}	Factor for estimating the number of background cells
q	MQ-RPIM shape parameter
d_c	A characteristic length proportional to the nodal spacing near the point of interest

5.6 Bibliography

- [1] R. Naslain. Design, Preparation and Properties of Non-Oxide CMCs for Application in Engines and Nuclear Reactors: An Overview. *Composites Science and Technology*, 64(2):155–170, 2004.
- [2] A.H. Rashed. Properties and Characteristics of Silicon Carbide, 2002.
- [3] GoodFellow. Silicon Carbide (SiC), Material Information.
- [4] J.J Brennan. Interfacial Characterization of a Slurry-Cast Melt-Infiltrated SiC/SiC Ceramic-Matrix Composite. *Acta Materialia*, 48(18-19):4619–4628, dec 2000.
- [5] A.M. Calomino and M.J. Verrilli. SiC Composite Turbine Vanes, 2006.
- [6] C Droillard and J Lamon. Fracture Toughness of 2-D Woven SiC/SiC CVI-Composites with Multilayered Interphases. *Journal of the American Ceramic Society*, 79:849–58, 1996.
- [7] David Roylance. Introduction to composite materials. pages 1–7, 2000.

-
- [8] F. C. Campbell. Introduction to Composite Materials. In *Structural Composite Materials*, chapter One. ASM International, 2010.
- [9] Nelson Vieira De Carvalho. *Understanding and Modelling the Mechanical Response of Woven Composites by*. PhD thesis, Imperial College London, 2012.
- [10] P Tan, L Tong, and G P Steven. Modelling for Predicting the Mechanical Properties of Textile Composites -A Review. *Composites Part A*, 28A:903–922, 1997.
- [11] Ping Tan, Liyong Tong, and Grant P Steven. Micromechanics models for the elastic constants and failure strengths of plain weave composites. *Composite Structures*, 47:797–804, 1999.
- [12] N K Naik and P S Shembekar. Elastic Behavior of Woven Fabric Composites : I-Laminate Analysis. *Journal of Composite Materials*, 26(15):2196–2225, 1992.
- [13] R. Yamada, T. Taguchi, and N. Igawa. Mechanical and thermal properties of 2D and 3D SiC/SiC composites. *Journal of Nuclear Materials*, 283-287:574–578, 2000.
- [14] S. Rudov-Clark and A. P. Mouritz. Tensile fatigue properties of a 3D orthogonal woven composite. *Composites Part A: Applied Science and Manufacturing*, 39:1018–1024, 2008.
- [15] David Cripps. *Woven Fabrics*, 2016.
- [16] L Giancarli, J.P Bonal, a Caso, G Le Marois, N.B Morley, and J.F Salavy. Design requirements for SiC/SiC composites structural material in fusion power reactor blankets. *Fusion Engineering and Design*, 41:165–171, 1998.
- [17] a. Tabiei and Y. Jiang. Woven fabric composite material model with material nonlinearity for nonlinear finite element simulation. *International Journal of Solids and Structures*, 36(18):2757–2771, 1999.
- [18] N. K. Naik, Y. Chandra Sekher, and Sailendra Meduri. Damage in woven-fabric composites subjected to low-velocity impact. *Composites Science and Technology*, 60:731–744, 2000.
- [19] SK Mital, BA Bednarczyk, S.M. Arnold, and J Lang. Modeling of melt-infiltrated SiC/SiC composite properties. Technical Report October, NASA, 2009.
- [20] O. Bacarreza, M. Aliabadi, and a. Apicella. Multi-scale failure analysis of plain-woven composites. *The Journal of Strain Analysis for Engineering Design*, 47(6):379–388, jun 2012.
- [21] S G Kulkarni and X Gao. Modeling of Mechanical Response and Progressive Failure of Tri-axially Woven SiCf-SiC Composites. *13th International Conference on Fracture*, pages 1–9, 2013.
-

- [22] Anurag Dixit, R.K. Misra, and Harlal Singh Mali. Finite Element Compression Modelling of 2x2 Twill Woven Fabric Textile Composite. *Procedia Materials Science*, 6(Icmpe):1143–1149, 2014.
- [23] HongBao Guo, PuRong Jia, Bo Wang, ChengPeng Yang, and Jun Li. Characterisation and analysis of the damage coupling effects of a 2D-C/SiC composite under proportional loading conditions. *Ceramics International*, 42(1):1007–1014, 2016.
- [24] R. Udhayaraman and Shantanu S. Mulay. Multi-scale approach based constitutive modelling of plain woven textile composites. *Mechanics of Materials*, 112:172–192, 2017.
- [25] Reference Blackketter, D.E. Walrath, and A.C. Hansen. Modeling Damage in a Plain Weave Fabric-Reinforced Composite Material. *Journal of Composites Technology & Research, JCTRER*, 15(2):136–142, 1993.
- [26] A. Matzenmiller, J. Lubliner, and R.L. Taylor. A constitutive model for anisotropic damage in fibre-composites. *Mechanics of Materials*, 20:125–152, 1994.
- [27] PH Wen and MH Aliabadi. Damage mechanics analysis of plain woven fabric composite micromechanical model for mesh-free simulations. *Journal of Composite Materials*, 46(18):2239–2253, 2012.
- [28] Ph. Vandeurzen, J. Ivens, and I. Verpoest. Micro-Stress Analysis of Woven Fabric Composites by Multilevel Decomposition. *Journal of Composite Materials*, 32(7):623–629, 1998.
- [29] Â Camus. Modelling of the Mechanical Behavior and Damage Processes of Fibrous Ceramic Matrix Composites : Application to a 2-D SiC / SiC. *International Journal of Solids and Structures*, 37:919–942, 2000.
- [30] H Ismar, F Schroter, and F Streicher. Modeling and numerical simulation of the mechanical behavior of woven SiC/SiC regarding a three-dimensional unit cell. *Computational Materials Science*, 19:320–328, 2000.
- [31] G. Couegnat, E. Martin, and J. Lamon. MULTISCALE MODELLING OF THE MECHANICAL BEHAVIOUR OF WOVEN COMPOSITE MATERIALS, 2010.
- [32] Min-ge Duan, Fei Xu, and Zhong-bin Tang. The damage evolution of 2D-Woven-C / SiC composite under tension loading. *13th International Conference on Fracture*, pages 1–9, 2013.
- [33] Guangyao Li and Ted Belytschko. Element-free Galerkin method for contact problems in metal forming analysis. *Engineering Computations*, 18(1/2):62–78, 2001.
- [34] Qiang Li and Kok-Meng Lee. An Adaptive Meshless Method for Analyzing Large Mechanical Deformation and Contacts. *Journal of Applied Mechanics*, 75:041014/1–10, 2008.

-
- [35] Kalilou Sidibe, Hamadoun Bokar, Amadou Ouane, and Tiecoura Sanogo. Meshfree Method for Contact-Impact Problems Analysis with lower integration scheme. 2008.
- [36] O. Bacarreza, D. Abe, M. H. Aliabadi, and N. Kopula Ragavan. Micromechanical modeling of advanced composites. *Journal of Multiscale Modelling*, 04(02):1250005 – (1–20), jun 2012.
- [37] Z. Ullah and C.E. Augarde. Finite deformation elasto-plastic modelling using an adaptive meshless method. *Computers & Structures*, 118:39–52, mar 2013.
- [38] E Barbieri and M Meo. A meshfree penalty-based approach to delamination in composites. *Composites Science and Technology*, 69(13):2169–2177, oct 2009.
- [39] P H Wen and M H Aliabadi. Mesh-Free Micromechanical Model for Woven Fabric Composite Elastic Moduli. *Journal of Multiscale Modelling*, 1(2):303–319, 2009.
- [40] E. Potter, S. T. Pinho, P. Robinson, L. Iannucci, and A. J. McMillan. Mesh generation and geometrical modelling of 3D woven composites with variable tow cross-sections. *Computational Materials Science*, 51:103–111, 2012.
- [41] L. Saucedo-Mora and T. J. Marrow. Multi-scale damage modelling in a ceramic matrix composite using a finite-element microstructure meshfree methodology. *Philosophical Transactions of the Royal Society A: Mathematical, Physical and Engineering Sciences*, 374(2071):20150276, 2016.
- [42] Steven K Boyd and Ralph Müller. Smooth surface meshing for automated finite element model generation from 3D image data. *Journal of biomechanics*, 39(7):1287–95, jan 2006.
- [43] L.Y. Li, P.H. Wen, and M.H. Aliabadi. Meshfree modeling and homogenization of 3D orthogonal woven composites. *Composites Science and Technology*, 71(15):1777–1788, oct 2011.
- [44] L. Li, F. Aliabadi, and P. H. Wen. Micromechanical Continuum Damage Analysis of Plain Woven Composites. *Journal of Multiscale Modelling*, 06(03):1550009, 2015.
- [45] D. A. Hills;, D. Nowell;, and A. Sackfield. *Mechanics of Elastic Contacts*. Butterworth-Heinemann Ltd, first edition, 1993.
- [46] T. Belytschko, W. J. T. Daniel, and G. Ventura. A monolithic smoothing-gap algorithm for contact-impact based on the signed distance function. *International Journal for Numerical Methods in Engineering*, 55(1):101–125, sep 2002.
- [47] M. Greco, H. B. Coda, and W. S. Venturini. An alternative contact/impact identification algorithm for 2d structural problems. *Computational Mechanics*, 34(5):410–422, 2004.
-

- [48] Bin Yang, Tod A. Laursen, and Xiaonong Meng. Two dimensional mortar contact methods for large deformation frictional sliding. *International Journal for Numerical Methods in Engineering*, 62(9):1183–1225, 2005.
- [49] M Renouf, V Acary, and G Dumont. 3D frictional contact and impact multibody dynamics. A comparison of algorithms suitable for real-time applications. In *Multibody Dynamics 2005, ECCOMAS Thematic Conference*, number June, pages 21–24, 2005.
- [50] R.A. Gingold and J. J. Monaghan. Smoothed particle hydrodynamics: theory and application to non-spherical stars. *Royal Astronomical Society*, 181:375–389, 1977.
- [51] T Belytschko, Y Y Lu, and L Gu. Crack propagation by element-free Galerkin methods. *Engineering Fracture Mechanics*, 51(2):295–315, 1995.
- [52] T. Belytschko and M. Fleming. Smoothing, enrichment and contact in the element-free Galerkin method. *Computers & Structures*, 71(2):173–195, apr 1999.
- [53] Tianxiang Liu, Geng Liu, and Q. Jane Wang. An Element-Free Galerkin-Finite Element Coupling Method for Elasto-Plastic Contact Problems. *Journal of Tribology*, 128(1):1–9, 2006.
- [54] Z. Zhang, G. Liu, T. X. Liu, and Q. J. Wang. Integrated adaptive element free Galerkin model for elastoplastic contact of engineering surfaces. *Tribology - Materials, Surfaces & Interfaces*, 1(2):87–97, 2007.
- [55] Carlos Tiago and Paulo M Pimenta. An EFG method for the nonlinear analysis of plates undergoing arbitrarily large deformations. *Engineering Analysis with Boundary Elements*, 32(6):494–511, jun 2008.
- [56] Rachid E L Jid and Hicham Fihri Fassi. Meshless Solutions of 2D Unilateral Contact Problems By Penalty and Moving Least Square Approach. *Journal of Mathematical Sciences: Advances and Applications*, 15(2):55–80, 2012.
- [57] S Li, W Hao, and W K Liu. Numerical simulations of large deformation of thin shell structures using meshfree methods. *Computational Mechanics*, 25(2-3):102–116, mar 2000.
- [58] Shaofan Li, Dong Qian, Wing Kam Liu, and Ted Belytschko. A meshfree contact-detection algorithm. *Computer Methods in Applied Mechanics and Engineering*, 190(24-25):3271–3292, mar 2001.
- [59] Guangyao Li, Kalilou Sidibe, and Guirong Liu. Meshfree method for 3D bulk forming analysis with lower order integration scheme. *Engineering Analysis with Boundary Elements*, 28(10):1283–1292, oct 2004.

-
- [60] Kalilou Sidibé and Guangyao Li. Meshfree Simulation of the Penetration of Thick Metal Structure by Rigid Penetrator. *International Journal of Modern Engineering Research*, 3(1):568–573, 2013.
- [61] Sheng-Wei Chi, Chung-Hao Lee, Jiun-Shyan Chen, and Pai-Chen Guan. A level set enhanced natural kernel contact algorithm for impact and penetration modeling. *International Journal for Numerical Methods in Engineering*, pages n/a–n/a, jul 2014.
- [62] Hui-Ping Wang, Cheng-Tang Wu, and Jiun-Shyan Chen. A reproducing kernel smooth contact formulation for metal forming simulations. *Computational Mechanics*, 54(1):151–169, apr 2014.
- [63] Do Wan Kim, Wing Kam Liu, Young-Cheol Yoon, Ted Belytschko, and Sang-Ho Lee. Mesh-free point collocation method with intrinsic enrichment for interface problems. *Computational Mechanics*, 40(6):1037–1052, feb 2007.
- [64] Youssef Belaasilia, Abdelaziz Timesli, Bouazza Braikat, and Mohammad Jamal. A numerical mesh-free model for elasto-plastic contact problems. *Engineering Analysis with Boundary Elements*, 82(April):68–78, 2017.
- [65] D.a. Hu, S.Y. Long, X. Han, and G.Y. Li. A meshless local Petrov–Galerkin method for large deformation contact analysis of elastomers. *Engineering Analysis with Boundary Elements*, 31(7):657–666, jul 2007.
- [66] Kie Chan Kwon and Sung Kie Youn. The least-squares meshfree method for rigid-plasticity with frictional contact. *International Journal of Solids and Structures*, 43:7450–7481, 2006.
- [67] Alex Grishin and Jami J Shah. A Meshfree B-spline Finite Element Formulation for Unilateral Contact Problems. *ASME*, pages 1–14, 2014.
- [68] F. Greco, A. Rosolen, L. Coox, and W. Desmet. Contact mechanics with maximum-entropy meshfree approximants blended with isogeometric analysis on the boundary. *Computers and Structures*, 182:165–175, 2017.
- [69] Bo Ren and Shaofan Li. Meshfree simulations of plugging failures in high-speed impacts. *Computers & Structures*, 88:909–923, aug 2010.
- [70] Daniel Iglesias Ibáñez and Juan C. García Orden. Galerkin meshfree methods applied to the nonlinear dynamics of flexible multibody systems. *Multibody System Dynamics*, 25:203–224, 2011.
- [71] C. A. Gerlach and G. R. Johnson. A contact and sliding interface algorithm for the combined particle-element method. *International Journal of Impact Engineering*, 113:21–28, 2018.
- [72] Xiaoying Zhuang, Yongchang Cai, and Charles Augarde. A meshless sub-region radial point interpolation method for accurate calculation of crack tip fields. *Theoretical and Applied Fracture Mechanics*, 69:118–125, 2014.
-

- [73] J. R. Xiao, B. A. Gama, J. W. Gillespie, and E. J. Kansa. Meshless solutions of 2D contact problems by subdomain variational inequality and MLPG method with radial basis functions. *Engineering Analysis with Boundary Elements*, 29:95–106, 2005.
- [74] Y. Li, G. R. Liu, K. Y. Dai, M. T. Luan, Z. H. Zhong, G. Y. Li, and X. Han. Contact analysis for solids based on linearly conforming radial point interpolation method. *Computational Mechanics*, 39:537–554, 2007.
- [75] Xiaoxiang Qian, Huina Yuan, Mozhen Zhou, and Bingyin Zhang. A general 3D contact smoothing method based on radial point interpolation. *Journal of Computational and Applied Mathematics*, 257:1–13, 2014.
- [76] R. Hill. A Self-Consistent Mechanics of Composite Materials. *Journal of Mechanics and Physics of Solids*, 12:213–222, 1965.
- [77] J. Mandel. Plasticite Classique et Viscoplasticite. *Springer-Verlag*, 1971.
- [78] M.H.; Aliabadi and C.A. Brebbia. *Computational Methods in Contact Mechanics*. Computational Mechanics Publications; Computational Mechanics Publications Ltd; Computational Mechanics Inc and Elsevier Science Publisher Ltd, 1993.
- [79] J. E. Mottershead. Lagrange multiplier formulaion for FEM. In M.H. Aliabadi and C.A. Brebbia, editors, *Computational Methods in Contact Mechanics*, chapter Three, pages 99–125. Computational Mechanics Publications; Computational Mechanics Publications Ltd; Computational Mechanics Inc and Elsevier Science Publisher Ltd, 1993.
- [80] G.R. Liu, G.Y. Zhang, Y.T. Gu, and Y.Y. Wang. A meshfree radial point interpolation method (RPIM) for three-dimensional solids. *Comput Mech*, 36:421–430, 2005.
- [81] Zhi-Hua Zhong and Larsgunnar Nilsson. A CONTACT SEARCHING ALGORITHM FOR GENERAL CONTACT PROBLEMS. *Computers & Structures*, 33(I):197–209, 1989.
- [82] K. W. Man;, M.H.; Aliabadi, and D. P. Rooke. Analysis of contact friction using the boundary element method. In M.H. Aliabadi and A.C. Brebbia, editors, *Computational Methods in Contact Mechanics*, chapter One, pages 1–60. Computational Mechanics Publications; Computational Mechanics Publications Ltd; Computational Mechanics Inc and Elsevier Science Publisher Ltd, 1993.
- [83] Jacob Aboudi. Microinechanical Analysis of Composites by the Method of Cells. *Appl Mech Rev*, 42(7):193–221, 1989.

- [84] N V De Carvalho, S T Pinho, and P Robinson. Reducing the domain in the mechanical analysis of periodic structures , with application to woven composites. *Composites Science and Technology*, 71(7):969–979, 2011.

6

Conclusion

In the process of modelling damage in turbine blades and their coatings, four studies were carried out in this thesis, outcomes of which are summarised here. The work in the first two chapters focused on the topic of Ni-based turbine blades and the damage in their TBC system; and the last two chapters focused on development of numerical models for studying the effect of micro-cracks in woven $\text{SiC}_f/\text{SiC}_m$ composites on its effective property.

- **Swelling as the Main Source of Rumpling in TBC, chapter 2** : In this work on modelling rumpling damage in TBCs, it was shown that swelling, which is a relatively new phenomenon, is the underlying source of rumpling growth in the TBC systems. Previously it was believed that source of rumpling growth is from phenomenon such as phase transformation and thermal mismatch that occur during the heating and cooling processes of a thermal cycle. However, the experimental results obtained from the work of Tolpygo & Clarke showed that without all of those phenomenon rumpling still grows in the TBC system, which proves that the underlying source of rumpling had not been discovered yet. In this project the existing analytical model of rumpling by Balint *et al.* was modified to include the swelling effect, and qualitatively reproduced the experimental results. Analysing the results from the model showed that most of the rumpling growth occurs in the dwell duration where only creep and swelling effects are active; effect of swelling was also apparent in the heating and cooling processes. Swelling is a volume expansion phenomenon which is accompanied by an increase in the stress level which in turn activates the creep deformation, leading to rumpling growth. Hence, rumpling growth can be considered to be mainly a result of the trade-off between the stress rise from swelling and stress relaxation from creep. While it can be argued that parameters such as phase transformation and thermal

mismatch can affect rumpling, but the main source for it is swelling.

- **Lateral Growth in the Bond Coat and Inter-diffusion Layers, chapter 3** : Chen *et al.* in their experimental work on measuring the lateral growth of the bond coat/inter-diffusion layers of TBC system after 50 hours of isothermal heat treatment at 1150°C, came across a puzzling result. Their results showed a large lateral deformation for the bond coat and almost none for the inter-diffusion layer. This was surprising because swelling effect which is a volumetric phenomenon, was observed in both layers, hence, it should have led to lateral swelling for the inter-diffusion layer as well. As a collaboration with Chen *et al.*, a postulation was put forward; given the relationship between the creep deformation and in-plane stresses, it is possible for the inter-diffusion layer to have a lower creep strength than the bond coat leading to higher stress relaxation and less lateral growth. This postulation was tested and verified using an analytical model of the stress in the layers, including swelling, and a finite element model with two coating layers. This two-layered model was used for a sensitivity study on elastic and creep properties of the inter-diffusion layer in order to match the lateral deformation of the system with the experimental results. While the outcome of this sensitivity study confirmed the proposed postulation but there was no reasonable combination of material properties that produced the experimental edge profile. This showed that a two-layered model of the coating system is not detailed enough to capture the true lateral behaviour of this system, mainly because the Ni/Al diffusion which are responsible for swelling, are not uniformly distributed across the coating thickness. This is why a four-layered coating model of the system was suggested; this four layered model of the coating system produced a qualitative match with the experimental results, which captured the main characteristics of the experimental edge profile. This outcome showed that the proposed four-layered coating model gives the tool for understanding the mechanical behaviour of the materials involved in this system; additionally, this model highlights the importance of the multi-layered nature of the bond coat on its swelling behaviour. Given the high sensitivity of rumpling growth on the swelling behaviour of the bond coat, particularly, at the region near the TGO, the fact that bond coat is found to be multi-layered in nature is very important. Therefore, it is clear that in order to model rumpling more accurately, one needs to develop a multi-layered model (analytical or others) of the bond coat layer.
- **MQ-RPIM Optimisation for Engineering Single Body Problems, chapter 4**: The focus in this chapter was on developing a step-by-step algorithm for finding the converged solution and optimum shape parameters of the general MQ-RPIM method when applied to different engineering single body problems, even if the analytical solution is not known. The introduced algorithm divides into three main parts; i) finding the best number of nodes, background cells and integration points for a converged solution; ii) finding the smallest support domain size that

gives the most accurate result; and iii) optimising the MQ-RPIM shape parameters, i.e. α_c and q , by choosing the combination that gives the lowest error. The application of this algorithm was demonstrated through three examples in both two- and three-dimensions, leading to a number of general conclusions about the MQ-RPIM method; i) while RPIM is slower than FEM for the same number of nodes, it is more flexible for complex geometries and reaches convergence at much faster rate; ii) use of linear polynomial terms in shape function calculations increases the accuracy but makes the choice of MQ-RPIM parameters problem dependent; and iii) the optimum MQ-RPIM shape parameters are different between two- and three-dimensional versions of the same example.

- **MQ-RPIM Model of Plain Woven Composite with Frictionless Contact, chapter 5:**

As part of the project on modelling micro-delaminations at the yarns-matrix interface of woven composite using meshfree methods, the first three-dimensional MQ-RPIM frictionless contact code was developed and verified using two Hertzian contact problems. This three-dimensional contact model was then successfully applied to the preliminary model of the plain woven composite unit cell, where the displacement profile of the model subject to an applied uniform strain was computed under two extreme conditions; i) full-stick (0% delamination) and ii) full-slip (100% delamination). This model forms the first building block towards the final model of the woven $\text{SiC}_f/\text{SiC}_m$ composite unit cell with frictional contact at the yarn-matrix interface.

7

Future Work

While the models in each of the chapters have produced a conclusive result for their corresponding topic, there are always ways that one can develop them further or apply them to different conditions. Here are a few suggestions for each individual chapter,

- **Swelling as the Main Source of Rumpling in TBC, chapter 2** : The work carried out in this chapter opened up the door to various projects that can be done around the topic of swelling. One of these possibilities which is directly related to this work, is to experimentally measure the swelling of the bond coat layer for a range of thermal cycling lowest temperature, and use the results together with the developed model here, to further understand the role of swelling in rumpling growth. One could also improve this model to a multi-layered coating case and study the effect of multiple-layer swelling on rumpling.
- **Lateral Growth in the Bond Coat and Inter-diffusion Layers, chapter 3** : Given the limited experimental information for the swelling behaviour of the bond coat and inter-diffusion layers as a four-layered system, one should experimentally measure the swelling of these four layers and use that in the four-layered model developed here to understand the mechanical behaviour of the inter-diffusion layer. Additionally, and more importantly, because of the multi-layered swelling behaviour of the bond coat, it is important to improve the existing or develop new rumpling models to incorporate this non-uniform swelling nature of the bond coat.
- **MQ-RPIM Optimisation for Engineering Single Body Problems, chapter 4**: The algorithm introduced in this chapter has been applied manually, it would be more efficient if the processes of this algorithm can be implemented in the code, so the user can define the error

indicators and let the code run until the optimum choices are found. Additionally, given that there are separate developments in the literature on different sections of the algorithm, one can update and adapt the new findings into the algorithm.

- **MQ-RPIM Model of Plain Woven Composite with Frictionless Contact, chapter 5 :**

Given the nature of the work here, there are a lot of avenues where this model can be improved. Two of the most immediate future works are i) application of the optimisation algorithm to the preliminary model of the woven composite unit cell, and ii) testing the capabilities of the developed RPIM contact code for the preliminary model of the unit cell when strains are applied in directions other than xx . On a longer term future works, there are two separate avenues that can be followed; i) work on speed optimisation of the RPIM contact models, and ii) development of the complete model of the woven SiC_f/SiC_m composite with frictional contact at the yarn-matrix interface.

For the speed optimisation, one way of decreasing the simulation time would be to use faster solvers; or make the use of penalty method for contact calculations, because the highest computational time was obtained during checking of contact conditions. There is one additional way to improve the computational time, which is directly related to the RPIM method; this approach only would work for small displacement problems, where it is possible to build the material \mathbf{K} matrix once and avoid re-building it throughout the convergence and optimisation process.

Development of a three-dimensional frictional contact model in RPIM which is capable of modelling micro-cracks at the yarn-matrix interface of woven composite, is a very long process; first part of which was developed here. The next step that follows from this works is the manual implementation of micro-cracks at various yarn-matrix interface locations in the unit cell using the slip-stick condition, where the contact between faces of the micro-cracked region is still frictionless. This statistical study can be used to study the effect of three important parameters on the behaviour of the unit cell; i) location, ii) length, and iii) total percentage of frictionless micro-delaminations. Once these primary studies on the effective property of the plain woven composite are carried out, the two- and three-dimensional RPIM frictional contact models can be developed and verified using Hertzian contact problems for frictional cases. Following the verification, the three-dimensional frictional contact model in RPIM can be used to create the final model of the woven SiC_f/SiC_m composite with frictional contact at the yarn-matrix interface.

Given the broad nature of this thesis, while there are individual future works that can be done on each chapter, there are possible cross paths where the methods developed in one chapter can be used for the work in other chapters. For example, one can use the analytical model developed for the

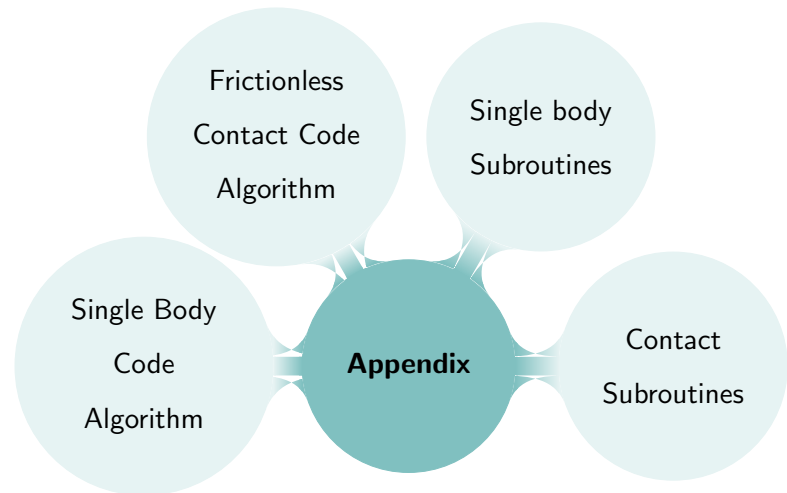
TBCs for studying the behaviour of environmental barrier coating (or EBCs) on the woven $\text{SiC}_f/\text{SiC}_m$ composites; or the meshfree contact model developed for woven composites can be adjusted and used for contact related problems in the TBC system such as crack growth, where using finite element methods produce distorted element or are inefficient in mesh refinement at crack tips. The second interchange is more realistically possible when the frictional model of the contact in RPIM is fully developed.

7.1 Outputs

As a result of this work, there are two publishable papers in preparation from chapter 2 and chapter 3, and a potential journal paper in the rise from chapter 4 and chapter 5:

- F. Ostovari, D. Balint. “On the relationship between bond coat swelling and oxide rumpling in thermal barrier coatings.”
- Y. Chen, F. Ostovari, P. Xiao, D. Balint. “Lateral swelling of a platinum-modified nickel aluminate bond coat during vacuum annealing and its correlation with surface rumpling.”
- F. Ostovari, M.H. Aliabadi, A. S. Nobari. “An optimisation algorithm for the parameters involved in radial point interpolation method and its application to 2D/3D examples including frictionless Hertzian contact problems.”

A



MQ-RPIM Code Structure

A.1 Introduction

While chapter 4 and chapter 5 explain the theories behind the MQ-RPIM codes developed in this work, this chapter gives an outline of the algorithm and subroutines used for them. The development and verification of the single body and frictionless contact RPIM models are the main products of the second part of this work. This is why understanding the algorithm and code structure used in these models is very important. In this chapter an outline of the algorithm used for each model and the underlying subroutines are explained. The code structure explained here goes hand in hand with the theories explained in chapter 4 and chapter 5.

Figure A.1 shows the algorithm behind the main MQ-RPIM code developed for single body and frictionless contact problems. These algorithms are the same for the two- and three-dimensional forms of the problem; the difference between them is embedded within the subroutines, as will be discussed later in this chapter. While these codes are written for MQ-RPIM method they are applicable to other forms of RPIM method. As can be seen from Figure A.1, there are many common subroutines between the two models, which is why the common subroutines are only explained once. Please note, because of the large size of the codes in this work (above 7600 lines including the subroutines), the codes are not included in this chapter.

In each model the code takes in the input parameters defined by the user and produces results file containing the displacement, stress, strain and error indicators for the given problem. For all the codes here, there is an additional file which shows the total simulation time of the model and its break down for every subroutine. This allows the user to find the places in the code where most of the

computational time is spent on, so if possible they, can improve upon the computational speed.

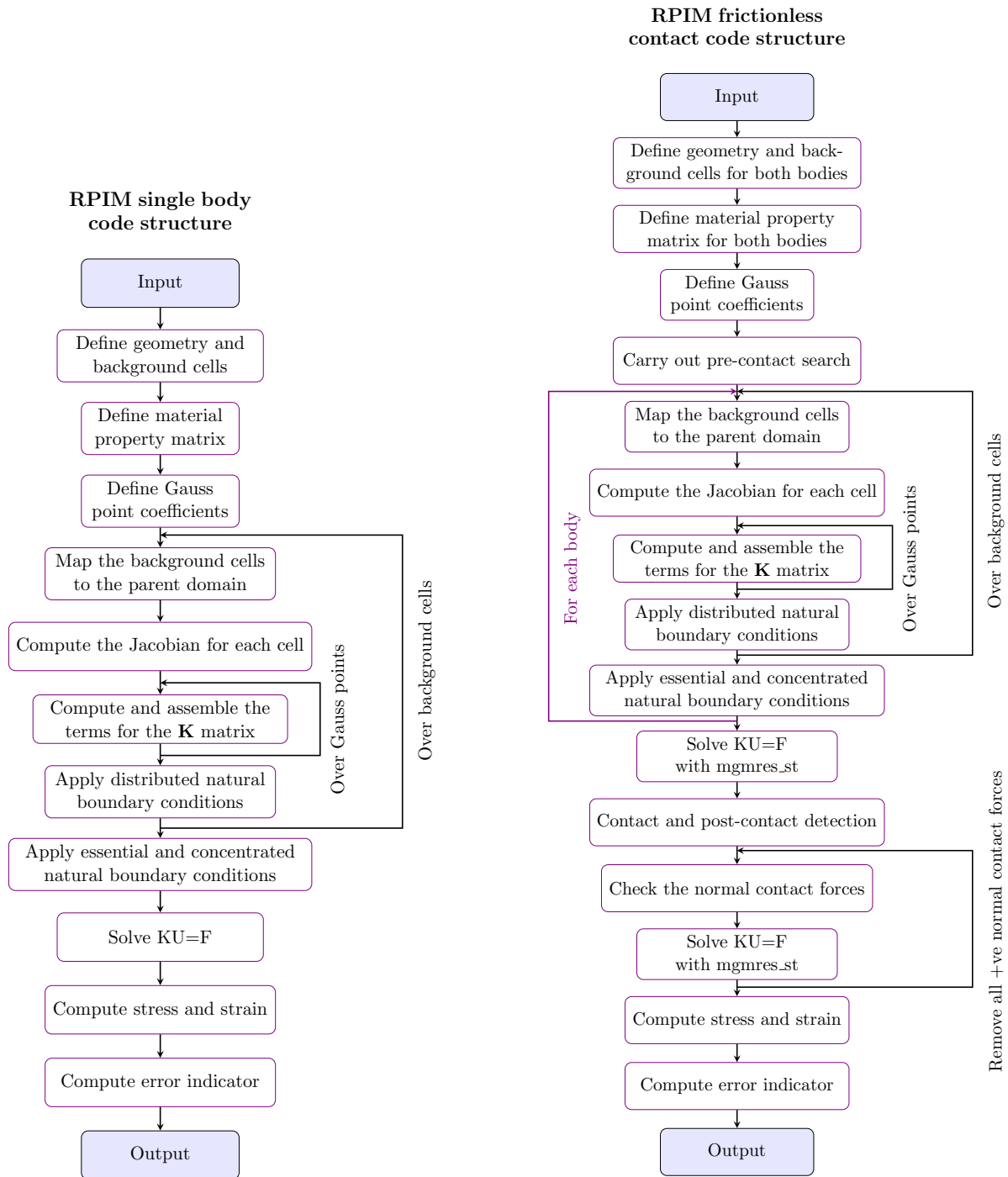


Figure A.1: The code structure used for the RPIM single body and frictionless contact problems.

A.2 RPIM Single Body Code Structure

In this section the subroutines used for the single body algorithm in Figure A.1 are discussed with the use of pseudocode, if necessary. The order by which the subsections are outline follows the algorithm shown in the Figure A.1.

A.2.1 Input

Input is a file called “parameter.h” where the user can define all the input parameters needed for the RPIM code. This file is used in all versions of the code, however, the parameters involved in it are different for single body and contact problems. For single body problems the parameters are defined for a single domain whereas, in the case of frictionless contact problem not only parameters are defined for every domain involved in the contact but also the parameters that are used in the contact between them.

For the single body examples the “parameter.h” file consists of different sections: i) variable precision, where the precision of the values used for the computations is defined, i.e. whether a variable is single or double precision; ii) constants, where any relevant constant values used in the calculations are defined, e.g. the number PI; iii) geometry parameters, where parameters required to produce the field nodes for a given geometry, including the node spacing are defined; iv) background cell parameters, where the variables required to produce the background cells for a given problem domain, including number of Gauss points per direction per background cell, are defined; v) material properties including but not limited to Young’s modulus and Poisson ratio; and vii) finally boundary conditions, where the relevant boundary values, such as the force magnitude, are defined by the user.

The parameters involved in the input file need to be adjusted for each problem, because for different materials, geometries and problems different parameters are needed, however, the parameters required for the MQ-RPIM shape function calculations are fixed for each problem. Unless, in contact between two bodies where the user can choose to define these parameters differently for different bodies; this option is not explored this work because it adds an additional degree of freedom in the code development.

A.2.2 Define Geometry and Background Cells

A.2.2.1 *Geometry*

To define the geometry of the problem at hand, the code takes the relevant input from “parameter.h” and produces the field nodes for that geometry. Please note this subroutine has to change for different shapes; one can also use other softwares to produce the nodes and then input them into the main code. However, for all the geometries involved in this work, a code is written from scratch.

A.2.2.2 *Background Cells*

Background cells are defined in a much simpler manner; for any given geometry this subroutine takes the relevant information from “parameter.h” and produces square (2D) or cube (3D) shaped cells for

the whole problem domain, which may also fall out of the boundaries of the problem domain. This is not an issue because later in the main code, the Gauss points that are outside of the problem domain are removed from the calculations. Additionally, in this subroutine for every node that forms one background cell, a local node number is assigned to for the computations in the parent domain. This node numbering, i.e. a in Equation 4.14, is used for computation of the Jacobian matrix, which is similar to the format used in finite element.

A.2.3 Define Material Property Matrix

This subroutine simply takes in the Young's modulus and the Poisson ratio, and produces the \mathbf{D} matrix as defined in Equation 4.8 and Equation 4.9 of chapter 4. Given that in these calculations the materials are assumed to be elastic and isotropic, the equations used in this subroutine are also accordingly defined. However, for more complex materials, the equations and definitions in this subroutine need to be changed accordingly.

A.2.4 Define Gauss Point Coefficients

This subroutine takes in the order of the Gaussian integration, i.e. ngp in Equation 4.10, and produces the factors required for using the Gauss point integration scheme, i.e. ξ and w in Equation 4.10 and Equation 4.11 of chapter 4. These factors are standard for Gaussian integration which can be calculated or taken from the available tables in the literature.

A.2.5 Mapping to the Parent Domain

Following the description of Figure 4.2 in chapter 4, this subroutine produces the coordinates of the background cell in the parent domain for both the two- and three-dimensional background cells. This subroutine takes in an empty array and the dimensions, and fills in the empty array with the relevant coordinates of the background cell in the parent domain.

A.2.6 Compute Jacobian

Jacobian is the determinant of the mapping matrix, i.e. Equation 4.14, between the real and parent spaces, as explained in chapter 4. Therefore, the information about the Gaussian coefficients, parent space, and background cells are taken by this subroutine and an array containing the Jacobian and relevant values for the Gaussian integration are produced.

A.2.7 Compute and Assemble \mathbf{K}

For every Gaussian point there is a support domain surrounding it, which defines the field nodes that contribute to approximation of its displacement, i.e. Equation 4.15. The rows and columns of the \mathbf{K}

matrix corresponding to every field node that is used for this approximation is computed in this section according to Equation 4.28. Once the nodal \mathbf{K} matrix terms are computed for the each Gaussian point, they are assembled in the global \mathbf{K} matrix as part of the main code, following Equation 4.29, which is shown in the following pseudocode.

```

!----- Assembling the global stiffness matrix
DO k_x = 1, DIM*ns
  DO k_y = 1, DIM*ns
    K_Global(Node_I(k_x), Node_I(k_y)) = &
      K_Global(Node_I(k_x), Node_I(k_y)) + &
      K_Nodal(k_x, k_y)
  ENDDO
ENDDO

```

A.2.8 Apply Boundary Conditions

There are three kinds of boundary condition that can be applied; i) distributed natural boundary conditions, ii) concentrated natural boundary conditions, and iii) essential boundary conditions. To apply the distributed boundary condition, the subroutine takes in the information about the background cells, value of the boundary condition, field nodes, and RPIM shape function and computes the equivalent force terms for the \mathbf{F} vector. This subroutine is applied as part of the loop that goes through every background cell, as shown in the algorithm in Figure A.1. The concentrated natural and essential boundary conditions, on the other hand, can be applied outside of the loop. To apply the concentrated natural boundary conditions, one can directly change the terms of the \mathbf{F} vector for the relevant nodes. For the essential boundary conditions, once the relevant field nodes are identified, one can use Equation 4.34 to apply displacement boundary conditions.

A.2.9 Solve $\mathbf{KU} = \mathbf{F}$

To solve the linear system of equations, i.e. $\mathbf{KU} = \mathbf{F}$, two existing codes are used; I) DGESV, which is a direct solver taken from ¹; and II) mgmres_st which is an iterative solver taken from ². For problems with small matrices such as 2D single body problems, the DGESV method is used because it gives an accurate solution; however for problems with large matrices such as 3D or contact problems, DGESV is very slow and inefficient, therefore, the mgmres_st iterative method is used to speed up the computation.

DGESV is a built-in subroutine in Fortran 90 so one can call this subroutine in the form of

¹<http://www.netlib.org/lapack/explore-3.1.1-html/dgesv.f.html>

²https://people.sc.fsu.edu/~jburkardt/f_src/mgmres/mgmres.f90

```
CALL DGESV(N, NRHS, A, LDA, IPIV, B, LDB, INFO),
```

to compute the solution to a real system of equations, i.e. $\mathbf{A} \mathbf{X} = \mathbf{B}$. Here N is the number of linear equations or size of \mathbf{A} matrix; $NRHS$ is the number of columns in \mathbf{B} which in this case is 1; \mathbf{A} is the \mathbf{K} matrix in these codes; LDA is the leading dimension of \mathbf{A} which for these codes will be size of \mathbf{K} ; $IPIV$ is the pivot indices that define the permutation matrix; \mathbf{B} is the \mathbf{F} vector in these codes; LDB is the leading dimension of \mathbf{B} ; and $INFO$ gives information about how the solution has been carried out. To learn about this subroutine one can refer to <http://www.netlib.org/lapack/explore-3.1.1-html/dgesv.f.html>.

`mgmres_st`, unlike, `DGESV` requires a preparation of the matrices before using the solver; it requires the zero terms to be removed from the matrices so the solver can work efficiently. This solver is a subroutine taken from https://people.sc.fsu.edu/~jburkardt/f_src/mgmres/mgmres.f90; for more information about how to use this subroutine please refer to this link.

A.2.10 Compute Stress and Strain

Once the system of linear equations is solved producing the final displacement of the whole problem domain, the stress and strain values for each field node can be computed using this subroutine, which is based on Equation 4.35. To compute the \mathbf{B} matrix, this subroutine uses the support domain and shape function subroutines. Once the displacement, stress and strain values are obtained, depending on what are the chosen error indicators for a given problem, the error indicators are computed.

A.3 RPIM Frictionless Contact Code Structure

The main subroutines and parts of the RPIM code, developed in this work for a single body problem, are shown in the previous section. For frictionless contact problem between two bodies, the same subroutines applies, however, now there are three additional parts to the code which tailors it to frictionless contact problems. As discussed in chapter 5, there are three steps in contact modelling introduced here; i) pre-contact search, ii) contact detection, and iii) Post-contact detection. These three steps are implemented in two subroutines and a part of the main code which are presented here.

For problems with contact between two bodies, all the parameters for the geometry, background cell and material property in “parameter.h” are defined for each body involved in the contact. Whereas, the parameters for the support domain and shape function remain the same for both bodies, (Please note for more flexibility at the cost of more complexity, one can also define these parameters separately for each body). Additionally, by introducing contact into the code, there are parameters that are solely

for the contact calculations; for example coefficient of friction, which is zero here, the factor defining the contact radius around one target sector or factors defining the contact territory.

A.3.1 Pre-Contact Search

The pre-contact search is written in a module called “PRE_CONTACT_DETECTION”, which consists of “BODY_TERR” and “TEST_PAIR_DETECT” subroutines. “BODY_TERR” subroutine takes the coordinates of the field node for each body and the relevant contact factors, and produces the target segments, the normal vector for each segment, normal vector for each field node on the surface of each body and contact territory for them as shown in Figure 5.6.

The second subroutine, or “TEST_PAIR_DETECT”, uses “BODY_TERR” to define the contact territory for each body and the target segments; those information are then used to identify the contactor field nodes that fall into the common contact territory and form test-pairs with the identified target segments, based on the discussion in subsection 5.2.2.1.

A.3.2 Contact Detection

Referring to Figure A.1, when the system of linear equations have been solved for the first time without addition of contact constraints, the post-contact subroutine is used to detect the contactor nodes that have penetrated through (or contacted) the target body. This module takes in the first time computed \mathbf{U} vector, the array of test-pairs and two empty arrays which later will be filled with the terms of \mathbf{K} matrix and \mathbf{F} vector related to the contact constraint.

Based on the displacement of each contactor node and its relation to the target segment, the contactor node that crosses the segment is considered as contacted. Once contacted node is identified, Equation 5.10, Equation 5.11, are used to compute the terms of \mathbf{K} matrix and \mathbf{F} vector. As an starting point in this subroutine, it is assumed that all the contactor nodes that have contacted the target have stuck to their corresponding target segment, however, in the next step of the code the results are checked against Equation 5.5 for slip and stick.

A.3.3 Checking the Normal Contact Forces

Once the \mathbf{K} matrix and \mathbf{F} vector are updated with the contact constraints, for each contacted node the conditions described in subsection 5.2.2.3 are checked. Firstly, the tangential conditions based on Equation 5.5 are checked where the code goes through each contacted contactor node and checks whether the stick assumption from the previous step is valid. If not, then the relevant terms of the \mathbf{K} matrix and \mathbf{F} vector are changed for that contactor node to incorporate for the slip condition. With the updated the \mathbf{K} matrix and \mathbf{F} vector system of equations is solved again. This process continues

until all the contacted nodes are checked.

Once all the slip and stick conditions are checked, the code goes to check the sign of the computed normal contact forces. For any contacted node if sign of the normal contact force is positive, that node is released which means its corresponding contact constraints are removed and the system of equations is solved again. This process continues until the sign of the normal force for all of the contacted contactor nodes is checked. This process of checking the contact conditions both normal and tangent to the contact surface has the longest computational time in the developed contact model in this work. In order to reduce the computational time for this contact code, one should reduce the computational time in this part of the code.

At the end the code computes the stress and strain for the problem domain and produces the output file. There is an additional output file in the contact code compared to the code for single body problems, which holds all the information about the nodes that are in the contact between two bodies.